Nouvelle lecture des structures funéraires de l'âge du Bronze en Mongolie via une analyse des éléments architecturaux, de leur agencement et de leur forme

Tanguy Rolland

THESE DE DOCTORAT DE L'ETABLISSEMENT UNIVERSITE BOURGOGNE FRANCHE-COMTE

PREPAREE A L'UNIVERSITE DE DIJON

Ecole doctorale n°594

SEPT - Sociétés, Espaces, Pratiques, Temps

Doctorat d'Archéologie

Par

M. Rolland Tanguy

Nouvelle lecture des structures funéraires de l'âge du Bronze en Mongolie via une analyse des éléments architecturaux, de leur agencement et de leur forme

Thèse présentée et soutenue à Dijon, le 14 décembre 2022

Composition du Jury :

M. Raffin Romain	Professeur des universités à l'Université Bourgogne - Franche-Comté	Président du jury
Mme. Fritz Carole	Directrice de recherche, Centre de Recherche et d'Etude pour l'Art Préhistorique Maison de la Recherche	Rapporteur
M. Deroin Jean-Paul	Professeur des universités, Université de Reims Champagne-Ardenne UFR Sciences Exactes et Naturelles	Rapporteur
M. Sonnemann Till	Full professor, Otto-Friedrich-Universität Bamberg	Examinateur
M. Monna Fabrice	Professeur des universités à l'Université Bourgogne - Franche-Comté	Directeur de thèse
M. Magail Jérôme	Chargé de recherche Musée D'Anthropologie Préhistorique de Monaco	Codirecteur de thèse
M. Wirth Stefan	Professeur des universités, Université Bourgogne - Franche-Comté	Invité

SEPT
ÉCOLE DOCTORALE

Titre : Nouvelle lecture des structures funéraires de l'âge du Bronze en Mongolie via une analyse des éléments architecturaux, de leur agencement et de leur forme

Mots clés : Archéologie, Analyse spatiale, Age du Bronze, Intelligence artificielle, Imagerie aérienne, Modélisation 3D

Résumé : Le paysage archéologique de Mongolie est marqué par la présence de nombreux monuments funéraires (les khirigsuurs) et de stèles gravées (les pierres à cerfs) érigés par les populations nomades de la fin de l'âge du Bronze. Les premières observations montrent une grande régularité dans le choix et l'agencement des éléments architecturaux et iconographiques utilisés lors de la construction de ces structures. Ceci semble indiquer l'existence de traditions partagées et d'une cohérence sociale entre les communautés nomades sur un territoire couvrant près de deux fois celui de la France. Les données aujourd'hui disponibles ne permettent pas de prendre assez de recul pour établir des modèles sociaux à l'échelle d'une province, et bien entendu encore moins à celle du pays. Une telle étude, encore jamais réalisée sur l'ensemble du territoire mongol, nécessiterait la mise en place de méthodes d'acquisition, d'analyse et de traitement de la donnée, adaptées à l'établissement de larges corpus fournis par la prospection. Ceci impliquerait nécessairement une réduction de la précision des informations recueillies, mais aussi un gain notable en termes d'exhaustivité et donc de représentativité statistique.

Les solutions proposées ici s'inspirent de nombreux domaines scientifiques. Elles sont appliquées à un échantillon de monuments appartenant à deux vallées du centre de la Mongolie. L'acquisition de ces structures est facilitée par la production massive de modèles 3D et d'orthomosaïques des sites, tous deux obtenus par photogrammétrie. Une méthode de mise en valeur du relief des modèles 3D a été développée afin de fournir une lecture tridimensionnelle des symboles gravés sur les stèles. À partir des orthomosaïques, les pierres composant les khirigsuurs ont été délimitées avec grande précision grâce à un apprentissage automatique supervisé ; le plan du monument devient alors facile à appréhender. De nouveaux systèmes de description des pierres à cerfs et des khirigsuurs ont été établis, puis appliqués pour produire des classifications non supervisées de ces structures.

Au final, de nouveaux concepts et outils ont été développés. Ils offrent de belles perspectives pour l'étude des pierres à cerfs et des khirigsuurs à très large échelle, tout en restant aisément transposables à d'autres problématiques archéologiques.

UBFC
UNIVERSITE
BOURGOGNE FRANCHE-COMTE

Université Bourgogne Franche-Comté
32, avenue de l'Observatoire
25000 Besançon

SEPT
ÉCOLE DOCTORALE

Title : A new reading of Bronze Age funerary structures in Mongolia by analysing of their architectural elements, arrangement and form.

Keywords : Archaeology, Spatial analysis, Bronze Age, Machine learning, Remote sensing, 3D model

Abstract : The archaeological landscape of Mongolia is marked by the presence of numerous funerary monuments (khirigsuurs) and engraved stelae (deer stones), erected by nomadic populations at the end of the Bronze Age. The first observations indicate great regularity in the choice and arrangement of the architectural and iconographic elements at the time when these structures were built. This regularity suggests the existence of shared traditions and social coherence between nomadic communities in a territory covering almost twice that of France. The data available today do not provide sufficient perspective to establish social models at the level of a province, and even less so at the scale of the country. Such a study, never before carried out over the entire Mongolian territory, would require the implementation of data acquisition, analysis, and processing methods adapted to the establishment of a large corpus obtained by archaeological prospection. This would necessarily imply some reduction in terms of precision with regard to the information collected, but would also offer significant gains in terms of exhaustiveness, and therefore in statistical representativity.

The solutions proposed here are inspired by many other scientific fields. They are applied to a series of monuments in two valleys in central Mongolia. The acquisition of these structures was facilitated by the production of hundreds of 3D models and orthomosaics of the sites, obtained by photogrammetry. A method for highlighting the relief of 3D models was developed in order to provide a three-dimensional reading of the symbols engraved on the stelae. From the orthomosaics, the stones composing the khirigsuurs were delineated with great precision through supervised machine learning approaches; understanding the layout of the monument was thus greatly facilitated. New systems for describing deer stones and khirigsuurs were established, and then applied in order to produce unsupervised classifications of these structures.

As a result, new concepts and tools were developed. They offer great prospects for the study of deer stones and khirigsuurs on a very large scale, while remaining easily transposable to other archaeological sites and issues.

UBFC
UNIVERSITE
BOURGOGNE FRANCHE-COMTE

Université Bourgogne Franche-Comté
32, avenue de l'Observatoire
25000 Besançon

Table des matières

Table des figures

Remerciements

Je souhaite tout d'abord adresser un immense merci à mes deux co-directeurs, Fabrice Monna et Jérôme Magail qui m'ont offert l'opportunité d'entreprendre cette grande aventure que représente le travail de thèse. Je leur suis reconnaissant pour tout ce qu'ils m'ont appris, ainsi que pour leur soutien tout au long du chemin.

Je tiens particulièrement à remercier Anne-Caroline Allard pour son aide précieuse sur le terrain, nos nombreuses discussions, ainsi que pour avoir immortalisé de précieux instants de nos missions de terrain qui me rappellent l'aspect humain présent derrière tout projet scientifique. Je lui souhaite le meilleur pour la thèse qu'elle prépare au moment où j'écris ces mots.

Merci à la mission conjointe Monaco-Mongolie du Musée d'Anthropologie préhistorique de Monaco de m'avoir permis de partir en Mongolie pour entreprendre la collecte des données utilisées lors de cette étude, mais également pour m'avoir permis de travailler en Sibérie.

Je remercie Josef Wilzcek et Yury Esin pour les données acquises sur le terrain avant le début de mon travail de doctorat, ainsi qu'Elodie Maronat pour l'encodage des symboles gravés sur les stèles.

J'exprime toute ma gratitude à Carole Fritz, Jean-Paul Deroin, Stefan Wirth, Till Sonnemann et Romain Raffin, membres du jury, qui ont accepté de prendre le temps de lire et d'évaluer mon travail.

Un remerciement spécial à toutes les personnes avec qui j'ai pu travailler, discuter et qui m'ont aidé à avancer sur certains points épineux de ce travail de thèse. Je pense tout particulièrement à Nicolas Navarro et à Jean-Francois Buoncristiani du laboratoire Biogéosciences, à Ludovic Granjon du pôle géomatique de la MSH de Dijon, à Benjamin Bohard, ainsi qu'à Catherine Labruère-Chazal et Ahmed Jébrane de l'Institut de Mathématiques de Bourgogne. Un grand merci à Carmela Chateau-Smith qui a relu et corrigé les projets d'articles en anglais, et cela malgré toutes les erreurs et coquilles.

Merci aux personnes qui travaillent au laboratoire ARTEHIS de Dijon, aux collègues et amis, pour leur accueil durant ces quatre années.

Je remercie toutes les personnes qui ont rendu possible les missions de terrain auxquelles j'ai eu la chance de participer (Mongolie, Sibérie, et Maroc).

Je remercie également ma famille et mes amis qui m'ont soutenu et encouragé tout au long de ce travail de thèse.

Ce travail a en partie été financé par un projet de recherche nommé ROSAS, soutenu par la mission conjointe Monaco – Mongolie, l'Université de Bourgogne et le Réseau National des MSH, que je remercie.

Introduction

L'âge du Bronze en Mongolie est considéré comme une période de grands changements sociaux. Les populations qui étaient sédentaires vont peu à peu adopter le pastoralisme monté et un mode de vie nomade. Les familles vivent désormais principalement de l'élevage de chevaux, de bovins et de moutons avec un cycle saisonnier de migrations entre plusieurs sites d'occupations. Ce changement de mode de vie s'accompagne d'une augmentation démographique, ainsi que d'une multiplication des interactions sociales. Tous ces facteurs ont fortement impacté le paysage monumental de l'époque avec l'apparition de deux types de constructions : les stèles gravées anthropomorphes nommées pierres à cerfs, et les complexes funéraires et rituels, connus sous le nom de khirigsuurs. Tous deux font l'objet de dépôts rituels de restes de chevaux qui montrent la place prédominante du cheval dans ces sociétés. On les retrouve répartis sur l'ensemble du territoire mongol et par-delà ses frontières (Fig. 1), présentant les mêmes éléments architecturaux, les mêmes organisations et les mêmes styles iconographiques. Malgré l'incertitude qui subsiste au sujet du rôle de ces monuments, une chose est sûre : ils sont le signe évident d'une pratique commune à l'ensemble des groupes de l'âge du Bronze en Mongolie. Ces monuments comptent parmi les rares traces associées à cette culture ; les sites d'habitats laissant peu de traces, ils sont très difficiles à identifier. Leur étude est d'autant plus intéressante qu'elle montre une évolution religieuse et hiérarchique dans les sociétés de l'époque qui formeront, au début de l'âge du Fer, la culture Xiongnu, c'est-à-dire le premier empire des steppes. La culture présente en Mongolie à l'âge du Bronze reste assez mal définie. Elle est le plus souvent caractérisée en mettant en parallèle les objets gravés sur les pierres à cerfs et ceux trouvés dans les fouilles des cultures voisines, tant spatialement que chronologiquement (e.g. Pazyryk, Tagar, Karasuk, Scythe).

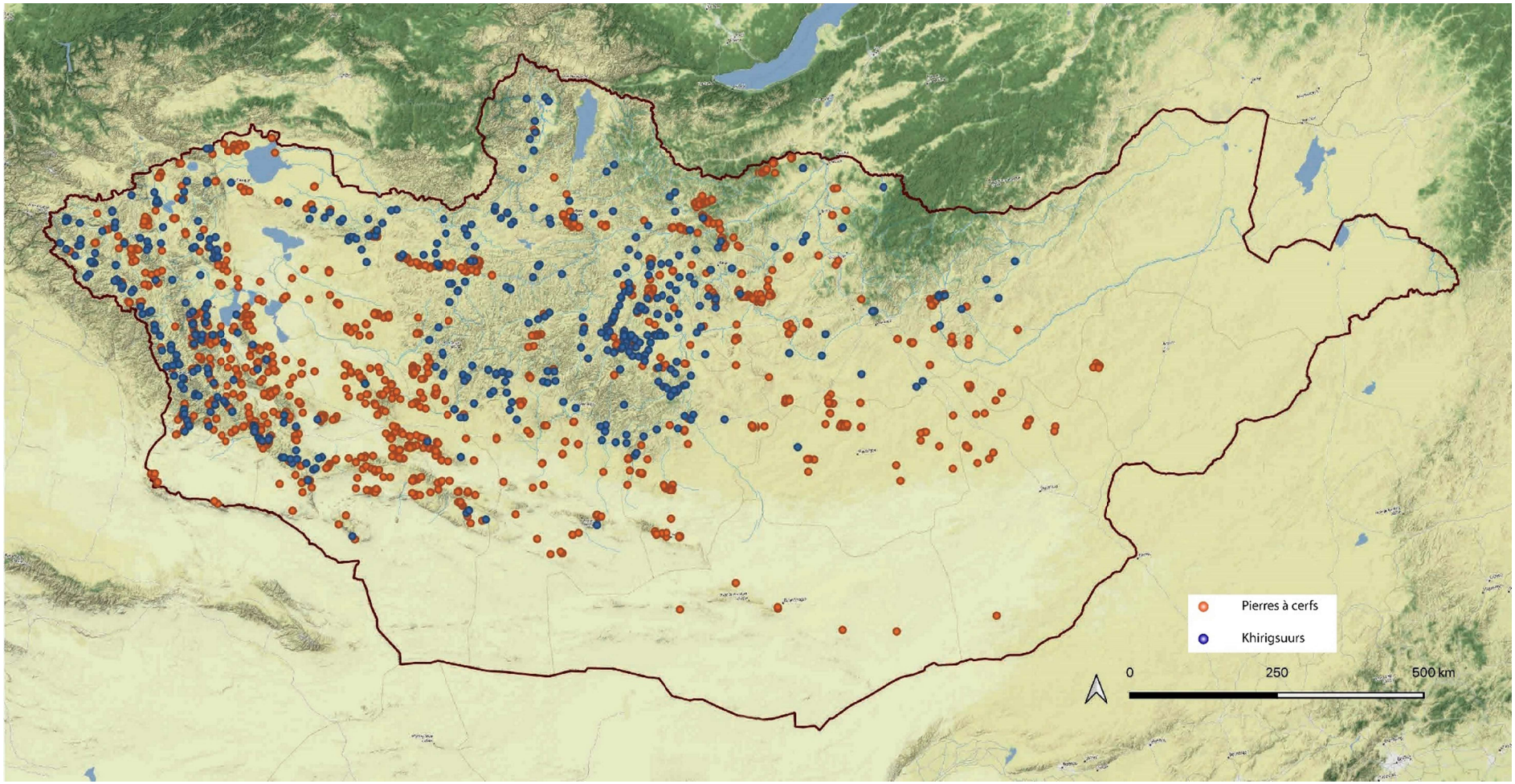

Fig. 1 Carte de répartition des pierres à cerfs et des khirigsuurs sur le territoire mongol (d'après Turbat et al.,2021)

Les pierres à cerfs sont des stèles gravées de l'âge du Bronze réparties sur une large zone géographique recouvrant le centre et le nord de la Mongolie, jusque dans les régions du sud de la Sibérie, et s'étendant à l'ouest jusqu'au Kazakhstan, et même l'Europe de l'Est pour certaines stèles (Fig. 2). Le dernier recensement réalisé par les chercheurs mongols dénombre 1318 stèles reparties sur l'ensemble de ce territoire (Turbat et al, 2021). Les pierres à cerfs se présentent souvent sous la forme de monolithes granitiques ou quartzitiques, avec une section horizontale carrée ou rectangulaire d'environ 30 cm à 60 cm de côté, et pouvant atteindre jusqu'à 4 m de hauteur (Fig. 3). Les gravures dont elles sont couvertes se divisent en trois thèmes (Magail, 2015): (*i*) le thème animalier, (*ii*) le thème des armes ou équipements du guerrier, et (*iii*) les figures géométriques.

Fig. 2 Exemples de pierres à cerfs (Photos A. C. Allard)

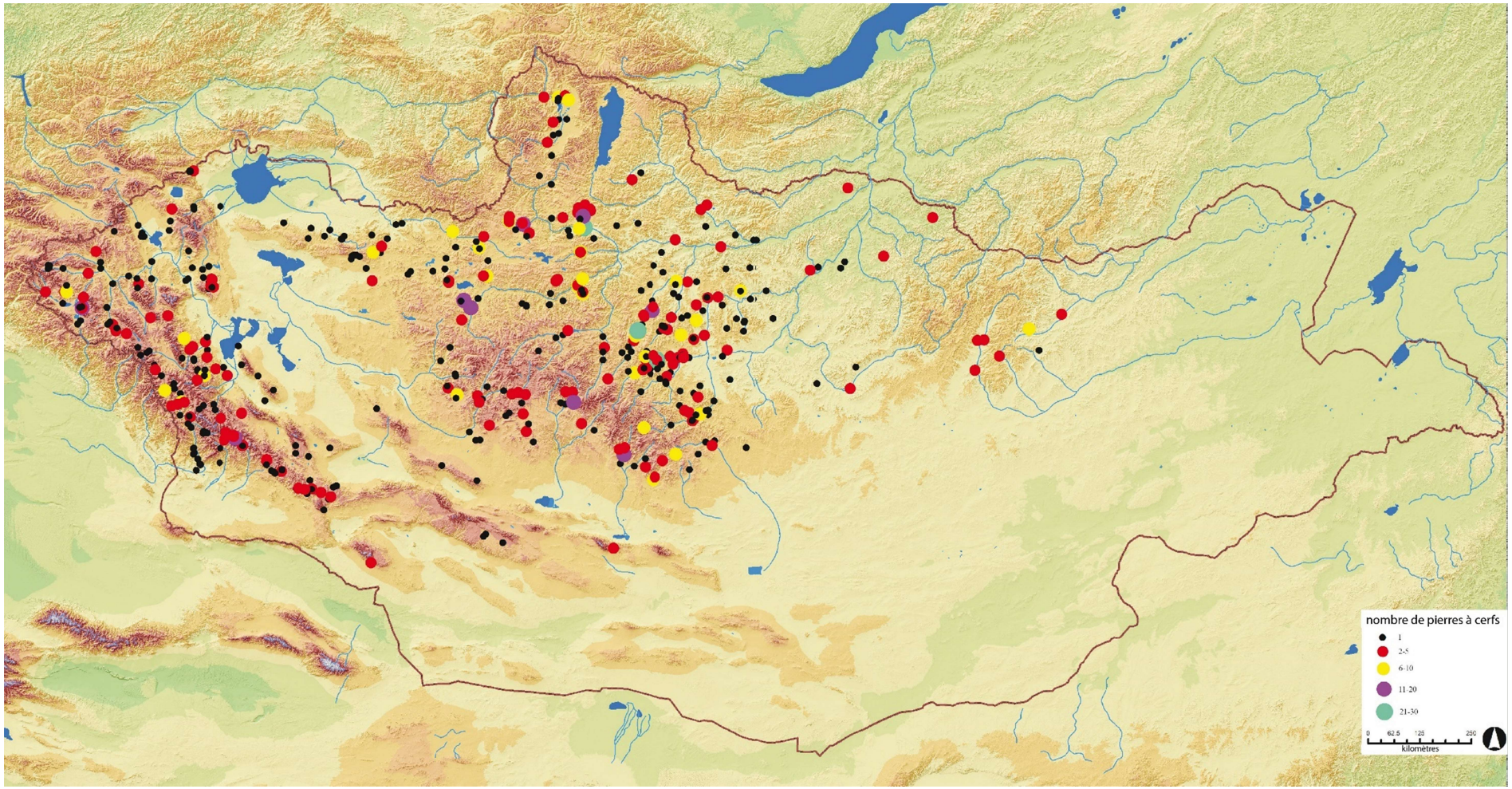

Fig. 3 Carte de répartition des pierres à cerfs sur le territoire mongol (d'après Gantulga et al., 2018)

Le thème animalier est largement dominé par la présence du cerf, ce qui leur a valu l'appellation de « pierres à cerfs ». D'autres animaux sont également représentés : e.g. cheval, sanglier, bouquetin, ou félin, pour ne citer que les plus communs. Deux styles iconographiques s'opposent pour la représentation des cerfs. Le premier style affiche des cerfs allongés, étirés sur la longueur, dont l'effet est accentué par un long et fin museau, parfois comparé à un bec (Fig. 4). Les animaux arborent de grands bois suggérant des représentations de mâles adultes. Le garrot est marqué par une saillie angulaire, parfois accentuée par la présence d'un trait barrant l'épaule de l'animal, de la saillie à la patte. Les pattes sont quant à elles repliées sous le ventre de la bête. L'image globale est celle d'un cerf bondissant, un peu fantastique, conjuguant son allure au mouvement. Ce style a très vite été rapproché du style animalier scytho-sibérien grâce à de multiples comparaisons avec le mobilier découvert, et notamment certaines

Fig. 4 Représentation du cerfs scytho-sibérien sur tois supports différents. A) Photographie d'une des faces de la pierre à cerfs n°6 de Tsatsyn Ereg. B) Appliques en bronze en forme de cerfs (Musée de Minusinsk). C) Rocher gravé de la vallée de la Khoid Tamir (Photo. A. C. Allard)

appliques en bronze (culture de Tagar) (Magail, 2008) (Fig. 4B). Ce style se retrouve également sur des sites d'art rupestre proche des pierres à cerfs (Fig. 4C). Le second style rattaché aux cerfs est jugé plus naturaliste dans la représentation de l'animal. Les proportions des différentes parties anatomiques sont respectées. La saillie au niveau du garrot est moins marquée, voire absente et les pattes sont dressées, comme si l'animal se tenait debout. La majorité les animaux est représentée de profil, avec un seul œil, une seule oreille, une seule patte à l'avant et à l'arrière. Il existe cependant des cas où l'artiste a surement voulu donner un sentiment de profondeur en représentant, par exemple, les quatre pattes de l'animal ou la paire de bois complète d'un cerf.

Le thème des armes et des équipements rassemble la représentation de diverses armes et outils associés à la panoplie des guerriers de l'époque. On y retrouve le couteau, le poignard, la hache, le bouclier, l'arc courbe asymétrique, le carquois, la pierre à aiguiser, des crochets de ceinture et d'équitation qui servaient à accrocher les rennes durant la chevauchée. Il est rare de voir l'ensemble de ces objets réunis sur une même stèle, et quand un objet est représenté il l'est rarement en double.

Le thème des figures géométriques renvoie à un ensemble de formes et de motifs comme des lignes, des cercles, des disques, des spirales, … Ces motifs sont parfois plutôt vus comme des objets (le disque assimilé à un miroir ou des boucles d'oreilles, par exemple), mais aussi comme la représentation symbolique d'astres ou de trajectoires.

L'utilisation de ces thèmes et le placement des motifs sur les stèles ne répondent pas à une logique narrative, mais plutôt à un code très strict. Malgré quelques différences dans la composition iconographique des pierres à cerfs, elles possèdent toute la même organisation. L'agencement des motifs sur la stèle délimite trois zones distinctes : la partie au sommet, la partie centrale, et le pied de la stèle assimilé aux domaines céleste, terrestre et souterrain (Fig. 5). La partie au sommet se compose de cercles, qui vont par paire, placés sur des faces opposées avec un semblant de symétrie. Parfois un visage peut être gravé sur l'une des faces. Cette zone est séparée de la partie centrale par une ligne ou un alignement de cupules encerclant la totalité de la stèle. La partie centrale, qui est généralement la zone la plus grande, accueille l'ensemble des représentations

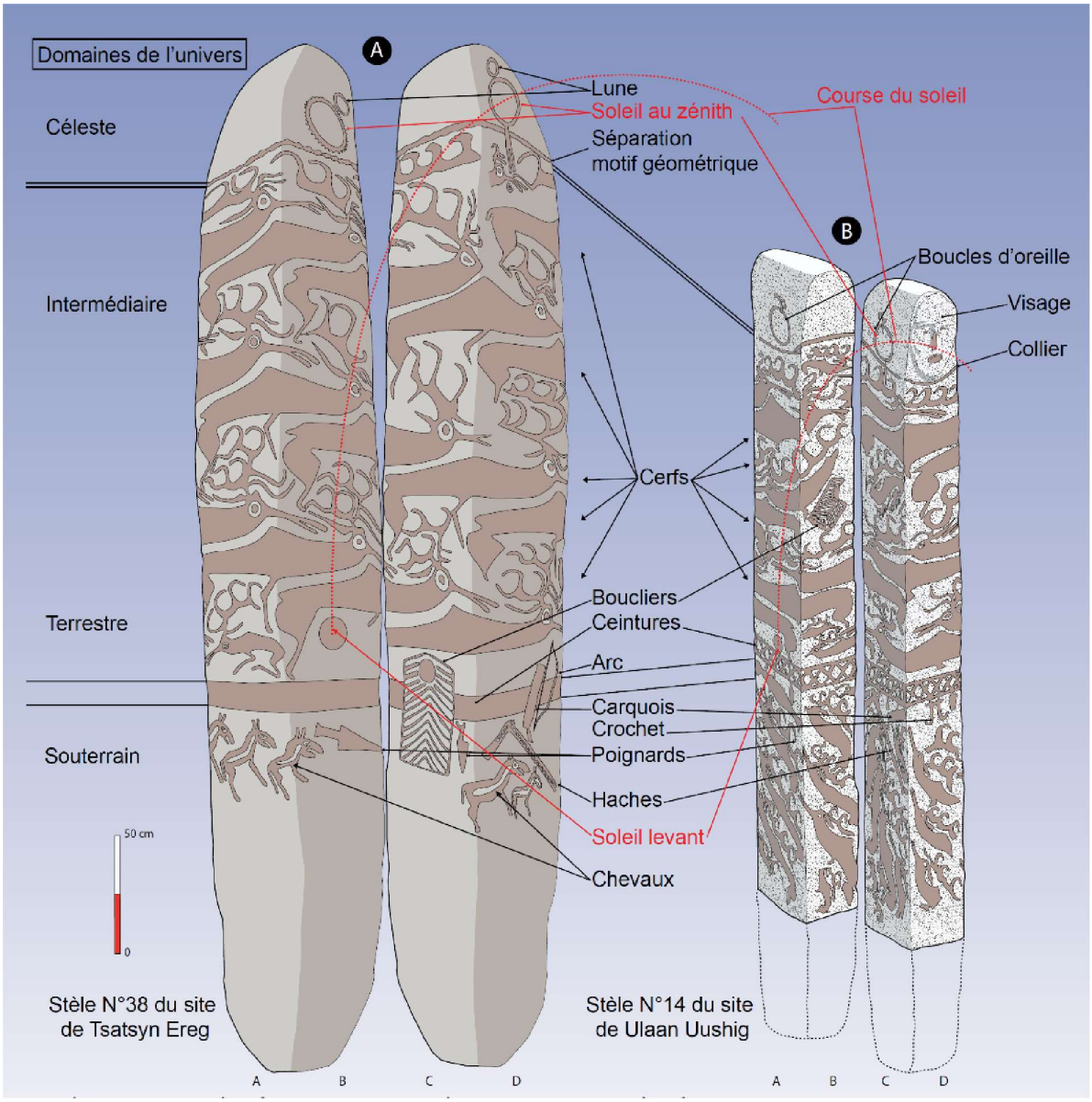

Fig. 5 Relevés de deux pierres à cerfs avec indication des trois différents domaines : céleste, terrestre et souterrain, et des motifs associés. Ces deux stèles sont distantes de 240 km. A) pierre à cerfs n° 38 de Tsatsyn Ereg. B) pierre à cerfs n° 14 de Ulaan Uushig. (d'après Magail et al., 2015 ; DAO F. Burle et J. Magail).

animales, notamment celles du cerf que l'on va retrouver par dizaines, organisées de telle sorte que les cervidés semblent se déplacer le long de la stèle dans un mouvement vertical ou hélicoïdal. Quelques motifs, tels qu'un disque ou un arc peuvent également être présents dans cette zone. Le pied de la stèle est souvent délimité par une bande large, assimilée à une ceinture qui enserre la stèle horizontalement. Aux abords de cette ceinture vont être placés tous les motifs relatifs à la panoplie guerrière.

Les premières estimations de l'âge de ces stèles sont réalisées par comparaison entre motifs gravés et mobilier connu (e.g. objets, iconographie du

cerf). Les cerfs ont très tôt été assimilés au style scytho-sibérien (Borovka, 1927). Okladnicov (1954) reprend cette idée sur le style des cerfs et va en outre rapprocher les armes et le cercle en sommet de stèle à des objets retrouvés dans le kourgane de Pazyryk. Il propose alors un âge aux alentours du VIIe – VIIIe siècle av. J.-C. N.L. Chlenova (1956) rattache les cerfs des stèles à ceux qui figurent sur certains objets de la culture Tagar, datés par ailleurs autour du VIIe siècle av. J.-C. également. Ce sont E. A. Novgorodova et V. V. Volkov qui offriront la plus grande étude comparative entre le mobilier et les éléments gravés sur les stèles (Novgorodova, 1989 ; Volkov et Novgorodova, 1975). Ils confirmeront et étofferont le lien qui existe entre les pierres à cerfs et les objets de la culture Karrasuk. Les récentes missions archéologiques apportent de nouvelles datations radiocarbone qui permettent de mieux estimer la période des pierres à cerfs, que l'on situe aujourd'hui entre 1300 ans et 700 ans av. J.-C. (Zazzo et al., 2019 ; Fitzhugh, 2010 ; Takahama et al., 2006).

N.N. Dikov(1958) est l'un des premiers à proposer une classification des pierres à cerfs. Les variations de forme et de style sans liens apparent l'orientent vers une classification purement stylistique composée de deux groupes : (*i*) représentation réaliste des animaux, (*ii*) représentation stylisée. Plus tard N.L. Chlenova (1962) présentera une classification basée sur deux types de stèles : avec et sans caractère anthropomorphe. C'est en 1981 que V.V. Volkov va proposer la classification qui restera celle que l'on connait aujourd'hui. Cette typologie reprend l'idée de N.N. Dikov en différenciant les stèles sur des critères principalement stylistiques. On y retrouve le groupe aux représentations stylisées, celui plus naturaliste, auxquels vient s'ajouter un groupe défini par l'absence de gravures zoomorphes. Les groupes sont nommés en fonction de leur répartition géographique : le type Eurasien, le type Sayan-Altaï et le type Mongol-Transbaïkal (Fig. 6). Plus tard, S. G. Savinov (1994) présente une classification basée sur l'évolution stylistique des pierres à cerfs dans le temps. Il détermine plusieurs phases dans cette évolution, depuis des stèles grossièrement taillées, tendant vers une norme avec des motifs stylisés, jusqu'à l'éclatement de cette norme. Même si cette classification n'est aujourd'hui pas appliquée, elle a le mérite d'avoir proposé une approche prenant en compte

l'organisation des motifs sur les stèles, ainsi que l'évolution d'un style qui semble prédominant et figé dans la classification actuelle.

Dans la classification actuellement utilisée, les stèles Eurasiennes (Fig. 6A) correspondent au groupe sans représentation zoomorphe. Seuls les armes et les motifs géométriques y sont présents. On y observe des cercles, des ceintures, des bandes obliques, des bandeaux et toute une panoplie d'armes. La composition iconographique est parfois assez complexe pour reconnaitre les trois espaces définis précédemment, avec la même distribution des types de

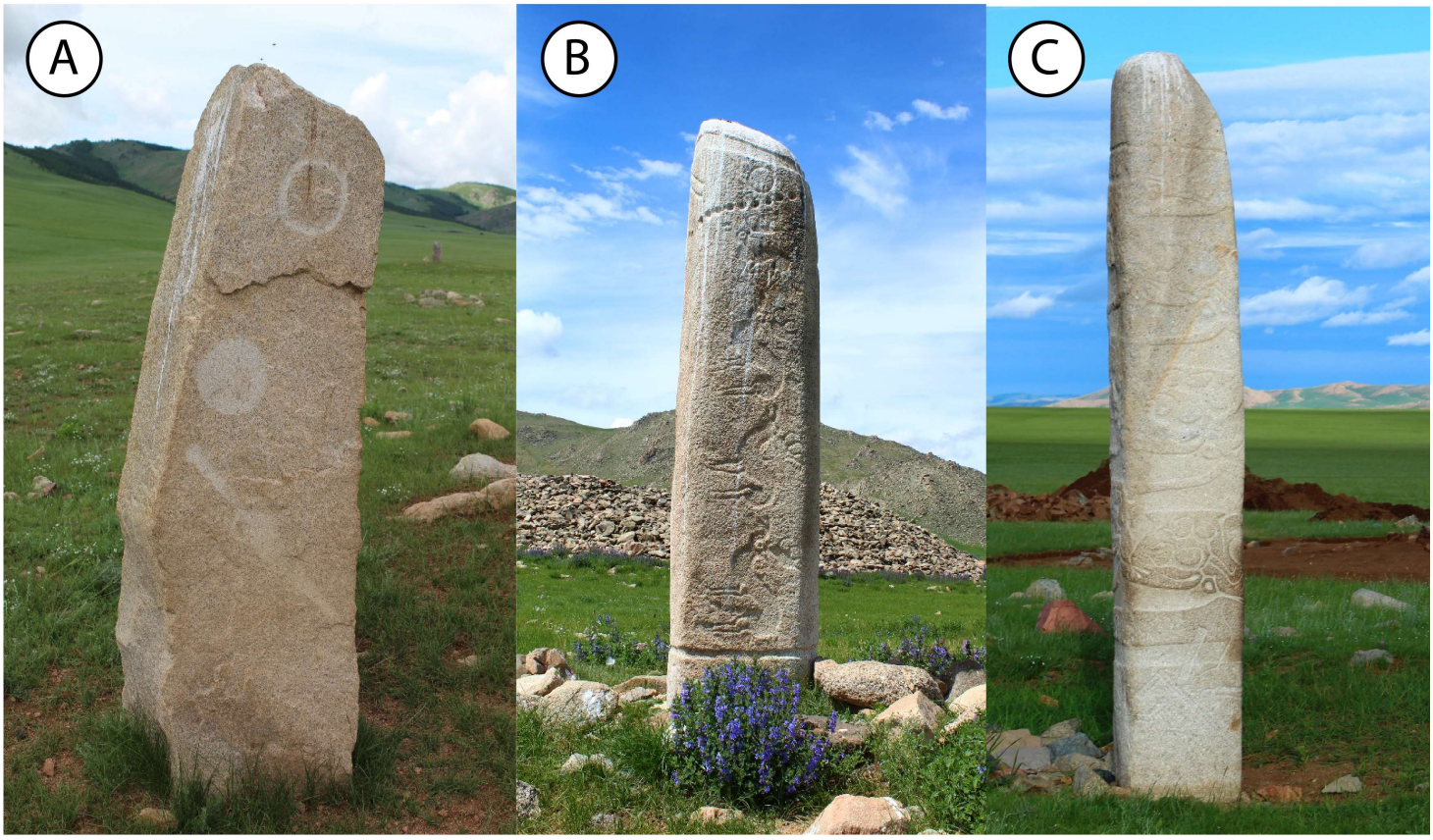

Fig. 6 Exemples des trois différents types de pierre à cerfs. A) Type Eurasien. B) Type Sayan-Altaï. C) Type Mongol-Transbaïkal. (Photos A. C. Allard)

motifs. Néanmoins, certaines stèles de ce type contiennent très peu de motifs, parfois un seul. Un total de 448 stèles a été répertorié sur l'ensemble du territoire mongol, soit 36,1% de l'ensemble des stèles (Turbat et al., 2021). Le groupe « Eurasien » représente le type majoritaire à l'ouest de la Mongolie près de l'Altaï, et il a la particularité de s'étendre loin à l'ouest des frontières mongoles, jusque dans le nord du Caucase et en Europe de l'Est.

Les stèles Sayan-Altaï (Fig. 6B) correspondent aux stèles avec des représentations zoomorphes dites réalistes, en opposition aux cerfs stylisés scytho-sibériens. L'organisation générale de la stèle reste classique dans répartition des thèmes sur la stèle, structurée par trois espaces. Ce type possède néanmoins le bestiaire le plus riche. Outre les cerfs, il est possible de retrouver des chevaux, des élans, des sangliers, des bouquetins, des oiseaux, des poissons, des bovidés, des canidés. Le groupe Sayan-Altaï ne représente que 5.8% du total des pierres à cerfs connues, avec seulement 72 individus enregistrés. Elles se répartissent sur l'ensemble du territoire mongol, sans concentration dans une région particulière.

Le type Mongol-Transbaïkal (Fig. 6C) regroupe les stèles avec les fameux cerfs stylisés. Les pierres à cerfs y sont les plus élaborées, en termes de nombre et de diversité des motifs. Le groupe Mongol-Transbaïkal comprend 721 stèles, soit 58% du total. Il est majoritairement représenté dans le centre et le nord de la Mongolie, et plus particulièrement dans les provinces de l'Arkhangaï (235 stèles) et de Hövsgol (227 stèles).

Les pierres à cerfs sont le plus souvent retrouvées en contexte funéraire, soit en position primaire, soit en réemploi, par exemple dans des tombes à dalles. En position primaire, elles sont généralement installées au sein de deux types de structures : des places rituelles dont Jargalant est l'exemple le plus remarquable (Fig. 7A) ; des monticules de terre situés en périphérie des khirigsuurs (Fig. 7B). Dans les deux cas les stèles sont entourées de structures de dépôts en pierres sèches que l'on retrouve également comme éléments constitutifs des khirigsuurs.

Les khirigsuurs font partie intégrante du paysage Mongol à l'âge du Bronze tardif (ca. 1400-700 cal av. J.-C.). Connus et étudiés depuis le XIXe siècle, on les retrouve sur une zone géographique très étendue, allant de l'est du Kazakhstan au centre de la Mongolie en remontant vers le sud de la Sibérie (Fig. 8). Les khirigsuurs ne sont pas répartis de manière homogène dans cet espace, mais se rassemblent plutôt en groupes dans des régions limitées (Volkov, 1981; Jacobson et al., 2001; Frohlich, 2010; Erdenebaatar, 2004 ; Allard et Edenebaatar, 2005). Malgré l'existence de nombreuses formes de khirigsuurs, de fortes similitudes sont observées dans les éléments architecturaux qui les composent, ainsi que dans la manière dont ces derniers s'organisent pour définir

le plan du monument (Fig. 9). Certaines variations régionales auraient été identifiées, sous-entendant la possibilité d'identifier des sous-groupes régionaux (Frohlich, 2010).

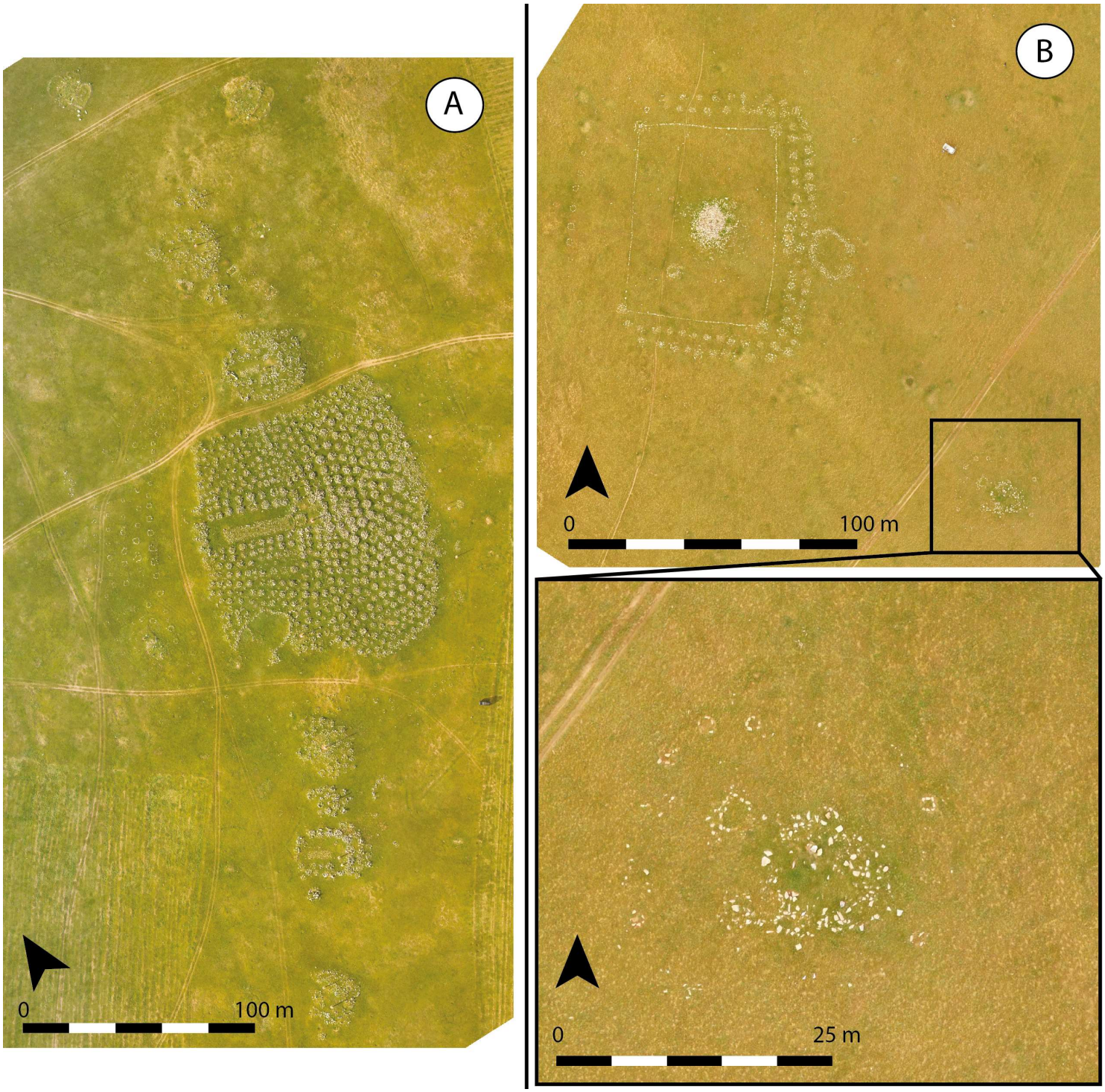

Fig. 7 Exemples de structures accueillant des pierres à cerfs en position primaire. A) Orthomosaïque du site de Jargalant. B) Orthomosaïque du khirigsuur et de la structure associée à la pierre à cerfs n° de Tsatsyn Ereg.

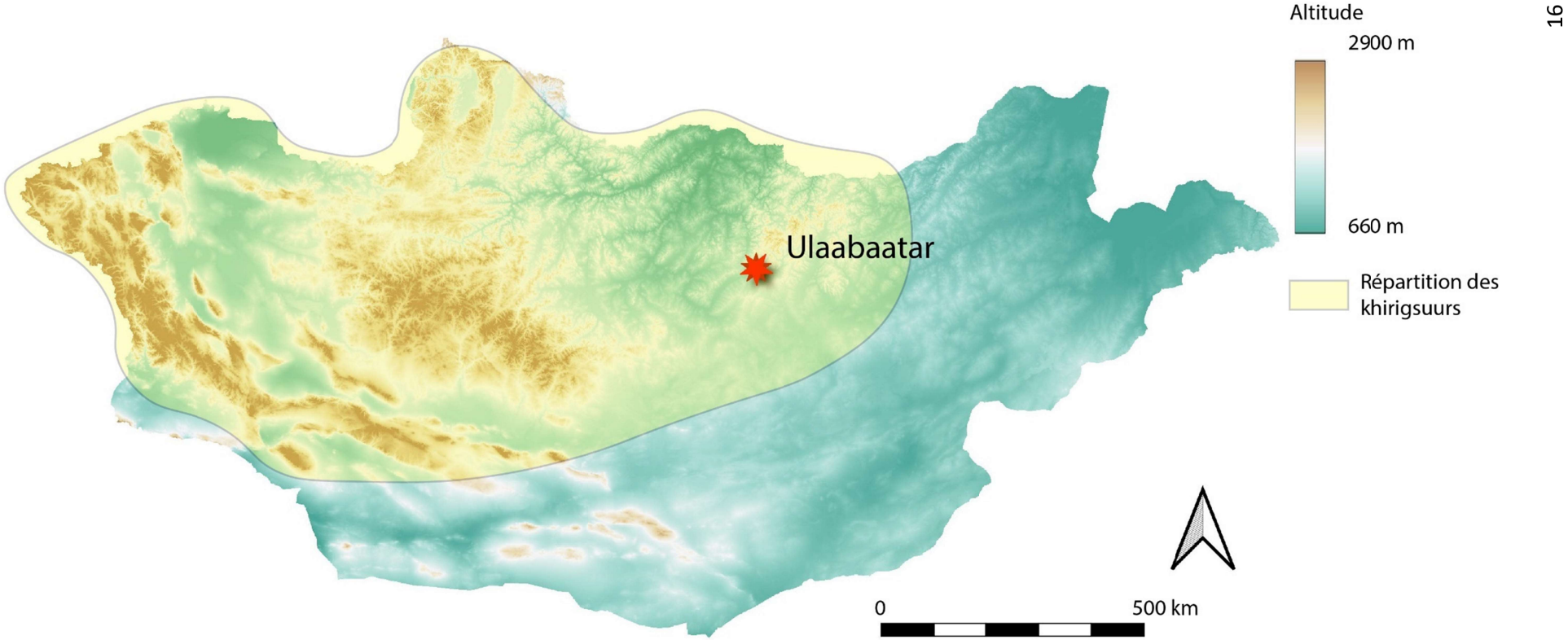

Fig. 8 Carte de répartion des khirigsuurs sur le territoire mongol.

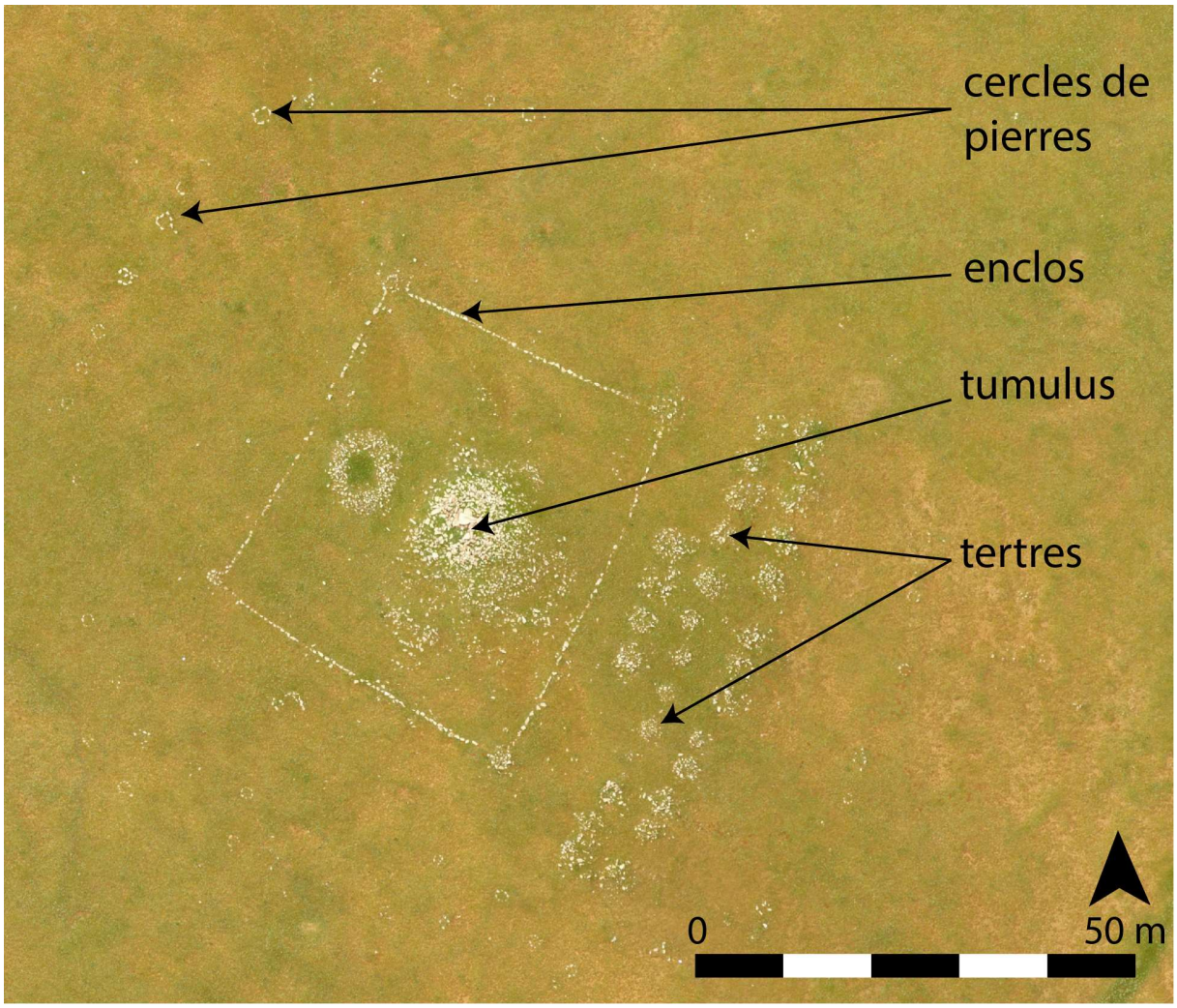

Fig. 9 Orthomosaïque d'un khirigsuurs.

Un khirigsuur consiste en une chambre funéraire placée au centre d'un tumulus de pierres sèches (entre 2 m et plusieurs dizaines de mètres de diamètre). La chambre peut être légèrement creusée dans le sol et est délimitée par des dalles. Quand des restes sont retrouvés, elle ne contient qu'un seul corps et toutes les catégories âge/sexe sont représentées. Un alignement de pierres définissant un enclos est généralement installé autour du tumulus. Il peut être de forme circulaire ou quadrangulaire, et couvrir quelques centaines de m² jusqu'à plusieurs hectares. Des tertres ou des pierres dressées marquent parfois ces enclos. Différentes structures ou éléments, comme des tertres et des cercles de pierres, peuvent être construits en périphérie de l'enclos. Les tertres extérieurs sont des petits monticules de pierres (entre 1 m et 5 m de diamètre) sous lesquels ont été déposées des têtes de chevaux. Ces dernières sont accompagnées parfois

des premières vertèbres et des sabots (Fig. 10). Le dépôt de ces têtes apparait comme une pratique très codifiée sur l'ensemble des sites qui ont fait l'objet de fouilles. Les crânes déposés sont toujours orientés vers l'est, avec une possible variation vers le nord-est ou le sud-est (Takahama, 2003, 2006 ; Allard et Erdenebaatar, 2005 ; Lepetz et al., 2019). Ils appartenaient à des chevaux majoritairement males, très âgés ou très jeunes (~2 ans). Un tertre contient en général un seul crâne, même si un cas de dépôts de plusieurs têtes a déjà été décrit. Les cercles de pierres (Fig. 10) se composent d'une dizaine de pierres positionnées en cercle d'environ 1 m de diamètre. Ces cercles font également l'objet d'un dépôt particulier car on peut y retrouver des esquilles d'os brulés d'ovi-caprinés, ainsi que du charbon (Allard et Erdenebaatar, 2005 ; Lepetz et al., 2019 ; Zazzo et al. 2019). Ces éléments n'auraient pas été brulés sur place, mais plutôt dispersés au sein de l'espace formé par les pierres. Le nombre de

Fig. 10 De gauche à droite et de haut en bas : tertre de pierre ST1 du complexe B10 ; restes de deux cranes de chevaux retrouvés sous ST1 ; cercle de pierres ST 107 du complexe B10 ; fragments d'os calcinés retrouvés dans les cercles de pierres. (D'apres Zazzo et al, 2019)

tertres et de cercles est très variable, allant de quelques individus à plus d'un millier autour de certains khirigsuurs monumentaux. D'autres éléments architecturaux (allées, alignements…) peuvent être identifiés, mais ils sont plus rares et ne sont pas considérés comme des éléments nécessaires à la définition d'un khirigsuur. Ce dernier point constitue notamment l'une des difficultés dans l'étude des khirigsuurs, car il n'existe pas de consensus sur ce qui est ou ne n'est pas un khirigsuur. Certains auteurs limitent l'appellation de khirigsuur aux monuments se composant des trois éléments présentés plus haut : tumulus, enclos et structures de dépôt (e.g. Houle, 2010 ; Allard et Erdenebaatar, 2005 ; Cybiktarov, 2003). D'autres sont plus inclusifs et considèrent comme khirigsuur tout monument avec au moins un tumulus et un enclos (e.g. Wright, 2007 ; Frohlich, 2010). Localement les khirigsuurs sont rassemblés en nécropoles accueillant des monuments de tailles et de formes variées. Ces nécropoles sont généralement installées dans les pentes avec une organisation des monuments partant des hauts de pente pour s'étendre jusqu'au pied de pente, parfois jusque dans la vallée.

A ce jour, plusieurs typologies sont disponibles dans la littérature pour catégoriser les khirigsuurs. Tsybiktarov (1995) définit 9 types de khirigsuurs (d'après Wright, 2014). Frohlich et al. (2008) proposent de diviser les khirigsuurs en trois classes définies par la pente sur laquelle le monument est installé. Les classes I à III regroupent respectivement : les monuments situés à basse altitude, dans une steppe globalement plane ; les monuments bâtis à la frontière entre la steppe et le flanc des collines ; les monuments situés dans les pentes. Wright (2007) établit une méthode de classification basée sur les éléments qui composent le khirigsuur avec, au final, 3 types exprimant la complexité des monuments. Enfin Houle (2009) divise les khirigsuurs en deux groupes : les monuments avec ou sans structures de dépôts. Contrairement aux pierres à cerfs dont la typologie est aujourd'hui plutôt bien admise et largement utilisée, la typologie des khirigsuurs reste sujette à discussion et, par conséquence, est très peu utilisée, hormis par leurs auteurs.

Le rôle des khirigsuurs dans les sociétés qui les ont bâtis fait encore débat. Tous s'accordent à dire que certains monuments ont un but funéraire puisque des restes humains y ont été découverts. Néanmoins, la pauvreté du

mobilier et l'absence totale de restes dans certains cas entretiennent le doute quant à leur but premier. Joshua Wright (2007) puis Honeychurch et al. (2009) rejettent l'idée que les khirigsuurs soient uniquement bâtis pour être des sépultures. Ils proposent plutôt de voir les khirigsuurs comme des monuments regroupant les activités d'une même communauté, construits avec une certaine régularité rappelant le cycle annuel de migration des populations nomades. Les monuments reflètent un besoin de s'affirmer en tant que groupe (Wright, 2014). Cette interprétation sera reprise (Honeychurch et Amartuvshin, 2006; Honeychurch et al., 2009). D'autres chercheurs pensent plutôt que les khirigsuurs ont pour but premier d'être des sépultures (Takahama et al., 2006; Frohlich et al., 2008, 2010 ; Littleton et al., 2012) et expliquent l'absence de reste par une mauvaise conservation des os. Littleton (2012) montre en effet que la préservation des os est fortement corrélée à la nature des sols et à la géographie, notamment à la valeur de la pente sur laquelle le monument est installé, ainsi qu'à l'âge de l'individu inhumé. La présence de zones propices à la dégradation des os pourrait expliquer l'absence quasi systématique de restes dans certaines fouilles, surtout quand celles-ci ne concernent qu'un petit nombre de monuments. Le travail de Littleton (2012) tend à montrer que les khirigsuurs sont avant tout des sépultures, tout en conservant bien entendu une fonction symbolique. Certains auteurs ont pu décrire les khirigsuurs comme des « autels » au centre des activités collectives (Jacobson, 1993; Allard et Erdenebaatar, 2005). D'autres y voient un symbole de pouvoir, un moyen pour une élite de s'affirmer et de se montrer (Houle, 2010 ; Cybiktarov, 2003).

L'architecture basée en grande partie sur des structures de dépôts, ainsi que la potentielle fonction rituelle des khirigsuurs amènent à se poser la question de l'évolution du plan des monuments au cours du temps. Cette question est légitime, surtout lorsque l'on considère que certains khirigsuurs monumentaux sont composés de milliers de structures de dépôts. Deux hypothèses sont possibles. La première envisage que l'ensemble des structures composant le khirigsuur sont synchrones, ce qui correspondrait à l'abattage de milliers de chevaux et de têtes de bétails au cours d'une seule cérémonie (Fitzhugh, 2009, 2017). La seconde hypothèse suggère que les dépôts sont diachroniques et que les populations de l'époque sont venues de manière plus ou moins régulière

enrichir le monument de nouveaux dépôts, jusqu'à que celui-ci présente sa configuration actuelle. (Wright, 2014). Une étude récente menée par Zazzo et al. (2019) à l'aide de datations radiocarbone dans la vallée de Tsatsyn Ereg indique une période de construction du complexe B10 entre 1050 et 950 ca. av. J.-C., en d'autres termes s'étalant sur plus d'une vie humaine (Zazzo et al., 2019 ; Magail, 2015).

La grande régularité que présentent les khirigsuurs et les pierres à cerfs démontre pour le moins un lien culturel fort entre les différentes populations nomades qui les ont érigées (Annexe 1). Malgré les distances qui les séparent, ces communautés obéissent aux mêmes codes architecturaux et iconographiques, sous-entendant les mêmes règles et les mêmes croyances. Ce phénomène culturel est assez puissant pour façonner le paysage monumental des steppes jusqu'à nos jours. Tout l'enjeu est de caractériser cette culture développée en Mongolie à l'âge du Bronze. Comment a-t-elle évolué sur l'ensemble de son territoire, sachant que les études menées jusqu'alors sont le plus souvent très localisées ? Une telle étude se confronte à la quantité et à la complexité des monuments conservés, soit plus de 1300 stèles et plusieurs milliers de khirigsuurs. De telles contraintes nécessitent le développement, puis la mise en place de méthodes adaptées pour l'enregistrement sur le terrain, la préparation des données, et leur analyse à des fins de classification, entre autres. Ces points constituent précisément les objectifs du présent travail de thèse. Notons cependant que les solutions proposées ne seront pas spécifiques aux structures étudiées en Mongolie, mais peuvent également répondre à d'autres problématiques archéologiques. Le plan de cette thèse suit la logique décrite ci-dessus : acquisition, préparation et analyse ; l'ensemble structuré autour de plusieurs articles scientifiques, publiés ou en voie de publication.

Le premier chapitre est une présentation de la zone d'étude, du corpus et des protocoles utilisés pour l'acquisition des données sur le terrain. Ces derniers se basent sur la photogrammétrie, au sol pour les pierres à cerfs, et aéroportée par drone pour les khirigsuurs.

Le second chapitre concerne l'application d'un traitement qui vise à mettre en valeur les reliefs d'un modèle 3D. Ce traitement permet, dans le cas des pierres à cerfs, une lecture claire des motifs gravés. Cette même méthode peut être

transposée au domaine de la géomorphologie en tant que nouveau traitement des modèles numériques de terrain.

Le troisième chapitre décrit l'utilisation de l'apprentissage automatique pour le traitement semi-automatique des prospections photos aéroportées.

Le quatrième chapitre présente une nouvelle classification des khirigsuurs obtenue grâce à une classification non supervisée, basée sur les éléments constitutifs des khirigsuurs, puis qui est confrontée aux paramètres géographiques.

Le cinquième chapitre propose un thésaurus pour la description des motifs gravés sur les pierres à cerfs, ainsi que les premiers résultats issus de son application pour une classification non supervisée.

Le sixième chapitre porte sur la sauvegarde et la valorisation des données.

Le septième chapitre consiste en une conclusion générale, et propose plusieurs pistes pour le futur.

Chapitre 1. Corpus et méthodes d'acquisition

1.1. Zone d'étude

La zone géographique envisagée pour cette étude se concentre principalement sur deux vallées voisines de la province de l'Arkhangaï, au centre de la Mongolie : la vallée de la Khoïd Tamir avec le site de Tsatsyn Ereg, et la vallée de la rivière Khunuin Gol, ainsi que plusieurs autres sites emblématiques répartis du centre au nord de la Mongolie. Ces deux vallées ont été choisies en priorité pour leur richesse en termes de vestiges, mais aussi parce que leur proximité géographique combinée aux infrastructures de la mission conjointe Monaco-Mongolie à Tsatsyn Ereg facilitent grandement le travail de terrain, dont la durée est strictement limitée dans le temps du fait de la rigueur des saisons.

La vallée de la Khoïd Tamir représente à elle seule 10% des stèles recensées sur l'ensemble du territoire mongol. Il est donc possible d'y enregistrer un grand nombre de monuments (stèles et khirigsuurs) afin de créer un échantillon représentatif. En outre, ces vallées sont largement documentées grâce à la mission conjointe Monaco-Mongolie qui prospecte, fouille et étudie la zone depuis 2006. Les autres sites étudiés sont bien connus dans la littérature : Ulaan Uushig, Shuuregtein uvur, Orkhon, Zunii Gol, Zulegtyn gol, Ulaan Tolgoï, Jargalant, Urt Bulag, Duruljiin am, (Fig. 11). Ils permettent l'élargissement du corpus au-delà de la zone principale d'étude.

Aujourd'hui deux méthodes principales sont utilisées pour effectuer le relevé d'une pierre à cerfs (Fig. 12). La première méthode est celle du calque (Fig. 12A-B). Elle consiste à plaquer une feuille de plastique sur la surface de la pierre et à dessiner ensuite les contours des motifs gravés. Les gravures peuvent être marquées au préalable pour mieux les distinguer une fois la feuille

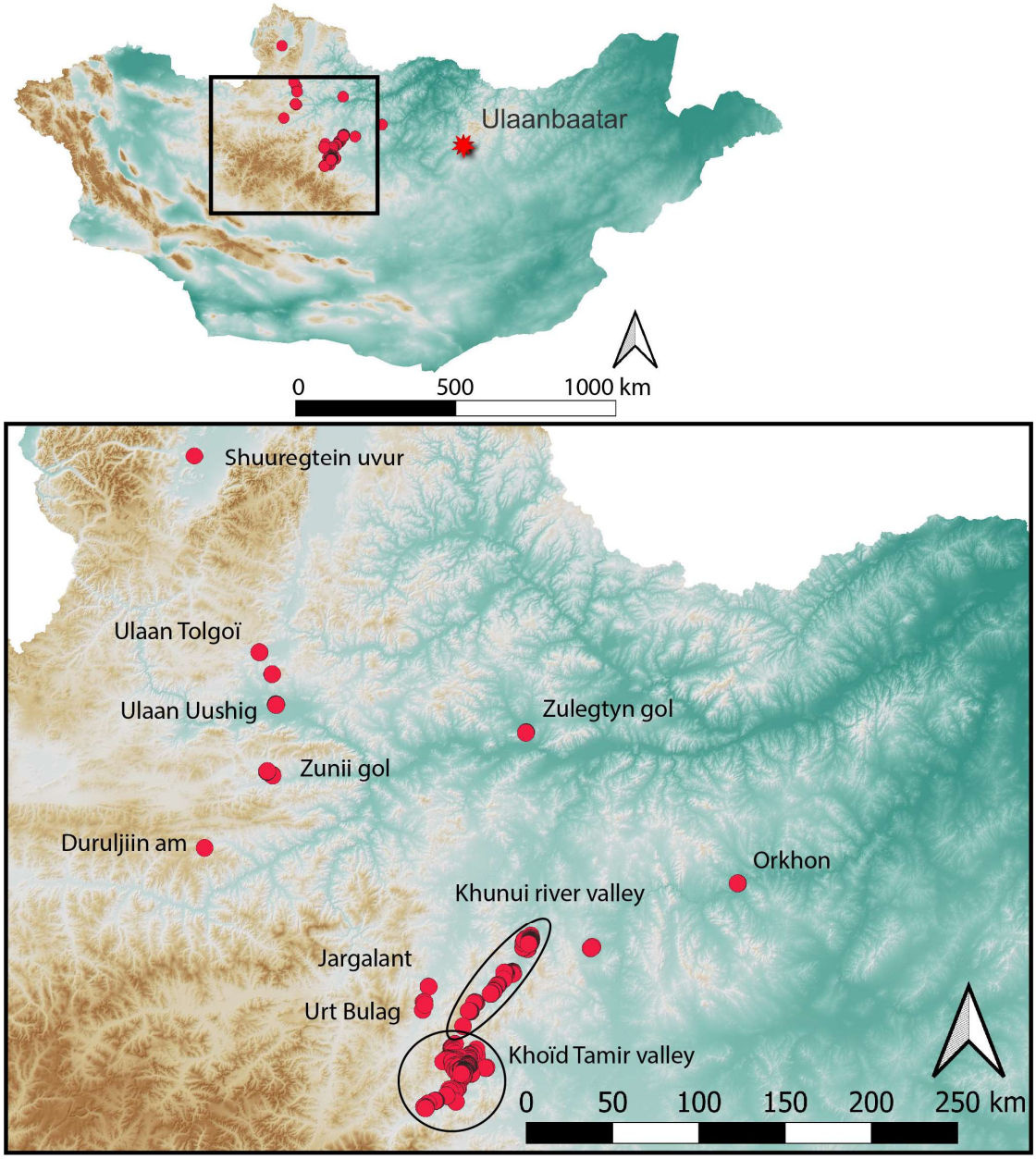

Fig. 11 Répartition des zones et sites prospecté pour cette étude

positionnée. La seconde méthode (Fig. 12C-D) utilise une feuille de papier plaquée contre la surface de l'objet. Les reliefs y sont ensuite imprimés à l'aide d'un papier carbone frotté par l'opérateur. Cette approche produit généralement les meilleurs résultats. En revanche, les deux méthodes nécessitent un contact physique avec l'objet qui peut s'avérer délétère. De plus, les conditions climatiques doivent être raisonnablement favorables en termes de précipitations et de vent. Pour le khirigsuur, la méthode de relevé du plan dépend de la précision souhaitée. Un simple croquis peut être réalisé, parfois seuls les

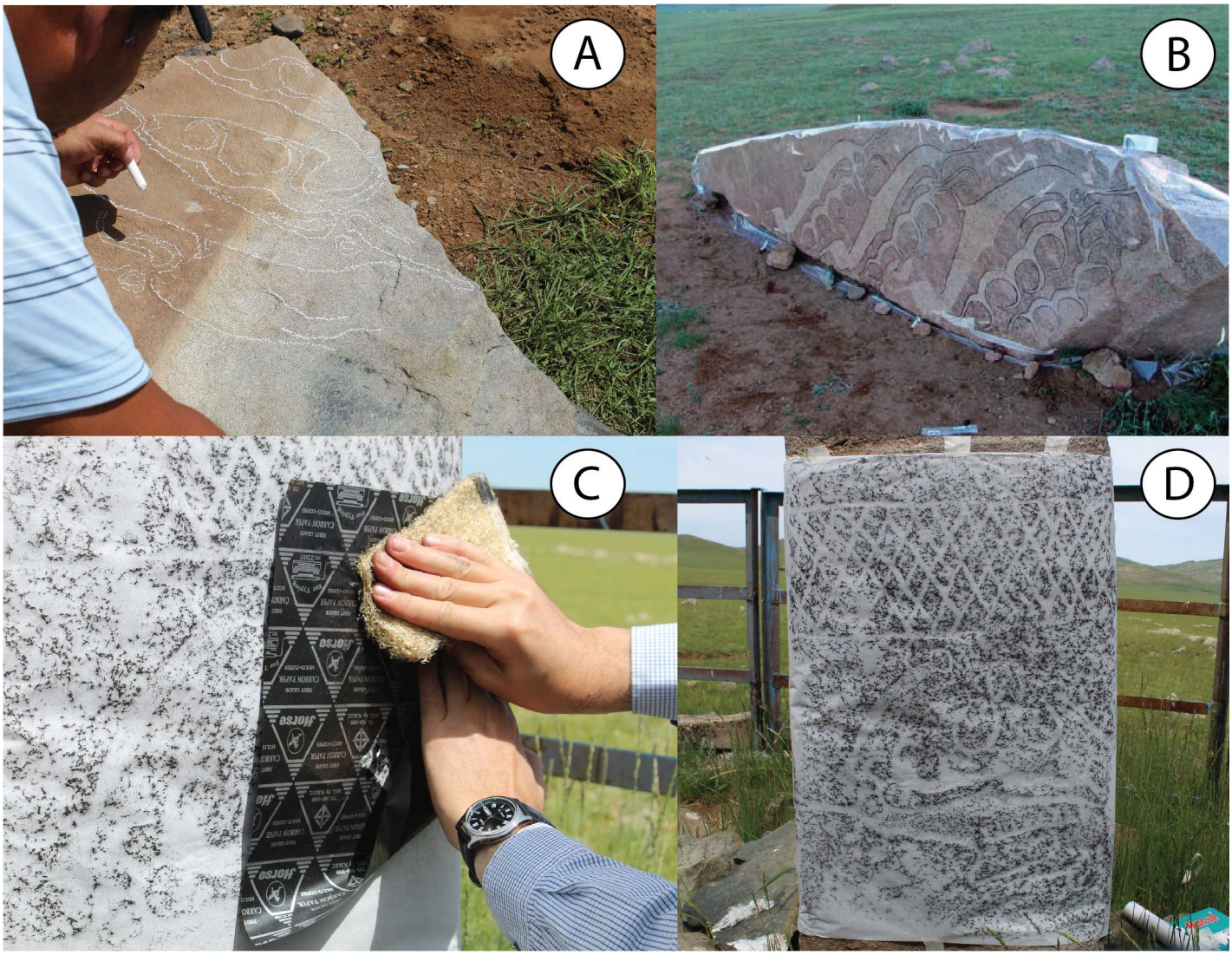

Fig. 12 Illustration des méthodes traditionnelles de relevé des pierres à cerfs. A) Détourage des limites des gravures sur la stèle. B) Résultat de la méthode du calque. C) Impression des reliefs sur la feuille en papier grâce au frottement d'un papier carbone. D) Résultat de la méthode avec papier carbone. (Photos A. C. Allard)

éléments constitutifs sont géolocalisés, tandis que pour un plan plus complet toutes les pierres sont dessinées. Toutes ces méthodes sont chronophages et ne sont donc pas appropriées à l'acquisition massive d'un très large corpus. La méthode envisagée pour cette étude est la photogrammétrie, aussi bien pour les stèles que pour les khirigsuurs. Aujourd'hui largement répandue en archéologie, la photogrammétrie est encore assez peu utilisée en Mongolie, à l'exception de quelques études (Miyamoto et al., 2017) où elle sert essentiellement à des fins illustratives. Pourtant, la versatilité de la méthode et sa facilité d'application à des terrains assez difficiles, comme la Mongolie (seul l'autonomie des batteries et la pluie étant limitants), en font une candidate parfaite pour l'enregistrement

des monuments. Pour les pierres à cerfs la photogrammétrie a pour but la création d'un modèle 3D, tandis que pour les khirigsuurs ce sont des orthomosaïques et des modèles numériques de terrain (i.e. des images raster contenant pour chaque pixel l'altitude de la surface correspondante) qui sont produits.

1.2. Acquisition et corpus

L'acquisition des stèles a été réalisée à la main (Fig. 13) à l'aide d'un SONY DSC-RX100 MIII (capteur 13.2 × 8.8 mm², 20 Mpix), avec une lentille 24-70 mm (équivalent 24 × 36) réglée à 24 mm, et un NIKON D800 semi-pro plein format (capteur 24 × 36 mm, 36 Mpix) équipé d'un objectif NIKKOR à focale fixe, 24 mm ou 50 mm. L'acquisition des khirigsuurs a été réalisée avec un drone (Fig. 13). Aujourd'hui, ce type d'appareil est largement utilisé pour la création de photos aériennes, d'orthomosaïques, de modèles numériques de terrain, ou encore de modèles 3D. Le drone a été utilisé de deux manières différentes durant les missions de terrain : soit pour couvrir des structures isolées en effectuant un seul vol, soit pour balayer une large zone de manière exhaustive en la divisant

Fig. 13 Illustration des différentes méthodes d'acquisition utilisée. A gauche : acquisition d'une stèle à la main. A droite : acquisition avec un drone.

en plusieurs sous-zones (ou dalles), couvrant chacune le maximum de surface possible sans changement de batterie. Les deux plus larges zones connexes survolées correspondent se situent dans la vallée de la rivière Khunui (~260 ha survolés) et dans celle de la Khoid Tamir (~700 ha survolés). Les photos ont été capturées avec deux drones : un DJI Phantom 3 PRO avec une caméra 12 Mpix et un objectif de 20 mm (équivalent 24 × 36) et un DJI MAVIC AIR avec une caméra 12 Mpix et un objectif de 24 mm (équivalent 24 × 36). Les plans de vols ont été programmés *via* l'application gratuite Pix4Dcapture (https://www.pix4d.com/) avec un taux de superposition des images fixé à 80%. La hauteur de vol varie entre 70 et 100 m pour une résolution au sol d'environ 3 cm/px, suffisante pour identifier les pierres constituant les khirigsuurs dont les dimensions avoisinent quelques dizaines de centimètres. Avec ces paramètres, et avec une autonomie de vol d'environ 15-20 min, la surface maximale couverte par un vol est d'environ 9 ha.

L'enregistrement des données a nécessité quatre missions d'un mois chacune (2016-2019). J'ai eu la chance de participer aux deux dernières, avant que la dégradation de la situation sanitaire stoppe toute acquisition sur le terrain. Au total, 78731 photos ont été prises pour la constitution de ce corpus : 33256 pour les stèles, et 45745 pour les khirigsuurs (Tableau 1). Les modèles, les orthomosaïques et les MNE ont été réalisés avec le logiciel Metashape (https://www.agisoft.com/). Les photos ainsi que les projets Metashape occupent environ 3 To d'espace de stockage, sans compter les 440 Go de films, photos et autres réalisations qui n'ont pas directement servi à l'élaboration du corpus, mais qui contextualisent les missions et le travail réalisé sur le terrain.

	Nombre de photos	Espace de stockage nécessaire
Pierres à cerfs	33256	437 Go
Khirigssurs	45475	263 Go
Total	78731	700 Go

Tableau 1 Nombres de photos prise pour créer le corpus de cette étude et espace nécessaire à leur stockage.

Au total, 226 modèles de stèles ont été créés et 1527 vestiges ont été repérés sur l'ensemble des orthomosaïques. Parmi ces vestiges, 907 khirigsuurs ont été identifiés, dont 117 jugés trop détériorés par les bouleversements naturels ou anthropiques pour être incorporés dans l'analyse (Fig. 14).

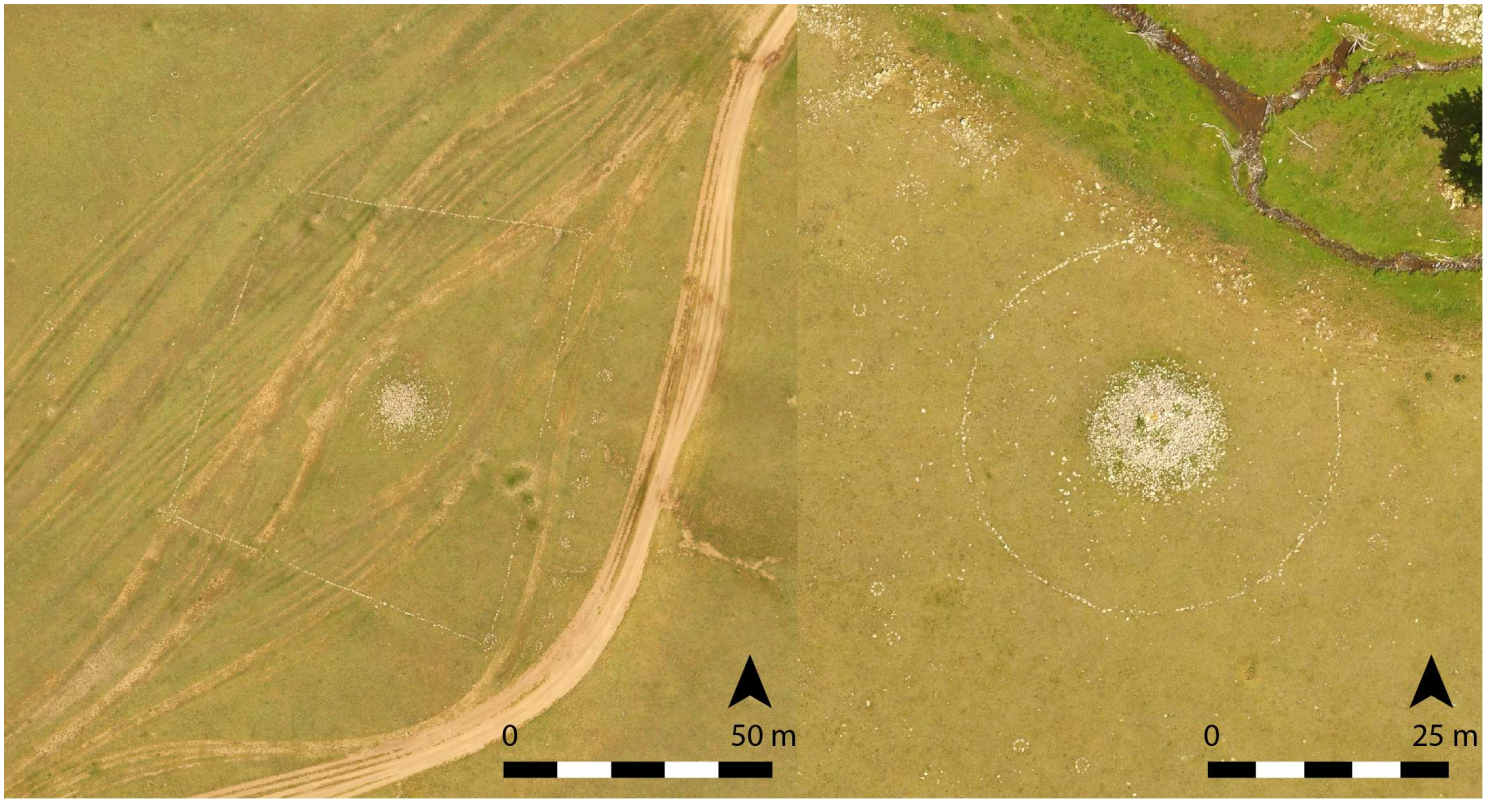

Fig. 14 Khirigsuurs détériorés par des bouleversements anthropiques (à gauche) et naturels (à droite).

Chapitre 2. Mise en valeur des reliefs

2.1) Occlusion ambiante et modèles 3D

Les apports de la modélisation 3D pour l'étude de l'art rupestre sont indéniables. Son application est donc devenue rapidement une évidence pour l'étude des pierres à cerfs. Pour des terrains difficiles comme la Mongolie, où le transport de matériel est une contrainte, la photogrammétrie reste la méthode d'acquisition la plus pratique, car elle ne nécessite qu'un seul appareil photo, puis au laboratoire, un logiciel spécialisé. L'obtention du modèle d'une stèle n'est que la première étape dans l'enregistrement des gravures présentes à sa surface. En soi, il n'est qu'une représentation virtuelle de l'objet, ce qui n'apporte rien ni à sa lecture, ni à son analyse, en dehors de la possibilité de le visualiser et de le manipuler aisément. Cela reste néanmoins un avantage intéressant quand l'accès à l'objet d'étude est difficile, ou bien quand ce dernier est trop massif pour en appréhender la globalité sur le terrain. Concernant l'étude des motifs gravés, il est donc indispensable de traiter le modèle pour obtenir une meilleure lecture, puis possiblement un relevé. Cette problématique existe depuis l'application de la modélisation dans l'étude de l'art rupestre, et de nombreuses solutions ont été proposées. Certains auteurs se tournent vers des méthodes basées sur l'illumination artificielle, en simulant une ou plusieurs sources de lumière venant éclairer la surface du modèle de façon oblique (Duffy,2010 ; Diaz-Guardamino, 2013 ; Cassen et al., 2014). Ces méthodes s'apparentent à la prise de photo en lumière rasante. D'autres chercheurs se sont plutôt penchés vers des méthodes d'analyses du relief utilisées en géographie, en assimilant la surface de la roche à une surface topographique (Monna et al., 2018; Carrero-Pazzos, 2016 ; Cassen et al., 2014). Toutes ces méthodes, bien que très efficaces, souffrent d'un principal inconvénient : la nécessité d'une surface qui soit majoritairement plane. Les méthodes d'illuminations sont peu efficaces quand

les variations locales du relief sont assez fortes pour masquer les gravures. Les méthodes d'analyses topographiques ne sont pas applicables sur un modèle 3D. Elles nécessitent au préalable de convertir la surface en modèle numérique d'élévation. Ceci pose deux problèmes quant à leur utilisation sur les pierres à cerfs. Le premier implique un découpage de la surface des stèles face par face (Monna et al., 2018), ce qui peut s'avérer délicat lorsque les géométries sont très complexes. Le second est la perte de la géométrie globale de l'objet au moment de l'extraction des faces, avec pour résultat des relevés en deux dimensions, entachés de possibles déformations près des angles et dans les zones à fort relief. L'enjeu est donc de traiter de façon appropriée le modèle 3D pour faciliter l'identification des gravures. Des solutions techniques sont à explorer dans le domaine du jeu vidéo et du cinéma, où les scènes virtuelles sont rendues les plus réalistes possibles. Parmi ces méthodes, il y en existe une qui permet de calculer la quantité de lumière reçue en tout point par le modèle : c'est l'occlusion ambiante. Le succès et l'efficacité qu'a connu cette méthode dès sa création conceptuelle a conduit au développement de nombreux algorithmes. Le travail qui suit consiste en une évaluation d'une partie de ces algorithmes dans une optique archéologique, en l'occurrence l'étude des pierres à cerfs.

Journal of Cultural Heritage 49 (2021) 28–37

Available online at
ScienceDirect
www.sciencedirect.com

Elsevier Masson France
EM|consulte
www.em-consulte.com/en

Original article

Documenting carved stones from 3D models. Part II — Ambient occlusion to reveal carved parts

Tanguy Rolland[a,*], Fabrice Monna[a], Jérôme Magail[b], Yuri Esin[c], Nicolas Navarro[d,e], Josef Wilczek[a,h], Jamiyan-Ombo Gantulga[f], Carmela Chateau-Smith[g]

[a] ARTEHIS, UMR CNRS 6298, Université Bourgogne–Franche Comté, 6 Boulevard Gabriel, Bat. Gabriel, 21000 Dijon, France
[b] Musée d'Anthropologie préhistorique de Monaco, 56 bis, boulevard du Jardin exotique, 98000 MC, Monaco
[c] Khakassian Research Institute for Language, Literature and History, 23, Shchetinkin Street, 655017 Abakan, Republic of Khakassia, Russia
[d] EPHE, PSL Research University, 21000 Dijon, France
[e] Biogéosciences UMR CNRS 6282, Université Bourgogne Franche-Comté, 6, boulevard Gabriel, 21000 Dijon, France
[f] Institute of Archaeology, Mongolian Academy of Sciences, Jucov Street-77, Ulaanbaatar 13343, Mongolia
[g] CPTC, EA4178, Université de Bourgogne, 4, boulevard Gabriel, 21000 Dijon, France
[h] Department of Archaeology, Philosophical Faculty of the University of Hradec Králové, Rokitanského 62, 50003 Hradec Králové, Czech Republic

ARTICLE INFO

Article history:
Received 25 May 2020
Accepted 5 March 2021
Available online 22 April 2021

Keywords:
Archaeology
Deer stone
Rock art
Late bronze age
Mongolia
Documentation
Volumetric obscurance

ABSTRACT

Revealing carved parts in rock art is of primary importance and remains a major challenge for archaeological documentation. Computational geometry applied to 3D imaging provides a unique opportunity to document rock art. This study evaluates five algorithms and derivatives used to compute ambient occlusion and sky visibility on 3D models of Mongolian stelae, also known as deer stones. By contrast with the previous companion work, models are processed directly in 3D, without preliminary projection. Volumetric obscurance gives the best results for the identification of carved figures. The effects of model resolution and parameters specific to ambient occlusion are then evaluated. Keeping tridimensional information intact allows accurate measurement of distance, volume, and depth. Objects augmented by ambient occlusion can easily be manipulated in 3D viewers, for seamless and effortless access to the overall organization of the figures, at the scale of the entire object. Qualitatively speaking, the 2D projected outputs are equivalent to, or even better than, existing archaeological documentation. The proposed workflow should be easily applicable in many situations, particularly as the functions provided for the free R programming software are fully configurable.

1. Introduction

In recent years, several authors have applied 3D modeling techniques to the documentation of rock art [1–6], benefiting from advances in computational power, and field operability, particularly when using photogrammetry [3,7–9]. Beyond the excellent correspondence between model geometry and the real-word artefact, two notable advantages of 3D capture over traditional methods (i.e., rubbing and tracing) are (*i*) the absence of potentially damaging contact with the object to be acquired, and (*ii*) the speed of the process, as time is a major limiting factor in the field. With textured 3D models, it is also possible to simulate, in virtual scenes, different lightning conditions, including grazing light. This long-standing photographical technique, together with reflectance transformation imaging (RTI), can be used by archaeologists to darken carved areas [10,11]. Recent approaches have considered geometry, when it is essentially planar, as a topographical surface to which geospatial methods can be applied. In this case, the geometry of the model is represented as a raster image, where pixel values correspond to altitude, producing a digital elevation model (DEM). Relief may be perceived using computed-generated lighting: analytical hill-shading, for example [12]. For essentially planar surfaces (e.g., engraved walls or slabs), an optimized trend removal procedure (e.g., local relief model, LRM) can also be used to delineate carvings [6]. The recent companion work proposed a practical workflow for dealing with less specific flat surfaces, such as roughly parallelipipedic objects [13]. The study focused on the famous Mongolian deer stones dating from the Late Bronze Age. These stelae, up to 4 m high, often made of granite or sandstone, are engraved with numerous decametric figures (animals, weapons, ornaments, etc.) on each side. After obtaining 3D meshes by photogrammetry, a 2.5D raster DEM was produced by planar projection on each of the four vertical

* Corresponding author.
E-mail address: tanguy.rolland@u-bourgogne.fr (T. Rolland).

https://doi.org/10.1016/j.culher.2021.03.006
1296-2074/

sides of the stela, to capture the entire set of figures. Projecting on the four sides of the stela was natural here, because it corresponds to the traditional representation of such parallelipipedic objects in archaeological documentation. Several algorithms based on differential geometry, sky visibility (sky-view factor [14–16] and positive openness [17,18]), and local morphology were then evaluated. Positive openness was identified as one of the most efficient algorithms for highlighting carved parts and surface condition of stelae. However, rock art is not only found on simple flat geometrical surfaces, such as parallelepipeds. It may also be found on irregular, curved, or concave surfaces, and even on volumetric solids. In such cases, the approaches enumerated above may be difficult to apply, and may strongly deform any symbols depicted in the final results. It would therefore be advantageous to process the entire 3D model in order to overcome these limitations, and not be limited to a subset of cases consisting mostly of roughly flat surfaces, such as those discussed in previous studies [1,10]. Incorporating the results directly into the 3D models, depicted over a color scale, would be an undeniable asset for further examination and better understanding of the carved object. One practical solution is ambient occlusion (AO), introduced at the end of the twentieth century [19–21], and developed since then by the video game industry [22–25]. The aim is to obtain a photorealistic rendering, with minimum computational cost, by simulating shadows in darkened concave and occluded parts of a scene, and by highlighting open areas. Ambient occlusion may be approximated in different ways, but is similar in approach to sky visibility methods, which were specifically designed for DEMs.

1.1. Research aims

The purpose of this study is to test several approaches previously developed to compute ambient occlusion (also including sky-view factor and positive openness computations adapted for entire 3D models) and, if possible, to propose guidelines for enhancing carved areas. Scripts were produced with a single programming platform, R, and are made freely available for a broad archaeological audience. The effect of several extrinsic (model resolution) and intrinsic parameters (specific to AO algorithms) are evaluated. The results are then compared to existing archaeological documentation, and to results previously published in the companion study for two deer stones in a good state of conservation, but with different surface conditions: well-marked carving and slightly marked carving.

2. Material & methods

2.1. Corpus

Deer stones, belonging to funeral structures built by nomads in the late 2nd – early 1st millennium BC, are widespread in Mongolia. More than 1200 deer stones have been identified, and classified into three groups [26,27]. The stelae studied here all belong to the same group, found mostly in Central and East Mongolia. They are decorated with numerous carved figures (both centimetric and decametric), among which deer are the most emblematic, with mature antlers, elongated heads, long necks, and legs folded under their bellies. Other subjects are represented, including several kinds of weapons, shields, belts, and necklaces, forming a well-structured composition. The vast number of visual elements on this type of deer stone makes them the most time-consuming to document. Two previously documented stelae (#35 and #36; in Ref. [13]), located in the Bayantsagaan valley of Khoid Tamir, are used here to evaluate the algorithms, and then compare results with those from the companion study. Eleven stelae, located at the Jargalantyn am complex site, Khanui River valley, Arkhangai, were also processed. All the 3D meshes were obtained by photogrammetry during the Monaco-Mongolian joint mission, undertaken in 2015. The entire acquisition workflow using Structure-from-Motion is detailed in the companion study [13]. Briefly, about thirty to a hundred pictures were captured at a distance varying from 2 to 5 m, with cameras placed approximately 1 m apart, depending on the size of the stelae. Pictures were treated with PhotoScan (https://www.agisoft.com/), and the resulting 3D model was scaled using a self-retracting metallic measuring tape, placed at the foot of the stela and incorporated into the pictures. Two different cameras were used: a hand-held NIKON D800 semi-pro fullframe DSLR (sensor 24 × 36 mm, 36 Mpix), equipped with NIKKOR 24 mm or 50 mm prime lenses (for stelae #35 and #36); a consumer grade compact SONY DSC-RX100 MIII (sensor 13.2 × 8.8 mm, 20 Mpix), 24–70 mm in 24 × 36 equivalent, was used with the focal set at 24 mm (for Jargalant stelae). With this setup, the ground pixel size can be estimated at between 0.2 mm and 0.5 mm. The planar accuracy is between 0.06 mm and 0.15 mm, and the depth accuracy between 0.12 mm and 0.75 mm [28]. Textured 3D models are in Polygon File Format (PLY) format, with a typical resolution of 1–3 mm (i.e., mean edge length between vertices) for 3D models with 3–12 M vertices.

2.2. The algorithms tested

2.2.1. Principle of ambient occlusion

Shadows play an important role in the perception of the world, as they provide information about the position of objects relative to each other, and their surface condition [20]. In virtual worlds, they result from direct or ambient illumination and are essential for realistic rendering. Ambient occlusion represents the amount of ambient light reaching a point in a 3D scene, so that points receiving little light are darkened. Real-time calculation capabilities using the "*screen-space*" approach appeared in 2007 [21,29]. The 3D scene is projected on to a 2D space and AO is calculated only on the visible parts. Distances between points and their projection in the image space are represented as a depth map (or depth buffer). The idea underlying screen-space is quite similar to the approach proposed in the companion study, where the four DEMs could be considered as four depth maps, and where the algorithms based on visible sky (i.e., sky view factor and positive openness) followed the same philosophy as AO. Here, the idea is rather to calculate AO using the "object-space" approach; in other words, by considering all points of the 3D scene, and not only those visible from the observer's point of view. Note that AO is not obtained by formal calculation, but by Monte Carlo approximation, applied to limited zones surrounding each vertex of the 3D model. The algorithms listed below were suited to our purpose: darkening the carved, concave areas of the deer stones, and highlighting the convex areas.

2.2.2. Ambient occlusion inspired by the Crytek approach

This process was originally developed in 2007 by Crytek, a video game company, for a game named Crysis. Each point, P, of the 3D model becomes the centre of a sphere of radius r, in which n sample points, s_i with $i \in [1;n]$, were randomly placed (Fig. 1a). Then AO was defined as the ratio between the number of samples visible from P, and the total number of samples:

$$AO = \frac{1}{n} \times \sum_{i=1}^{n} V(s_i) \quad (1)$$

with $V(s_i) = 1$ if s_i was visible from P, and 0 otherwise. Some authors have suggested adapting this method using only one hemisphere instead of the complete sphere [30]. In this study, the hemisphere was positioned by making its zenith coincide with either (*i*) the normal vector of P, $\vec{n}_P$, (Fig. 1b), or (*ii*) the normal of a 3D best-fit

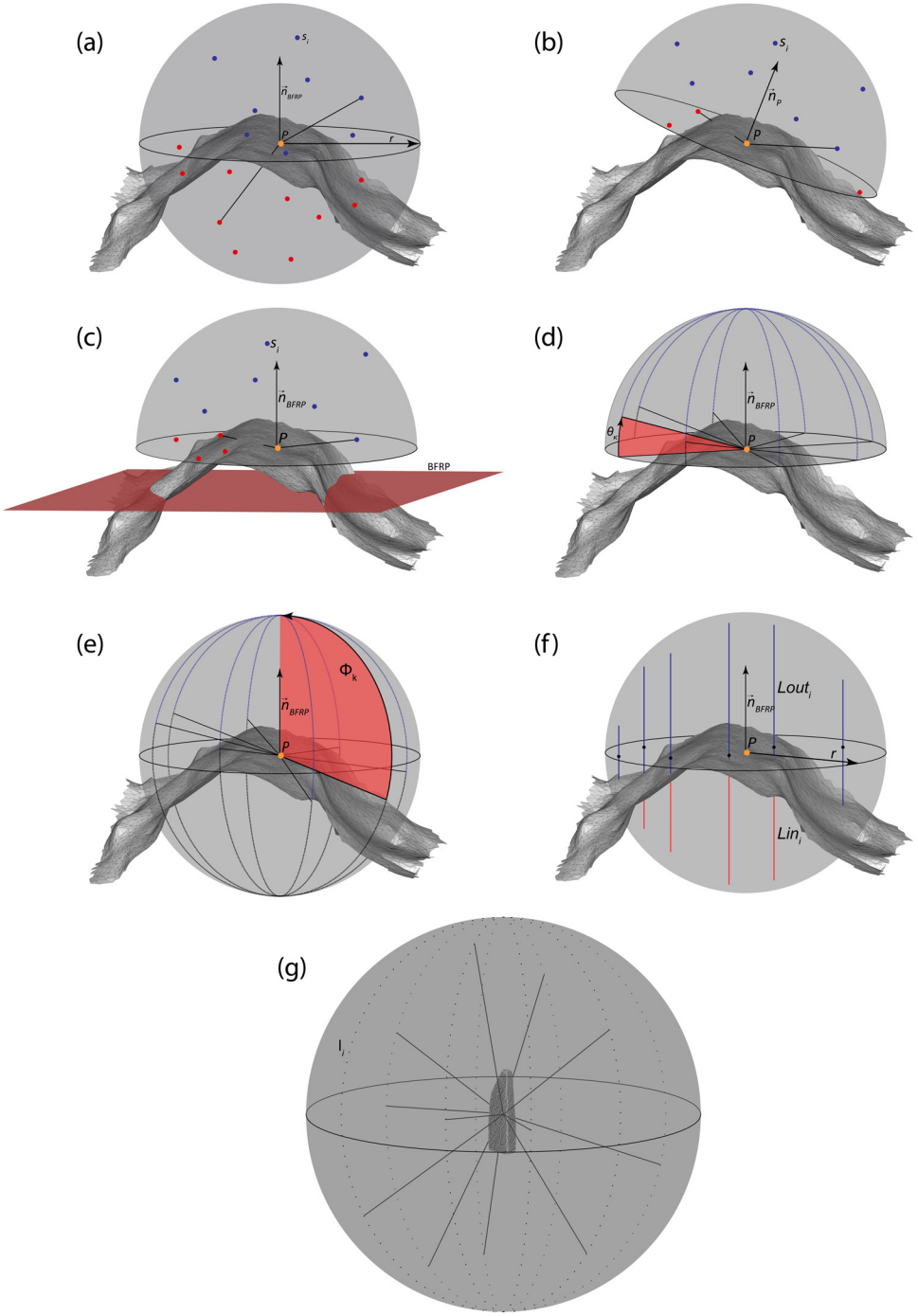

Fig. 1. Illustration of the approaches tested. (a) Crytek-based approach using spherical area sampling. (b) Crytek-based approach using hemispherical area sampling oriented by normal of P. (c) Crytek-based approach using hemispherical area sampling oriented by the BFRP. Blue points represent samples seen by P, and red points samples that are not seen. (d) 3D-Sky-view factor. (e) 3D-Positive openness. (f) Volumetric obscurance-based approach. Blue lines represent segment parts outside the mesh, and red lines parts inside the mesh. (g) Global illumination method with examples of ray tracing to determine whether samples on the surface can see points on the model (For interpretation of the references to colour in this figure legend, the reader is referred to the web version of this article).

regression plane (BFRP) of vertices with the radius r, $\vec{n}_{BFRP}$ (Fig. 1c). In all three cases, AO was obtained by Eq. (1). and values $\in$ [0;1].

2.2.3. *Ambient occlusion deriving from sky-view factor and positive openness*

These two methods, commonly used in spatial analysis [14–18] to treat DEMs, have been adapted to process 3D models. In both cases, the purpose is to determine the portion of visible sky limited by the relief. Here, the Sky-view factor adapted for 3D models, namely 3D-SVF, takes into account one hemisphere (orientated either with $\vec{n}_{BFRP}$ - cf. Fig. 1d -, or with $\vec{n}_P$, not shown), decomposed into k (commonly 8) radial portions. The altitude angles, θ_k, from which the sky becomes visible, are then computed, and hence the 3D-SVF, ranging between 0 and 1, is calculated similarly to the normal SVF following:

$$3D - SVF = 1 - \frac{\sum_{i=1}^{k} \sin(\theta_k)}{k} \quad (2)$$

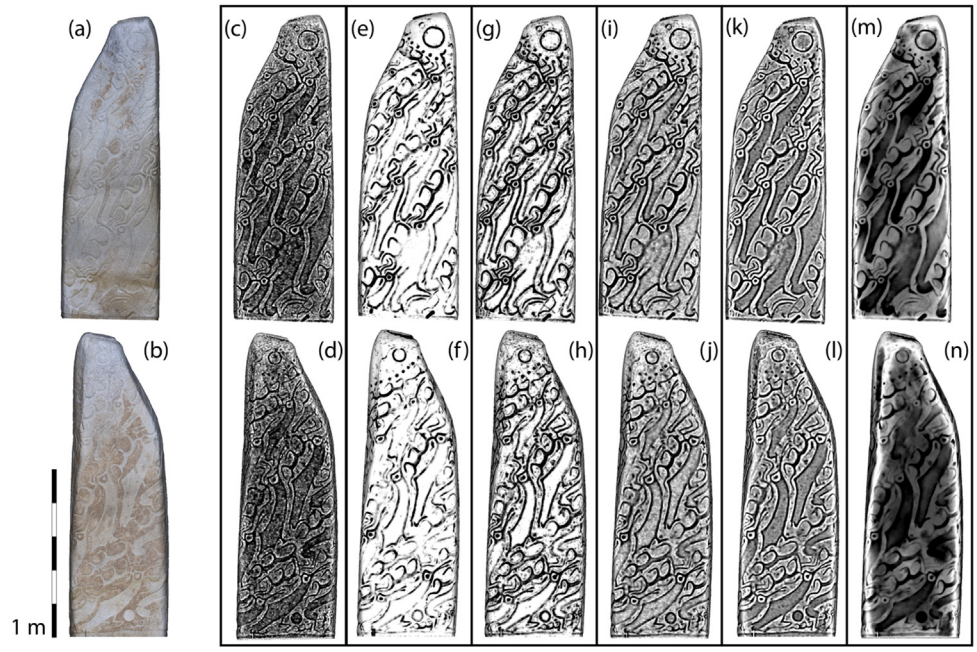

Fig. 2. Comparison between the rendering of the tested methods applied to stela #35. (a,b) Orthomosaic. (c,d) Crytek-based approach using spherical area sampling. (e,f) Crytek-based approach using hemispherical area sampling. (g,h) 3D-Sky-view factor. (i,j) 3D-Positive openness. (k,l) Volumetric obscurance-based approach. (m,n) Global illumination.

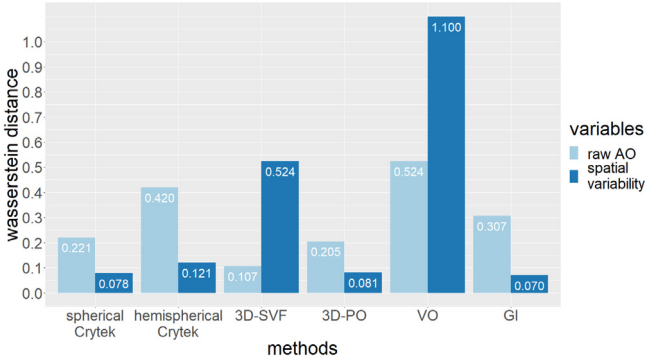

Fig. 3. Wasserstein distances between carved and uncarved parts for a subset of stela #35. Data for AO in light blue, and spatial variability of AO in dark blue. Note that input data were first standardized. AO: ambient occlusion (For interpretation of the references to colour in this figure legend, the reader is referred to the web version of this article).

Positive openness, PO, is also defined by eight radial directions. For each of them, the greatest angle Φ_k, relative to the zenith (and not to the horizon) was computed (Fig. 1e). For 3D models, 3D-PO values correspond to the average of these angles [18], after making the zenith coincide with $\vec{n}_P$:

$$3D-PO = \frac{\Phi_0 + \Phi_{\pi/8} + \ldots + \Phi_{7\pi/8}}{8} \quad (3)$$

so that 3D-PO $\in [0;\pi]$. Programmatically, j samples were placed evenly along the celestial meridian for 3D-SVF (or terrestrial meridian for 3D-PO), for each radial direction.

2.2.4. Volumetric obscurance-based method, VO

This AO is defined as the ratio between the volume inside the model and the volume outside the model of a given sphere centred at point P [31]. A line sampling strategy is used to approximate these two volumes. A total of n sample points was first placed randomly on a disc of radius r, centred on P, and parallel to the BFRP. The lines sampled in this study were those between each sample point and its projection on to the surface of both hemispheres following the normal direction of the disc (Fig. 1f). Finally, VO was defined as the ratio between the total lengths of the segments outside the model, $Lout_i$, and those inside, Lin_i; VO $\in]0;+\infty[$:

$$VO = \frac{\sum_{i=1}^{n} Lout_i}{\sum_{i=1}^{n} Lin_i} \quad (4)$$

2.2.5. Global illumination, GI

In its simplest form, AO can be obtained from global illumination. In practice, lighting is simulated from n light sources, l_i, scattered on the surface of a sphere with a radius much greater than that of the object size (Fig. 1g). The GI was defined by the rate of illumination that a vertex received:

$$GI = \frac{1}{n} \times \sum_{i=1}^{n} W(l_i) \quad (5)$$

with $W(l_i) = 1$, if the vertex P received the light l_i, and 0 otherwise.

2.3. Numerical comparison of the enhancement capabilities of each algorithm

A subset of the model for stela #35 was retained for formal comparison of the enhancement capabilities of the six methods. The carved parts were represented by manually selected vertices corresponding to the limits of the carvings, comprised between the top and the foot of the slope. The remaining vertices correspond to uncarved parts (see Supplementary material S1). Two variables were considered: (i) the ambient occlusion (AO) computed by each method, as described above, and (ii) the spatial variability of the AO, using the inverse distance weighting variance as a proxy, calculated within a radius r (the same measurement was used for AO computation). The 1D-Wasserstein distance, W_1, which measures the area between two cumulative distribution functions, was used as the

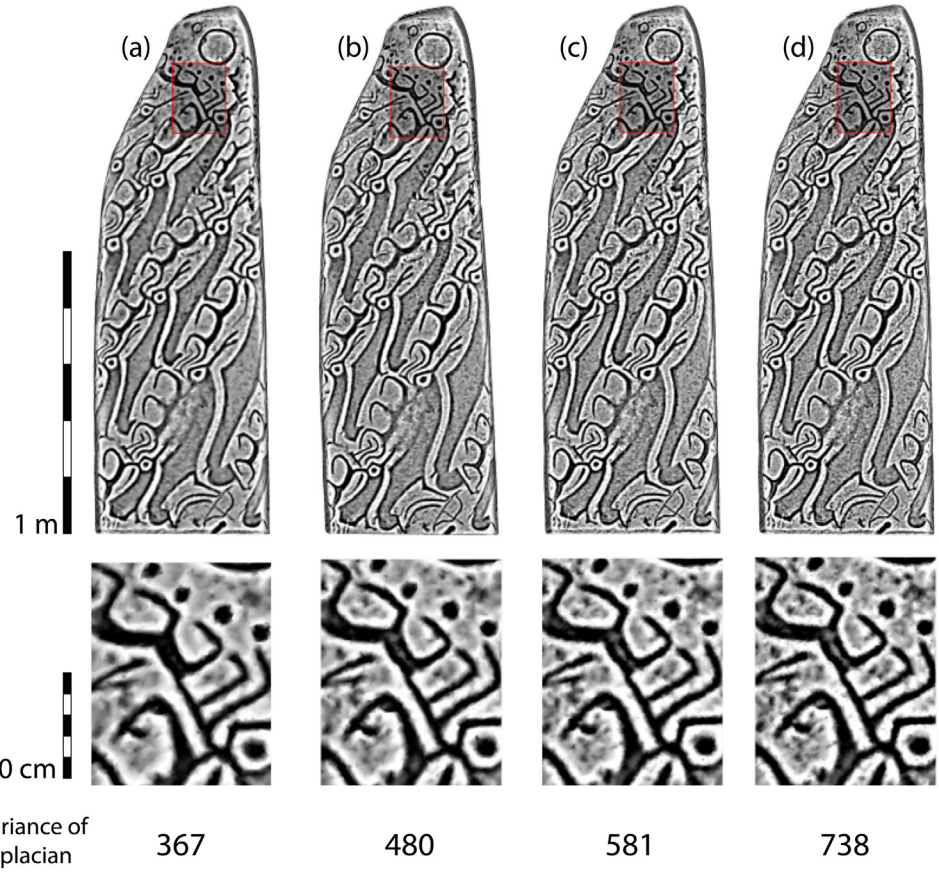

Fig. 4. Effect of model resolution, using stela #35 as an example, with the volumetric obscurance-based approach. Number of faces tested: 250,000 (a), 500,000 (b), 1 M (c) and 2 M (d). From top to bottom: projection of one side after processing the entire stela, a close-up corresponding to the red inset, the value of the variance of Laplacian computed from the projection (For interpretation of the references to colour in this figure legend, the reader is referred to the web version of this article).

metric to evaluate the differences between carved and uncarved parts, following [32–34]:

$$W_1 = \int_{-\infty}^{+\infty} \left| F(x) - G(x) \right| dx \tag{6}$$

where F(x) and G(x) are the cumulative distribution functions to be compared. In practice, all tested variables were first standardized to eliminate the scale factor. A higher value for the Wasserstein distance (W_1) indicates greater difference between carved and uncarved parts, based on their distributions for each variable, thus leading to easier recognition of the engravings.

2.4. Programming implementation

Scripts for producing AO were written using the free R software (https://www.r-project.org/), with the help of the functions included in the Rvcg [35], rgl [36], Morpho [37], cwhmisc [38], HI [39] and doParallel [40] packages. Briefly, the position or visibility of sample points in relation to the model is obtained by raytracing. To improve performance, partition by nearest neighbour search was operated by kd-tree. Additional details can be found in the script files provided as supplementary materials (see Supplementary material S2). The proposed method should be easily applicable; the functions provided are configurable and adjustable to any acquisition workflow based on 3D modelling.

3. Results and discussion

3.1. Algorithm comparison

Most of the algorithms were tested with a sphere or hemisphere of 1 cm radius, a value previously found appropriate to enhance the figures carved on these particular stelae [13]. For the GI method, 1024 lights were distributed at 100 m from the object (i.e., a value much greater than the normal size of a deer stone of ca. 1–4 m). When required (in the VO- and Crytek-approaches), a total of 200 points was sampled. Tests were carried out on unsmoothed models of stelae #35 and #36, decimated to 500 000 faces. The AO values obtained were then truncated at the 1st and 9th deciles, and converted into grey scale. This step greatly improves the overall contrast and facilitates visual comparisons between different renderings. Note that algorithms using hemisphere orientation with either the normal of P or of BRFP produced similar results (see Supplementary material S3 for more detail), so that only the outputs using BRFP are presented in the following.

The symbols carved on the two largest sides of stela #35 are barely visible (Fig. 2a,b). The Crytek-based approaches computed using either the sphere (Fig. 2c,d) or the hemisphere (Fig. 2e,f) produce very different, but clearly sub-optimal outcomes. With the sphere, the carved parts were darkened, but they were not clearly distinguished from the surrounding area, which was also dark, and even noisy. With the hemisphere, the stela appeared mainly whitish, with almost only the footslopes of the deeply carved parts strongly darkened (Fig. 2e,f). The less pronounced depressions were barely visible, while information about the surface condition of the stone was lost. The 3D-SVF (also using the hemisphere, Fig. 2g,h)

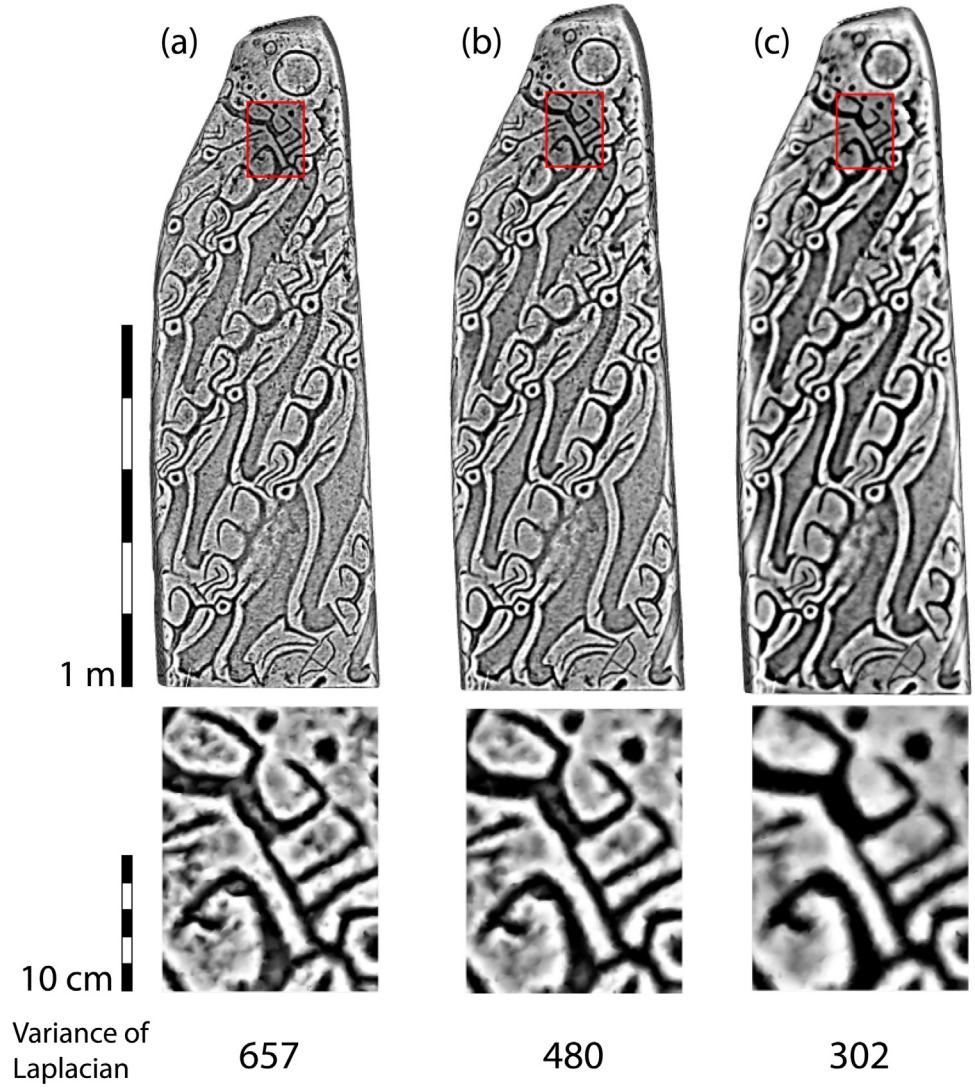

Fig. 5. Effect of radius of influence, *r*, using stela #35 as an example, with the volumetric obscurance-based approach. The three radii tested are 0.5 cm (a), 1 cm (b), 2 cm (c). From top to bottom: projection of one side after processing the entire stela, a close-up corresponding to the red inset, the value of the variance of Laplacian computed from the projection (For interpretation of the references to colour in this figure legend, the reader is referred to the web version of this article).

generally suffered from the same drawbacks, but a little more detail could be perceived, particularly in the shallow areas. Although 3D-PO (Fig. 2i,j) follows the same underlying idea as 3D-SVF, their respective outputs were quite different. With 3D-PO, the deer were fully marked, as were small irregularities on the surface of the stone that did not adversely affect the overall reading of the stela. This result is mainly due to the capacity of 3D-PO to account for convex parts, while 3D-SVF cannot distinguish planes from convex areas [14]. Such behavior was already observed on DEMs, and it is for this reason that PO was previously preferred to other methods, including SVF [13]. The VO-based approaches (Fig. 2k,l) produced similar results to those obtained with 3D-PO. The central part of the deer appeared darker, and less noisy, whereas the carved edges were much more strongly contrasted. Interestingly, in principle, VO is less prone to be affected by small surface irregularities close to the point of interest P, because calculations are based on volume, and not on visibility, which can be drastically affected by any protruding neighbors blocking the view. The VO approach should therefore produce more readable results, even with stelae presenting rather granular surfaces. The general appearance with GI (Fig. 2m,n) was smoother than that obtained with all the other methods. Concave areas, whatever their dimensions, were clearly enhanced, as were the carved edges. Although results were acceptable on the essentially convex side (Fig. 2m), they were locally less so on the opposing, slightly concave side (Fig. 2n). The GI method appears to be very dependent on the overall shape of the object. However, even if GI seems to be unsuitable for complex 3D objects, it may be effective for flat carved surfaces (see Supplementary material S4, for an example).

Computed Wasserstein distances for AO and AO spatial variability are reported in Fig. 3, and cumulative distribution functions are displayed in Supplementary material S5. These results confirm the first observations by the naked eye. Among all tested methods, the VO algorithm produces the highest Wasserstein distances for both variables, especially for spatial variability. This is a clear sign of high local contrast and strong discontinuities in carved parts, which should make the figures more easily identifiable.

3.2. Optimal parameters

The influence of all parameters, both extrinsic (model resolution) and intrinsic (radius and sampling points), should be examined to optimize the VO algorithm for the delineation of carved figures. As computation time increases with each of these

variables, the goal is to obtain relevant output (for our purpose) without computational overload.

3.2.1. Model resolution

The aim here was to assess the minimum model resolution at which carvings can be properly highlighted. The VO algorithm was applied to four models of stela #35, originally with ca. 3 M faces, and progressively decimated to 2 M, 1 M, 500 k, and 250 k faces, thus producing resolutions of 1.99 mm, 2.80 mm, 3.96 mm, and 5.62 mm, for the average edge length (Fig. 4). The variance of the Laplacian was used as a metric for sharpness [41,42]. Its value increases from 367 to 738 (see Fig. 4), indicating slightly more detailed outputs as the number of faces grows, thus improving pattern contour accuracy. In all cases, the carvings always remain easily readable, whatever the model resolution tested. Surface states of the object are slightly better rendered with models possessing more faces. Here, one million faces is more than adequate to identify and study figures.

3.2.2. Influence of the radius r

The radius must be set according to the size of the details to be highlighted. It is well known that smaller *r* values tend to capture more noise, while higher *r* values essentially provide information about the overall shape of the object [14]. Three radii were tested: 0.5 cm, 1 cm, and 2 cm, on a model possessing 1 M faces (Fig. 5). The variance of the Laplacian was again used to analyze the outputs. The increase of the radius leads to a clear decrease in sharpness, with values falling from 657 to 302 (Fig. 5). At a radius of 0.5 cm, both patterns and surface irregularities were well marked. At 1 cm, only the smallest irregularities disappeared, while pattern boundaries remained clearly distinguishable from model roughness. At 2 cm, surface roughness was no longer rendered, and figure boundaries were somewhat blurred. As a result, a radius of 1 cm was a good compromise: figure edges were easily identifiable, and the information about surface condition was preserved, without being overly affected by potential noise.

3.2.3. Influence of number of sample points

Theoretically, with more samples, the estimation of the volume of interest should be more accurate.

Three different setups for processing VO were tested: 10, 100, and 1000 samples. The reference considered here was 1000 samples. Between 100 and 10 samples, the mean absolute errors increase slightly from 0.011 ± 0.011 (1SD) to 0.027 ± 0.031 (1SD), meaning a deviation of only about 1–3% (see Supplementary material S6). Such deviations can be considered insignificant, providing no visual difference in terms of rendering (Fig. 6). In addition, no systematic bias could be identified for either of the two cases (see Supplementary material S6). As a result, 10 samples should be enough to properly enhance the relief, while saving computation time. Such a finding is in agreement with the sampling parameters commonly used in ambient occlusion algorithms, i.e., 8–16 samples [21,31].

3.3. 2D projection and comparison with current documentation

At this point, it is worth recalling that, by contrast with the previous companion study, the figures are now enhanced directly on the 3D model itself, and not from a set of 2D projections. The operator can therefore manipulate the object in a dedicated viewer, to examine the relationships between the figures, and thus perceive their organization in a true 3D space. Measurements that were impossible (or at least difficult) in the 2D projected space are now achievable: e.g., volumes, Euclidian or geodesic distances, and depth (Fig. 7). Working from an enhanced 3D model also offers new and very flexible possibilities for projecting archaeological

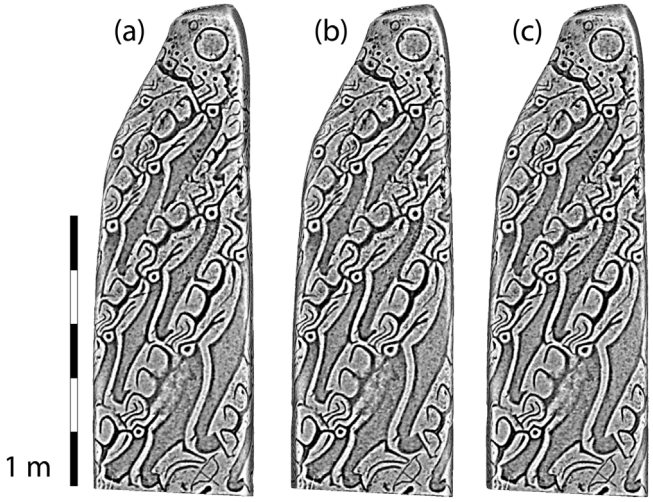

Fig. 6. Effect of the number of sampling points, using stela #35 as an example, with the volumetric obscurance-based approach. Number of samples tested: 10 (a), 100 (b), 1000 (c).

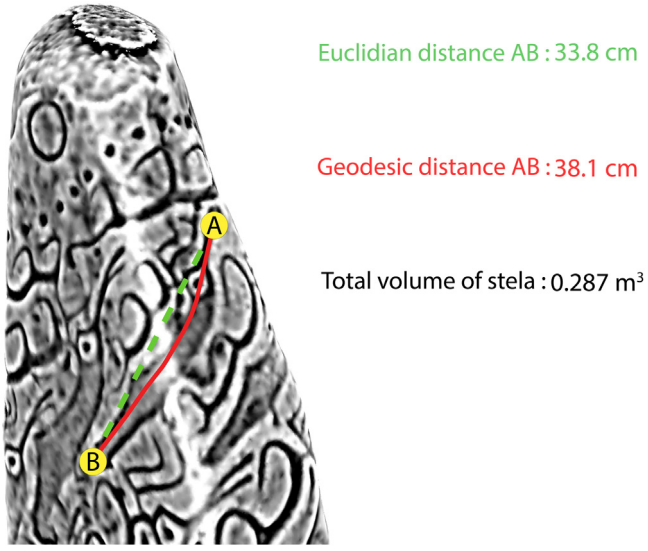

Fig. 7. Example of measurement, using stela #35 as an example. Euclidian distance (green dotted line) and geodesic distance (red line) between points A and B (For interpretation of the references to colour in this figure legend, the reader is referred to the web version of this article).

objects appropriately (more particularly for objects with irregular geometries) in order to produce accurate 2D documentation. To assess the effectiveness of the approach proposed in this study (Fig. 8), the results for the targeted side of stela #36 extracted from existing documentation, for orthomosaic (Fig. 8a), rubbing (Fig. 8b), and SAGA-based positive openness applied on a DEM (Fig. 8c) were compared with results obtained using the VO-based approach (Fig. 8d). Fig. 8c is based on results in Ref. [13], which used the same 3D model as the present study, but limited the DEM to a resolution of 1 mm per pixel, judged sufficient to extract the geometry of the carved areas.

Shape and position of the figures are virtually identical for all techniques, except for orthomosaic, which is not informative. Although the deepest figures can be systematically identified (e.g., the circle at the top of the stela and all the deer), rendering appears much more contrasted with the VO-based approach (Fig. 8d), so that figures are generally better distinguished. The faintly carved bow and horse (Fig. 8e,f), barely visible with PO, are better distin-

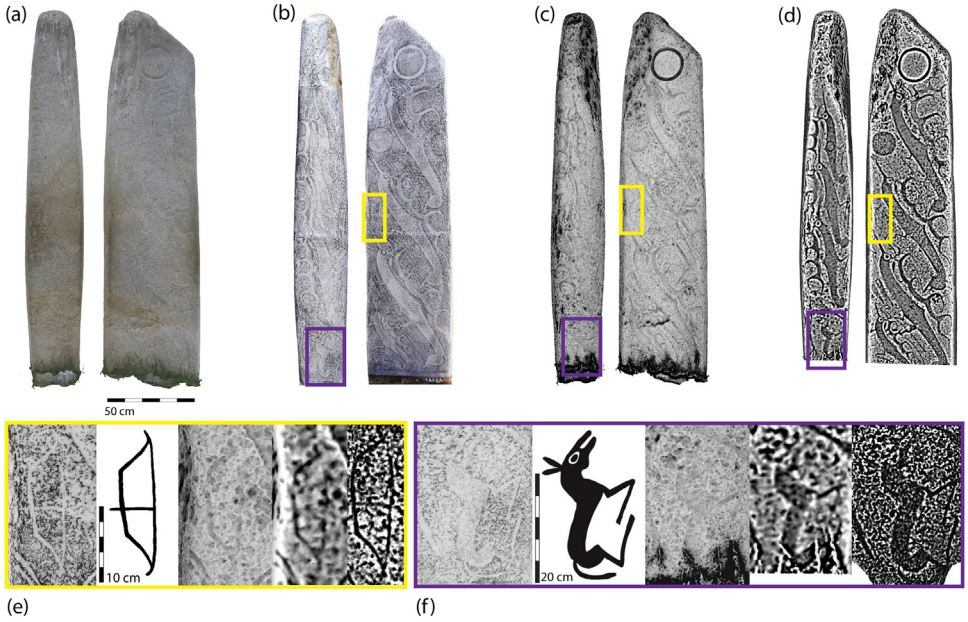

Fig. 8. Comparison between the results of rubbing, positive openness, and the volumetric-based approach on two faces of stela #36. (a) Orthomosaic, (b) Rubbing, (c) Positive openness on DEMs, (d) Volumetric-based approach, (e) bow detail (yellow outline), (f) horse detail (purple outline). For both (e) and (f), from left to right: rubbing, archaeological drawing from rubbing, treatment by positive openness of a DEM, see Ref. [13], volumetric-based approach with 3D models with a resolution of either 2.7 mm or 0.4 mm (For interpretation of the references to colour in this figure legend, the reader is referred to the web version of this article).

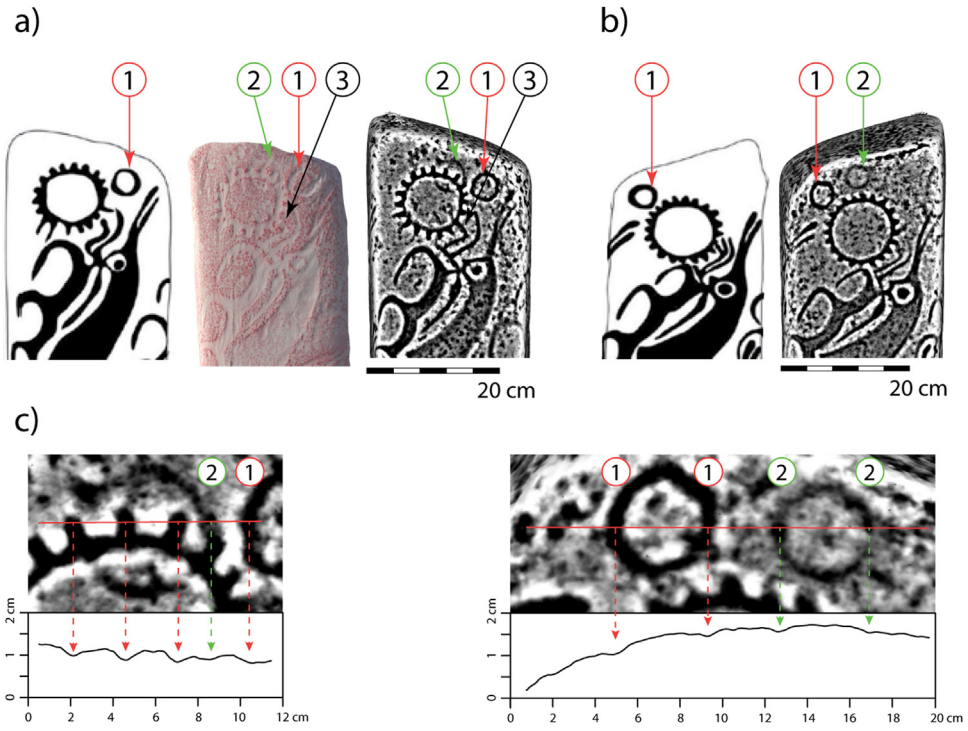

Fig. 9. Comparison between the results of tracing, rubbing and the volumetric-based approach on the top of two faces of Jargalant N°2-2 stela. (a) from left to right, results of tracing, rubbing and the volumetric-based approach. (b) from left to right, results of tracing and the volumetric-based approach. (c) Cross-section of stela faces with plots showing variations in relief. (1) in red: circles recorded by tracing. (2) in green: circles visible with the VO-based approach (For interpretation of the references to colour in this figure legend, the reader is referred to the web version of this article).

guished with VO. Note, however, that rubbing still provides the best outputs for these details. Neither the arrow and the top of the bow, nor the horse's ears and nose can be detected with VO. This drawback should not be formally imputed to the VO-based approach, but to the resolution of the original model, which was not detailed enough to record such discreet surface features. The bow, as well as the details of the horse, do in fact become discernable when a supplementary 3D model, produced at better resolution (0.4 mm), is used as input (Fig. 8e,f).

The method described can be applied routinely. As an example, eleven stelae from the Jargalantyn am complex site, processed by volumetric obscurance and projected on their four main sides can be found (see Supplementary material S7), as well as the enhanced 3D models in PLY format (see Supplementary material S8). A close

examination of the upper part of the treated Jargalant N°2–2 stela, compared to the corresponding available documentation [43] (Fig. 9), plainly reveals the attractive potential of the approach presented here. In addition to circles well recorded by tracing (noted #1 in Fig. 9a–c), two new small circles are now clearly visible with the VO-based approach on the 3D model (noted #2 in Fig. 9a–c). The reason is probably their shallower depth of carving: roughly 2 mm for the new figures vs. 3–4 mm for the already recorded figures (Fig. 9c). Here, the large, deep circle with rays resembling both the sun and one of the types of earrings from the Late Bronze Age in the eastern steppes appears to overlap one of these small circles (arrow Fig. 9a,c), and the front part of the deer's antler (noted #3 in Fig. 9a), providing information about phasing in carved figures. During the first stage, the deer and the two previously unidentified circles must have been carved. Later, these circles must have been almost completely erased to incorporate the "sun" and another circle. This is supported by the fact that there are never two such small circles on the same side of deer stones. Rubbing succeeded better than tracing in identifying all figures covering this stela, and probably also in illustrating differences observed in carving depth. However, in contrast with rubbing, the interpretations drawn from VO are not only based on visual inspection of the outputs. A return to the original 3D model, containing the tridimensional geometry, is always possible for further measurements. Here, the acquisition process was not adapted to a techno-traceological study, but the algorithms described could straightforwardly be applied to another model acquired specifically for this purpose.

4. Conclusion

Ambient occlusion, straightforwardly assessed by volumetric obscurance from 3D meshes, is a powerful tool to reveal carvings. Although the suggested configuration operates well in our case, it is recommended that researchers take advantage of the versatility of the proposed method by tuning the parameters for their specific purposes. The ability to routinely produce of a set of 3D models, textured by a choice of ambient occlusion algorithms, should help archaeologists to trace outlines of carved figures in a great variety of conditions. Grayscale rendering greatly facilitates the identification of carved images, which are underlined by strongly contrasted edges. Relief enhancement also provides information about the surface condition of the stone, at the time of acquisition. Keeping the tridimensional knowledge of the object intact throughout the whole process is an undoubted asset. One of the most significant advances concerns the extended handling capacity for rock art survey. As preliminary 2D projections are not necessary, information loss does not occur and complex reprojection of documentation is not required. Distance, volume, and depth can be accurately measured, and enhanced objects can easily be manipulated in 3D viewers, making it simpler to perceive the organization of (possibly overlapping) figures, which may be present on all sides. The operator is in full control, and can select whichever 2D projection best fits the objectives of the study. This flexibility is particularly appreciable for complex shapes. Note that the augmented version of the 3D models may advantageously incorporate virtual scenes for purposes of communication to a broader audience [44]. Although convex protruding areas, such as the edges of the stelae, may be partly bleached, which may somewhat mask carvings, the VO-based approach is nevertheless much more versatile than tracing or rubbing, which are difficult to apply to very irregular objects. Although the conservation state of the carved areas on the objects and the quality of 3D modelling will obviously affect the quality of the outputs, the results obtained with the VO-based approach almost equal, and sometimes even surpass, existing archaeological documentation, while preventing possible degradation of the surface, and significantly reducing the time required on site for acquisition.

Acknowledgements

This research was funded by the Joint Mission Mongolia–Monaco and the project ROSAS (uB-FC and RNMSH).

Appendix A. Supplementary data

Supplementary material related to this article can be found, in the online version, at doi:https://doi.org/10.1016/j.culher.2021.03.006.

References

[1] A. Simpson, P. Clogg, M. Díaz-Andreu, B. Larkman, Towards three-dimensional non-invasive recording of incised rock art, Antiquity 78 (301) (2004) 692–698, http://dx.doi.org/10.1017/S0003598X00113328.
[2] M. Carrero-Pazos, A. Vázquez-Martínez, B. Vilas-Estévez, AsTrend: towards a new method for the study of ancient carvings, J. Archaeol. Sci. Rep. 9 (2016) 105–119, http://dx.doi.org/10.1016/j.jasrep.2016.06.044.
[3] J.L. Lerma, S. Navarro, A. Seguí, M. Cabrelles, Range-based versus automated markerless image-based techniques for rock art documentation, Photogramm. Rec. 29 (2014) 30–48, http://dx.doi.org/10.1111/phor.12054.
[4] G. Plets, W. Gheyle, G. Verhoeven, J. De Reu, J. Bourgeois, J. Verhegge, B. Stichelbaut, Three-dimensional recording of archaeological remains in the Altai Mountains, Antiquity 86 (333) (2012) 884–897, http://dx.doi.org/10.1017/S0003598X00047980.
[5] S. Cassen, V. Grimaud, Enregistrements, représentations et analyse structurale d'une stèle néolithique gravée dans l'ouest de la France. Kermaillard à Sarzeau (Morbihan, France), Bolletino del Centro camuno di Studi Preistorici 43 (2017) 33–56.
[6] R. Hesse, LiDAR-derived Local Relief Models – a new tool for archaeological prospection, Archaeol. Prospect. 17 (2010) 67–72, http://dx.doi.org/10.1002/arp.374.
[7] A. Velios, J.P. Harrison, Laser scanning and digital close range photogrammetry for capturing 3D archaeological objects: a comparison of quality and practicality Archaeological Informatics: Pushing the Envelope CAA 2001, vol. 1016, British Archaeological Reports International Series, Oxford, UK, 2001, pp. 567–574.
[8] M. Vavulin, I. Nevskaya, L. Tybykova, Digital MACRO-PHOTOGRAMMETRY in documentation of old Turkic runiform inscriptions in the Altai Mountains, Mediterr. Archaeol. Archaeomet. 19 (2) (2019) 81–104.
[9] G. Plets, G. Verhoeven, D. Cheremisin, R. Plets, J. Bourgeois, B. Stichelbaut, W. Gheyle, J. De Reu, The deteriorating preservation of the Altai Rock art: assessing three-dimensional image-based modelling in rock art research and management, Rock Art Res. 29 (2013) 139–156.
[10] M. Díaz-Guardamino, L. García Sanjuán, D. Wheatley, V. Rodríguez Zamora, RTI and the study of engraved rock art: a re-examination of the Iberian southwestern stelae of Setefilla and Almadén de la Plata 2 (Seville, Spain), in: Digital Applications in Archaeology and Cultural Heritage 2, Elsevier, 2015, pp. 41–54.
[11] G. Palma, M. Corsini, P. Cignoni, R. Scopigno, M. Mudge, Dynamic shading enhancement for reflectance transfor-mation imaging, ACM J. Comput. Cult. Herit. 3 (2010) 2, http://dx.doi.org/10.1145/1841317.1841321, Article 6 (September 2010), 20 p.
[12] M. Carrero-Pazos, B. Vilas-Estévez, A. Vázquez Martínez, Digital imaging techniques for recording and analysing prehistoric rock art panels in Galicia (NW Iberia), Digit. Appl. Archaeol. Cult. Herit. 8 (2018) 35–45, http://dx.doi.org/10.1016/j.daach.2017.11.003.
[13] F. Monna, Y. Esin, J. Magail, L. Granjon, N. Navarro, J. Wilczek, L. Saligny, S. Couette, A. Dumontet, C. Chateau, Documenting carved stones by 3D modelling – Example of Mongolian deer stones, J. Cult. Herit. 34 (2018) 116–128, http://dx.doi.org/10.1016/j.culher.2018.04.021.
[14] K. Zaksek, K. Ostir, Z. Kokalj, Sky-view-factor as a relief visualization technique, Remote Sens. (Basel) (3) (2011) 398–415.
[15] J. Dozier, J. Frew, Rapid calculation of terrain parameters for radiation modeling from digital elevation data, IEEE Trans. Geosci. Remote Sens. 28 (1990) 963–969.
[16] T.E. Oke, Boundary Layer Climates, Routledge Ed, 1987, 464 p.
[17] M. Doneus, Openness as visualization technique for interpretative mapping of airborne Lidar derived digital terrain models, Remote Sens. (Basel) 5 (2013) 6427–6442, http://dx.doi.org/10.3390/rs5126427.
[18] R. Yokoyama, M. Shirasawa, R.J. Pike, Visualizing topography by openness: a new application of image processing to digital elevation models, Photogramm. Eng. Remote Sens. 68 (3) (2002) 257–265.
[19] G. Miller, Efficient algorithms for local and global accessibility shading, SIGGRAPH' 94: Proceedings of the 21st Annual Conference on Computer Graphics and Interactive Techniques (1994) 319–326, http://dx.doi.org/10.1145/192161.192244.
[20] M.S. Langer, S.W. Zucker, Shape-from-shading on a cloudy day, J. Opt. Soc. Am. A 11 (2) (1994) 467–478.

[21] M. Mittring, Finding next gen: cryengine 2 (course notes), in: ACM SIGGRAPH 2007 Courses, ACM, SIGGRAPH, 2007, pp. 97–121, 2007.
[22] J. Bokšanský, A. Pospíšil, J. Bittner, VAO++: practical volumetric ambient occlusion for games, in: Eurographics Symposium on Rendering - Experimental Ideas & Implementations, The Eurographics Association, 2017, pp. 31–39, http://dx.doi.org/10.2312/sre.20171192.
[23] D. Holden, J. Saito, T. Komura, Neural network ambient occlusion, in: SIGGRAPH ASIA 2016 Technical Briefs, ACM, 2016, 4 p.
[24] M. McGuire, B. Osman, M. Bukowski, P. Hennessy, The alchemy screen-space ambient obscurance algorithm, in: HPG' 11 Proceedings of the ACM SIGGRAPH Symposium on High Performance Graphics, ACM, 2011, pp. 25–32.
[25] K. Vardis, G. Papaioannou, A. Gaitatzes, Multi-view ambient occlusion with importance sampling, in: I3D' 13 Proceedings of the ACM SIGGRAPH Symposium on Interactive 3D Graphics and Games, ACM, 2012, pp. 111–118.
[26] V.V. Volkov, Olennye Kamni Mongolii, Nauchnyi Mir, Moscow, 2002, pp. 248 (in Russian).
[27] T. Turbat (Ed.), Mongol ba bus nutgiin bugan khushuunii soyol. Erdem shinzhilgeenii katalog, in 2 vol, ADMON, Ulaanbaatar, 2018 (in Mongolian).
[28] B. P.Hudzietz, S. Saripalli, An experimental evaluation of 3D terrain mapping with an autonomous helicopter, Int. Arch. Photogramm. Remote Sens. Spatial Inform. Sci. XXXVIII-1/C22 (2011) 137–142.
[29] C. Dachsbacher, J. Kautz, Real-time global illumination for dynamic scenes screen space techniques, in: SIGGRAPH' 09 ACM SIGGRAPH 2009 Courses, ACM, 2009, 33 p.
[30] D. Filion, R. McNaughton, Effects & techniques, in: ACM SIGGRAPH 2008 Games, ACM, New York, NY, USA, SIGGRAPH' 08, 2008, pp. 133–164.
[31] B.J. Loos, P.-P. Sloan, Volumetric obscurance, Proceedings of the 2010 ACM SIGGRAPH Symposium on Interactive 3D Graphics and Games (2010) 151–156, ACM.
[32] A. Ramdas, N.G. Trillos, M. Cuturi, On Wasserstein Two-Sample testing and related families of nonparametric tests, Entropy 19 (47) (2017) 15, http://dx.doi.org/10.3390/e19020047.
[33] G. Freitag, C. Czado, A. Munk, A nonparametric test for similarity of marginals—with applications to the assessment of population bioequivalence, J. Stat. Plan. Inference 137 (2007) 697–711, http://dx.doi.org/10.1016/j.jspi.2006.06.003.
[34] E. Del Barrio, J. Cuesta-Albertos, C. Matran, J. Rodriguez-Rodriguez, Tests of goodness of fit based on the L2-Wasserstein distance, Ann. Stat. 27 (4) (1999) 1230–1239 http://www.jstor.org/stable/120161.
[35] S. Schlager, G. Francois, 2017, http://github.com/zarquon42b/Rvcg. 43 p.
[36] D. Adler, D. Murdoch et al., 2018, https://r-forge.r-project.org/projects/rgl/. 153 p.
[37] S. Schlager, G. Jefferis, D. Ian, 2018, https://github.com/zarquon42b/Morpho. 162 p.
[38] C.W. Hoffman, 2018, http://www.echoffmann.ch. 91 p.
[39] G. Petris, L. Tardella, 2013, https://cran.r-project.org/web/packages/HI/HI.pdf. 9 p.
[40] R. Calaway, Microsoft Corporation, S. Weston, D. Tenenbaum, 2017, https://cran.rproject.org/web/packages/doParallel/doParallel.pdf. 4 p.
[41] J.L. Pech Pacheco, G. Cristobal, J. Chamorro-Martinez, J. Fernandez-Valdivia, Diatom autofocusing in brightfield microscopy: a comparative study, Pattern Recognition, Proceedings, 15th International Conference on (2000) 314–317, http://dx.doi.org/10.1109/ICPR.2000.903548, 3.
[42] S. Pertuz, D. Puig, M. García, Analysis of focus measure operators in shape-from-focus, Pattern Recognit. 46 (2012) 1415–1432, http://dx.doi.org/10.1016/j.patcog.2012.11.011.
[43] T. Turbat, J. Bayarsaikhan, D. Batsukh, N. Bayarkhuu, DEER STONES of the JARGALANTYN AM, Mongolian Tangible Heritage Association NGO, 2011, 192 p.
[44] F. Monna, N. Navarro, J. Magail, R. Guillon, T. Rolland, J. Wilczek, Y. Esin, C. Chateau, Contextualization of archaeological information using augmented photospheres, viewed with head-mounted displays, Sustainability 11 (3894) (2019) 13, http://dx.doi.org/10.3390/su11143894.

2.2) Occlusion ambiante et MNE

L'occlusion ambiante s'avère être une solution efficace pour la mise en valeur des gravures. Elle rend désormais possible l'étude de la relation spatiale entre motifs en rapport avec la forme du support, ce qui serait difficile, voire impossible avec une documentation 2D conventionnelle. La méthode de calcul basée sur le volume d'une sphère virtuelle qui se déplacerait sur tous les points du modèle (i.e. Volumetric Obscurance - VO) semble être la plus efficace parmi celles testées (voir section précédente). Entre gravures rupestres et analyse topographique, l'objet d'étude reste le même : le relief. Les seules différences sont les caractéristiques recherchées, et la lecture qu'on en fait. Dans les deux cas, l'objectif est de mettre en valeur les arêtes, les talwegs, et les ruptures de pente. C'est la raison pour laquelle de nombreux chercheurs se sont tournés vers les approches topographiques pour étudier les gravures. Selon un chemin inverse, la VO pourrait être un outil efficace pour l'étude topographique. Comme pour le travail sur l'occlusion ambiante, où des méthodes de traitement du paysage ont été modifiées pour s'appliquer à un objet 3D, il s'agit d'adapter la VO aux objets raster. Ce nouvel indice a donc été comparé à ceux produits par un lot d'algorithmes couramment employés en géomorphologie (sky-view factor, positive openness, Topographic Position Index, …), et cela à partir de plusieurs MNE, présentant un large spectre d'échelles (voir article ci-après).

Il m'a été donné l'occasion de travailler sur le site de Anza, près d'Agadir (Maroc) pour une étude visant à enregistrer de façon la plus exhaustive possible des traces de dinosaures sur des dalles de grès. En paléo-ichnologie, les relevés des empreintes animales s'effectuent essentiellement sur photos et par reconnaissance visuelle. C'est un travail de longue haleine, qui nécessite un haut niveau de compétence. Pourtant, les questions qui occupent les chercheurs durant la phase d'acquisition sont finalement identiques à celles exposées plus haut : identifier des traces à partir des variations du relief. L'étude reproduite en annexe (Annexe 2) compare les possibilités de reconnaissance par traitements de MNE produits par photogrammétrie et l'enregistrement effectué par des paléontologues dans le passé, suivant la procédure traditionnelle.

remote sensing

MDPI

Article

Volumetric Obscurance as a New Tool to Better Visualize Relief from Digital Elevation Models

Tanguy Rolland [1,*], Fabrice Monna [1], Jean François Buoncristiani [2], Jérôme Magail [3], Yury Esin [4], Benjamin Bohard [5] and Carmela Chateau-Smith [6]

1 ARTEHIS, UMR CNRS 6298, Université de Bourgogne–Franche Comté, 6 Boulevard Gabriel, Bat. Gabriel, 21000 Dijon, France; fabrice.monna@u-bourgogne.fr
2 Biogéosciences UMR CNRS 6282, Université de Bourgogne–Franche Comté, 6 Boulevard Gabriel, Bat. Gabriel, 21000 Dijon, France; jfbuon@u-bourgogne.fr
3 Musée d'Anthropologie préhistorique de Monaco, 56 bis, boulevard du Jardin exotique, 98000 Monte Carlo, Monaco; jerome.magail@map-mc.com
4 Khakassian Research Institute for Language, Literature and History, 23, Shchetinkina Street, 655017 Abakan, Russia; esin2006@yandex.ru
5 Cadoles, 29 bis rue de l'Arquebuse, 21000 Dijon, France; bbohard@cadoles.com
6 CPTC, EA4178, Université de Bourgogne–Franche Comté, 4, boulevard Gabriel, 21000 Dijon, France; carmela.chateau@u-bourgogne.fr
* Correspondence: tanguy.rolland@u-bourgogne.fr; Tel.: +33-(0)-380395797

Abstract: The use of digital elevation models (DEMs) has become much more widespread in recent years, thanks to technological developments that facilitate their creation and availability. To exploit these data, a set of processing techniques has been developed to reveal the characteristic structures of the relief. This paper presents a new method based on the volumetric approach, and two derivatives. These methods are evaluated on three DEMs at different resolutions and scales: a freely accessible DEM from JAXA DEM covering part of North-East Tanzania, a DEM corresponding to rock art in Siberia, and a DEM of an archaeological Bronze Age funeral structure. Our results show that with the volumetric approach, concave and convex areas are clearly visible, with contrast marking slope breaks, while the overall relief is attenuated. Furthermore, the use of volume reduces the impact of noise, which can occur when processing is based on sky visibility (e.g., sky-view factor or positive openness) or second derivatives. Finally, the volumetric approach allows the implementation of a vertical exaggeration factor, the result of which will enhance the particular characteristics of the landscape. The present study comes with a standalone executable program for Windows, a QGIS plugin, and the scripts written in Python, including GPU compute capability (via CUDA) for faster processing.

Keywords: digital elevation model (DEM); relief mapping; visualization; volumetric approach; data processing

Citation: Rolland, T.; Monna, F.; Buoncristiani, J.F.; Magail, J.; Esin, Y.; Bohard, B.; Chateau-Smith, C. Volumetric Obscurance as a New Tool to Better Visualize Relief from Digital Elevation Models. *Remote Sens.* **2022**, *14*, 941. https://doi.org/10.3390/rs14040941

Academic Editor: Peter Reinartz

Received: 7 December 2021
Accepted: 9 February 2022
Published: 15 February 2022

1. Introduction

The study of landforms is an essential step in many research fields, such as geomorphology, geology, hydrology, archaeology, civil engineering, and mining. Quantitative analyses are mainly based on digital elevation models (DEMs), a generic term for models including vegetation or human structures (i.e., digital surface model), as well as those describing only ground elevation (i.e., digital terrain model). Both are available in the form of a raster grid. Nowadays, such resources can be produced by many different techniques, with photogrammetry, synthetic aperture radar interferometry (InSAR or IfSAR), and light detection and ranging (LiDAR) among the most common. As recent technological developments have greatly facilitated both acquisition and processing, the production and analysis of DEMs has become a standard, especially since low resolution DEMs covering

the entire Earth are freely available from several governmental agencies (e.g., SRTM, Aster GDEM, and ALOS WORLD 3D 30). A set of procedures has been developed to highlight geomorphological features (e.g., valleys, peaks, and ridges), and elevation anomalies of anthropogenic origin (e.g., ancient or recent quarries, mines, and walls) [1]. These procedures are based on color cast [2], differential geometry including slope and different expressions of curvature [1,3–5], trend removal [6,7], sky visibility [8–10], artificial illumination [11–14], pattern analysis [15], and aspect changes [16], to cite the main algorithms. Each of these tools produces a different picture of the relief, with associated advantages and drawbacks. Note that combining these procedures for a single image may be particularly informative [17].

The widely used analytical hill-shading simulates directional illumination. Its outputs are straightforwardly interpretable and quite effective for revealing small elevation variations on flat surfaces, but they may be inefficient in the case of linear anomalies, parallel to the illumination direction [13]. Topographic Position Index (TPI) is defined as the difference in altitude between a central pixel and the mean of the surrounding cells in the DEM within a radius r [18]. For convenience, the final TPI values are generally standardized (mean equals 0 and standard deviation equals 1). The TPI emphasizes valleys, peaks, and edges well, but fails to provide an overall view of the landscape. Mean curvature is based on second derivatives. It is defined as the average of the two principal (minimal and maximal) curvatures [19]. It varies between positive values for convex and negative for concave landforms, while a zero value denotes a planar surface, steep or horizontal. In that sense, it resembles TPI. Methods like sky-view factor (SVF, [8]) and positive openness (PO, [9,10]) rely on the portion of sky visible from all points. The SVF is based on a hemispherical influence zone, and elevation angles are calculated from the horizon, whereas PO uses a sphere and calculates angles from the nadir. Both are efficient for concave areas [10], but behave differently on convex structures and slopes. They also suffer from sampling, as the portion of visible sky is estimated from a predefined number of directions (usually 8), while the presence of noise, even at a low level, in the close vicinity of the point of interest may produce spurious results. More recently, Hu et al. (2021) focused on changes in aspect direction (downslope direction). The underlying idea is to compute projected aspect change vectors (PACV), quantifying terrain plan concavity and convexity without any need of curvature, which is known to be scale dependent and sensitive to DEM errors. Shadows play an important role in our perception of the world [20,21], which is why analytical hill-shading is so popular. Another method, also based on shading, is ambient occlusion, which has become widely democratized during the past two decades for processing 3D scenes. It was developed in the video-game industry [22–26] to obtain a realistic rendering by darkening the concave parts that naturally receive less light. In its simplest form, ambient occlusion is obtained by simulating ambient light, coming from all directions at the same time. This method soon resulted in a multitude of algorithms for rapid processing of 3D models, all seeking to achieve a good balance between computational needs and quality. One of these algorithms, volumetric obscurance (VO), is based on volumes [23]. It produces a sphere centered on the point of interest, and considers the volume of this sphere outside the 3D mesh as a proxy for illumination.

The aim of this study is to adapt the VO approach, initially designed for 3D models, to the study of DEMs, and to evaluate the resulting outputs by comparing them to those obtained with more classical methods, such as SVF, PO, mean curvature, TPI, and PACV. The effects of two parameters are examined: (*i*) the radius of the sphere determining the influence zone around each cell of the grid, which is an intrinsic parameter of VO, and (*ii*) vertical exaggeration, which is a multiplying factor applied to the DEM values. Three DEMs, with different resolutions, used for different purposes, illustrate the capabilities of the proposed method. The first is used for geomorphological analysis in a volcanic setting in Tanzania. The other two DEMs were produced and processed for archaeological purposes. One represents a carving at a Siberian rock art site, and the other represents funeral structures in the Arkhangai region, Mongolia.

2. Material and Methods

2.1. Corpus

The first DEM used in this study (Figure 1a) was freely obtained from JAXA DEM (provided by AW3D30, JAXA). This DEM, with a 30 m/px resolution, covers a region in the northeast of Tanzania, on the margin of the East African Rift System. It extends from the Serengeti Plain in the west to the Ngorongoro highland in the east, encompassing the Salei Plain. Geomorphologically, this region is very contrasted, with a marked dendritic river pattern, plateaus, and volcanic edifices with steep slopes [27–29].

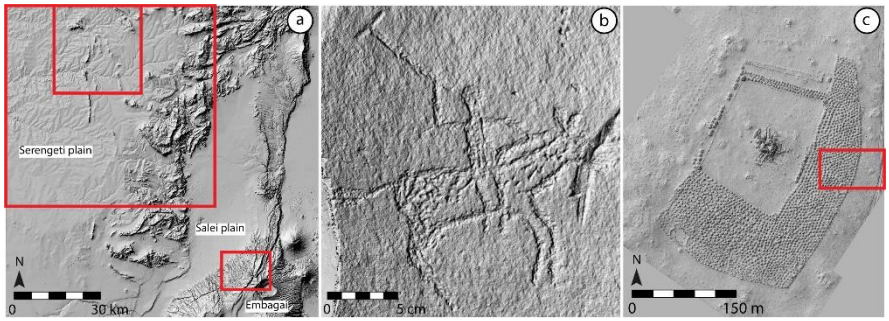

Figure 1. The three DEMs, all processed with analytical hill-shading. Red rectangles indicate specific zones studied. (**a**) DEM of study area in Tanzania. (**b**) DEM of rock art representing a rider, Shalabolino, Siberia. (**c**) DEM of funeral structure, Urt Bulag 2, Mongolia.

The other two DEMs used here were produced by photogrammetry with Agisoft Metashape (https://www.agisoft.com/, accessed on October 2020) specifically for archaeological purposes. The Siberian DEM (Figure 1b) illustrates a petroglyph from the Shalabolino rock art site, Minusinsk Basin, which has been well documented in many methodological and stylistic studies [30–34]. This remarkable site exhibits carved and painted figures dating from the Stone Age to the Early Middle Ages [30,31]. The example processed here is a rider from the Tagar culture, dating from the Early Iron Age. It was produced from photographs captured by a Sony DSC-RX100M3. The surface measures 22×22 cm^2, with a resolution of 0.1 mm/px. The depth of the carved parts is approximately 1 mm. The third DEM (Figure 1c) shows one of the larger Mongolian Bronze Age funeral monuments: the khirigsuur Urt Bulag 2, located in the Khanuy River Valley (Figure 1c). This monument is composed of a central stone tumulus (ca. 3 m high), surrounded by hundreds of stone mounds and stone circles. Photographs were captured using a DJI Phantom 3 PRO unmanned aerial vehicle. The entire DEM measures 359×426 m^2, with a resolution of 3 cm/px, and a subset was extracted for further processing (red rectangle in Figure 1c).

2.2. Volumetric Approach

Volumetric Obscurance (VO), which determines the amount of occlusion around a point of interest, P, was originally developed for processing 3D models. It was defined as:

$$V(P) = \int_S \rho(d(P,s))O(s)ds \quad (1)$$

where S is a surrounding sample sphere, $O(s)$ an occupancy function that takes the value 0 when s is inside the geometry, and is otherwise 1; ρ is a fall-off function, which is defined to be 1 at P, possibly d0ecreasing progressively to 0, at a certain distance from P, $d(P,s)$. Loos et al., 2010 [23] performed several experiments, and observed that using a complex fall-off function, for instance under a quadratic form, was unnecessary because of the computation cost. These authors, therefore, retained a constant function only. In our case, Volumetric Obscurance is computed after creating a spherical volume around a point of interest (P, Figure 2a), from a DEM, and not from a 3D model. The portion of this sphere's

volume located above the surface described by the DEM is then calculated (Figure 2b). Two additional processes were developed, based on the hemispherical volume used in SVF. The process based on the zenith-oriented hemisphere (Figure 2c) will calculate the volume above the surface (VOP: Volumetric Obscurance, "positive"). The process based on the nadir-oriented hemisphere (Figure 2d) will calculate the volume below the surface (VON: Volumetric Obscurance, "negative").

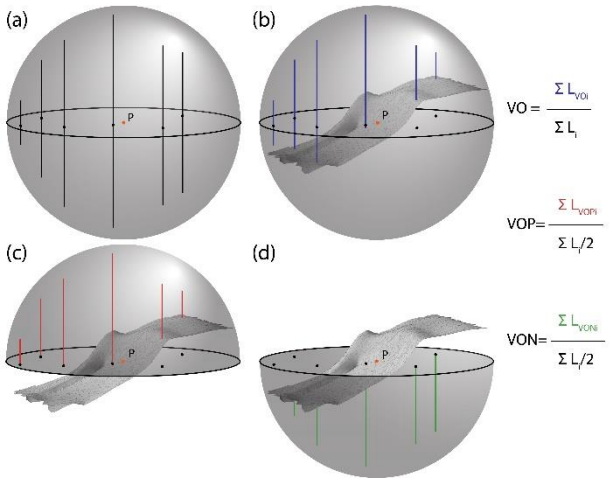

Figure 2. Illustration of the line sampling scheme for the three volumetric approaches, and related equations. Different colored segments are used for each approach: (**a**) black segments sample the sphere volume; (**b**) blue is used for VO calculation; (**c**) red for VOP; (**d**) green for VON.

The main difference with VO calculation, as described above in Equation (1), is that volume portions assessed here are normalized to total sphere or hemisphere volumes. The results are, therefore, comprised between 0 and 1, thus facilitating further readings and comparisons.

$$\mathrm{VO} = \frac{\text{sphere volume above surface}}{\text{total sphere volume}}, \mathrm{VO} \in [0,1] \quad (2)$$

$$\mathrm{VOP} = \frac{\text{hemisphere volume above surface}}{\text{total hemisphere volume}}, \mathrm{VOP} \in [0,1] \quad (3)$$

$$\mathrm{VON} = \frac{\text{hemisphere volume below surface}}{\text{total hemisphere volume}}, \mathrm{VON} \in [0,1] \quad (4)$$

A line-based strategy is used to approximate these volumes [23]. Segments run perpendicular to the horizon from the landform surface to their intersections with the sphere (Figure 2). Segment lengths are summed for the targeted part: ΣL_{VOi} for VO (Figure 2b), ΣL_{VOPi} for VOP (Figure 2c), and ΣL_{VONi} for VON (Figure 2d). These approximated volumes are normalized using that of the entire sphere (using ΣL_i) for VO, and that of a hemisphere (using $1/2\ \Sigma L_i$) for VOP and VON. Note that VO is linked to VOP and VON by:

$$\mathrm{VO} = \frac{\mathrm{VOP} - \mathrm{VON}}{2} + 0.5 \quad (5)$$

2.3. Algorithm

The raster format of DEMs is well adapted to line-based volume approximation as each pixel can be used as the starting point to compute a segment length. The first step is to define a grid where each pixel within a circle of radius *r* (Figure 3a) contains the value of the zenith altitude of the hemisphere, h, taking into account the DEM resolution. This grid becomes the reference for segment length calculation in the following (Figure 3b). Consider now the case of any point, P, in a DEM for VO calculation: the second step is to

shift the DEM, such that the altitude at P becomes 0 (Figure 3c). The altitude of each pixel of the DEM around P is then subtracted from the altitude of the corresponding pixel in the reference grid (Grid_value) to obtain the altitude of the sphere located above the relief. If that difference, Δh, is negative (case 1 in Figure 3c), the relief is above the sphere, and the new pixel value is therefore set to 0. When the difference is positive, but less than twice that of the Grid_value (case 2 in Figure 3c), then the new pixel value becomes Δh. Finally, if Δh exceeds twice the value of the grid, the relief is below the sphere (case 3 in Figure 3c), and the new pixel value is set at twice that of the Grid_value. These new values correspond to the L_{VOi} used to compute the value of VO for the point P. This process is repeated for each DEM pixel. Both VOP and VON are computed following the same principles. The only difference between VO and VOP is that Δh is compared to Grid_value, instead of 2 × Grid_value. For VON, the subtraction is reversed, thus calculating segment lengths from below the landform.

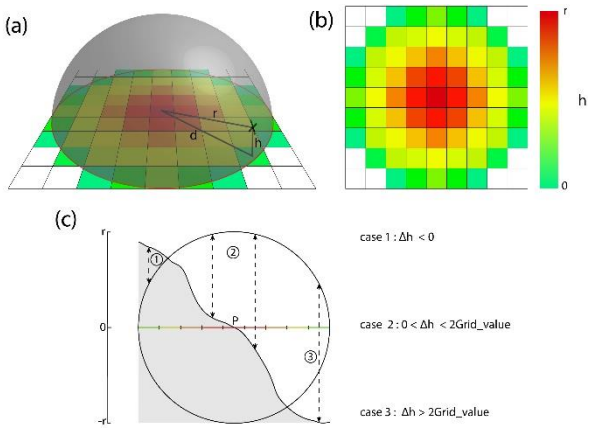

Figure 3. Computational volumetric approaches. (**a**) Representation of hemisphere projection on grid; (**b**) Reference grid with colored values; (**c**) Illustration of the three possible positions of the ground surface in relation to the sphere. Case 1: above the sphere. Case 2: within the sphere. Case 3: below the sphere.

2.4. Implementation

The three methods presented above were implemented in Python, provided here as an open-source script (SM1), as a standalone executable program for Windows (SM2), and as a QGIS 3.X plugin (SM2). The vSky program uses the following Python libraries: PyQT 5.9.2, Numpy 1.16.4, Pillow 6.1.0, Scipy 1.2.1, Cupy 6.0.0, and Gdal 3.0.2. This code allows any projected DEM to be loaded and processed, provided that the resolution is the same in X and Y. Three parameters are tunable: the radius of the sphere and/or hemisphere influence, the strength of smoothing (which is obtained by applying a Gaussian kernel and fast Fourier transform convolution), and the vertical exaggeration (Figure 4). Smoothing and vertical exaggeration optionally pre-process the DEM. The first reduces aliasing and noise by attenuating high-frequency relief, while vertical exaggeration applies a multiplying factor to the altitude, exaggerating or attenuating variations in relief. Vertical exaggeration is often used in combination with analytical hill-shading to adjust the visual aspect. After calculation, results are saved as georeferenced raw data rasters, optionally together with an 8-bit version for each of the three treatments, and an RGB three-channel image combining VO, VOP, and VON. The 8-bit images are produced after linear and saturation stretching within a 2nd–98th percentile interval. In this process, the outputs ϵ [0,1] are remapped to fit the 0–255 range for grayscale rendering. These simplified additional outputs are produced for rapid visual inspection; any further calculation from this documentation should therefore be avoided.

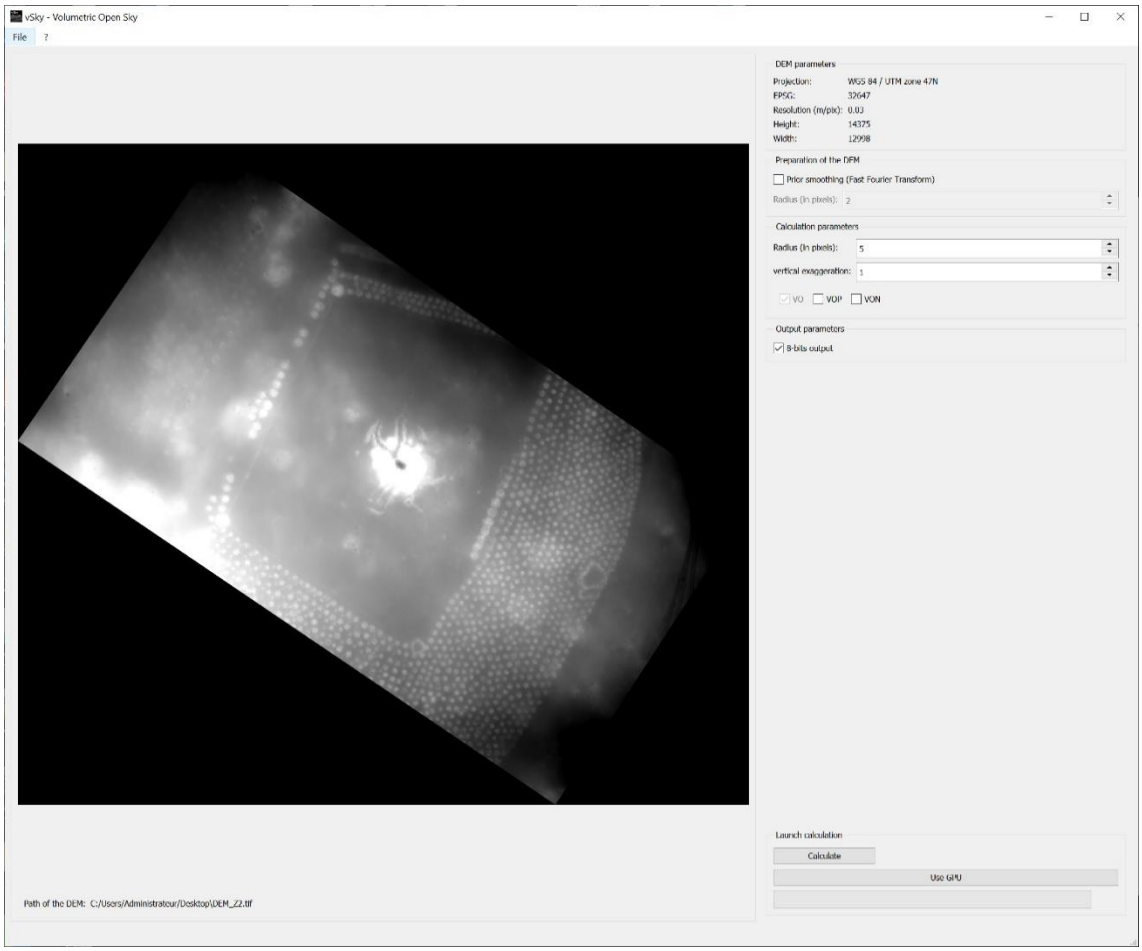

Figure 4. Capture of vSky software, showing a grayscale image of the DEM and its characteristics, as well as the parameters that need to be defined in this method.

3. Experiments

3.1. Algorithm Comparison

In the following, the three new processes—VO, VOP, and VON—are applied to the Tanzanian JAXA DEM and are compared to results from TPI, mean curvature, PO, and SVF (Figure 5a), computed with SAGA GIS (http://www.saga-gis.org/en/index.html, accessed on October 2020). In addition, the correlation matrix between raw outputs is provided in Figure 5b. This specific area was selected because it is among the examples used to introduce the SVF algorithm [8]. To facilitate further comparison, processing was systematically performed without pre-smoothing or vertical exaggeration, and a 300 m influence radius (i.e., 10 pixels) was applied because this value has already been found to be appropriate to study geomorphological features [8]. In the VO output (Figure 5a), the overall perception of the landscape is somewhat lost, as the zones with constant slope values, whether flat or regularly sloping, appear mid-gray (VO $\approx$ 0.5). Only convex and concave areas are highlighted, where edges, ridges, and protruding parts (VO value > 0.5) tend toward white, and thalwegs and bottoms (VO value < 0.5) tend toward black. The TPI and, to a lesser extent, mean curvature rasters are almost the same as VO ($r_{TPI\text{-}VO}$ = 0. 997 and $r_{M.CURV\text{-}VO}$ = 0.924; Figure 5b), at least in the present configuration (i.e., without vertical exaggeration); this point will be discussed later. With VOP, summits and flat areas are essentially white (VOP $\approx$ 1), while concave parts are darkened (when concavity increases, VOP decreases). Non-null slopes are displayed in mid-gray (Figure 5a). Almost the same results are observed with SVF ($r_{VOP\text{-}SVF}$ = 0.891, Figure 5b), and to some extent with PO ($r_{VOP\text{-}PO}$ = 0.822, Figure 5b), where constant slopes and flat surfaces are represented in

similar ways [10]. Although whitish overall, the VON raster exhibits darkened convex parts (VON decreases when convexity increases) and whitened concave and flat parts (VON ≈ 1), i.e., inversely to the other methods. One could, therefore, suppose that VON in some way produces mirror images of VOP, SVF, and PO. In fact, the situation is more complex; different types of information are extracted. Both SVF and VOP specifically focus on the relief present in the hemisphere above the surface (limited by the horizontal plane passing through the point of interest), while VON is based only on the surface inside the lower hemisphere. The SVF and VOP methods saturate if the relief is flat, and therefore cannot capture convexity (Figure 6). By contrast, although VON is more efficient to describe convex relief, it does not capture concavity, and saturates with flat relief (Figure 6). As a result, poor inverse correlations are observed between VON and SVF ($r_{VON\text{-}SVF} = -0.080$, Figure 5b) and between VON and VOP ($r_{VON\text{-}VOP} = -0.096$, Figure 5b). The PO and VO methods take into account everything that is above the relief (Figure 6), including parts below the point of interest. Therefore, they share common elements with VON, which explains why the strength of the linear relationship is greater with PO ($r_{VON\text{-}PO} = -0.370$), and especially with VO ($r_{VON\text{-}VO} = -0.715$) (Figure 5b). This is also true for the relationship between VOP and VO, which are positively correlated ($r_{VOP\text{-}VO} = 0.765$), but convexity cannot be differentiated from flatness by VOP, while VO can describe the full range of relief, from extreme concavity to extreme convexity (Figure 6).

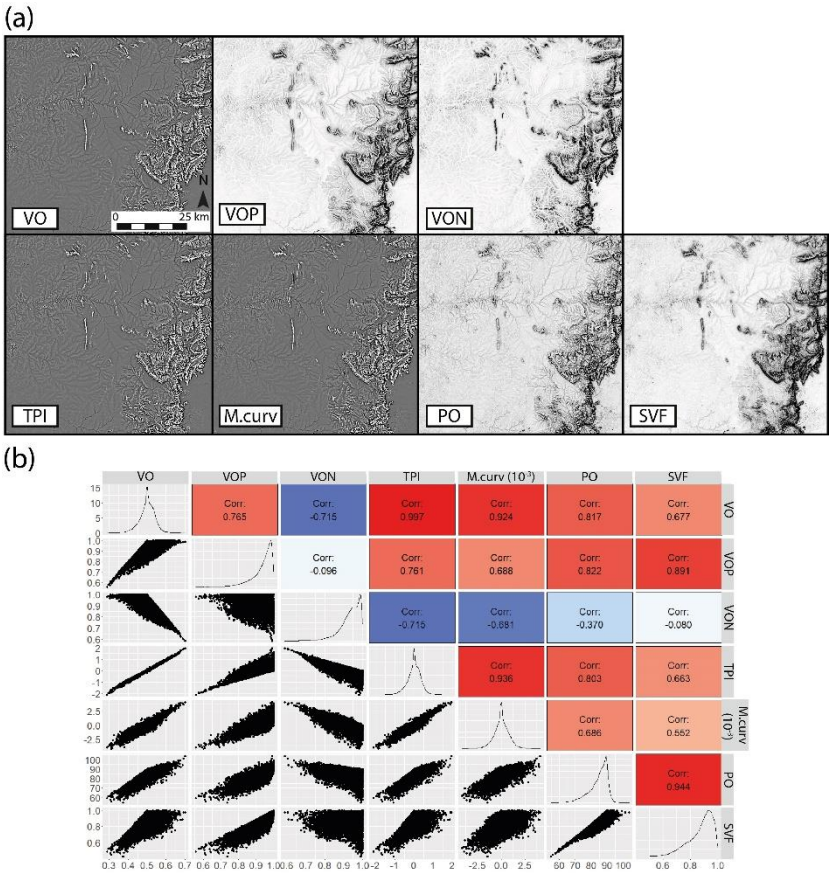

Figure 5. (**a**) Comparison between VO, VOP, VON, TPI, mean curvature (M.curv) PO, and SVF processing applied to the Tanzanian DEM. (**b**) Diagram summarizing pairwise linear correlations for all methods tested. The upper triangle reports the correlation coefficients. The diagonal cells present the distribution values for each method. The lower triangle depicts pairwise scatterplots.

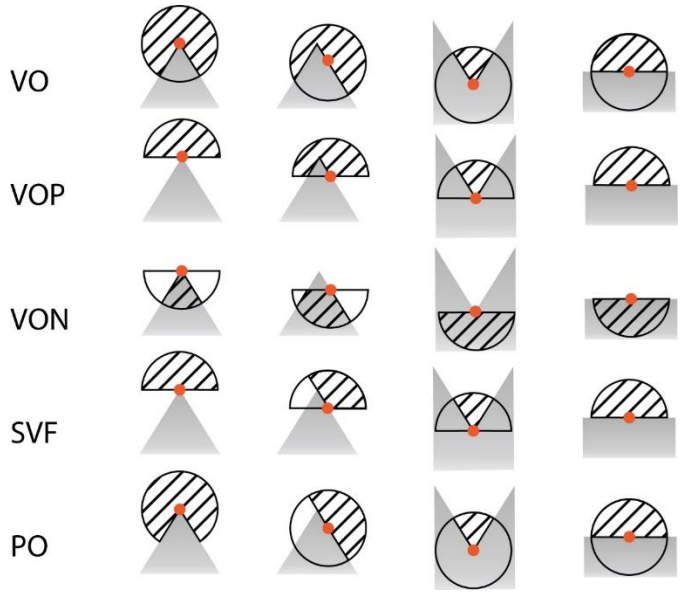

Figure 6. Sketches where hatching depicts the zones taken into account by the VO, VOP, VON, SVF, and PO methods, applied to different topographic cases.

Figure 7 displays a 2.8 km topographic cross-section (AB in Figure 7), oriented SW/NE, across the northern hillside of the Embagai crater, and the values resulting from each method (again with an influence radius of 300 m). The overall shape along the cross section is largely lost (large-scale variations), whatever the processing applied. By contrast, all topographical variations compatible with the set radius are emphasized (smaller-scale variations). This is especially true for VO and VOP, which depict well the subtle altitudinal variations inside the valleys (mark 1 in Figure 7), while the VON algorithm produces the smallest relative amplitude and reacts less than the others to the abrupt changes in altitude (the edge marked 2 in Figure 7). The SVF and PO profiles are noticeably more jagged than those drawn from volumetric approaches, and from TPI and mean curvature (see ridge at mark 3 in Figure 7). The VO, VOP, VON, TPI, and mean curvature processes also produce slightly less sharp images than SVF and PO in Figure 5a. The reason is that the first four methods take into account the entire relief within the radius *r*, and not only the position of the relief limiting the sky (see changes between the first and second columns in Figure 6, and [8,10]). This characteristic is an asset when the point of interest is surrounded by small surface irregularities. The SVF and PO methods, based on visibility, are so sensitive to this issue that a noise remover is introduced as an option in the Relief Visualization Toolbox (RVT) software in order to reduce the deleterious influence of any protruding neighbors blocking the view [8,35].

3.2. Parameter Influence

3.2.1. Vertical Exaggeration and Sphere Radius

Without vertical exaggeration (a pre-processing step commonly applied to increase relief contrast), results from VO, TPI, and mean curvature appear almost identical (Figure 5). For TPI calculation, if vertical exaggeration is applied by multiplying DEM values by a scalar *a*, the differences in altitude between the point of interest and its surroundings are also multiplied by *a*, (as well as mean and standard deviation) (Figure 8a). Once TPI values are standardized and remapped on to a 0–255 range for a grayscale rendering, the resulting map remains unchanged (Figure 8b). Vertical exaggeration, thus, has no effect on TPI, or on mean curvature, for the same reason. For VO, the situation is quite different: when the topography changes, the influence zone (the sphere) remains the same (Figure 8a). Consequently, the volume of the sphere above the DEM is affected by vertical exaggeration,

making this process more versatile than TPI and mean curvature because it can be adapted to a greater variety of situations (Figure 8b).

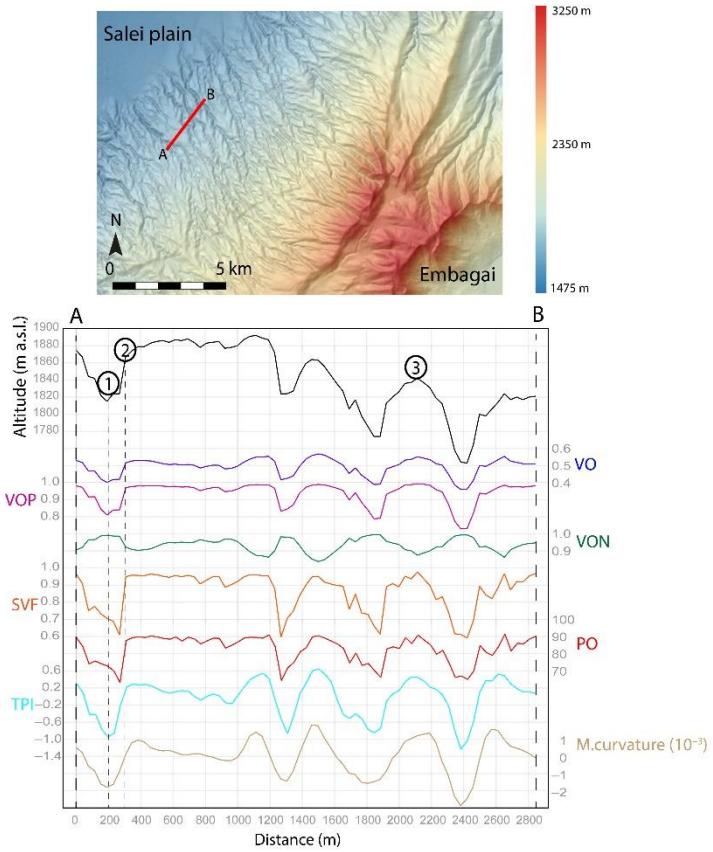

Figure 7. Plot of the topographic section, AB, across the northwestern slope of the Embagai crater, associated with values of VO, VOP, VON, SVF, PO, TPI, and mean curvature (using a 10-pixel radius, except for mean curvature, which uses a 5-pixel radius, as it is better adapted to the study area). The altitude in meters is represented in black, VO in blue, VOP in purple, VON in green, SVF in orange, PO in red, TPI in light blue, and mean curvature in light brown.

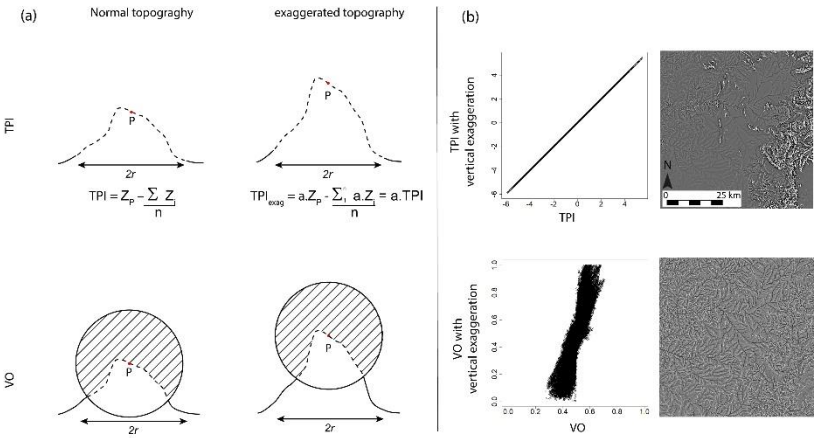

Figure 8. The TPI and VO methods, without exaggeration and with exaggeration, applied on part of the Tanzanian DEM. (**a**) Theoretical topographic profiles, without exaggeration and with x 2 exaggeration, for TPI and VO; (**b**) Scatterplots without exaggeration vs. with exaggeration (a = 1000), and resulting DEM.

Beside optional vertical exaggeration, volumetric methods basically possess one key tunable parameter, the sphere radius, which must be adapted to the size of the features to be highlighted, as with SVF and PO [8,10]. To examine the combined influence of vertical exaggeration and sphere radius, the Shalabolino rock art DEM (resolution 0.1 mm/px) was processed with VO by crossing three values for the *r* radius: 5, 20, and 40 pixels (equivalent to 0.5, 2 and 4 mm), with three vertical exaggerations: none (i.e. ×1), ×5, and ×20 (Figure 9a–i). The tiniest, sub-horizontal cracks near the rider's feet and the horse's rump are identified at the smallest radius, corresponding to 0.5 mm, but not with the two other radii, which nevertheless better isolate the rider and the steed, at the expense of overall smoothing (Figure 9a, see also SM3 for a zoomable version of Figure 9). Exaggerating the relief allows better delimitation of the bottoms of the engraved parts, but also an increase in the salt-and-pepper effect, due to irregularities in the rock surface (see the upper part of the DEM, in particular in Figure 9e,f,i). The optimal adjustment between radius and vertical exaggeration needs to be sought in relation to the purpose: good perception of the shape engraving, or a more detailed focus on how the carving was made, including the surface condition of the rock.

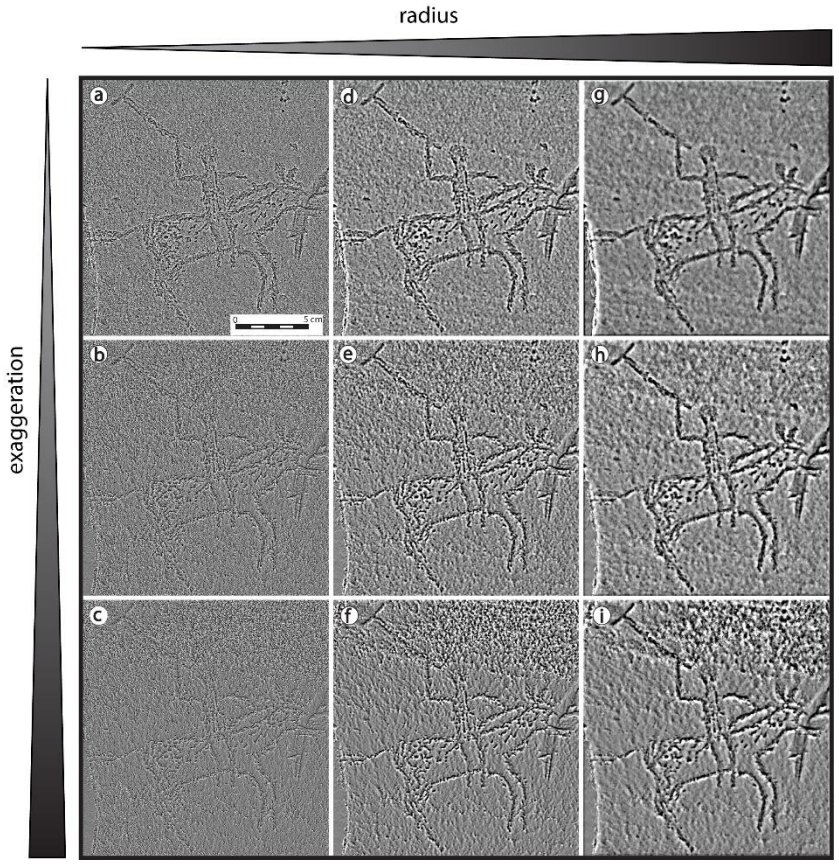

Figure 9. Resulting combinations between influence radius of the sphere and vertical exaggeration for the Shalabolino DEM, processed with VO. Columns correspond to sphere radius values of 5 px (i.e. 0.5 mm), 20 px (2 mm), and 40 px (4 mm). Rows correspond to vertical exaggeration factors of 1 (no exaggeration), 5, and 20.

The hydrologic network of the Serengeti plain provides another example to demonstrate the capabilities of vertical exaggeration applied before VO calculation (Figure 10). Analytical hill-shading was processed without exaggeration to facilitate good understanding of the topography (Figure 10a), while a factor of 1000 was applied before computing VO, SVF, and PO (Figure 10b–d), with a 10-pixel radius, and without pre-smoothing or noise removal. The hydrologic network is revealed whatever the approach, and the valley bottoms are well marked in all cases, as expected. However, the VO image is crisper with

narrower talwegs (Figure 10b). The SVF and PO rasters exhibit a more pronounced salt-and-pepper effect, due to the greater sensitivity of these algorithms to noise, as mentioned above (Figure 10c,d). Hu et al. (2021) [16] suggested using changes in aspect (namely PACV) to quantify concavity and convexity from DEMs, thus better identifying ridges and valleys. Here, PACV was computed using a modified version of the Python scripts made available by Hu et al. (2021) at https://github.com/NJNU-DTA/PACV (accessed on October 2020) (Figure 10e). Interestingly, an equivalent output can be obtained with the VO algorithm, when the DEM is adequately smoothed and exaggerated (Figure 10f). As PACV is not scale dependent, exaggeration has no effect on its output, whereas VO can be freely tuned using exaggeration for more versatility.

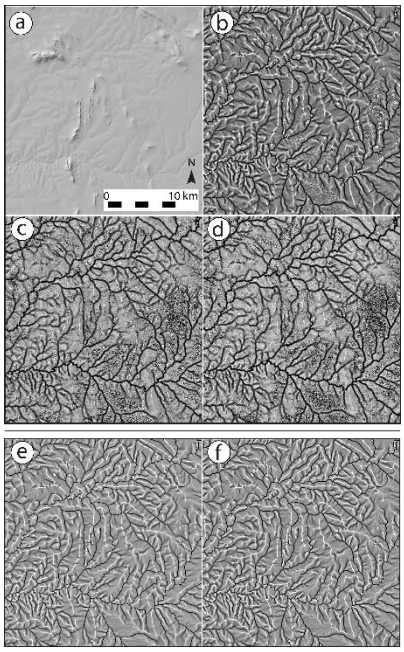

Figure 10. Tanzanian DEM subset on the Serengeti Plain, processed by (**a**) analytical hill-shading without vertical exaggeration, (**b**) VO, (**c**) SVF, (**d**) PO, with vertical exaggeration of 1000 and a radius of 10 px, corresponding to 300 m; (**e**) PACV from a non-exaggerated DEM, and an aspect raster map with a radius of 5 px, (**f**) VO with vertical exaggeration of 1000, a radius of 5 px, and a smooth factor of 10.

3.2.2. VO as Feature Input for Automatic Recognition

The DEMs are often pre-processed to bring out more clearly the particular signature of the features sought, such as crater ridges [36,37], archaeological structures [38,39], roads [40], and valley embankments related to mining [41]. As previously shown, VO provides well-contrasted results at the level of slope breaks, making it possible to identify ridges, valley bottoms, and positive and negative anomalies, thus providing a potentially effective source for automatic detection. As an example, the stones are clearly identifiable from every volumetric output (i.e., VO, VOP, VON) processed on part of the Urt Bulag 2 DEM (Figure 11a–c). Interestingly, these three processes can be combined to form a single RGB image (Figure 11d), where processing fills each of the color channels. Flat parts appear in light blue, convex parts (mound tops) in yellow, and concave parts in dark blue. Red corresponds to strong slopes (>25–30°). Such an image should not be used for calculation, but it may be more straightforward to interpret, at a glance, without closely examining VO, VOP, and VON, one after the other. Interestingly, it may be used as input for automatic detection of structures, with algorithms using RGB images, such as object detection via deep learning [42].

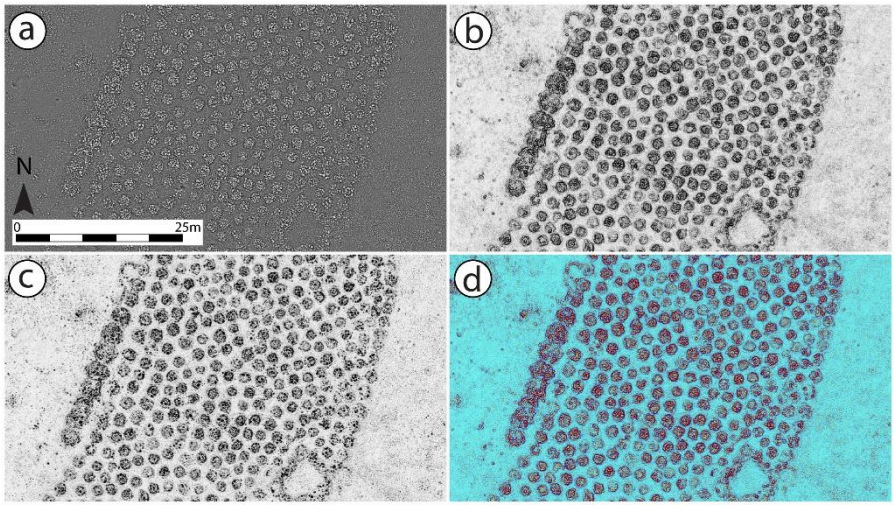

Figure 11. Subset of the Urt Bulag 2 DEM, processed with (**a**) VO, (**b**) VOP, and (**c**) VON; (**d**) represents an RGB combination of the three processes, filling each of the RGB channels. All methods use a radius of 6 px (18 cm), without exaggeration.

4. Conclusions

This study introduces three new DEM processing methods based on volumetric approaches: VO, VOP, and VON. The principle is to consider the entire volume above or below the relief within the area of influence, which is spherical for VO, and hemispherical for VOP and VON. Although the procedures proposed here share common properties with existing algorithms, they possess several interesting assets. First, there is no need to sample a set of directions, as with SVF and PO calculation. Second, the assessment of a volume instead of a sky-limiting relief is much less affected by possible noise, a frequent problem in the case of SVF and PO, which may require nearest neighbors to be ignored. That is also true because the volumetric approach does not require derivatives, which generally suffer from numerical instability. Finally, vertical exaggeration, which has no effect on TPI, mean curvature, and PACV, can be applied before VO computation to enhance specific landscape features. The VO essentially yields gray results, attenuating the overall relief, with strong black-white contrast on slope breaks. Its interpretation may appear less intuitive than that provided by analytical hill-shading, but it is much more specific (and informative) for relief anomalies at a given scale; note that VON and VOP can also be examined in combination, to better apprehend the overall landform. These three new processing tools can be efficiently used in all research fields exploiting DEMs, and at any scale, for semi-automated detection based on thresholding or deep learning. Advantageously, they can provide almost the same information as the traditional processing tools (SVF, PO, TPI, mean curvature, and the more recent PACV approach) by simply using adequate tunings, which are limited to only three parameters: level of smoothing, exaggeration, and radius. A standalone executable Windows program, which includes GPU compute capability (via CUDA) for faster processing, together with a QGIS plugin, the Python snippet, and an accompanying user manual are freely obtainable in (SM1–2). Such availability should promote testing, and hopefully, dissemination to a broader audience for research purposes.

Supplementary Materials: The following supporting information can be downloaded at: https://gitlab.huma-num.fr/fmonna/vsky/-/tree/Paper_Supp_Mat (accessed on 26 January 2022). SM1: Python open-source script of vSky. SM2: Standalone executable version of vSky for Windows with user guide and DEMs examples as well as the QGIS 3.X plugin of vSky. SM3: Full resolution version of the Figure 9.

Author Contributions: Conceptualization, T.R. and F.M.; methodology, T.R., F.M. and J.F.B.; software, F.M. and B.B.; validation, T.R., F.M. and J.F.B.; formal analysis, T.R. and F.M.; data curation, B.B.; writing—original draft preparation, T.R., F.M. and J.F.B.; writing—review and editing, T.R., F.M., J.F.B., J.M., Y.E., B.B. and C.C.-S.; visualization, T.R.; supervision, T.R. and F.M.; funding acquisition, F.M. and J.M. All authors have read and agreed to the published version of the manuscript.

Funding: This research and APC were funded by the Joint Mission Mongolia–Monaco and the project ROSAS (uB-FC and RNMSH).

Data Availability Statement: ALOS/PRISM AW3D30: https://doi.org/10.5069/G94M92HB.

Acknowledgments: This research was funded by the Joint Mission Mongolia–Monaco and the project ROSAS (uB-FC and RNMSH). The data used for this paper were provided by ALOS/PRISM AW3D30 of the Japan Aerospace Exploration Agency and the joint Mission Mongolia–Monaco. We are grateful for comments by the anonymous reviewers, which have greatly improved the manuscript.

Conflicts of Interest: The authors declare no conflict of interest.

References

1. Wood, J. *The Geomorphological Characterisation of Digital Elevation Models*; University of Leicester: Leicester, UK, 1996.
2. Challis, K. Airborne laser altimetry in alluviated landscapes. *Archaeol. Prospect.* **2006**, *13*, 103–127. [CrossRef]
3. Smith, M.; Goodchild, M.F.; Longley, P.A. *Geospatial Analysis: A Comprehensive Guide to Principles, Techniques and Software Tools*; Matador: Leicester, UK, 2009.
4. Longley, P. (Ed.) *Geographic Information Systems & Science*, 3rd ed.; Fully Updated; Wiley: Hoboken, NJ, USA, 2011.
5. Minár, J.; Evans, I.S.; Jenčo, M. A comprehensive system of definitions of land surface (topographic) curvatures, with implications for their application in geoscience modelling and prediction. *Earth-Sci. Rev.* **2020**, *211*, 103414. [CrossRef]
6. Hesse, R. LiDAR-derived Local Relief Models—A new tool for archaeological prospection. *Archaeol. Prospect.* **2010**, *17*, 67–72. [CrossRef]
7. Reitberger, J.; Krzystek, P.; Stilla, U. Analysis of full waveform LIDAR data for the classification of deciduous and coniferous trees. *Int. J. Remote Sens.* **2008**, *29*, 1407–1431. [CrossRef]
8. Zakšek, K.; Oštir, K.; Kokalj, Ž. Sky-View Factor as a Relief Visualization Technique. *Remote Sens.* **2011**, *3*, 398–415. [CrossRef]
9. Yokoyama, R.; Shirasawa, M.; Pike, R.J. Visualizing Topography by Openness: A New Application of Image Processing to Digital Elevation Models. *Photogramm. Eng. Remote Sens.* **2002**, *68*, 257–265.
10. Doneus, M. Openness as Visualization Technique for Interpretative Mapping of Airborne Lidar Derived Digital Terrain Models. *Remote Sens.* **2013**, *5*, 6427–6442. [CrossRef]
11. Horn, B.K.P. Hill shading and the reflectance map. *Proc. IEEE* **1981**, *69*, 14–47. [CrossRef]
12. Hobbs, K.F. An investigation of RGB multi-band shading for relief visualisation. *Int. J. Appl. Earth Obs. Geoinf.* **1999**, *1*, 181–186. [CrossRef]
13. Devereux, B.J.; Amable, G.S.; Crow, P. Visualisation of LiDAR terrain models for archaeological feature detection. *Antiquity* **2008**, *82*, 470–479. [CrossRef]
14. Kennelly, P.J.; Stewart, A.J. General sky models for illuminating terrains. *Int. J. Geogr. Inf. Sci.* **2014**, *28*, 383–406. [CrossRef]
15. Jasiewicz, J.; Stepinski, T.F. Geomorphons—A pattern recognition approach to classification and mapping of landforms. *Geomorphology* **2013**, *182*, 147–156. [CrossRef]
16. Hu, G.; Dai, W.; Li, S.; Xiong, L.; Tang, G.; Strobl, J. Quantification of terrain plan concavity and convexity using aspect vectors from digital elevation models. *Geomorphology* **2021**, *375*, 107553. [CrossRef]
17. Kennelly, P.J. Terrain maps displaying hill-shading with curvature. *Geomorphology* **2008**, *102*, 567–577. [CrossRef]
18. Weiss, A.D. *Topographic Position and Landforms Analysis*; The Nature Conservancy: San Diego, CA, USA, 2001.
19. Grosse-Brauckmann, K. Triply periodic minimal and constant mean curvature surfaces. *Interface Focus* **2012**, *2*, 582–588. [CrossRef] [PubMed]
20. Langer, M.S.; Zucker, S.W. Shape-from-shading on a cloudy day. *J. Opt. Soc. Am. A* **1994**, *11*, 467. [CrossRef]
21. Phong, B.T. Illumination for computer generated pictures. *Commun. ACM* **1975**, *18*, 311–317. [CrossRef]
22. Mittring, M. *Finding Next Gen: CryEngine 2. ACM SIGGRAPH 2007 Courses—SIGGRAPH 07 [Internet]*; ACM Press: San Diego, CA, USA, 2007; [cited 29 March 2021]; p. 97. Available online: http://dl.acm.org/citation.cfm?doid=1281500.1281671 (accessed on October 2020).
23. Loos, B.J.; Sloan, P.-P. *Volumetric Obscurance. Proc ACM SIGGRAPH Symp Interact 3D Graph Games—I3D 10 [Internet]*; ACM Press: Washington, DC, USA, 2010; [cited 29 March 2021]; p. 151. Available online: http://dl.acm.org/citation.cfm?doid=1730804.1730829 (accessed on October 2020).
24. McGuire, M.; Osman, B.; Bukowski, M.; Hennessy, P. *The Alchemy Screen-Space Ambient Obscurance Algorithm. Proc ACM SIGGRAPH Symp High Perform Graph—HPG 11 [Internet]*; ACM Press: Vancouver, BC, Canada, 2011; [cited 29 March 2021]; p. 25. Available online: http://dl.acm.org/citation.cfm?doid=2018323.2018327 (accessed on October 2020).

25. Holden, D.; Saito, J.; Komura, T. *Neural Network Ambient Occlusion. SIGGRAPH ASIA 2016 Tech Briefs [Internet]*; ACM: Macau, 2016; [cited 29 March 2021]; pp. 1–4. Available online: https://dl.acm.org/doi/10.1145/3005358.3005387 (accessed on October 2020).
26. Bokšanský, J.; Pospíšil, A.; Bittner, J. VAO++: Practical Volumetric Ambient Occlusion for Games. In *Eurographics Symposium on Rendering: Experimental Ideas & Implementations*; The Eurographics Association: Dublin, Ireland, 2017; pp. 31–39.
27. Hay, R.L. *Geology of the Olduvai Gorge: A Study of Sedimentation in a Semiarid Basin*; University of California Press: Berkeley, CA, USA, 1976.
28. Hay, R.L.; Kyser, T.K. Chemical sedimentology and paleoenvironmental history of Lake Olduvai, a Pliocene lake in northern Tanzania. *GSA Bull.* **2001**, *113*, 1505–1521. [CrossRef]
29. Dawson, J.B. *The Gregory Rift Valley and Neogene-Recent-Volcanoes of Northern Tanzania*; Geological Society of London: London, UK, 2008.
30. Pyatkin, B.N.; Martinov, A.I. *Shalabolinskie Petroglify*; Izd-vo Krasnoyarskogo Universiteta: Krasnoyarsk, Russia, 1985.
31. Pyatkin, B.N. The Shalabolino petroglyphs on the river Tuba (middle Yenisei). *Int. Newsl. Rock Art* **1998**, *20*, 26–30.
32. Delvet, E. *Recent Rock Art Studies in Northern Eurasia, 2005–2009*; Oxbow: Oxford, UK; David Brown Book Company [Distributor]: Oakville, CT, USA, 2012; pp. 124–148.
33. Zotkina, L.V. On the Methodology of Studying Palimpsests in Rock Art: The Case of the Shalabolino Rock Art Site, Krasnoyarsk Territory. *Archaeol. Ethnol. Anthropol. Eurasia* **2019**, *47*, 93–102. [CrossRef]
34. Zotkina, L.V.; Kovalev, V.S. Lithic or metal tools: Techno-traceological and 3D analysis of rock art. *Digit. Appl. Archaeol. Cult. Herit.* **2019**, *13*, e00099. [CrossRef]
35. Kokalj, Ž.; Somrak, M. Why Not a Single Image? Combining Visualizations to Facilitate Fieldwork and On-Screen Mapping. *Remote Sens.* **2019**, *11*, 747. [CrossRef]
36. Gallwey, J.; Eyre, M.; Tonkins, M.; Coggan, J. Bringing Lunar LiDAR Back Down to Earth: Mapping Our Industrial Heritage through Deep Transfer Learning. *Remote Sens.* **2019**, *11*, 1994. [CrossRef]
37. Liu, Q.; Cheng, W.; Yan, G.; Zhao, Y.; Liu, J. A Machine Learning Approach to Crater Classification from Topographic Data. *Remote Sens.* **2019**, *11*, 2594. [CrossRef]
38. Monna, F.; Magail, J.; Rolland, T.; Navarro, N.; Wilczek, J.; Gantulga, J.-O.; Esin, Y.; Granjon, L.; Allard, A.-C.; Chateau-Smith, C. Machine learning for rapid mapping of archaeological structures made of dry stones—Example of burial monuments from the Khirgisuur culture, Mongolia–. *J. Cult. Herit.* **2020**, *43*, 118–128. [CrossRef]
39. Soroush, M.; Mehrtash, A.; Khazraee, E.; Ur, J.A. Deep Learning in Archaeological Remote Sensing: Automated Qanat Detection in the Kurdistan Region of Iraq. *Remote Sens.* **2020**, *12*, 500. [CrossRef]
40. Zakariya Jasim, O. Using of machines learning in extraction of urban roads from DEM of LIDAR data: Case study at Baghdad expressways, Iraq. *Period. Eng. Nat. Sci. PEN* **2019**, *7*, 1710. [CrossRef]
41. Maxwell, A.E.; Pourmohammadi, P.; Poyner, J.D. Mapping the Topographic Features of Mining-Related Valley Fills Using Mask R-CNN Deep Learning and Digital Elevation Data. *Remote Sens.* **2020**, *12*, 547. [CrossRef]
42. Zhao, Z.-Q.; Zheng, P.; Xu, S.; Wu, X. Object Detection with Deep Learning: A Review. *arXiv* **2019**, arXiv:180705511. Available online: http://arxiv.org/abs/1807.05511 (accessed on October 2020).

Chapitre 3. Documentation assistée par intelligence artificielle

3.1. Dessin pierre à pierre

Les principales difficultés pour l'étude des khirigsuurs sont leur nombre ainsi que l'immensité de l'aire de répartition. Certains complexes peuvent s'étendre sur plusieurs km², rendant l'organisation de l'espace extrêmement difficile à appréhender depuis le sol. La création des plans de ces complexes est souvent longue. Parfois plusieurs campagnes sont nécessaires (Monna et al. 2020, Frohlich et al., 2008, surtout si le plan du khirigsuur est recherché au plus grand détail (i.e. pierre à pierre). La photographie aérienne permet de prendre du recul par rapport au site et de mieux comprendre l'agencement des éléments du monument, les uns par rapport aux autres. Jusqu'à très récemment, les méthodes pour réaliser ce type de photos étaient assez limitées : ballons ou cerfs-volants. Aujourd'hui, avec la démocratisation des drones, la photographie aéroportée est facilitée. Elle rend possible la capture de photos aériennes d'un site, mais surtout, grâce à la photogrammétrie, la création d'orthomosaïques et de MNE. Cette technologie permet de couvrir de grandes zones en peu de temps. Le drone donne donc un nouvel élan dans l'étude de l'organisation des khirigsuurs en apportant rapidement, et à bas coût, une quantité importante de données. Intervient alors un autre facteur limitant : le temps de traitement nécessaire pour que les images produites soient exploitables dans une optique de recherche. Dessiner une à une les pierres constituant le khirigsuur à partir des orthomosaïques est peu réaliste. L'idée serait donc de trouver une solution pour extraire le plan des khirigsuurs à partir des orthomosaïques, ou du moins les pierres qui composent les monuments. Il est donc question ici de classer les pixels des images en fonction

de leur attribut : pierre ou non pierre. La solution envisagée est celle de l'apprentissage automatique supervisé. Elle consiste à entrainer un algorithme qui va « apprendre » à reconnaitre des schémas (pierre/non pierre) à partir d'un jeu de données (valeurs des pixels). L'apprentissage se fait à partir de données préparées par l'utilisateur contenant des individus (ici des pixels) déjà classés. Une fois l'entrainement achevé, l'algorithme est capable de classer les individus non rencontrés jusqu'alors.

Journal of Cultural Heritage 43 (2020) 118–128

Available online at
ScienceDirect
www.sciencedirect.com

Elsevier Masson France
EM|consulte
www.em-consulte.com/en

Original article

Machine learning for rapid mapping of archaeological structures made of dry stones – Example of burial monuments from the *Khirgisuur* culture, Mongolia –

Fabrice Monna[a,*], Jérôme Magail[b], Tanguy Rolland[a], Nicolas Navarro[c,d], Josef Wilczek[a,e,1], Jamiyan-Ombo Gantulga[f], Yury Esin[g], Ludovic Granjon[h], Anne-Caroline Allard[i], Carmela Chateau-Smith[j]

[a] *ARTEHIS, UMR CNRS 6298, Université de Bourgogne–Franche Comté, 6 Boulevard Gabriel, Bat. Gabriel, 21000 Dijon, France*
[b] *Musée d'anthropologie préhistorique de Monaco, 56, boulevard du Jardin exotique, 98000 MC, Monaco*
[c] *EPHE, PSL Research University, 21000 Dijon, France*
[d] *Biogéosciences UMR CNRS 6282, Université Bourgogne Franche-Comté, 6, boulevard Gabriel, Bat. Gabriel, 21000 Dijon, France*
[e] *Ústav archeologie a muzeologie, Masarykova univerzita, Arna Nováka 1, 602 00 Brno, Czech Republic*
[f] *Bronze and Early Iron Age Department, Institute of History and Archaeology, Mongolian Academy of Sciences, Jucov street-77, Ulaanbaatar-51, Mongolia*
[g] *Khakassian Research Institute for Language, Literature, and History, 23, Shchetinkin Street, 655017 Abakan, Republic of Khakassia, Russia*
[h] *MSH de Dijon, USR CNRS 3516, Université Bourgogne Franche-Comté, 6, esplanade Erasme, 21066 Dijon, France*
[i] *Institut d'Art et d'Archéologie, Université Paris IV Sorbonne, 3, rue Michelet, 75006 Paris, France*
[j] *CPTC, Université de Bourgogne, 4, boulevard Gabriel, 21000 Dijon, France*

ARTICLE INFO

Article history:
Received 28 June 2019
Accepted 7 January 2020
Available online 22 January 2020

Keywords:
Pixel classification
Grey level co-occurrence matrix
RGB colour space
Texture
Topographic position index
Photogrammetry
Burial complex planigraphy
Mongolia
Bronze age
Iron age

ABSTRACT

The present study proposes a workflow to extract from orthomosaics the enormous amount of dry stones used by past societies to construct funeral complexes in the Mongolian steppes. Several different machine learning algorithms for binary pixel classification (i.e. stone *vs* non-stone) were evaluated. Input features were extracted from high-resolution orthomosaics and digital elevation models (both derived from aerial imaging). Comparative analysis used two colour spaces (RGB and HSV), texture features (contrast, homogeneity and entropy raster maps), and the topographic position index, combined with nine supervised learning algorithms (nearest centroid, naive Bayes, *k*-nearest neighbours, logistic regression, linear and quadratic discriminant analyses, support vector machine, random forest, and artificial neural network). When features are processed together, excellent output maps, very close to or outperforming current standards in archaeology, are observed for almost all classifiers. The size of the training set can be drastically reduced (to ca. 300 samples) by majority voting, while maintaining performance at the highest level (about 99.5% for all performance scores). Note, however, that if the training set is inadequate or not fully representative, the classification results are poor. That said, the methods applied and tested here are extremely rapid. Extensive mapping, which would have been difficult with traditional, manual, or semi-automatic delineation of stones using a vector graphics editor, now becomes possible. This workflow generally surpasses pedestrian surveys using differential GPS or a total station.

Introduction

Soon after the start of aerial photography, which became fully operational during WW1, archaeologists realized the potential of this technique for discovering new sites, apprehending large complexes in a new way, and understanding the spatial organisation of archaeological structures [1]. For a long time, greyscale pictures were captured in low sunlight to reveal elevation anomalies as shadow marks [2]. Later, the introduction of colour photography became an important asset to identify subtle colour variations, which may occur in field crops, either because soils above buried walls generally retain less moisture, or because water may accumulate close to the structures [3]. Nowadays, the range of acquisition techniques in aerial archaeological investigation is huge, from satellites to small unmanned aerial vehicles (UAVs), and images are

* Corresponding author.
E-mail address: Fabrice.Monna@u-bourgogne.fr (F. Monna).
[1] Present address: Katedra archeologie, Univerzita Hradec Králové, Rokitanského 62, Czech Republic.

https://doi.org/10.1016/j.culher.2020.01.002
1296-2074/

produced in both in visible and invisible spectra (e.g. [4]). However, because of their low cost and versatility, UAVs are often privileged by archaeologists over other solutions. High-definition surveys over several km^2 are possible with UAVs, by dividing the area of interest into several smaller tiles (depending on UAV flight capacity). In contrast with pioneering works, photographs are now often acquired not only to provide aerial images, but also high-definition, georeferenced orthomosaics, and digital elevation models, also known as DEMs [5]. Landscape representations are then reconstructed with the help of photogrammetry, a technique that is about to become the new standard in archaeology for field documentation [6,7]. Scientists dealing with such a massive information flow may, however, encounter serious difficulties in producing documentation suitable for further exploitation in a reasonable amount of time [8], particularly when stones or archaeological structures are delineated manually with a vector graphics editor. The burial structures in the Arkhangai province (Mongolia) are a perfect example of this type of bottleneck. This region is extremely rich in funeral monuments dating from the Bronze Age and the Iron Age. Funeral complexes from the Iron Age are composed of decametric dry-stone arrangements [9,10], sometimes encompassing several km^2. Even for a skilled expert, it is extremely difficult to identify any clear organisation of the monument from the ground, mainly due to the vast area covered. By contrast, orthomosaics provide extremely valuable information [11]. Almost every individual stone can be distinguished in the open steppes, especially when the grass is low due to livestock grazing. In this specific example, as in many other situations of this kind, a rapid and accurate procedure to extract, at least semi-automatically, stone boundaries from the data acquired by UAV would be a valuable improvement in the acquisition speed of archaeological documentation. The problem, in a nutshell, consists of a binary pixel classification (stone *vs* non-stone), and solutions can be sought in the numerous machine learning algorithms increasingly used in archaeology [12–15]. Colour information is an obvious candidate for input data, as stones are clearly visible in the images. Other variables, such as those related to the spatial arrangement of the tonal information (also known as textural features) may also be highly relevant, as demonstrated in various fields, such as remote sensing, ecology, etc. [16,17]. Local altitudinal variations may also be useful as input data for classification [18].

Research aim

To treat the set of input features mentioned above, supervised learning should be privileged in the present case, because the operator determines the number of output classes (here two) in a very specific way, in conformity with the objectives, unlike unsupervised learning [19]. Although this approach inevitably introduces a manual and relatively time-consuming training step, outcomes should be much closer to documentation directly exploitable from an archaeological point of view. Here, our objective is to compare several solutions for binary pixel classification, by combining different input features: colour, textural parameters, and topography, with nine supervised machine learning algorithms: nearest centroid, naive Bayes, *k*-nearest neighbours, logistic regression, linear and quadratic discriminant analyses, support vector machine, random forest, and artificial neural network. For the first example, the famous 9-ha site of Jargalant, descriptive features were progressively introduced into the algorithms, and classification performance was investigated statistically and then empirically, by assessing the archaeological potential of the maps obtained. Once the best approach had been selected, it was applied to the larger area of Tsatsiin Ereg, and the results were evaluated.

Material and methods

The sites

The photogrammetric campaign took place during three summer periods (2016–2018), within the framework of the "Joint Monaco-Mongolian Archaeological Mission". It focused mainly on the site of Tsatsiin Ereg, in the Khoid Tamir valley, located about 500 km southwest of Ulaanbaatar, but also on other smaller sites, either in the vicinity of Tsatsiin Ereg, or in Jargalant, a site famous for its deer stones, about 80 km away [20]. The site of Tsatsiin Ereg is characterized by a remarkable concentration of large, well-preserved complexes, including barrows, satellite quadrangles, circles, enclosures, and stone alignments formed by the accumulation of dry stones. The most sophisticated complexes, which can extend over several square kilometres, date from the late 2nd to early 1st millennium BC [21–23]. The plethora of structures composing these funeral complexes makes it difficult to understand the precise chronology of the building phases. However, the repetition of certain elements, related to funeral practices, sacrificial rituals, and artistic style, indicates cultural coherence shared over a large area by past nomadic societies, which should be studied to better apprehend cultural interactions.

Orthomosaic and DEM production

Pictures were captured by an unmanned aerial vehicle (UAV), a DJI Phantom 3 PRO equipped with a GPS and a 12 Mpix camera. The lens was a 20 mm (equivalent 35 mm) f/2.8, producing a diagonal field of view of 94°. The flight plan was programmed *via* a free Android application (Altizure App, https://www.altizure.com/), where target area positioning is facilitated by displaying a satellite image as background. The operator sets the height flight above ground, the size and orientation of the region of interest, as well as the capture density, by choosing the amount of forward and side overlap (typically 75–80%). The UAV can then automatically follow a zigzag pattern, taking a series of photographs in the nadir direction. As sensor definition and focal of the lens are fixed, the distance between the centres of two consecutive pixels at ground level, also known as the ground sample distance (GSD), depends only on the height of flight [24]. At this point, it is worth recalling that GSD should be at least half the size of the smallest details to be captured optically. If the smallest stones of interest measure approximately 20 cm, they should be recognisable at a flight height of 100−150 m (GSD of 4.3–6.5 cm/px, theoretically). In practice, the areas studied were divided into smaller square regions of interest of approximately 9−10 ha, which can be covered by UAV without battery replacement at a flight height of 100−150 m, a value typically used. Ground control points were placed before acquisition, and the distances between them were measured with a laser telemeter Leica Disto D510, able to work in sunlight up to 200 m, with a precision of ca 1 mm. Typically 80–110 pictures were captured per tile, taking 15−20 min in the field. In the laboratory, orthomosaics and DEMs were produced by the Photoscan PRO software, v. 1.4.3 from Agisoft. Picture alignment and subsequent sparse cloud construction were strongly constrained by the distances between GCPs. This step, which helps to structure the 3D model, was useful here, as wind causing movement of long grass (which dominates the landscape studied) may lead to the accumulation of slight alignment errors between pictures. The workflow then consisted in densifying the cloud, producing height field models, DEMs, and orthomosaics, at a fixed resolution of 5 cm/pixel for Tsatsiin Ereg and 8 cm/pixel for Jargalant (see Refs. [22,25] for more details about the photogrammetrical workflow). It is worth mentioning that the use of GCPs precisely georeferenced with differential GPS, for example, would have been optimal for accurate positioning of the maps produced.

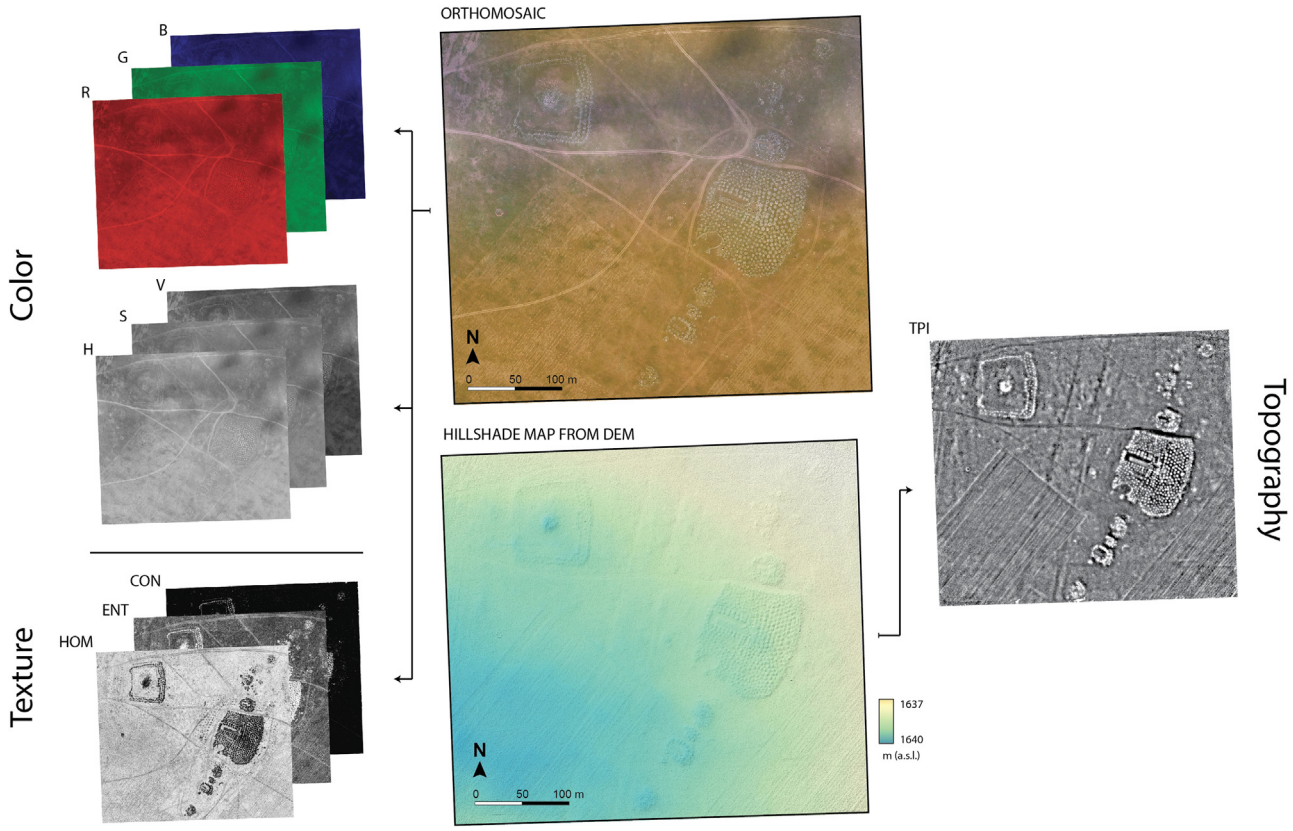

Fig. 1. Scheme of feature engineering. Colour as RGB and HSV colour space; texture features as HOM (homogeneity), ENT (entropy), and CON (contrast). TPI for topographic position index, deduced from DEM, displayed as colour hill-shaded map.

Although georeferencing here only derives from the GPS embarked into the drone because of logistic constraints, the relative error of the models produced does not exceed 10–20 cm, while absolute error, assessed by projecting orthomosaics on Google Earth (considered as true reference), does not exceed 1–3 m.

Feature inputs

In order to evaluate which input feature (or combination of features) is the most pertinent for binary classification (i.e. stone *vs* non-stone), several image representations were obtained from original orthomosaics and DEMs.

RGB colour space

In its most common version: 24-bit encoding, the image is composed of one channel for each of the three primary colours processed by cameras and computers: red, green, and blue. Each is encoded on 8 bits, producing 256 possible discrete values per channel, and a palette of 16 777 216 discrete combinations. This colour space uses additive colour mixing to compose the final image. In the following, images are split into 3 channels (namely R, G, and B), and each colour channel is treated separately as a single feature (Fig. 1).

HSV colour space

Colour transformations into non-RGB colour space have sometimes been shown to enhance classification performance [26]. Similarly to the RGB colour model, the HSV colour space is composed of three channels (for hue, saturation, and value), denoting colour property, perceived colour intensity, and perception of brightness (Fig. 1) [27]. The HSV channels are obtained from those composing the RGB.

Grey level Co-occurrence matrix (GLCM) and texture parameters

Developed by Haralick et al. [28], GLCM texture parameters belong to the family of statistics describing the arrangement of pixels separated by a certain distance, in different directions. Originally 14 parameters were proposed as image texture features, but only three of them are used in the following: contrast (CON), homogeneity (HOM), and entropy (ENT), because they have been recognized to enhance classification accuracy [29,30]. Their calculation is a two-step process: the computation of the grey level co-occurrence matrix from an image with g grey levels (obtained from the RGB image), and the calculation of the descriptors from this matrix (see Ref. [31] for details). The contrast descriptor, calculated for each pixel, illustrates the local variation of pixel intensity within a certain spatial range, while homogeneity and entropy describe the local sameness of grey levels of pixels, in other words the tonal variations in space. Three parameters must therefore be tuned: spatial scale (i.e. window size), the number of grey levels in the image to be processed, and the directions for which GLCM is computed (Note that calculations covered all directions using 32 grey levels and a window size of 9×9 pixels, i.e. representing typically 0.2–0.5 m^2. See Fig. 1 for map examples).

Topographic position index (TPI)

This index, widely used for automatic landform classification [32], is simply defined as the difference in altitude between a central pixel and the mean of the surrounding cells in the DEM [33]. The TPI depends only on topography and the size of the search window defining neighbours. In the present case, this size should be larger than the elements of interest, to highlight them as positive or negative anomalies (In the following, a square window of 201×201 pixels, covering about 100–250 m^2, was found appropri-

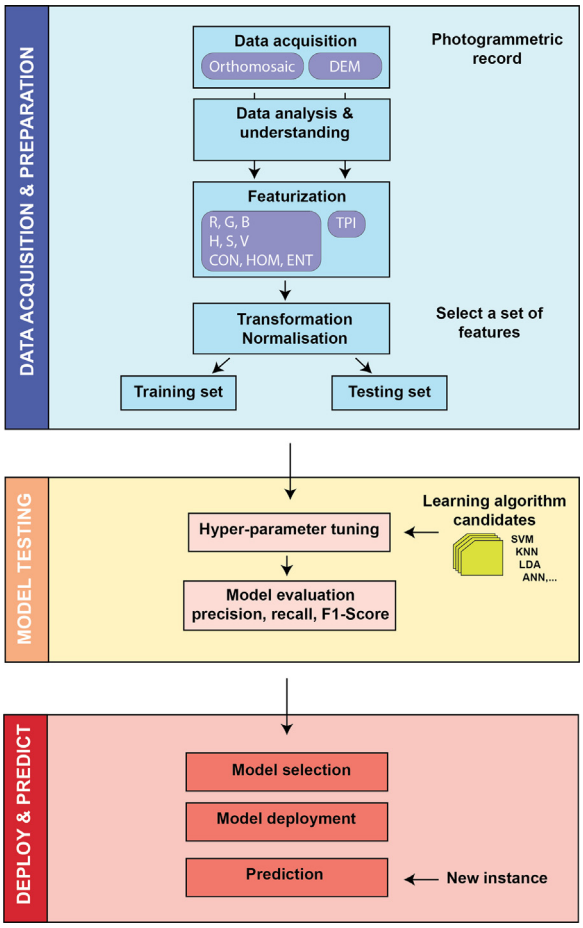

Fig. 2. The machine-learning pipeline for binary pixel classification.

ate. See Fig. 1, where the DEM is coloured and hill-shaded for better understanding).

Machine learning algorithms

Underlying idea

Here, the aim is to predict, for each pixel, the presence or absence of stone, from a set of features selected among those enumerated above (i.e. colour channels, texture maps, and TPI). Let Y be the class ensemble composed, in our case, of two categories: y_c, (with $c \in [0,1]$), and $\mathbf{x}$ a vector describing the set of n features, $\mathbf{x} = \{x_1,\ldots,x_n\}$. In supervised learning, the operator first teaches the mathematical model, labelling by hand a set of pixels with and without stones. From that training set or a subset of it, patterns are sought in $\mathbf{x}$ to predict class labels, Y. The classifier tries to find a mapping function (i.e. a decision rule), $f(\mathbf{x}) \rightarrow Y$, which is then used to map new, unseen data. Nine popular classifiers listed below were tested in this study. As they are extensively explained in many textbooks [34–36], they are only briefly described, to facilitate clearer understanding for readers unfamiliar with machine learning, and a simplified pipeline is provided in Fig. 2.

Naive Bayes (NB)

This classifier is one of the simplest algorithms used for binary classification. As indicated by its name, it is based on the Bayes' theorem, and is naïve as it assumes that every pair of features is independent, a situation rarely met in real-world data. Continuous variables are assumed to follow Gaussian distributions within each class, allowing the calculation of conditional probabilities, $p(x_i|y_c)$, from the training set [37]. Combined with the independence assumption, a class label, $\hat{y}_{NB}$, corresponding to the most probable class (that with maximum *a posteriori* probability) is assigned following:

$$\hat{y}_{NB} = \underset{c}{\operatorname{argmax}}\ p(y_c)\prod_{i=1}^{n} p(x_i|y_c)$$

Nearest centroid (NC)

It simply compares the position of a sample in the feature space to the centroid of each class determined from the training set, and labels it with the class where the mean, μ_c, is the closest (see Supplementary Material S1a for an illustration):

$$\hat{y}_{NC} = \underset{c}{\operatorname{argmin}}\ \left|\boldsymbol{\mu}_c - \boldsymbol{x}\right|$$

*k-nearest neighbours (*KNN*).* For the classification task, the *KNN* algorithm identifies the k nearest neighbours in the feature space of the training samples, $T = \left\{S_1^{NN},\ldots,S_k^{NN}\right\}$, and proceeds by majority voting to assign a class label, $\hat{y}_{KNN}$ (Supplementary Material S1b):

$$\hat{y}_{KNN} = \underset{c}{\operatorname{argmax}} \sum_{S_i \in T} I(y_c = y_i^{NN})$$

with y_i^{NN} the class label of the i-th neighbour among the k nearest neighbours, and $I(y_c = y_i^{NN})$ equal to 1 if the classes of S_1^{NN} and y_c are the same, and 0 otherwise. Despite its simplicity, this algorithm often provides competitive results, but the value of k (usually odd) needs to be set by the operator, or optimized [38]. The operator may also choose the metric used for distance, e.g. Euclidian, Manhattan, and possibly a weight, inversely proportional to the distance of each of the k neighbours, which may be useful when classes are clearly unbalanced.

Logistic regression (LR)

A new variable, z, is first built as input from a linear combination of weights and sample features: $z = \mathbf{w}^T\mathbf{x}$. Then, the logistic function, also known as a sigmoid cumulative logistic distribution, quashes the range of possible outputs within the [0,1] range that can be interpreted in terms of probabilities (Supplementary Material S1c). From these results, a class label is assigned as follows [35]:

$$\hat{y}_{LR} = \underset{c}{\operatorname{argmax}}\ p(y_c|\boldsymbol{x},\boldsymbol{w})$$

Several different strategies exist to optimize the weights, $\mathbf{w}$, and to perform a regularization step, to handle collinearity among features, as well as to prevent overfitting. Logistic regression performs well for classes that are linearly separable (details can be found in Ref. [39]).

Linear and quadratic discriminant analyses (LDA & QDA)

These models assume a Gaussian density for each class. Bayes' rule is applied to calculate conditional probabilities, $p(y_c|\boldsymbol{x})$, and hence to predict classes, by choosing c, which maximizes $p(y_c|\boldsymbol{x})$. For LDA, all classes are supposed to have the same covariance matrix, and decision boundaries are linear (Supplementary Material S1d), but not for QDA (Supplementary Material S1e), which makes decision boundaries more flexible [40].

Support-vector machine (SVM)

This very popular algorithm for classification seeks to maximize the margin between the decision boundary hyperplane and the closest training samples from this hyperplane, which are called support vectors [41]. The idea behind this procedure is to produce a clear gap between samples belonging to both categories (Supplementary Material S1f). Interestingly, SVM can also be used for data

not linearly separable, after the application of a mapping function, which transforms the input data, in a higher dimensional space where classes become linearly separable. This step takes advantage of the so-called "kernel trick" for computation, by applying, most often, a radial basis function (RBF), which is in fact a Gaussian kernel [42].

Random forest (RF)

It belongs to the class of ensemble methods, capable of both classification and regression, in the case of linear and non-linear problems. The algorithm proceeds by aggregating a bunch of classification trees built randomly: instead of constructing splits on the basis of feature importance, the best feature is sought among a random subset of input variables (Supplementary Material S2a). The idea behind the algorithm is that predictions made by individual decision trees may not be correct but, once they have been combined, label predictions will be more accurate and stable [43]. Several parameters must be tuned for forest construction (e.g. number of trees, number of levels in each decision tree, etc.), and concerning the method used for sampling data points.

Artificial neural network (ANN)

This algorithm is vaguely inspired by the human brain [44]. Several hidden layers composed of several nodes are placed between input (i.e. features) and output (class labels) layers. Each node receives input values from the previous layer. Values are pondered by weights and biased, and then passed through an activation function, used to determine whether and to what extent the signal moves to the next layer (Supplementary Material S2b). Weight and bias values are optimized by iterating the following steps: (i) predicted output calculation (feedforward step), and (ii) update of weight and bias (backpropagation step) [36]. The operator must set the number of hidden layers and units, the learning rate, the type of activation function, etc.

Hard voting

Hard voting consists in aggregating predictions made by each individual classifier, or a subset of them, and then predicting the class by simple majority voting (Supplementary Material S2c). The underlying idea is that several models are probably more reliable than just one.

Hyperparameter tuning and metrics for model evaluation

Basically, a good practice to evaluate the capacity of the models produced to generalize to unseen data is to split the supervised data into two groups, one for training (here 70% of the dataset), with the remainder (30%) as a test dataset [36]. However, depending on learning strategies, as mentioned above, several model hyperparameters (some of them tackling overfitting *via* regularization) have to be fine-tuned. This optimization step is operated by a brute force search on a grid of possible hyperparameter values, using inner cross-validation on the training set. For final model evaluation, two strategies are possible. The first simply applies the model to the test dataset. This method provides a single evaluation value, which is unbiased, as these data were not used to build the models [44]. Note, however, that results may depend on how the data were split into training and test sets. The second strategy computes an outer cross-validation by splitting the data into k folds, applying the model to k-1 folds, keeping the remainder for performance evaluation, and repeating the operation k times [45]. Results are almost unbiased [46] and, interestingly, may be expressed in terms of confidence intervals. Both strategies were used here.

Several metrics are available to evaluate the models, including precision, recall, F1-score, and accuracy [36]. Let TP, TN, FP, and FN be the True Positive, True Negative, False Positive and False Negative, respectively (with positive being a stone).

$$\text{Precision} = \frac{TP}{TP + FP}$$

$$\text{Recall} = \frac{TP}{TP + FN}$$

F1-Score deals with both precision and recall. It is the harmonic of both scores:

$$F1 - \text{Score} = 2.\frac{\text{Precision} \,.\, \text{Recall}}{\text{Precision} + \text{Recall}}$$

Accuracy is defined as the percentage of correct predictions:

$$\text{Accuracy} = \frac{TP + TN}{TP + FP + TN + FN}$$

Most archaeologists prefer to save all the stones if possible, even if they need to perform a minor *a posteriori* cleaning of false positives. As a consequence, hyperparameters were tuned to maximize recall.

Practical implementation

Computation of GLCM and TPI used the glcm package and a homemade script, both written for the free R software (https://www.r-project.org/). Colour manipulation, application of machine learning algorithms to standardized data, and georeferencing of the maps produced used the scikit-learn 0.20.3, opencv 4.1.1, rasterio 1.0.22, gdal 2.4.2, and scipy 1.2.1 libraries for Python 3.7.1 (https://www.python.org/). Final results, expressed as georeferenced polygon vector layers, were integrated using the free QGIS software (https://www.qgis.org). Point pickup to produce the training dataset used ImageJ (https://imagej.nih.gov/ij/), or a homemade snippet based on OpenCV.

Results and discussion

Feature engineering and choice of machine learning algorithm

Tests to select the best combination of features and algorithm were conducted, for the Jargalant site, on images extending over 5043 × 4546 pixels. Six feature combinations: (i) R + G + B, (ii) H + S + V, (iii) H + S, (iv) CON + HOM + ENT, (v) R + G + B + CON + HOM + ENT, and (vi) R + G + B + CON + HOM + ENT + TPI were evaluated with each of the 9 algorithms listed above. Such a progressive scheme of feature selection aims at identifying the most relevant features in the classification process, thus building a better classifier without computational overload. Results, expressed as precision, recall, F1-Score, and accuracy using an inner cross-validation on the training set are summarized for each combination in Table 1 (see also Supplementary Material SM3 for scores from test set). Pixels were manually picked out on the orthomosaic to train the model with 363 positive and 1010 negative cases. Such a dataset may appear oversized and time-consuming for a procedure requiring manual operation. This is especially true when repeated several times for large sites, covering several square kilometres. However, the objective here was to evaluate the influence of the size of the training set, in terms of performance, which therefore required a vast number of samples.

RGB as input features

Results appear to be good, most of the time >93%, up to 98.5%, whatever the algorithm applied to the RGB information alone (Table 1). These good scores are all the more remarkable in that they include some rather basic procedures, such as naive Bayes,

Table 1
Scores and standard deviation (obtained using an inner cross-validation on the training set) of combinations between features and machine learning algorithms for the site of Jargalant. Note that for such high values, close to 100%, the standard deviation calculation is no longer correct. It is nonetheless provided for comparison purposes. NB for Naive Bayes, NC for nearest centroid, KNN for *k*-nearest neighbours, LR for logistic regression, LDA and QDA for linear and quadratic discriminant analyses, SVM for support vector machine, RF for random forest, ANN for artificial neural network. Texture features encompass contrast, homogeneity, and entropy. In bold, the results corresponding to the four feature combinations: RGB, texture (CON + HOM + ENT), RGB + texture, RGB + texture + TPI, presented in Fig. 3.

		RGB			HSV			Texture			Texture + RGB			Texture + RGB + TPI		
NB	precision	90.3	±	2.0	88.1	±	4.1	94.8	±	2.0	94.8	±	2.0	94.6	±	3.5
	recall	96.7	±	1.1	91.7	±	3.4	98.9	±	1.0	99.2	±	0.7	99.5	±	0.7
	F1-Score	93.4	±	1.2	89.8	±	2.4	96.8	±	0.8	96.9	±	0.9	96.9	±	2.0
	accuracy	96.4	±	0.7	94.5	±	1.4	98.3	±	0.5	98.3	±	0.5	98.3	±	1.1
NC	precision	87.6	±	2.5	84.9	±	3.9	96.0	±	1.1	96.6	±	1.3	98.1	±	2.3
	recall	91.1	±	1.2	98.1	±	1.4	97.8	±	0.7	99.4	±	0.7	99.4	±	1.1
	F1-Score	92.8	±	1.8	91.0	±	2.6	96.9	±	0.7	98.0	±	0.6	98.8	±	1.5
	accuracy	95.9	±	1.0	94.8	±	1.6	98.3	±	0.4	98.9	±	0.3	99.3	±	0.8
KNN	precision	98.0	±	1.5	96.4	±	2.1	99.4	±	1.1	99.7	±	0.5	99.2	±	1.1
	recall	93.4	±	3.6	94.2	±	2.8	97.0	±	1.6	98.6	±	1.5	99.2	±	1.1
	F1-Score	95.6	±	1.9	95.3	±	2.3	98.2	±	1.0	99.2	±	0.7	99.2	±	0.8
	accuracy	97.7	±	1.0	97.5	±	1.2	99.1	±	0.5	99.6	±	0.4	99.6	±	0.4
LR	precision	97.2	±	1.4	91.9	±	2.7	**99.4**	±	**1.1**	**99.7**	±	**0.6**	99.4	±	1.1
	recall	96.4	±	1.9	93.1	±	2.6	**98.3**	±	**1.0**	**98.9**	±	**0.6**	99.2	±	1.1
	F1-Score	96.4	±	1.3	92.5	±	2.4	**98.9**	±	**0.9**	**99.3**	±	**0.4**	99.3	±	1.1
	accuracy	98.3	±	0.7	96.0	±	1.3	**99.4**	±	**0.5**	**99.6**	±	**0.2**	99.6	±	0.6
LDA	precision	98.0	±	0.7	88.9	±	3.5	98.3	±	1.0	99.2	±	1.1	99.2	±	1.1
	recall	95.9	±	2.5	96.4	±	2.2	96.4	±	1.9	98.6	±	0.0	98.9	±	1.0
	F1-Score	96.9	±	1.5	92.5	±	2.7	97.4	±	1.2	98.9	±	0.6	99.0	±	0.8
	accuracy	98.0	±	0.8	95.9	±	1.6	98.6	±	0.6	99.4	±	0.3	99.5	±	0.4
QDA	precision	94.7	±	2.3	88.3	±	3.2	95.3	±	1.3	95.8	±	1.9	96.1	±	2.5
	recall	97.0	±	2.0	92.8	±	2.9	98.9	±	1.0	99.4	±	0.7	99.7	±	0.6
	F1-Score	95.8	±	1.8	90.5	±	2.6	97.0	±	0.7	97.6	±	0.9	97.9	±	1.4
	accuracy	97.7	±	1.0	94.8	±	1.4	98.4	±	0.4	98.7	±	0.5	98.8	±	0.8
SVM	precision	**98.6**	±	**1.5**	98.4	±	1.6	99.5	±	1.1	98.4	±	1.6	98.9	±	1.6
	recall	**96.1**	±	**2.0**	96.4	±	2.6	98.4	±	1.0	98.6	±	1.5	99.4	±	1.1
	F1-Score	**97.3**	±	**1.6**	97.3	±	1.4	98.9	±	0.3	98.5	±	0.7	99.2	±	1.3
	accuracy	**98.6**	±	**0.8**	98.6	±	0.7	99.4	±	0.2	99.2	±	0.4	99.6	±	0.7
RF	precision	95.8	±	1.6	96.4	±	2.6	99.4	±	1.1	99.5	±	0.7	99.7	±	0.6
	recall	94.2	±	3.5	94.2	±	2.9	97.8	±	0.7	99.2	±	1.1	99.5	±	0.7
	F1-Score	95.0	±	2.3	95.3	±	2.5	98.6	±	0.8	99.3	±	0.6	99.6	±	0.6
	accuracy	97.4	±	1.1	97.5	±	1.3	99.3	±	0.4	99.6	±	0.3	99.8	±	0.3
ANN	precision	97.0	±	1.6	96.2	±	2.3	99.4	±	0.7	98.9	±	1.0	98.1	±	1.8
	recall	96.1	±	2.0	95.3	±	1.9	97.5	±	1.6	98.9	±	0.6	98.9	±	1.0
	F1-Score	96.5	±	1.3	95.7	±	0.7	98.5	±	1.1	98.9	±	0.5	98.5	±	1.3
	accuracy	98.2	±	0.7	97.7	±	0.4	99.2	±	0.5	99.4	±	0.3	99.2	±	0.7
Voting hard	precision													**99.6**	±	**0.6**
	recall													**99.7**	±	**0.3**
	F1-Score													**99.6**	±	**0.5**
	accuracy													**99.7**	±	**0.4**

nearest centroid, and, to a lesser extent, linear discriminant analysis, which is among the four best results (Table 1). It is worth mentioning that the passage of clouds during aerial picture acquisition resulted in colour inhomogeneity, especially in the northern half of the orthomosaic (cf. Fig. 1). This could have affected the classification performance based on colour, but an appropriate training set circumvented this problem. The SVM procedure was finally selected, because it slightly outperformed the other procedures. Another reason for this choice is the capacity of SVM, in comparison with the other algorithms, to train relatively quickly at this level of quality, although convergence between the training and cross-validation scores was not reached, even when 1000 samples were processed for training (Fig. 3a). In terms of archaeological output, the map produced by SVM is acceptable (Fig. 3b), but several bare soil areas, corresponding to car tracks, were erroneously classified as dry stones. As a result, serious manual cleaning would be necessary before producing usable documentation.

HSV or HS as input features

When HSV channels were applied as alternative input features to RGB, results were, at best, similar to those obtained by RGB (e.g. SVM, RF, ANN), or exhibited worse performances (e.g. NB, LR, LDA, QDA) (Table 1). Using H and S alone could be a better option, because of the gain in robustness (for H and S) against illumination changes (V) [47], whereas the RGB colour space is generally sensitive to this parameter (Sural et al. [27]). This was not the case here, as the results obtained from H and S (not shown) decreased dramatically in comparison with those based on HSV, similarly to results already observed in other circumstances [26]. As a consequence, the RGB colour space will be preferred in the following.

Texture features alone

The combination of contrast, homogeneity, and entropy yields an excellent classification for all algorithms, always surpassing RGB by a few percent, which is noticeable at this level of performance (Table 1). The logistic regression model was selected for its efficiency, and because convergence is reached quickly, after 300–400 total samples, at a level of accuracy close to 99.3% (Fig. 3c). This procedure provides a map where car tracks have now disappeared, demonstrating the power of texture features for classification (Fig. 3d).

Combining both texture features and RGB

Such a combination should take into account both spatial arrangement of the tonal information, and spectral distribution

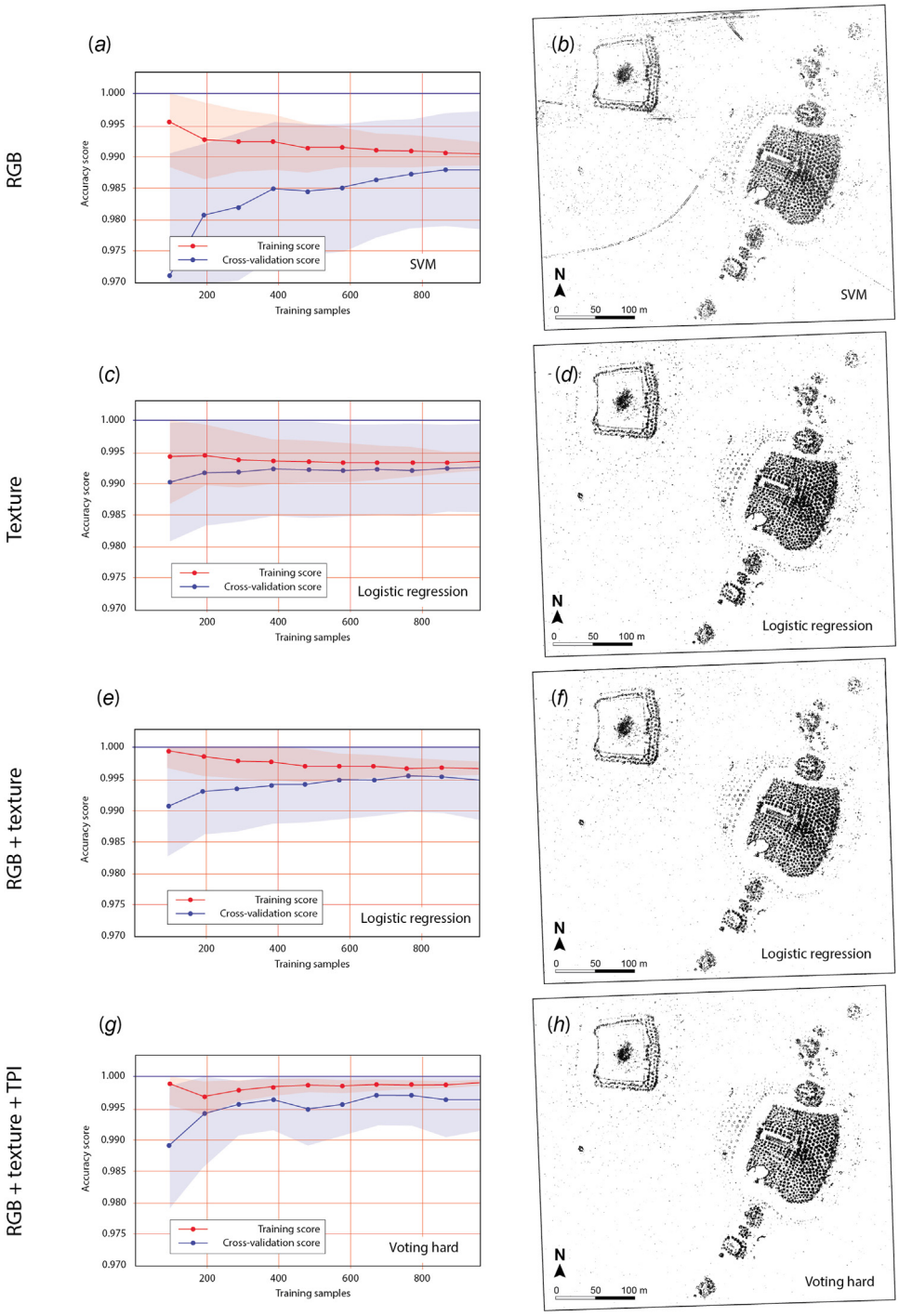

Fig. 3. Feature selection and best machine learning algorithm for the site of Jargalant. Four feature combinations are presented: RGB, texture (CON + HOM + ENT), RGB + texture, RGB + texture + TPI. Left: training and cross-validation scores with their 95% confidence interval as a function of the size of the training dataset; right: output map with the model selected.

of light; two sets of features which are not fully independent because the former is, in part, deduced from the latter, but which should describe two different sides of the image. This might push classification capabilities a little further [48]. Table 1 confirms this expectation, as performances increased slightly, almost systematically (note however that these improvements cannot be statistically demonstrated, considering confidence intervals). The classifier trained quickly (Fig. 3e), and several isolated false positives have vanished from the resulting map, although such an improvement is difficult to see at the scale of the document (Fig. 3f).

Combining texture features, RGB and TPI

Stone mounds exhibit positive relief with respect to their immediate surroundings, while hollows are expected for furrows resulting from agricultural activities, or car tracks in the steppes. As a consequence, information derived from topography might efficiently enrich the feature set. When TPI is introduced as a new input variable, together with RGB colour and texture, performance scores tend to improve by a further few tenths of a percent (Table 1). Random forest, logistic regression, and SVM slightly surpass other approaches, and produce scores that generally exceed 99.5%. How-

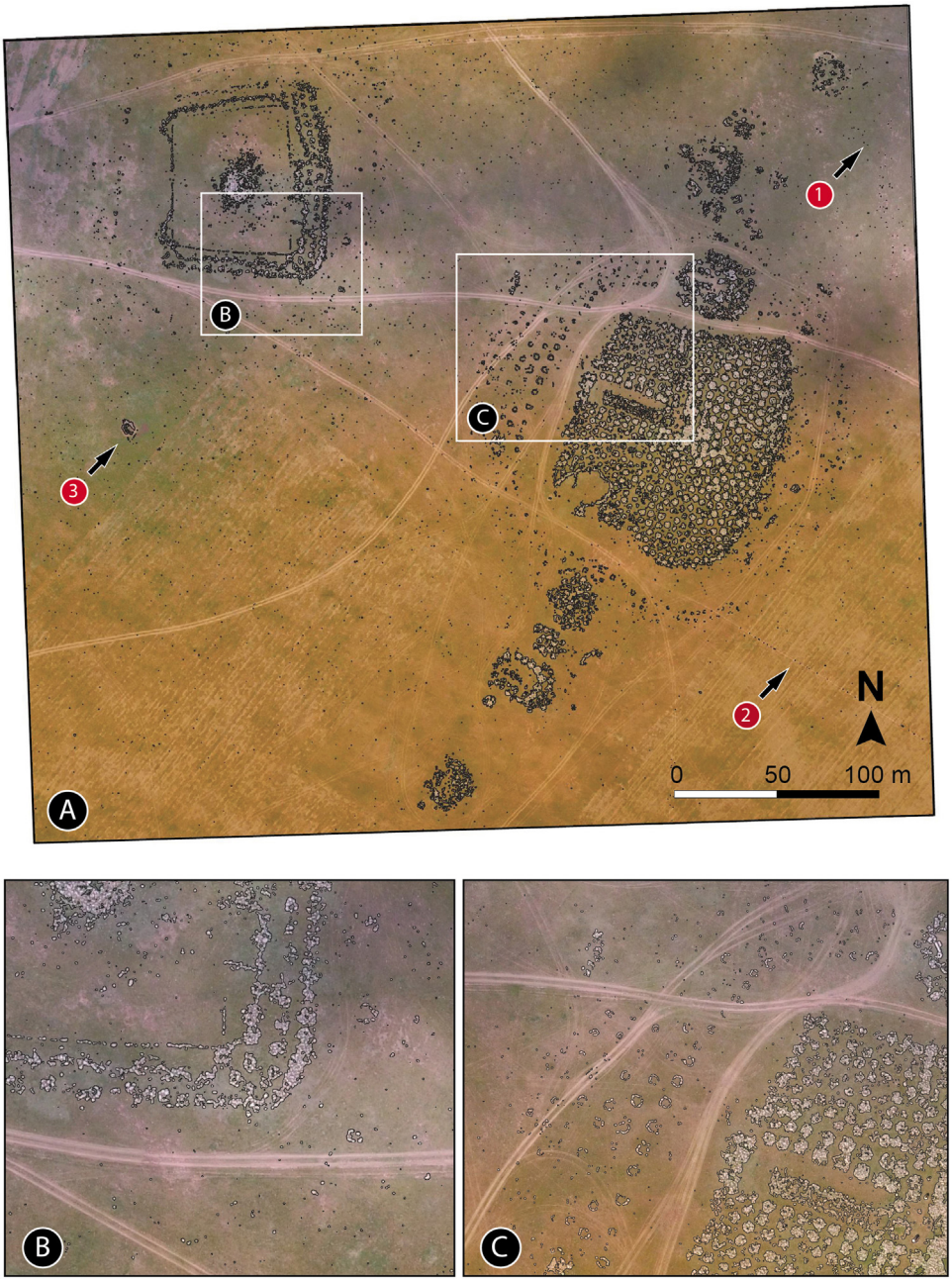

Fig. 4. Original orthomosaic of Jargalant overlain by a vector layer corresponding to a polygonised black and white map obtained by hard voting (A); two close-ups (B and C). Three arrows (1–3) point out specific areas.

ever, attention must be paid to training speed in addition to performance scores, because the more rapidly the model learns, the less time-consuming will be the supervision step. Here, even for the most favourable case, at least 400 samples were necessary to reach convergence between the training and cross-validation scores (not shown). Hard voting was therefore tested, using the results of the KNN, SVM, LR, LDA, RF and ANN classifiers, in the hope of reducing this number, if possible, without impacting score quality. This ensemble-based method reached correct convergence for only 200 training samples (Fig. 3g), while maintaining scores at their highest levels: >99.5% for precision, F1-Score, and accuracy (Fig. 3h displays the resulting map). Note that gradient boosting and adaboost (i.e. adaptive boosting), which seek to transform a set of weak learners into strong learners [49], were also tested. Both methods produced scores comparable to those of hard voting, but at a lower learning speed. As a consequence, hard voting was preferred.

Visual evaluation of the Jargalant output map

Introducing complexity into a model to improve classification performance by only a few percent or tenths of a percent in comparison with the use of RGB alone might appear, at first glance, not really relevant, but purely academic. It must, however, be kept in mind that a gain of only 0.1% in terms of accuracy corresponds to more than 20 000 pixels in an image of more than 20 Mpix. Any improvement, even minimal, may therefore save a considerable amount of time during post-processing, so that efforts must be made in this direction. Fig. 4a displays the original orthomosaic of Jargalant, overlain by a vector layer corresponding to a polygonised black and white map, obtained by hard voting (i.e. Fig. 3h), and a close-up of two particular areas (Fig. 4b,c). At this scale, the quality of the output map is undeniable. All archaeological structures com-

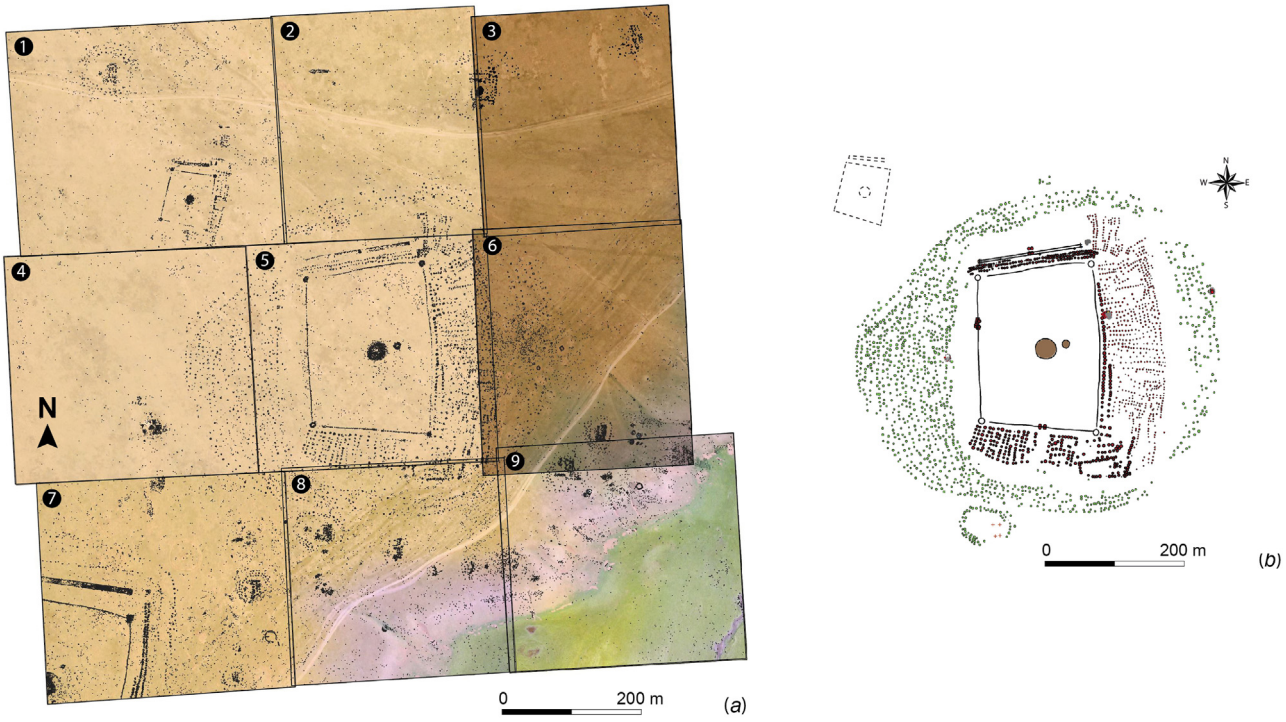

Fig. 5. Comparison between delineation of stones obtained by machine learning (a) and the map resulting from pedestrian survey by topographers equipped with a total station (b) for the funeral structure B10, Mongolia. The figure (a) displays 9 orthomosaics, noted 1–9, overlain by vector layers corresponding to polygonised black and white maps, obtained by hard voting.

posed of accumulations of dry stones were precisely delineated, while bare soils were not misclassified as stones (see Fig. 4b,c), except in very few instances in the north-east (arrow 1), on the car track in the south-east (arrow 2), and for the livestock enclosure in the west of the orthomosaic (arrow 3). Some positive cases were also delineated in the fields, but they correspond to actual stones raised to the surface by ploughing.

Performance of the method for a large site and evaluation of the operational framework

At Tsatsiin Ereg, archaeological structures cover several square kilometres. However, only nine tiles, of about 10 ha each, corresponding to the B10 complex are presented here (Fig. 5a), because this area has already been the object of a precise survey by two topographers, equipped with a total station during 2 missions, each lasting 1 month (Fig. 5b). Each of the 9 orthomosaics was produced from about 100 pictures acquired in 2016, and hard voting was applied to RBG + texture + TPI, following the procedure described above. About 200–250 samples per tile for both positive and negative cases were selected manually, so that, without the test subset, the total number of training samples finally used for learning was around 300; a value sufficient to reach an acceptable convergence between training and cross-validation scores.

During the past 3000 years, rain erosion has almost certainly led to the accumulation of a thin slope-wash layer made of granitic arena, but as it is only 5–10 cm thick, even small stones can be recognized. Dry stone structures are therefore perfectly visible in the steppes and can be correctly delineated. The method proposed clearly outperforms pedestrian surveys. It appears more precise, partly because human error during topographic surveys of an area very dense in anthropogenic structures can be avoided. From flight programming to photo processing, the gain in working time for the operator is considerable (cf. Table 2). Only 15–20 min of flight are necessary to cover an area of $400 \times 400\,m^2$, which is remarkable,

Table 2
Time necessary for processing one tile of about $300 \times 300\,m^2$ (final images of ca. 40 Mpix). These times must be compared to the two months needed for two people in the field to record only the B10 structure (see Fig. 5). *: maximum time provided for cleaning vectorized outputs of Jergalant. Note that this value may be different, depending on the area targeted. Both DEMs and orthomosaics were produced using a computer equipped with an i7 5960X CPU, 64 Go of RAM, and two NVIDIA GeForce GTX 980 mounted in SLI.

	Time consumed
Picture acquisition by drone (automatic)	15 min
Production of DEM and orthomosaic by photogrammetry (automatic)	2 h 30–3 h 00
Production of texture maps (automatic)	40 min
Production of TPI map (automatic)	5 min
Point selection for training dataset (manual)	10 min
Classification by hard voting and construction of vector layers (automatic)	15 min
Post-production & wrong polygon cleaning (manual)	<30 min*

considering that time spent in the field is the main limiting factor for massive recording. Interestingly, the operator can also evaluate orthomosaics the same day, to detect possible technical problems, and so perform the operation again if necessary. Note that several isolated rocks are recorded. Depending on the final objective, these positive cases could be easily removed, either by hand (taking typically less than 30 min), or automatically using an algorithm, taking into account the local density of positive cases, and/or the distance to the nearest positive neighbours.

One final test was performed to examine if the time spent acquiring the training dataset could be significantly reduced. Tiles n°5 and n°3 were treated with their specific training dataset, but also with that acquired to process tile n°4 (Fig. 6). Good results were anticipated for n°5, since the images were captured the same day, approximately at the same time, and thus in the same lightning and topsoil moisture conditions, but there was some doubt about tile

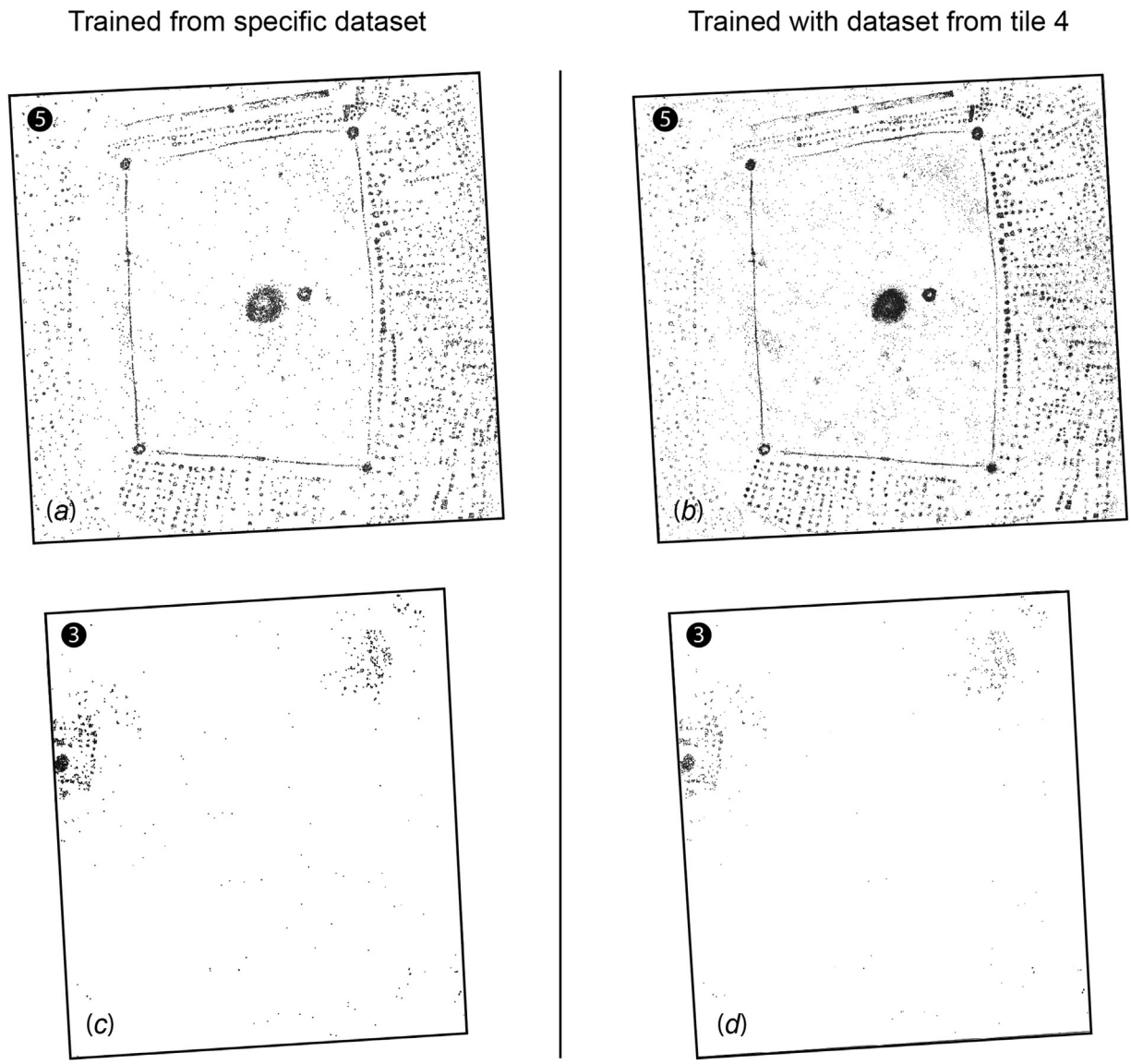

Fig. 6. Comparison between delineation of stones obtained by a model trained using a dataset specifically acquired for tiles n°5 and n°3, respectively (a) and (c), and delineation obtained with a common training dataset acquired from tile n°4 (b) and (d).

n°3, which exhibits greener images (like tile n°6), probably because the images were taken after a rainy event. In fact, both treatments produce comparable outcomes (Fig. 6a,b and c,d), because texture variables are less prone to variation than colour variables. However, it must be noticed that, when training used samples from tile n°4, more false positives were observed for tile n°5, while a few stones were missed on tile n°3. Again, depending on the final objective, the operator will be able to decide between optimal accuracy, but a relatively time-consuming training step, or simplified training by picking pixels from only a single tile.

Conclusion

In the context of large archaeological sites, covering several hectares, with little vegetation, acquiring images by drone, with treatment by appropriate methods, is a very effective solution for further automatic archaeological mapping. The low cost and simple logistics, especially in remote field conditions, undeniably argue for this type of aerial photogrammetry. The method proposed for treating the data generally surpasses pedestrian surveys, as it is almost fully automatic, rapid, and accurate, while a traditional record by GPS or total station is time-consuming, and may lead to errors difficult to avoid when archaeological structures are small and numerous. Acquisition speed is a strong asset, as one of the most limiting factors is the time spent in the field, especially for studies undertaken overseas, where field campaigns are often time-constrained. With the increasingly high resolution of images, and technological progress making it possible to collect hundreds of images for each flight, applying machine learning algorithms becomes indispensable. The operator intervenes significantly during two crucial steps. The first is the manual selection of the training dataset. In the examples presented, it was very important to sample different kinds of stones, but also grass, car tracks, bare soil, etc., because if the training data is inadequate or not adequately representative, poor classification results are to be expected. The second step concerns feature engineering. While the selection of the best learning model and hyperparameter tuning can be performed almost automatically, the workflow consisting in reformatting, processing, enriching, calibrating, and finally selecting features requires some experience. In the present case, the use of colour information in the RGB colour space, three texture parameters among those available, and one feature derived from

the topography produced suitable outputs for almost all classifiers tested. That is probably a good start for undertaking such mapping in other circumstances, but it is likely that some adjustments will be necessary to attain optimal results. Depending on the final objective, it may be interesting (or not) to keep isolated stones. In our examples, their position might be useful for cultural heritage preservation, by better understanding of stone displacements caused by livestock perambulation or water runoff. By contrast, for studying the spatial organisation of archaeological structures, these isolated stones can be removed manually, or alternatively by using an appropriate algorithm. For the sake of completeness, it must however be mentioned that this study takes place in a part of the world where conditions are optimal: the archaeological structures are not masked by vegetation, and they have almost never been buried or disturbed since their construction. Such a situation is rarely met in other environments, probably making the application of the proposed workflow more difficult. Finally, although binary pixel classification was here proved to perform well, other extremely powerful approaches, such as deep learning for object detection, should also be tested in the near future.

Acknowledgements

This research was funded by the Join mission Mongolia – Monaco, and the project ROSAS (uB-FC and RNMSH). We are grateful for helpful comments by an anonymous reviewer and the editor, which have greatly improved the manuscript.

Appendix A. Supplementary data

Supplementary material related to this article can be found, in the online version, at doi:https://doi.org/10.1016/j.culher.2020.01.002.

References

[1] J. Bourgeois, M. Meganck, Aerial photography and archaeology 2003 A Century of Information, 4, Archaeological Reports Ghent University Ghent: Academia Press, 2005.
[2] D.N. Riley, The technique of air-archaeology, Archaeol. J. 101 (1946) 1–16.
[3] R.S. Solecki, Practical aerial photography for archaeologists, Am. Antiq. 22 (1957) 337–351.
[4] N.G. Smith, L. Passone, S. al-Said, M. al-Farhan, T.E. Levy, Drones in archaeology: integrated data capture, processing, and dissemination in the al-Ula Valley, Saudi Arabia, Near East. Archaeol. 77 (2014) 176–181.
[5] D.C. Cowley, C. Moriarty, G. Geddes, G.L. Brown, T. Wade, C.J. Nichol, UAVs in context: archaeological airborne recording in a national body of survey and record, Drones 2 (2018) 2.
[6] I. Aicardi, F. Chiabrando, A. Lingua, F. Noardo, Recent trends in cultural heritage 3D survey: the photogrammetric computer vision approach, J. Cult. Herit. 32 (2018) 257–266.
[7] S. Campana, Drones in archaeology. State-of-the-art and future perspectives, Archaeol. Prospect. 24 (2017) 275–296.
[8] A. Traviglia, A. Torsello, Landscape pattern detection in archaeological remote sensing, Geosciences 7 (2017) 128.
[9] J. Magail, Tsatsiin Ereg, site majeur du début du 1er millénaire en Mongolie, Bull. Musee Anthrop. Prehist. Monaco 48 (2008) 107–120.
[10] W.W. Fitzhugh, The Mongolian deer stone-khirigsuur complex: dating and organization of a late bronze age menagerie, in: J. Bemmann, H. Parzinger, E. Pohl, D. Tseveendorzh (Eds.), Current Archaeological Research in Mongolia, (Bonn Contributions to Asian Archaeology 4, vfgarch.press uni-bonn, Bonn, 2009, pp. 183–199.
[11] J. Magail, F. Monna, Y. Esin, J. Wilczek, C. Yeruul-Erdene, J.-O. Gantulga, Application de la photogrammétrie à la documentation de l'art rupestre, des chantiers de fouilles et du bâti, Bull. Musee Anthrop. Prehist. Monaco 56 (2017) 69–92.
[12] A.R. Gansella, J.-W. van de Meent, S. Zairis, C.H. Wiggins, Stylistic clusters and the Syrian/South Syrian tradition of first-millennium BCE Levantine ivory carving: a machine learning approach, J. Archaeol. Sci. 44 (2014) 194–205.
[13] C. Hörr, E. Lindinger, G. Brunnett, Machine learning based typology development in archaeology, JOCCH 7 (2014) 2.
[14] J. Wilczek, F. Monna, M. Gabillot, N. Navarro, L. Rusch, C. Chateau, Unsupervised model-based clustering for typological classification of Middle Bronze Age flanged axes, J. Archaeol. Sci. Rep. 3 (2015) 381–391.
[15] G. Barone, P. Mazzoleni, G.V. Spagnolo, C. Raneri, Artificial neural network for the provenance study of archaeological ceramics using clay sediment database, J. Cult. Herit. 38 (2019) 147–157.
[16] X. Zhang, J. Cui, W. Wang, C. Lin, A study for texture feature extraction of high-resolution satellite images based on a direction measure and gray level co-occurrence matrix fusion algorithm, Sensors 17 (2017) 1474.
[17] A. Kobler, S. Dzeroski, I. Keramitsoglou, Habitat mapping using machine learning-extended kernel-based reclassification of an Ikonos satellite image, Ecol. Model. 191 (2006) 83–95.
[18] C.J. Abolt, M.H. Young, A.L. Atchley, C.J. Wilson, Rapid machine-learning-based extraction and measurement of ice wedge polygons in high-resolution digital elevation models, Cryosphere 13 (2019) 237–245.
[19] S. Raschka, Python Machine Learning, Packt Publishing, 2015, pp. 454.
[20] T. Turbat, J. Bayarsaikhan, D. Batsukh, N. Bayarkhuu, Deer Stones of the Jargalantyn Am, Mongolian Tangible Heritage Association NGO, Oulan-Bator, 2011, pp. 192.
[21] J. Magail, J.-O. Gantulga, C. Yeruul-Eredene, M. Tsengel, Inventaire et relevés des pierres à cerfs de Tsatsiin Ereg, Bull. Musee Anthropol. Prehist. Monaco 50 (2010) 77–114.
[22] F. Monna, Y. Esin, J. Magail, L. Granjon, N. Navarro, J. Wilczek, L. Saligny, S. Couette, A. Dumontet, C. Chateau, Documenting carved stones by 3D modelling – example of Mongolian deer stones, J. Cult. Herit. 34 (2018) 116–128.
[23] Y. Esin, J. Magail, C. Yeruul-Erdene, J.-O. Gantulga, Au sujet des traces de peintures sur les stèles ornées de Mongolie de la fin de l'âge du Bronze et du début de l'âge du Fer, Bull. Musee Anthropol. Préhist. Monaco 58 (2018) 145–156.
[24] J.C. Leachtenauer, R. Driggers, Surveillance and Reconnaissance Imaging Systems: Modeling and Performance Prediction, Artech House, 2001, pp. 416.
[25] G. Verhoeven, Taking computer vision aloft–archaeological three-dimensional reconstructions from aerial photographs with photoscan, Archaeol. Prospect. 18 (2011) 67–73.
[26] H. Seong, H. Son, C. Kim, A comparative study of machine learning classification for color-based safety vest detection on construction-site images, KSCE J. Civ. Eng. 22 (2018) 4254–4262.
[27] S. Sural, G. Qian, S. Pramanik, Segmentation and histogram generation using the HSV color space for image retrieval, ICIP (2002), http://dx.doi.org/10.1109/ICIP.2002.1040019.
[28] R.M. Haralick, K. Shanmugam, I. Dinstein, Textural features for image classification, IEEE transactions on systems, Man Cybernet. 3 (1973) 610–620.
[29] M. Hall-Beyer, Practical guidelines for choosing GLCM textures to use in landscape classification tasks over a range of moderate spatial scales, Int. J. Remote Sens. 38 (2017) 1312–1338.
[30] I. Vrbik, S.J. Van Nest, P. Meksiarun, J. Loeppky, A. Brolo, J.J. Lum, A. Jirasek, Haralick texture feature analysis for quantifying radiation response heterogeneity in murine models observed using Raman spectroscopic mapping, PLoS One (2019) 1–12.
[31] L.-K. Soh, C. Tsatsoulis, Texture analysis of SAR sea ice imagery using gray level co-occurrence matrices, IEEE Trans. Geosci. Remote Sens. 37 (1999) 780–795.
[32] J. De Reu, J. Bourgeois, M. Bats, A. Zwertvaegher, V. Gelorini, P. De Smedt, W. Chu, M. Antrop, P. De Maeyer, P. Finke, M. Van Meirvenne, J. Verniers, P. Crombé, Application of the topographic position index to heterogeneous landscapes, Geomorphology 186 (2013) 39–49.
[33] J.C. Gallant, J.P. Wilson, Primary topographic attributes, in: J.P. Wilson, J.C. Gallant (Eds.), Terrain Analysis: Principles and Applications, Wiley, New York, 2000, pp. 51–85.
[34] S.Y. Kung, Kernel Methods and Machine Learning, Cambridge University Press, 2014, pp. 572.
[35] C.M. Bishop, Pattern Recognition and Machine Learning, Springer-Verlag New York Inc., 2006, pp. 738.
[36] B. Lantz, Machine Learning With R, 2nd edition, Packt Publishing, 2015, pp. 452.
[37] P. Domingos, M. Pazzani, On the optimality of the simple bayesian classifier under Zero-One loss, Mach. Learn. 29 (1997) 103–130.
[38] G. James, D. Witten, T. Hastie, R. Tibshirani, An Introduction to Statistical Learning, Springer-Verlag New York Inc, 2013, pp. 426.
[39] D.W. Hosmer Jr, S. Lemeshow, R.X. Sturdivant, Applied Logistic Regression, 3rd ed, John Wiley & Sons, USA, 2013, pp. 528.
[40] P.A. Lachenbruch, M. Goldstein, Discriminant analysis, Perspect. Biometry Biometr. 35 (1979) 69–85.
[41] C. Cortes, V. Vapnik, Support-vector networks, Mach. Learn. 20 (1995) 273–297.
[42] M. Hofman, Support vector machines - Kernel and the kernel trick, Houptseminar Rep. (2006).
[43] T. Hastie, R. Tibshirani, J. Friedman, The Elements of Statistical Learning, 2nd ed, Springer, 2008, pp. 745.
[44] M. Kuhn, K. Johnson, Applied Predictive Modeling, Springer, 2013, pp. 600.
[45] M. Piragnolo, A. Masiero, F. Pirotti, Open source R for applying machine learning to RPAS remote sensing images, Open Geospat. Data Softw. Stand. 2 (2017) 16.
[46] S. Raschka, Python Machine Learning, 2nd edition, Packt Publishing, 2015, pp. 454.
[47] B.D. Zarit, B.J. Super, F.K.H, Quekc comparison of five color models in skin pixel classification, in: ICCV'99 International Workshop on Recognition, Analysis, and Tracking of Faces and Gestures in Real-Time Systems, Corfu, Greece, 1999, pp. 58–63.
[48] S. Rathore, M. Hussain, M.A. Iftikhar, A. Jalil, Ensemble classification of colon biopsy images based on information rich hybrid features, Comput. Biol. Med. 47 (2014) 76–92.
[49] Y. Freund, R.E. Schapire, A decision-theoretic generalization of on-line learning and an application to boosting, J. Comput. Syst. Sci. 55 (1997) 119–139.

3.2. L'apprentissage profond comme outil de prospection

Les capacités d'acquisition du drone combinées à la classification supervisé par apprentissage automatique ont permis de cartographier des milliers de monuments dans deux vallées voisines dans un laps de temps assez court (quelques semaines). Ce protocole mis en place s'adapte donc bien à l'étude détaillée de l'architecture funéraire à l'échelle d'une vallée.

Il serait intéressant de réaliser une étude sur la répartition des complexes funéraires à plus large échelle, sur une province, voire sur le pays tout entier. Plusieurs contraintes se profilent déjà. L'utilisation du drone sur de telles surfaces étant impossible, il faudrait s'appuyer sur la photographie aérienne ou satellitaire. Cela va nécessairement introduire une perte de résolution par rapport à l'acquisition par drone. Le détail architectural des khirigsuurs ne sera probablement plus reconnaissable. En revanche il sera toujours possible de les situer et d'identifier l'emplacement des nécropoles, ce qui représente assez informations pour entreprendre une analyse spatiale. La méthode par apprentissage automatique pour détecter les pierres n'est pas adaptée à ce type de problème. L'idée néanmoins est d'éviter un inventaire manuel de tous les khirigsuurs sur une zone donnée en adoptant une démarche de détection automatique des objets. Ce domaine de recherche appartenant à la vision par ordinateur est largement étudié. Il a notamment été médiatisé grâce à la reconnaissance automatique des visages ou des piétons, pour une application dans les voitures autonomes, par exemple.

L'opportunité m'a été donnée de travailler sur un sujet très similaire concernant la détection de maisons traditionnelles sur l'île de Sumba, située dans l'archipel des petites îles de la Sonde, en Indonésie. Ces maisons possèdent un toit avec une surélévation appelée tour, très reconnaissables depuis les photos satellites. Tout comme les khirigsuurs, ces maisons ont la particularité d'être rassemblées, non pas en complexes mais en villages. Elles forment ainsi de multiples regroupements dont l'agencement spatial peut être caractérisé, puis interprété en termes anthropologiques. Sumba a l'avantage d'être un territoire limité en taille (11 000 km², soit environ la surface de la Corse, contre environ

1,5 M km² pour la Mongolie). La couverture satellitaire y est bien meilleure qu'en Mongolie, à la fois en termes de résolution d'image, mais aussi d'homogénéité colorimétrique (Fig. 15). Les toits des maisons vernaculaires possèdent un schéma et une taille plus régulières que les khirigsuurs. Ces qualités sont propices à un bon apprentissage. De ce fait, cette étude peut être considérée comme un travail préliminaire à ce qui pourra être appliqué un jour sur le territoire mongol, avec pour objectif la cartographie la plus exhaustive possible des monuments funéraires de l'âge du Bronze.

Fig. 15 Comparaison des photos satellites disponibles avec une orthomosaïque réalisé à l'aide d'un drone pour le territoire de Sumba (en haut) et le territoire mongol (en bas).

Journal of Cultural Heritage 52 (2021) 171–183

Contents lists available at ScienceDirect

Journal of Cultural Heritage

journal homepage: www.elsevier.com/locate/culher

Original article

Deep learning to detect built cultural heritage from satellite imagery. - Spatial distribution and size of vernacular houses in Sumba, Indonesia -

Fabrice Monna[a,*], Tanguy Rolland[a], Anthony Denaire[a], Nicolas Navarro[b,c], Ludovic Granjon[d], Rémi Barbé[d], Carmela Chateau-Smith[e]

[a] ARTEHIS, UMR CNRS 6298, Université de Bourgogne–Franche Comté, 6 boulevard Gabriel, Bât. Gabriel, F-21000 Dijon, France
[b] EPHE, PSL Research University, F-21000 Dijon, France
[c] Biogéosciences UMR CNRS 6282, Université Bourgogne Franche-Comté, 6, boulevard Gabriel, Bat. Gabriel, F-21000 Dijon, France
[d] MSH de Dijon, USR CNRS 3516, Université Bourgogne Franche-Comté, 6, esplanade Erasme, F-21000 Dijon, France
[e] CPTC, Université de Bourgogne, 4, boulevard Gabriel, F-21000 Dijon, France

ARTICLE INFO

Article history:
Received 6 May 2021
Accepted 12 October 2021

Keywords:
Object detection
Data augmentation
Spatial distribution
Settlement
Geographical information system
Scan statistics
Histogram of gradients

ABSTRACT

In Sumba Island – Indonesia, the implantation of vernacular houses, inside and outside traditional villages, is considered to be an efficient proxy for the on-going complex cultural transformations resulting from globalization. This study presents an easily reproducible workflow allowing buildings to be automatically detected from satellite imagery, demonstrating how modern computer vision methods based on deep learning can help in this task, which would be far too time-consuming when undertaken by hand. Eight deep learning architectures based on convolutional neural networks were compared in terms of ability to identify and locate precisely traditional houses from satellite images. By combining a Faster R-CNN ResNet 101 architecture with artificial data augmentation, the model was taught properly using 1033 instances of vernacular houses (AP@.50:.95 = 71.9). Once 14 952 traditional houses had been detected, the Histogram of Orientated Gradients (HOG) was computed and processed by several machine learning algorithms to assess their surface area, as this parameter conveys pertinent information about the economic and political position of the householder. The best classifier was found to be a support vector regressor (SVR, $R^2 = 0.88$), although the other classifiers tested also provided good results ($R^2 > 0.76$). Spatial analysis was used to draw conclusions from an anthropological / cultural identity point of view. More generally, these techniques not only offer a simple increase in recording capabilities for tangible cultural heritage, they open up new research perspectives, at greater scales.

1. Introduction

The massive introduction of satellite imagery into daily life has modified our perception of space by enabling people to visualize the diversity of our planet, while experiencing perilous exploration from the comfort of their homes. This wealth of documentation, including digital images in visible spectra and beyond, has led to considerable advances in many fields of research [1–4]. This source of knowledge has opened new research perspectives for cultural heritage and archaeology at much vaster scales [5–9]. The digital era has nevertheless produced a bottleneck: human beings may be unable to deal with this huge flow of information in a reasonable amount of time [10–12], particularly when identifying a given structure among a myriad of images. Fortunately, this mundane repetitive task can now be tackled using methods based on machine learning, freeing scientists to devote their expertise to more complex problems [13,14]. Interest in deep learning, a subset of these methods, has increased considerably over the past two decades [15,16], profiting from rapid technical improvements, and key breakthroughs in mathematics, especially in optimization [17]. These techniques are designed to learn from data and make predictions on new instances with a minimum error rate. The architecture of the models is composed of several layers of convolutional artificial neurons, where information flows after being nonlinearly transformed [18,19]. Relevant features are then learnt from a high level of data abstraction [17]. Three main objectives are applied to images: classification [20], object detection [21], and object segmentation [22]. These approaches, based on state-of-the-art deep learning algorithms, have been successfully applyied for

* Corresponding author.
E-mail address: Fabrice.Monna@u-bourgogne.fr (F. Monna).

https://doi.org/10.1016/j.culher.2021.10.004
1296-2074/

proper management and protection of cultural heritage. For example, models have been developed to detect damage to historical buildings automatically [23–24], to map lithology of stones from images [25], or to identify types of weathering in historical stones [26], in order to optimise the choices made in conservation and restoration practices. In this study, we focus on object detection through deep learning, seeking to identify and locate vernacular houses on Sumba Island (Indonesia), from a huge set of satellite images. These traditional houses, known as *rumah adat* in Indonesian, are targeted because they are emblematic of the indigenous local culture [27,28]. They are characterized by a high-pitched central peak in the roof, materializing the connection with the spirits. Ancestral settlements generally contain a few to a few dozen of these houses, organized in circles, or in parallel rows facing each other, together with collective megalithic funeral monuments. Varying in size, these monuments appear to be extensions of clan-houses [29,30]. With economic development and recent cultural globalization, more people are leaving traditional villages, gradually abandoning the traditions, rituals, and religious beliefs of their *marapu* culture [27,30]. These recent mutations disrupt to some extent the traditional way of life and its ancestral cultural foundations.

2. Research aim

Our objective is to propose an easily reproducible workflow allowing human structures to be detected from satellite imagery, and to demonstrate how modern computer vision methods based on deep learning can help to apprehend the on-going complex transformations described above. The implantation of vernacular-style houses, inside and outside traditional villages, is considered an effective proxy. Eight of the most powerful deep learning architectures, belonging to two families of detectors, were compared for their ability to identify and locate traditional houses from a set of satellite images covering the region of Waikabubak, where such houses are abundant. Solutions based on artificial data augmentation were sought to teach the models properly, even with fewer instances. The reason is not only that the labelling phase takes time, but above all because a limited number of examples during the learning phase may present a serious obstacle to the truly effective application of deep learning [12]. Although vernacular houses are plentiful on Sumba Island, such solutions would be very helpful in archaeology, where the available instances may be far scarcer. Once the best approach had been selected, the procedure was extended to the whole of Sumba Island. After separating isolated houses from those belonging to traditional villages, spatial analysis was used to draw conclusions from an anthropological / cultural identity point of view. Several regression algorithms were also applied to estimate the size of the roofs thus identified, as this parameter conveys pertinent information about the economic and political position of the householder.

3. Material and method

3.1. The site

Sumba Island (*Pulau Sumba*), ca. 1500 km ESE of Jakarta, belongs to the Indonesian Lesser Sunda Islands (Fig. 1a). The territory covers ca. 11 000 km^2, with a maximum elevation of 1 225 m asl. Geologically, the island is predominantly composed of sedimentary rocks, with some volcanic / intrusive rocks (Fig. 1b, [31] and references cited therein). The topography of sedimentary formations is mainly coastal terraces and rugged karsts. The tropical dry climate is characterized by seasonal precipitation, abundant only from December to March, with the driest zones along the north and northeast coasts. The population of about 800 000 is mostly rural, concentrated in the hilly fertile western part of the island, except for the largest town of about 40 000 inhabitants [32], Waingapu, located in the northeast (Fig. 1a). The territory is administratively divided into West and East Sumba, corresponding approximately to cultural domains, represented in Fig. 1c by the ethnolinguistic distribution. East Sumba is more linguistically homogeneous than West Sumba. Two large natural parks were created in 1998 on the south coast because of their exceptional biodiversity (Fig. 1a): (*i*) the Manupeu Tanah Daru National Park, covering 870 km^2 and consisting mainly of lowland forests developing on steep slopes, and (*ii*) the Laiwangi Wanggameti National Park, covering 880 km^2 and composed of steppe (60%), and lowland or mountainous rainforest (40%).

3.2. Corpus

Several thousands of typical high-towered houses are present at Sumba, either as isolated buildings or clustered, forming villages and hamlets in the traditional way. Houses are almost square-shaped, from ~6 m to ~20 m in size (Fig. 2). Although originally constructed from pieces of wood and bamboo linked with vegetal ropes, reinforced concrete is often used today. The dense thatch of *alang-alang* grass (a local plant) used to build the roof (Fig. 2a-b) is now increasingly replaced by raw corrugated metal (Fig. 2c; [33]). Note that a few resorts and official buildings imitate the style of these indigenous constructions.

Automatic detection algorithms were evaluated on satellite imagery distributed by Microsoft Bing™ (https://zoom.earth/). The vast majority of images at the highest level of definition available (ca. 0.3 m/px) were neither too dark nor too bright, with almost no clouds. A home-made Python snippet collected tiles 256 × 256 px in size over the targeted geographical extent. They were then merged to produce larger images of 640 × 645 px (corresponding to 187.5 m × 188.5 m), a size suitable for further application of deep learning (Fig. 3a). Reconstructed GeoTIFF images were made to overlap each other by 80 pixels (ca. 25 m) in all directions, to ensure that all houses are complete at least once [34]; see houses 1 and 2 in Fig. 3b, truncated with a blue square, but complete with yellow and red squares. Due to overlap, some complete houses are seen on two or more images (e.g. houses 3 and 4 in Fig. 3b). They were automatically removed using a simple rule: if the centres of their bounding boxes were less than 6 m apart (a value lower than the minimum size of a house), only the most probable item was kept.

Images around Waikabubak (Fig. 1a), within a geographical latitudinal-longitudinal extent of (−9.680°; −9.588°) / (119.360°; 119.470°), were first processed to select the best model. This model was then applied to the whole island with a geographical extent of (−10.346°; −9.271°) / (118.912°; 120.870°). About 700 000 files remained after removing useless offshore tiles.

3.3. Labelling

Before training any object detection model, the operator needs to point out target locations of houses manually in a set of images considered as representative. At that point, two approaches can be applied, using either polygons (and subsequently, models dedicated to segmentation) or simple rectangular bounding boxes (ground-truth boxes), defined by the pixel coordinates of their upper-left and lower-right corners [35]. For the sake of simplicity, we decided to use the latter approach. It is generally admitted that a model is able to detect an object that a human can identify by looking at the image for just 1–2 s. In our case, traditional houses were almost always easy to spot, whatever the roofing material used (Fig. 4), because of their typical square shape, combined with the distinctive shadows produced by the high roof tower. The relatively

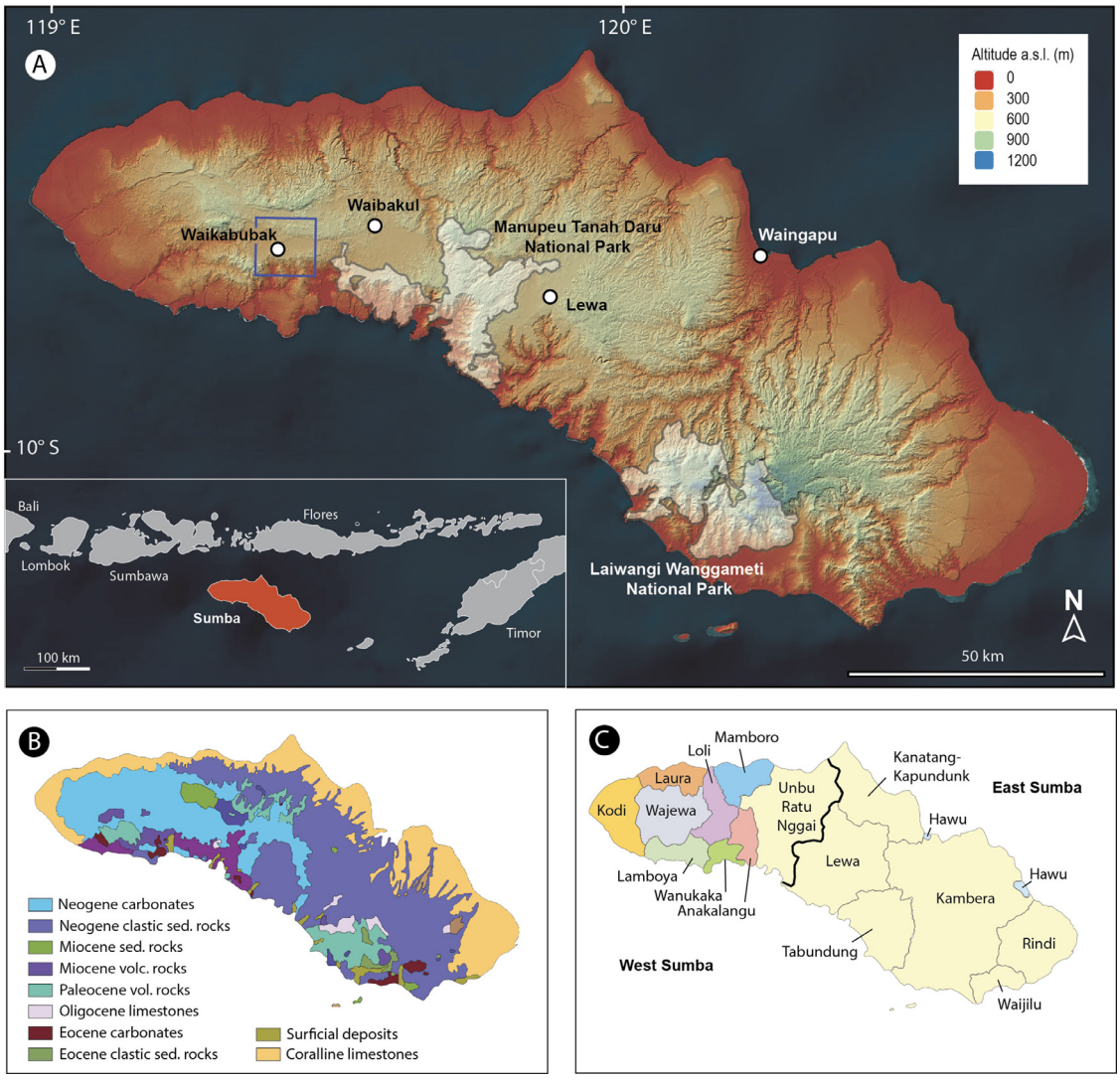

Fig. 1. Geographical, geological, and ethnolinguistic maps of Sumba. (a): hill-shaded, coloured, 30-m resolution digital elevation model (https://www.eorc.jaxa.jp/ALOS/en/aw3d30/); (b): combined bedrock, and superficial geology and age map (http://portal.onegeology.org/OnegeologyGlobal/); (c): approximate geographical locations of the 16 main dialects (Edwards and UBB, 2018).

Fig. 2. Some examples of vernacular houses found at Sumba. (a): collective funeral monuments in the foreground and several vernacular houses in the background; (b) aerial view of a village, with houses exhibiting a high-pitched central peak in their roofs; houses are clustered and organized in rows facing each other because of the limited space on the top of the hill; (c) houses at Mamboro, including a large recent house with a raw corrugated metal roof.

steady downward-facing views from the satellite facilitate this task, although some satellite pictures were also captured in oblique view, and then post-processed by orthorectification before diffusion. This process generated some noticeable deformation, transforming squares into diamonds, but did not affect identification or bounding box positioning (not shown here). When the triangular structure on the roof was not clearly identified, the houses were not labelled (see 1 and 2 in Fig. 4). The annotating step used LabelImg, a free software (https://github.com/tzutalin/labelImg). Note that bounding boxes of houses partly masked by vegetation were kept approximately square by including the supposed position of the building below the canopy. A total of 494 images for the region of Waikabubak produced 1 396 bounding boxes of traditional houses.

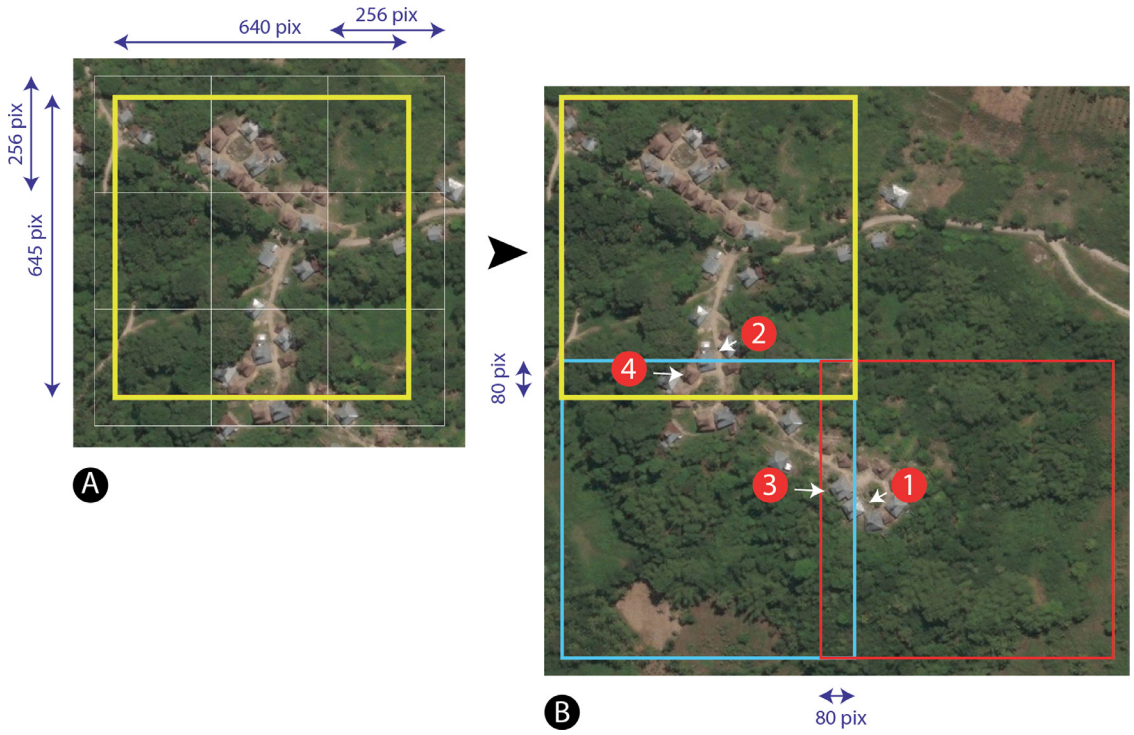

Fig. 3. Composition of images used for further deep learning. (a) images of 640 × 645 px (in yellow) are composed by merging individual 256 × 256 tiles (in white); (b) georeferenced images (in yellow, blue and red) overlap each other by 80 pixels in all directions; objects 1 and 2 are complete in only one image, while objects 3 and 4 are seen completely in two images. (For interpretation of the references to color in this figure legend, the reader is referred to the web version of this article.)

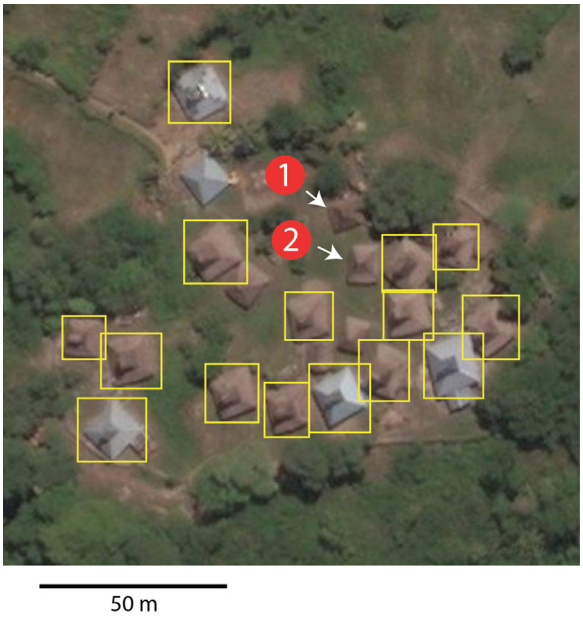

Fig. 4. Final bounding boxes annotated as vernacular houses (in yellow), for one example of a reconstructed image. Manually positioned, they locate the object of focus for deep learning models. The houses with a relatively dark roof summit (see objects 1 and 2), to some extent like those of triangular towers, were not targeted here because they do not present the clear characteristics of true high-towered houses. (For interpretation of the references to color in this figure legend, the reader is referred to the web version of this article.)

3.4. Object detection models

Our intention here is not to describe extensively the complex architectures of the models tested, but to provide basic information to explain the underlying principles of deep learning applied to object detection. More details can be found in the abundant specialized literature [17,21,36], many textbooks [37–40], and web sites dedicated to deep learning. Object detectors can be divided into two main categories, one- and two-stage detectors [40,41]. In two-stage detectors, such as Faster R-CNN, the input image is passed through a convolutional neural network (CNN) to obtain a feature map of the image. This part is referred to as the "backbone" network. The map is then used by a Region Proposal Network (RPN), which is a fully convolutional network proposing regions characterized by reference anchor boxes of fixed scales and aspect ratios, placed evenly on the original image. These regions are then filtered by a Non-Maximum Suppression algorithm, whose purpose is to decrease the number of candidate objects to an acceptable level. Bounding box extraction and classification are then obtained for each candidate using regression from the Region of Interest (RoI) pooling layer [42]. The Single Shot Detector (SSD) belongs to the one-stage detector group [43]. It may operate in real-time with a decent trade-off between performance and speed [41,43]. Such a speedy process is obtained by running a convolutional network on the input image only once, and then calculating a feature map. A small convolutional kernel is operated on this feature map to predict bounding boxes and compute classification probabilities. The SSD also uses anchor boxes. It predicts bounding boxes after multiple convolutional layers, which may be of different scales. Results are aggregated, and redundant information is eliminated by applying a non-maximum-suppression algorithm, as with Faster R-CNN. The two-stage detectors may, however, provide better results at the expense of speed. The algorithm schematics of SSD and Faster R-CNN are available in Supplementary SM1, modified after [23] and [44]. Although many of the available models have already been evaluated through various challenges, using for instance the Common Object in Context dataset (i.e. COCO, http://cocodataset.org/#home; [45]), eight different object detection models were tested here: two based on the SSD cat-

Table 1
Performance scores of different architectures, pre-trained on the COCO dataset (models are downloadable at the following address: https://github.com/tensorflow/models/blob/master/research/object_detection/g3doc/detection_model_zoo.md); Training is performed following two configurations including either 480 or 1033 instances of houses. Evaluation is performed on the same 124 instances of houses. No data augmentation is applied. *: stride value between parentheses. See text for definitions of AP@.50:.95, AP @.50, and AP @.75.

Metrics (expressed in%)	AP @.50:.95	AP @.50	AP @.75	AP @.50:.95	AP @.50	AP @.75
Number of instances used for training	480			1033		
Name as in the Tensorflow detection model zoo homepage						
ssd_inception_v2_coco	54.5	95.6	56.6	61.4	98.4	70.0
ssd_resnet_50_fpn_coco	62.0	93.5	76.7	67.2	98.7	84.7
faster_rcnn_inception_v2_coco	53.5	93.6	54.1	59.7	97.1	68.3
faster_rcnn_inception_resnet_v2_atrous_coco (8)*	64.7	96.6	77.2	68.2	98.6	84.9
faster_rcnn_resnet50_coco (16)*	60.1	96.5	70.5	63.6	98.7	78.9
faster_rcnn_resnet50_coco (8)*	65.1	97.1	81.1	68.3	99.5	84.6
faster_rcnn_resnet101_coco (16)*	62.0	95.3	75.7	67.3	97.7	85.2
faster_rcnn_resnet101_coco (8)*	**68.4**	97.4	85.7	**71.9**	98.7	88.7

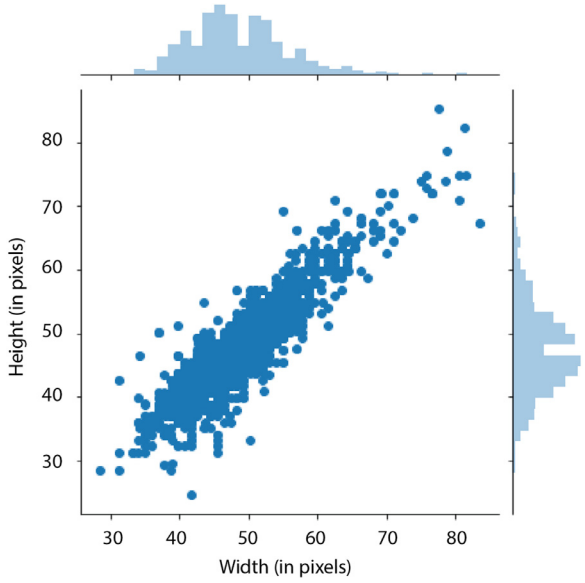

Fig. 5. Shape variation of manually positioned bounding boxes, expressed as height as a function of width (in pixels). The light blue histograms at the top and the right represent the distributions of width and height, respectively.

egory, and six on Faster R-CNN [46]. They are listed in Table 1, with different convolutional neural network backbones, codenamed inception [47], ResNet [48] and inception-ResNet, with or without feature pyramid networks (namely FPN; [49]) as feature extractors. The idea was to reuse these models, already trained for a different task, as the starting point for a custom dataset and specific problem [50]. This approach, known as transfer learning, is expected to speed up the training step and to improve overall performance when sensitive parameters are fine-tuned [38].

3.5. Tuning for house shape and size

For both SSD and Faster R-CNN, a very dense set of potential candidates with different scales and aspect ratios is evenly distributed on the images. The parameters controlling the density, size and shape of these anchor boxes are of primary importance, especially when detecting small objects [51]. An initial guess can be made from the joint distribution of height and width for house bounding boxes observed in the annotated set (Fig. 5). Here, the problem is relatively simple because the bounding boxes will remain square whatever the house orientation (i.e. the houses lie on or around the $y = x$ line in Fig. 5), while their size varies relatively little, between ca. 30^2 and 80^2 pixels (Fig. 5). After applying a k-nearest neighbours' algorithm ($k = 3$), three main sizes can finally be retained {0.15, 0.2, 0.25}, corresponding to 38^2, 51^2 and 64^2 pixels respectively (given a base anchor of 256×256), while two aspect ratios {0.9; 1.1} appeared to be sufficient, since the overall shape is quite regular. Output strides and padding for the extractor are two other important parameters, as they control how deep the abstraction goes to extract features [51]. Denser and more accurate predictions are generally obtained using low strides, but this will notably increase running time [52]. Two values, {8, 16} pixels, were tested here to assess their efficiency in extracting small objects from optical remote sensing images.

3.6. Data augmentation

Deep learning skills are conditioned by the availability of the data feeding the model. While popular datasets used for challenges may contain tens of thousands of images, instances may be much rarer in cultural or archaeological studies. A simple technique, known as data augmentation, has been developed to enlarge the dataset artificially in such cases [53]. This technique supplements the original set of images by new synthetically produced data, obtained by combining geometrical transformations and colour alterations sequentially [54]. Here, six augmentations were tested: 90° rotation, horizontal and vertical flipping, grey level conversion, random colour distortion, and random jitter of box corners by 1 to 4 pixels (see Supplementary Material SM2). A total of 64 experiments (i.e. 2^6 for 6 investigated factors, each with 2 levels: applied / not applied) would be required to evaluate the individual influence of each factor on model performance. As such a full factorial design is time-consuming, factors were selected by building a reduced 2^{6-2} fractional design [55]. Let A, B, C, D be the first four factors; the remaining two: E and F, were chosen so that $E = A^*B^*C$ and $F = B^*C^*D$ (Table 2). This resolution-IV design represents only ¼ of the full 2-level, 6-factor design. Thus, the main effects are not confounded with two-factor interactions, but only aliased with 3-factor and higher-order interactions, which may reasonably be considered insignificant [56].

3.7. Model performance

Three-quarters of the images were randomly selected for training, with the remainder kept for evaluation. Average Precision (AP), a common metric in deep learning, was used to measure the performance of the detectors on the evaluation set. The AP calculation considers the common trade-off between precision and recall, observed at different degrees of correctness for the predicted bounding boxes. These degrees of acceptability are obtained using different thresholds for the Intersection over Union (IoU), a parameter defined as the area of overlap between the predicted box

Table 2
Results of the fractional design (16 carefully chosen experiments) to assess the effect of each individual factor for data augmentation: horizontal and vertical flip of the image, rotation 90°, colour adjustment, grey level conversion, and bounding box jitter. 1 means that the factor is applied (i.e. high level), −1 for not applied (i.e. low level). On the right, the performance scores using as metrics AP@.50:.95, AP@.50, and AP@.75. See text for definition. Experiments were performed using the same 480 and 124 instances of houses for training and evaluation.

	Factor						Metric		
	A Horiz. flip	B Vert. flip	C Rot.	D Colour adj.	E Grey level	F Jitter BB	AP@.50:.95	AP@.50	AP@.75
Exp. #									
1	−1	−1	−1	−1	−1	−1	68.4	97.4	85.7
2	1	−1	−1	−1	1	−1	71.1	98.6	90.7
3	−1	1	−1	−1	1	1	71.7	97.8	89.8
4	1	1	−1	−1	−1	1	70.4	98.5	88.7
5	−1	−1	1	−1	1	1	70.4	98.5	88.6
6	1	−1	1	−1	−1	1	69.4	98.1	87.1
7	−1	1	1	−1	−1	−1	69.9	97.6	85.1
8	1	1	1	−1	1	−1	71.3	98.4	92.0
9	−1	−1	−1	1	−1	1	71.0	97.8	87.2
10	1	−1	−1	1	1	1	70.7	97.3	89.5
11	−1	1	−1	1	1	−1	70.5	97.4	89.3
12	1	1	−1	1	−1	−1	70.8	97.6	88.2
13	−1	−1	1	1	1	−1	70.2	98.2	89.2
14	1	−1	1	1	−1	−1	69.8	98.4	89.1
15	−1	1	1	1	−1	1	70.5	97.6	89.0
16	1	1	1	1	1	1	71.0	97.7	91.5

and the ground truth, divided by the area of their union [57]. The IoU ranges between 0 and 1, with high values indicating more accurate prediction. The metric used is that of the COCO challenge [45], with ten IoU thresholds, from 0.5 to 0.95, at a step of 0.05 (noted AP@.50:.95. AP). It is produced by averaging over the 10 IoU thresholds and tends to reward models that are better at precise localization. In any case, AP@.50:.95 is less generous than IoU $\geq$ 0.5, or the stricter IoU $\geq$ 0.75 limit, which are reported for information.

3.8. Operational settings

For all the experiments, the maximum training epoch was set at 50 000, using an initial learning rate of 3.10^{-4} for the first 10 000 steps, 3.10^{-5} up to 20 000 steps, and then 5 10^{-6}. For Faster R-CNN models, a batch size of 1 (corresponding to a Stochastic Gradient Descent optimization algorithm, [58]) was set, together with a momentum of 0.9, while a batch size of 4 was used for SSD. At a certain point, training loss may continue to decrease, but testing loss may start to increase. This is a clear sign of overfitting, where the model learns well from the training dataset, but fails to generalize this knowledge to make correct inferences on new instances. That is why training was always stopped before 50 000 iterations (often after 15 000 – 45 000). The evolution of the total loss observed on the training set, together with the AP value computed from the evaluation set are reported in Supplementary Information SM3 (using a Faster R-CNN ResNet 101 model).

3.9. Separating houses forming villages from isolated houses

A Density-Based Spatial Clustering of Applications with Noise, DBSCAN [59], algorithm was applied to differentiate isolated houses from those forming villages. When density decreases below a certain point, houses are assumed to lie outside groups. Two sensitive parameters must be set: the minimum number of items necessary for a group, and the maximum distance for clustering with the nearest neighbour. Based on our knowledge of Subanese villages, a 'traditional village' is a cluster of at least three vernacular houses, less than 70 m from their nearest neighbour. Houses that do not fulfil these conditions are defined as 'isolated'. In rare cases, these settings mask the reality of the terrain: in the Loli district, for example, Tarung and Waitabar, two separate villages, were clustered because of their proximity. Without complementary field investigations, such a scenario cannot be identified, but most villages lie hundreds of metres apart.

3.10. Clustering by under- or over-representation of isolated houses

Scan statistics [60], a procedure often used in epidemiology, was applied to examine whether the ratio of isolated houses / houses in villages is the same throughout Sumba territory (i.e. spatial homogeneity) or not (i.e. an underlying geographical structure). Briefly, it consists in scanning the space gradually, centring from one house to another, and counting the number of houses belonging to each type, within expanding circles. Considering a Bernoulli model, a likelihood ratio test is computed for each location and size of the scanning window, using as an alternative hypothesis a high (or low) ratio of isolated (or village) houses within the search window.

3.11. Estimating the surface of recognized houses

With satellite imagery, it is impossible to know the precise house surface area when roofs overhang walls for protection from rainfall. The difference may reach 25%, but roof area is always proportional to house surface area. With houses systematically orientated North – South (or East – West), the problem would be trivial since bounding boxes would approximately match roofs. Here, house orientation is variable. Given its roughly square geometry, a roof can be considered as a square inscribed in another square (bounding box), so that the surface of the roof is comprised between ca. 50% and 100% of the box surface, depending on house orientation. A supervised machine learning approach was developed for further assessment. The distribution of local intensity gradients or edge directions was chosen as input feature. The method, known as Histogram of Orientated Gradients (HOG), has been widely applied for face detection [61]. In brief, it consists in dividing the image into several small cells of $N \times N$ px (Fig. 6a), where gradient intensities and orientations are computed (Fig. 6b). Fig. 6c demonstrates how well local appearance and overall house silhouette are described by gradient distributions, suggesting that this set of variables could be a good candidate to predict roof ori-

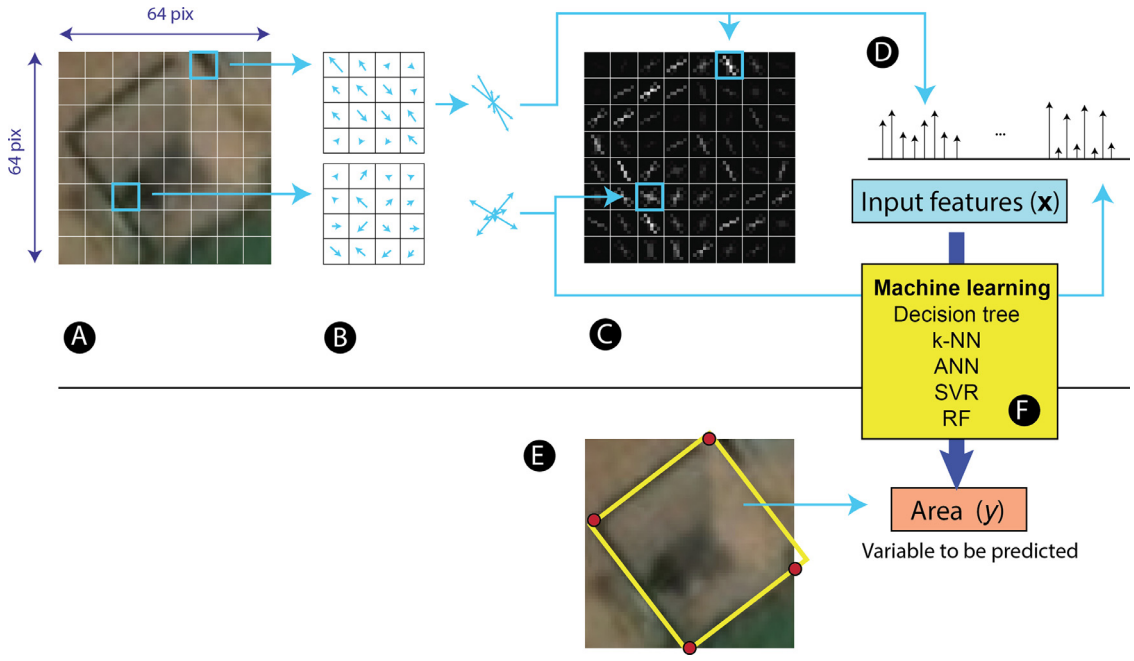

Fig. 6. The machine learning pipeline for assessing the size of vernacular houses, modified after Carcagni, et al. (2015). (a): the image, rescaled at 64 × 64 px, is divided into a 8 × 8 grid; (b): gradients are computed following 12 orientations within every cell; (c): the orientated gradients allow the orientation of the house to be visualized clearly; (d): construction of the input feature vector, **x**; (e): four points manually positioned close to the corners of the roof (in red), and its corresponding minimum bounding rectangles (in yellow), where the surface area is the variable to be predicted: *y*; (f) five machine learning algorithms are applied to input features (a set of oriented gradients). (For interpretation of the references to color in this figure legend, the reader is referred to the web version of this article.)

entation (see also two additional examples of houses, differently orientated in Supplementary Material SM4). Histograms are then built for each cell of the dense grid covering the image (Fig. 6d). In practice, the images of 363 houses were resized to 64 × 64 px to produce an 8 × 8 grid, where each cell represents 8 × 8 px. A total of 12 orientations was evaluated within each cell, producing an input feature vector, **x**, of 768 values (12 orientations × 64 cells), characteristic of each image (Fig. 6d). In addition, four points were manually placed at (or close to) the four corners of the roof for each of the 363 houses. The surfaces of the minimum bounding rectangles were computed, representing the variable to be predicted: *y* (Fig. 6e). A total of 288 houses was used for training, while the remaining 75 houses were kept for evaluation. Five machine learning algorithms: decision tree, *k*-nearest neighbours, artificial neural networks, support vector machine regression, and random forest, were tested by applying a grid search approach combined with cross-validation to fine-tune the hyperparameters (Fig. 6f; [62]). Their prediction capabilities were evaluated, using coefficients of determination, mean relative errors, and maximum relative errors as quality scores. The best model was then applied to the entire set of houses detected over the Sumba territory.

3.12. Implementation

Object detection models were produced and evaluated using Python 3.7 (https://www.python.org/), and the free TensorFlow object detection API (v. 1.13 including GPU capabilities). Pre-trained models are available at the Tensorflow detection model zoo homepage. The homemade Python snippet for assessing house size relies on the numpy, gdal, scikit-learn, scikit-image, csv, and pandas libraries, and a modified version of the min_bounding_rect.py snippet (https://gist.github.com/kchr/77a0ee945e581df7ed25). Results are expressed as georeferenced polygon vector layers. The homemade snippet for DBSCAN relies on the scikit-learn library [63]. The identification of geographical clusters by scan statistics used the 64-bit SaTScan v9.6 software (http://www.satscan.org/, [60], see user manual for *p*-value calculation with a Monte-Carlo approach).

4. Results and discussion

4.1. Comparing object detection models

The first experiments trained the candidate models using 480 and 1033 instances of traditional houses, and an evaluation set composed of 124 and 363 items, respectively, without any synthetic data augmentation. As expected, performance is better with the largest training set: the gain is ca. 3.5–7% for AP@.50:.95, 1.5–5% for AP@.50, and 3–13% for AP@.75 (Table 1). At first glance, all models provide acceptable outputs, extracting most of the houses, with AP@.50:.95 above 50%, and AP@.50 greater than 90%. Although SSD is fast, it is known to perform less well for small objects, compared with state-of-the-art models based on Faster R-CNN. Using output stride and padding of 8 instead of 16 proves beneficial to the overall achievement of the Faster R-CNN detectors based on ResNet 50 and ResNet 101 (Table 1), as AP@.50:.95 increases by 5–6%, AP@.75 by 4–10%, and AP@.50 by 1–2%. The Faster R-CNN model with a ResNet 101 backbone is retained as it greatly surpasses the other models whatever the number of instances used for training. Despite an increase in running time, an output stride for the extractor of 8 pixels is used, because houses must only be extracted once from satellite images. As no synthetic data augmentation is applied, the performances reported in Table 1 can be considered as the baseline.

4.2. Data augmentation strategy

The question then arises whether the use of an appropriate data augmentation strategy can push significantly further the capabilities for a training dataset of fixed size. The results of the 16 experiments for the fractional design built to assess the effect of each individual factor (i.e., horizontal and vertical flip, rotation, colour

Table 3
Main effect of factors used for data augmentation, i.e. application of random horizontal flip, vertical flip, rotation by 90°, colour adjustment, grey level conversion, and bounding box jitter on AP value. The intercept term corresponds to the last column. The last line corresponds to the best augmentation strategy: 'High' for augmentation applied, 'Low' for not applied.

Factor	A	B	C	D	E	F	Intercept
	Horiz. flip	Vert. flip	rot. 90°	colour adj.	Grey level	Jitter BB	
Main effect (%)	0.13	0.31	−0.14	0.13	0.42	0.20	70.4
Optimal level	High	High	Low	High	High	High	–

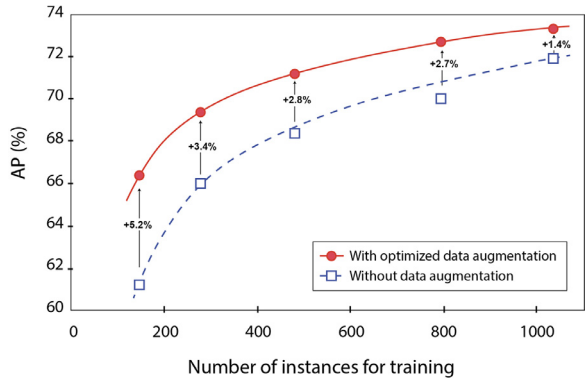

Fig. 7. Evolution of average precision (AP, expressed in%, see text for calculation) as a function of the number of instances used for training. Open blue squares for evaluations made without data augmentation, and red dots for optimal data augmentation; the solid red line and the dashed blue line correspond to interpolated evolutions. The percentages, in black, correspond to the gain obtained using data augmentation for various numbers of instances used for training. (For interpretation of the references to color in this figure legend, the reader is referred to the web version of this article.)

adjustment, grey level conversion, and jitter of bounding boxes) are presented in Table 2. Note that training involved the lesser of the two configurations used in the previous experiment: the same sets of 480 and 124 instances of houses for training and evaluation, respectively. It appears that AP@.50:.95 increased notably, from no data augmentation (68.4% for exp #1 in Table 2) to data augmentation applying all factors (71.0% for exp #16). Estimates of main effects associated with each factor are reported in Table 3. All factors, except to some extent rotation, therefore seem to be profitable in terms of AP (Table 3). Grey level conversion has the largest (beneficial) effect, followed by vertical flip, and jitter of bounding boxes. The application of horizontal flip and colour adjustment seems to contribute only slightly to AP improvement. It must nevertheless be pointed out that AP is computed with a model frozen after an early stop during the training phase. Identifying this optimal moment is not easy, or at least not perfectly reproducible. Output results (i.e. AP values) may thus suffer somewhat from slight assessment errors of ca. 0.1–0.2%. Given that these uncertainties are of the same order of magnitude as each of the main factor effects (Table 2), it becomes tricky to evaluate with precision their individual contribution to AP. The accumulation of slightly influential factors by applying optimal data augmentation strategy as reported in Table 2 undoubtedly produces a sizable increase in AP values. Such improvements are observed systematically whatever the number of instances used for training (from 144 to 1033; Fig. 7). However, the larger the dataset, the lower the gain, because one cannot afford an explosive increase in terms of AP when numerous instances already illustrate most of the house variability encountered in the field. Note that even when 1033 instances are used for training, the AP value does not reach an asymptotic plateau (Fig. 7). Slight but significant progress might be achieved using more data for learning.

4.3. Inference on all Sumba Island tiles

The final model trained using 1033 instances of houses and data augmentation was used to make inferences on the entire collection of ca. 700 000 tiles covering Sumba Island. After a few days of computation, a total of 22 397 traditional houses was identified, with a confidence score above 0.5 (Supplementary Material SM5). After duplicate removal, 19 143 items remained. Close examination in GIS, using BING satellite imagery as basemap, revealed the presence of several false positives, i.e. objects wrongly identified as traditional houses. These defects were essentially associated with low confidence scores close to (or barely above) 0.5. A cut-off of 0.8 was therefore applied, keeping false negatives (traditional houses missed) at a very low level. A few obvious false positives remained in open spaces, such as rice fields, with isolated trees producing shadows resembling those of house roof towers, or in river talwegs, where shadows from rocks have a similar appearance. After a quick check, most of these mistakes were manually removed, as well as known administrative buildings (e.g. at the airport) and resorts constructed in traditional Sumbanese style. The procedure may nevertheless miss some large houses spotted in the field. These failures are often due to rare poor-quality images, or simply because satellite imagery is not up-to-date (Supplementary Material SM6). Fig. 8a depicts the position of the remaining 14 952 traditional houses throughout Sumbanese territory, after increasing the probability threshold and operating manual cleaning, together with the density gradient (in blue) on the map.

4.4. Identifying traditional villages and isolated vernacular houses

The threshold value of 70 m used to discriminate isolated houses from those belonging to traditional villages is coherent with the abrupt drop observed in the distribution of the distance to the nearest neighbour between houses (see the distribution in Supplementary Material SM7). After calculation, 8 799 houses were considered as isolated (Fig. 8b1 and, at another scale, turquoise dots marked 1 in Fig. 9), while a total of 6 153 houses was assumed to belong to traditional villages (Fig. 8b2, white dots for houses and villages marked 2 in Fig. 9). A total of 1 144 villages, generally with fewer than 5 traditional houses (but up to a maximum of 46), was identified using the above-mentioned rules (see the distribution of the number of houses forming a village in Supplementary Material SM8). Their central positions were then estimated by computing the geographical centroid of village houses (Fig. 8c, yellow stars in Fig. 9). It should be noted that mistakes remain possible: (*i*) the smallest villages will not be identified if they do not contain three traditional houses (see 3 in Fig. 9), (*ii*) two different villages, close to each other, may be grouped together if their nearest houses are less than 70 m apart (see 4 in Fig. 9), (*iii*) several recent houses in the vernacular style, implanted along the main road may be erroneously grouped to form a village, due to their proximity. Such drawbacks, together with the rare mistakes observed during the object detection phase, should not be seen as critical flaws, because the main strength of the

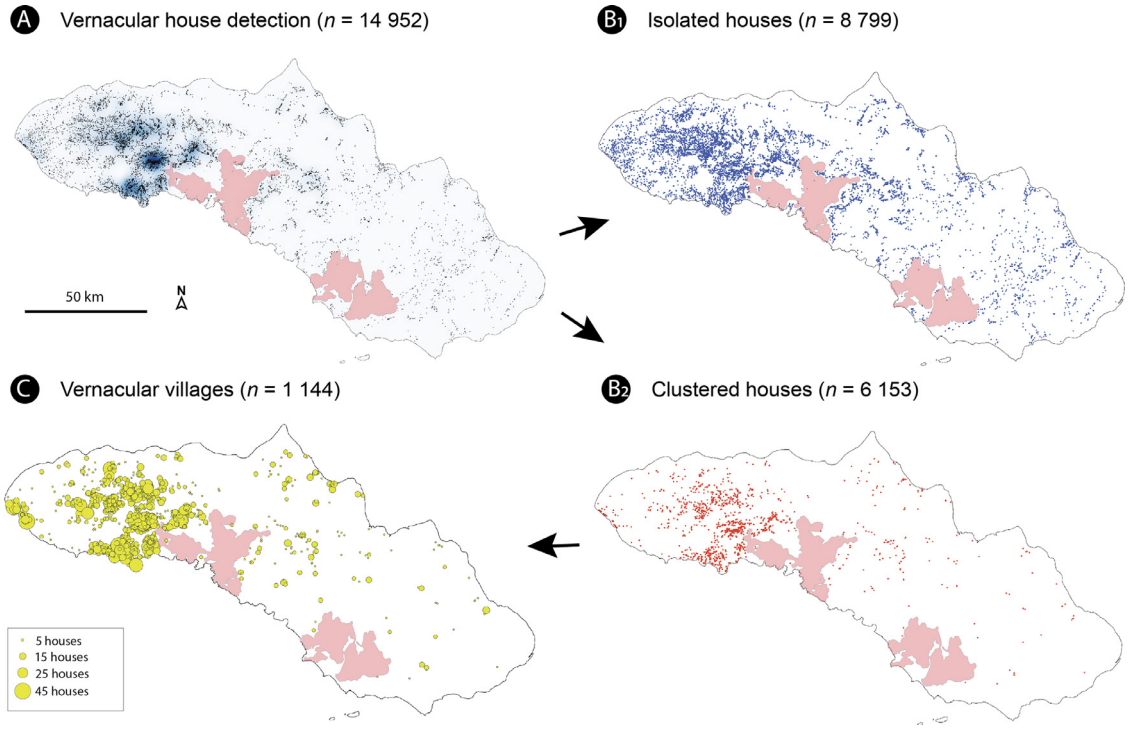

Fig. 8. Vernacular houses and traditional villages identified over the entire Sumba territory. (a): Position of the 14 952 houses identified and density map represented using a blue gradient; darker blue means higher density; (b_1) positions of the 8 799 isolated houses and (b_2) the 6 153 houses forming traditional villages; (c) position of the 1 144 traditional villages, with symbol size varying in relation to the number of vernacular houses forming the village. The pale pink polygons correspond to the two national parks.

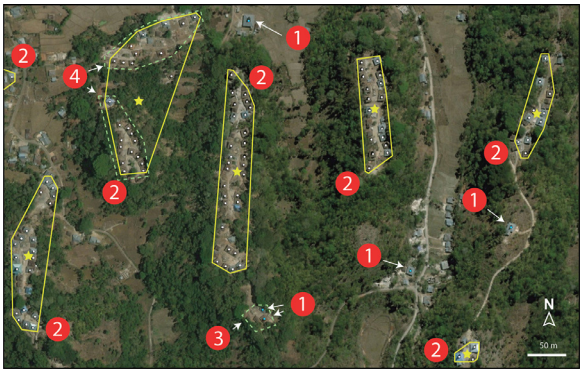

Fig. 9. Close-up in the region of Waikabubak depicting the identified vernacular houses, either isolated (turquoise dots) or organized in traditional villages (white dots); 1 for isolated houses; 2 for villages (yellow polygons, yellow star for centroid); 3 for a traditional village missed because it only contains two vernacular houses; 4 for two separate villages erroneously combined into one single entity. (For interpretation of the references to color in this figure legend, the reader is referred to the web version of this article.)

approach is that it tends toward exhaustivity over a large territory; these potential shortcomings will have no effect on statistical analysis.

Scan statistics demonstrate spatial structuration: the ratio of isolated (or village) houses is clearly not homogeneous throughout the study area. Three main clusters, which cannot be attributed to random effects, are statistically recognized (Fig. 10a). The first, centred on Waikabubak, presents a higher ratio of houses in villages (in blue in Fig. 10a). The second covers East Sumba almost entirely, with a higher-than-expected ratio of isolated houses (in red in Fig. 10a). The third, also with a higher ratio of isolated houses, is located at the extreme west of the island (in red in Fig. 10a).

Table 4
Algorithm performance scores: decision tree, *k*-NN for *k*-nearest neighbour regression, neural network, SVR for support vector machine for regression, and random forest; R^2 for coefficient of determination of the prediction, MRE for mean relative error, and MaxRE for maximum relative error. Several sets of feature variables were tested: the full set, namely without PCA, and four reduced sets allowing 50%, 65%, 80%, and 95% of the total variance to be explained. In bold, the best result obtained, corresponding to the method used.

	Without PCA	With PCA			
Variance explained (%)	100	95	80	65	50
Decision tree					
R^2	0.704	0.775	0.775	0.761	0.764
MRE (%)	8.4	7.3	7.3	7.0	7.5
MaxRE (%)	26.9	20.9	20.9	24.5	20.0
k-NN					
R^2	0.859	0.855	0.845	0.845	0.859
MRE (%)	5.7	5.6	5.7	5.8	5.5
MaxRE (%)	17.7	18.0	19.4	19.3	19.6
Neural network					
R^2	0.673	0.734	0.813	0.858	0.840
MRE (%)	8.7	6.6	5.9	5.6	5.9
MaxRE (%)	21.8	25.9	15.9	15.3	18.7
SVR					
R^2	0.787	0.848	0.868	**0.883**	0.870
MRE (%)	6.6	5.7	5.5	**5.3**	5.1
MaxRE (%)	17.7	14.7	14.9	**13.6**	16.5
Random Forest					
R^2	0.793	0.839	0.837	0.812	0.818
MRE (%)	6.7	6.1	6.1	6.4	5.9
MaxRE (%)	19.3	16.9	17.3	20.1	18.3

4.5. House size

Table 4 presents the results of the five machine learning algorithms tested, and their performance in assessing house size from oriented gradient values. This was computed using either the complete raw dataset as input, or a reduced set obtained by Princi-

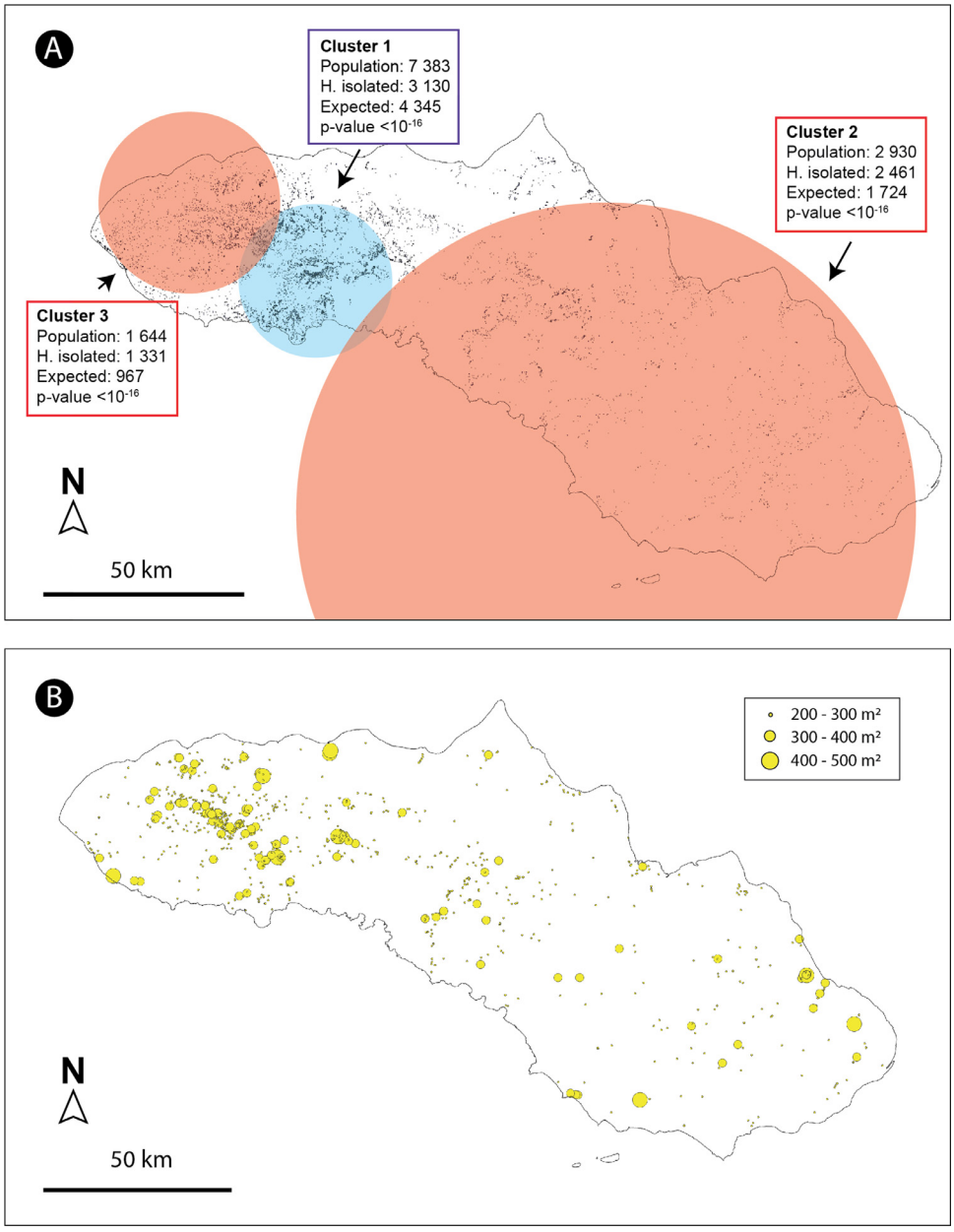

Fig. 10. (a): Results of the scan statistics processing over the entire Sumba territory, for all identified isolated houses, and those forming villages. The blue circle represents a cluster with a high ratio of vernacular houses belonging to villages; the two red circles correspond to areas with high ratios of isolated houses. For each cluster, the total number of houses within the circles, the number of isolated houses, the expected number under the null hypothesis (spatial homogeneity), and the *p*-value of the existence of a cluster, are provided. (b): Spatial distribution of house roofs larger than 200 m^2. The size of the circles varies with roof size. (For interpretation of the references to color in this figure legend, the reader is referred to the web version of this article.)

pal Component Analysis (PCA) to capture maximum total variance with lower dimensionality. Using the entire set of 768 values as input data (i.e. without PCA transformation), performance scores are satisfactory, with high R^2 values, varying from 0.67 to 0.86, whatever the method. The best results are obtained with *k*-nearest neighbours. The score of all models tends to improve with data reduction, except for the *k*-nearest neighbour algorithm that remains steady. The biggest boost is observed for the artificial neural network, with a notable R^2 increase of almost 0.2. This score is slightly lower than that of the support vector machine algorithm with PCA retaining 65% of the explained variance, where R^2 reaches almost 0.9, while the mean and maximum relative errors are around only 5% and 14%, respectively (see Supplementary Material SM9 for comparison between ground truth and predicted surface). Note, however, that approaches based on mask R-CNN, which extract pixels belonging to the objects of interest, could also be used to determine house size. This option was not chosen here, but the results presented above indicate that oriented gradients are also quite efficient to estimate house size rapidly and accurately, given that errors of only ca. 15% (at the most) are perfectly acceptable in our case. Roof size varies between 50 and 440 m^2, with a mean of 136 m^2 (see Supplementary Material SM10). A total of 1 027 roofs exceeded 200 m^2 in surface area (Fig. 10b). Interestingly, the size distribution of isolated houses appears to be statistically different from those belonging to villages, with larger roofs for isolated houses (KS = 0.1, *p*-value $< 10^{-16}$ for 2-sample Kolmogorov-Smirnov statistic, see also Supplementary Material SM11 depicting cumulative distributions for both groups).

4.6. Cultural implications

Most traditional houses are in West Sumba (~ 80%), especially in the Loli and Wanukaka territories, and to some extent in the Wajewa area (see Figs. 8a and 1c for ethnolinguistic subdivisions). This distribution tends to follow the implantation of the Sumbanese population, whether the inhabitants live in traditional houses or not (except for the large town of Waingapu). The greatest house density is found over Neogene carbonates (Fig. 1b), in particular on the hilly terrains surrounding the rice fields of the Waikabubak and Waibakul lowlands, where fertile soils must have attracted populations. In the Loli and Wanukaka territories, ancestral clan-house settlements were often established at the top of hills for defensive purposes ([64]; see Figs. 8c and 9 depicting an area located to the south of the Waikabubak lowland, where villages are massively implanted along the ridges). Another good reason for building there is that the air is drier than in the lowlands, close to the rice fields [29]. Some large villages are also found in the Kodi territory, located to the extreme west of the island (Fig. 8c), where the inhabitants exploit the few agricultural plots developed on coralline limestones (Fig. 1b). Other small settlements are present in the western part of the island, but they have not been identified here, because they are essentially composed of normal (not high-pitched) houses, which do not fulfil the criteria to label them as traditional. Today, there is no need for defence, so that isolated houses are quite numerous. In West Sumba, they mostly correspond to buildings in medium-sized villages, or along the main communication routes (Fig. 8b$_1$). With the rising standard of living, people have progressively left ancestral settlements for modern accommodation and related services (e.g. regular water supply, salaried employment, etc.). Others have built their homes closer to the fields they exploit for practical reasons. These modern houses ("garden houses") are generally larger and more comfortable than those originally found in traditional villages. However, the break with tradition is only partial as these new houses are frequently built close to the original village of their owner, and often imitate traditional Sumbanese style. Around Waikabubak, the ratio of isolated houses is lower than over the rest of the island (Fig. 10a), suggesting that the ancestral structure of society is more prevalent there. In East Sumba, the situation is very different. Traditional houses are scarcer (Fig. 8a), except to some extent in the region of Lewa, where numerous agricultural fields are exploited. The dominance of Neogene clastic sedimentary rocks as bedrocks (Fig. 1b), combined with steep slopes (Fig. 1a) and low rainfall makes the terrains of East Sumba not very productive and difficult to exploit. Even where traditional houses are present, they are often scattered in response to environmental constraints, so that only a few traditional villages can be identified (Fig. 8c). The political functions of these villages were, however, not the same as in the western part of the island. In the early 20th century, travellers reported that a single aristocrat assisted by a few vassals reigned over the eastern part of the island, while no such centralized power existed in the western domain. The sovereign ruled over a strongly stratified society, where possessing slaves was a sign of a high-ranking social and economic position. Note that slavery was abolished in 1860 in the Dutch East Indies, but castes still persist today, despite the efforts of the democratic Indonesian government. The villages and their activity are still centred on these aristocratic houses, whose size and position are clearly related to the social standing of their owners, their prestige, political power, wealth, and connection to the spirits (see as an example Fig. 2c, depicting an aristocratic house in the foreground of the picture). There are virtually no vernacular houses within the two large natural parks established in 1998 on the south coast (Fig. 8), which are predominantly established on volcanic substrates (Fig. 1b). Yet some ancient collective graves, testifying to the presence of former villages, have been identified here and there. This area has a low agricultural potential, and the creation of the two protected areas has probably incited the remaining population to abandon the area and to move elsewhere.

5. Conclusion

Applying an appropriate set of techniques based on machine learning can help to bridge the gap between tangible and intangible heritage, by rapidly producing maps for further spatial analyses undertaken with specific objectives. Nevertheless, it should be mentioned that the overall quality of satellite imagery is a strong limiting factor for applying deep learning in good conditions. Here, images were neither too dark nor too bright, with almost no cloud, always remaining perfectly readable at the highest resolution available (about 0.3 m/px), which is quite sufficient for our purpose. Some of the examples provided, however, demonstrate that the period during which satellite images have been acquired may introduce errors, because the situation is continuously evolving. Note also that if the labelling phase is inadequate or not fully representative, the accuracy of detection will be greatly impaired. Whatever the precautions taken, the techniques described here inevitably introduce some false positives and false negatives, which the researcher will have to manage. Automatic clustering of houses to identify villages implies a choice of settings. Even if the settings are appropriate, errors may also be introduced at that step. That is why a solid knowledge of the context is always highly desirable. Returning to the field for verification or for further investigation is an option that should never be neglected.

Our attempts to explain the distribution of vernacular houses are rendered complex as both environmental and societal factors almost certainly play a role, in competition with recent developments in Sumbanese society that are reshuffling the cards. The growing importance of 'garden houses' merits particular attention. It could be interesting to examine whether the situation of isolated houses without towers is similar, as differences in architecture may reflect the personal relationship of the owner to tradition. Further research could complete the data with surveys over time, or could repeat the study on available aerial images, prior to the societal changes mentioned.

Technically, several types of object detectors are available but, beyond this crucial choice, the researcher must be aware that other important parameters may heavily impact the overall performance of the model (output stride, augmentation strategy, etc..). The number (and diversity) of instances used for training is among these sensitive variables. In the present case, the experiment shows that using more than 1000 instances probably does not reach the maximum performance score. Nonetheless, it would have been absurd to increase the size of the training set to the point of labelling almost all the houses that must be detected. This issue is a matter of balance, which must be adapted to the problem to be solved. Interestingly, using an appropriate deep learning model for object detection, followed by a machine learning approach with HOG values as feature inputs, the size of houses can be estimated with good accuracy. Although the proposed workflow is sufficiently efficient here, instance segmentation, which straightforwardly extracts pixels belonging to houses, could also be evaluated in the future.

In the light of this summary, a novice might be afraid of the technicity required and the potential difficulties related to practical implementations. It would however be an error because all tools, freely available, come with detailed documentation. Even though time will be required during development, the gain will be huge for objects to be detected at very large scales, an impossible task if done by hand. In the present example, only one single class was involved, but it is entirely possible to detect several objects, at one

and the same time. The potential of deep learning applied to various situations related to the recording (and thus to the preservation or the study of the dynamics) of tangible cultural heritage is huge. These techniques not only offer a simple increase in recording capabilities, they provide a whole new order of magnitude for research perspectives.

Acknowledgements

This research was funded by the Conseil Régional de Bourgogne – Franche Comté. We are grateful for comments by the anonymous reviewers and by the editor, which have greatly improved the manuscript.

Supplementary materials

Supplementary material associated with this article can be found, in the online version, at doi:10.1016/j.culher.2021.10.004.

References

[1] T.J. Schmugge, W.P. Kustas, J.C. Ritchie, T.J. Jackson, A. Rango, Remote sensing in hydrology, Adv. Water Resour. 25 (2002) 1367–1385.
[2] D.S. Boyd, F.M. Danson, Satellite remote sensing of forest resources: three decades of research development, Prog. Phys. Geogr. 29 (2005) 1–26.
[3] N. Horning, J.A. Robinson, E.J. Sterling, W. Turner, S. Spector, in: Remote Sensing for Ecology and Conservation: a Handbook of Techniques, OUP Oxford, 2010, p. 496.
[4] R.P. Gupta, in: Remote Sensing Geology, 3rd ed., Springer, 2017, p. 428.
[5] S.H. Parcak, in: Satellite Remote Sensing For Archaeology, Routledge, 2009, p. 320.
[6] G. Caspari, Mapping and damage assessment of "Royal" burial mounds in the Siberian Valley of the Kings, Remote Sens. 12 (2020) 773.
[7] L. Luo, X. Wang, H. Guo, R. Lasaponara, X. Zong, N. Masini, G. Wang, P. Shi, H. Khatteli, F. Chen, S. Tariq, J. Shao, N. Bachagha, R. Yang, Y. Yao, Airborne and spaceborne remote sensing for archaeological and cultural heritage applications: a review of the century (1907–2017), Remote Sens. Environ. 232 (2019) 111280.
[8] G. Caspari, P. Crespo, Convolutional neural networks for archaeological site detection – Finding "princely" tombs, J. Archaeol. Sci. 110 (2019) 104998.
[9] D.S. Davis, Geographic disparity in machine intelligence approaches for archaeological remote sensing research, Remote Sens. 12 (2020) 921.
[10] A. Traviglia, A. Torsello, Landscape pattern detection in archaeological remote sensing, Geosciences (Basel) 7 (2017) 128.
[11] F. Monna, J. Magail, T. Rolland, N. Navarro, J. Wilczek, J.O. Gantulga, Y. Esin, L. Granjon, A.-.C. Allard, C. Chateau-Smith, Machine learning for rapid mapping of archaeological structures made of dry stones – example of burial monuments from the Khirgisuur culture, Mongolia, J. Cult. Herit. 43 (2020) 118–128.
[12] F. Emmert-Streib, Z. Yang, H. Feng, S. Tripathi, M. Dehmer, An Introductory review of deep learning for prediction models with big data, Front. Artif. Intell. 4 (2020) 1–23.
[13] K. Lambers, W.B. Verschoof-van der Vaart, Q.P.J. Bourgeois, Integrating remote sensing, machine learning, and citizen science in Dutch archaeological prospection, Remote Sens. 11 (2019) 794.
[14] M. Soroush, A. Mehrtash, E. Khazraee, J.A. Ur, Deep learning in archaeological remote sensing: automated Qanat detection in the Kurdistan region of Iraq, Remote Sens. 12 (2020) 500.
[15] G.E. Hinton, S. Osindero, Y.-.W. Teh, A fast learning algorithm for deep belief nets, Neural Comput 18 (2006) 1527–1554.
[16] A. Krizhevsky, I. Sutskever, G. Hinton, ImageNet classification with deep convolutional neural networks, Proc. Adv. Neural Inf. Process. Syst. 25 (2012) 1090–1098.
[17] Y. LeCun, Y. Bengio, G. Hinton, Deep learning, Nature 521 (2015) 436–444.
[18] S. Lawrence, C.L. Giles, A.C. Tsoi, A.D. Back, Face recognition: a convolutional neural-network approach, IEEE Trans. Neural Netw. 8 (1997) 98–113.
[19] V. Nair, G.E. Hinton, Rectified linear units improve restricted Boltzmann machines, in: Proceedings of the 27th International Conference on Machine Learning (ICML-10), 2010, pp. 807–814.
[20] T. Chan, K. Jia, S. Gao, J. Lu, Z. Zeng, Y. Ma, PCANet: a simple deep learning baseline for image classification? IEEE Trans. Image Processing 24 (2015) 5017–5032.
[21] Y. Xiao, Z. Tian, J. Yu, J.X. Wu, A review of object detection based on deep learning, Multimed. Tools Appl. 79 (2020) 23729–23791.
[22] K. He, G. Gkioxari, P. Dollar, R. Girshick, Mask r-cnn, 2017, arXiv:1703.06870.
[23] N. Wang, X. Zhao, P. Zhao, Y. Zhang, Z. Zou, J. Ou, Automatic damage detection of historic masonry buildings based on mobile deep learning, Autom. Construct. 103 (2019) 53–66.
[24] Z. Zou, X. Zhao, P. Zhao, F. Qi, N. Wang, CNN-based statistics and location estimation of missing components in routine inspection of historic buildings, J. Cult. Herit. 38 (2019) 221–230.
[25] M.E. Hatır, İ. İnce, Lithology mapping of stone heritage via state-of-the-art computer vision, J. Build. Eng 34 (2021) 101921.
[26] M.E. Hatır, M. Barstuğan, İ. İnce, Deep learning-based weathering type recognition in historical stone monuments, J. Cult. Herit. 45 (2020) 193–203.
[27] C. Jeunesse, Sacrifice et partage dans l'île de Sumba (Indonésie), L'archéologue 150 (2019) 66–69.
[28] M. Devanastya, The transformation of form and discourse of identity in Sumbanese houses and settlements, in: Proceedings of the 3rd International Conference on Dwelling Form (IDWELL 2020), 2020, pp. 149–160.
[29] R.L. Adams, A. Kusumawati, The social life of tombs in West Sumba, Indonesia. In Adams, K. L., and King, S. M. (eds.), Residential Burial: A Multiregional Exploration, Archeological Papers No. 20, American Anthropological Association, Wiley, Hoboken, NJ, (2010) 17–32.
[30] C. Jeunesse, Dualist socio-political systems in South East Asia and the interpretation of late prehistoric European societies, in: Habitus? The Social Dimension of Technology and Transformation, Edited by Sławomir Kadrow & Johannes Müller, Sidestone Press Academics, Leiden, 2019, 181–213.
[31] C.I. Abdullah, J.-.P. Rampnoux, H. Bellon, R.C. Maury, R. Soeria-Atmadja, The evolution of Sumba Island (Indonesia) revisited in the light of new data on the geochronology and geochemistry of the magmatic rocks, J. Asian Earth Sci. 18 (2000) 533–546.
[32] Badan Pusat Statistik Kabupaten Sumba Timur, Kota Waingapu Dalam Angka, 2020, 128 pp.
[33] J.W. Mross, Cultural and architectural transitions of Southwestern Sumba island, Indonesia. Acs4 2000 International Conference, 260–265.
[34] Y. Koga, H. Miyazaki, R. Shibasaki, A method for vehicle detection in high-resolution satellite images that uses a region-based object detector and unsupervised domain adaptation, Remote Sens. 12 (2020) 575.
[35] A. Géron, in: Hands-On Machine Learning With Scikit-Learn and TensorFlow: Concepts, Tools, and Techniques, 2nd Ed., O'Reilly, 2019, p. 566.
[36] K.L. Masita, A.N. Hasan, T. Shongwe, Deep learning in object detection: a review, in: 2020 International Conference on Artificial Intelligence, Big Data, Computing and Data Communication Systems (icABCD), Durban, South Africa, 2020, pp. 1–11.
[37] I. Goodfellow, Y. Bengio, A. Courville, in: Deep Learning, MIT Press, 2016, p. 800.
[38] A. Gulli, A. Kapoor, S. Pal, in: Deep Learning with TensorFlow 2 and Keras: Regression, ConvNets, GANs, RNNs, NLP, and More With TensorFlow 2 and the Keras API, 2nd Edition, Packt Publishing, 2019, p. 646.
[39] A. Géron, in: Deep Learning avec Keras et TensorFlow - 2e éd. - Mise en œuvre et Cas concrets: Mise en œuvre et Cas Concrets, 2nd Ed., O'Reilly, 2020, p. 576.
[40] S. Agarwal, J.O. Du Terrail, F. Jurie, Recent advances in object detection in the age of deep convolutional neural networks, ArXiv:1809.03193.
[41] L. Liu, W. Ouyang, X. Wang, P. Fieguth, J. Chen, X. Liu, M. Pietikäinen, Deep learning for generic object detection: a survey, Int. J. Comput. Vis. 128 (2020) 261–318.
[42] J. Dai, Y. Li, K. He, J. Sun, RFCN: object detection via region based fully convolutional networks, in: NIPS, 2016, pp. 379–387.
[43] W. Liu, D. Anguelov, D. Erhan, C. Szegedy, S. Reed, SSD: single shot multibox detector, 2015, arXiv:1512.02325v2.
[44] A.N. Veeranampalayam Sivakumar, J. Li, S. Scott, E.J. Psota, A. Jhala, J.D. Luck, Y. Shi, Comparison of object detection and patch-based classification deep learning models on mid- to late-season weed detection in UAV imagery, Remote Sens. 12 (2020) 2136.
[45] T. Lin, M. Maire, S. Belongie, J. Hays, P. Perona, D. Ramanan, P. Dollár, L. Zitnick, Microsoft COCO: common objects in context, in: ECCV, 2014, pp. 740–755.
[46] S. Ren, K. He, R. Girshick, J. Sun, Faster R-CNN: towards real-time object detection with region proposal networks, in: NIPS, 2015, pp. 91–99.
[47] C. Szegedy, W. Liu, Y. Jia, P. Sermanet, S. Reed, D. Anguelov, D. Erhan, V. Vanhoucke, A. Rabinovich, Going deeper with convolutions, in: Proceedings of the IEEE Conference on Computer Vision and Pattern Recognition, 2015, pp. 1–15.
[48] K. He, X. Zhang, S. Ren, J. Sun, Deep residual learning for image recognition, in: Proceedings of the IEEE Conference on Computer Vision and Pattern Recognition, 2016, pp. 770–778.
[49] T.-.Y. Lin, P. Dollar, R. Girshick, K. He, B. Hariharan, S. Belongie, Feature pyramid networks for object detection, in: Proceedings of the IEEE Conference on Computer Vision and Pattern Recognition, 2017, pp. 2117–2125.
[50] K. Weiss, T.M. Khoshgoftaar, D. Wang, A survey of transfer learning, J. Big Data 3 (2016) 9.
[51] Y. Ren, C. Zhu, S. Xiao, Small object detection in optical remote sensing images via modified Faster R-CNN, Appl. Sci. 8 (2018) 813.
[52] J. Yan, H. Wang, M. Yan, W. Diao, X. Sun, H. Li, IoU-adaptive deformable R-CNN: make full use of IoU for multi-class object detection in remote sensing imagery, Remote Sens. 11 (2019) 286.
[53] D.M. Montserrat, Q. Lin, J. Allebach, E.J. Delp, Training object detection and recognition CNN models using data augmentation, in: IS&T International Symposium on Electronic Imaging, 2017, pp. 27–36.
[54] C. Shorten, T.M. Khoshgoftaar, A survey on image data augmentation for deep learning, J. Big Data 6 (2019) 60.
[55] J.L. Goupy, in: Methods for Experimental Design, Elsevier, 1993, p. 465.
[56] T. Lundstedt, E. Seifert, L. Abramo, B. Thelin, A. Nyström, J. Pettersen, R. Bergman, Experimental design and optimization, Chemometr. Intell. Lab. Syst. 42 (1998) 3–40.
[57] H. Rezatofighi, N. Tsoi, J. Gwak, A. Sadeghian, I. Reid, S. Savarese, Generalized intersection over union: a metric and a loss for bounding box regression, CVPR, 2019.

[58] L. Bottou, Large-Scale machine learning with stochastic gradient descent, in: Proc. COMPSTAT'2010, 345, 2010, pp. 177–186.
[59] M. Ester, H.-.P. Kriegel, J. Sander, X. Xu, A density-based algorithm for discovering clusters in large spatial databases with noise, in: Proceedings of the 2nd International Conference on Knowledge Discovery and Data Mining, 1996, pp. 226–231.
[60] M. Kulldorff, Spatial scan statistics: models, calculations, and applications. In Recent Advances on Scan Statistics (eds J. Glaz and N. Balakrishnan), Boston: Birkhauser. (1999) 303–322.
[61] N. Dalal, B. Triggs, Histograms of oriented gradients for human detection, in: International Conference on Computer Vision & Pattern Recognition (CVPR '05), San Diego, United States, Jun 2005, pp. 886–893.
[62] S. Raschka, V. Mirijalili, in: Python Machine Learning: Machine Learning and Deep Learning with Python, Scikit-Learn, and TensorFlow, 2nd Ed., Packt Publishing, 2017, p. 622.
[63] F. Pedregosa, G. Varoquaux, A. Gramfort, V. Michel, B. Thirion, O. Grisel, M. Blondel, P. Prettenhofer, R. Weiss, V. Dubourg, J. Vanderplas, A. Passos, D. Cournapeau, M. Brucher, M. Perrot, E. Duchesnay, Scikit-learn: machine learning in Python, J. Mach. Learn. Res. 12 (2011) 2825–2830.
[64] A. Denaire, C. Jeunesse, F. Monna, L. Waldvogel, Quelques remarques sur les enceintes en pierre sèche des habitats traditionnels actuels de l'île de Sumba (Indonésie), in: le phénomène des enceintes dans le Néolithique du nord-ouest de l'Europe, 33e colloque interrégional sur le Néolithique, Saint-Dié-des-Vosges, 8-9 novembre 2019, in press.

3.3. L’apprentissage automatique appliquée aux peintures rupestres

De récentes études ont démontré que les pierres à cerfs associaient gravures et peintures (Gantulga et al., 2013; Tishkin, 2013; Olkhovsky, 2005, Esin et al., 2017). Des traces de pigments rouges ont été retrouvées sur la surface de plusieurs stèles (Fig. 16). La coloration des stèles pouvait jouer deux rôles différents. Dans le premier cas, la peinture remplit les motifs déjà gravés, comme les

Fig. 16 Stèle n°24 de Tsatsyn Ereg présentant des traces de pigments à sa surface (à gauche) et une reconstitution de sa coloration originale (à droite) (d’après Esin et al., 2017).

cerfs ou les contours des armes, par exemple. Le pigment sert ici à renforcer les images. Dans le second cas, la peinture est utilisée sur des surfaces préparées et ne suit pas des motifs déjà gravés, mais dessine de nouveaux motifs, créant de nouveaux éléments dans la composition de la stèle. Malheureusement, ces traces sont généralement mal conservées et peu visibles à cause du lessivage par les agents atmosphériques. Les traces identifiées proviennent de stèles qui ont été enterrées volontairement ou qui sont tombées, ce qui les a protégés de l'altération. Une croûte de calcite est parfois présente sur les stèles, là où elles ont été en contact avec le sol. Celle-ci a pu favoriser la préservation des pigments.

Dans l'art rupestre, reconnaissance et lecture des peintures sont les prérequis pour toute étude ultérieure. Les surfaces, comme dans le cas des stèles, ont pu être lessivées ou altérées au cours du temps. Il devient alors difficile d'identifier à l'œil nu la présence de pigments sur la pierre. Néanmoins, l'introduction de la photographie numérique dans l'étude de la peinture rupestre offre de nouvelles possibilités dans la détection des pigments les plus ténus. Une image numérique 3 x 8 bits (pour un encodage RGB) peut contenir jusqu'à 16.7 millions de couleurs différentes, soit bien plus de nuances que ce que l'homme est capable de différencier à l'œil nu. La photographie numérique offre cependant la possibilité de manipuler les couleurs de l'image afin d'accentuer le contraste entre les zones peintes et non peintes, afin de révéler les pigments, puis de tracer le contour des motifs peints. Pour effectuer ces manipulations, les chercheurs se sont tournés vers différentes solutions. Certains, minoritaires, utilisent des programmes d'édition d'images, tels qu'Adobe Photoshop ® ou Gimp, mais la solution la plus répandue reste l'utilisation du logiciel Dstrech®, introduit en 2005 par Jon Harman (Harman, 2005) en tant qu'extension du logiciel de traitement d'image ImageJ (https://imagej.nih.gov/ij/). Cette extension a pour but d'enrichir la palette de couleurs de l'image en décorrélant les trois canaux RGB. Plus récemment, Rogerio-Candelera *et al.* (2011) ont également introduit un logiciel : PyDRA qui en plus de traiter l'image, inclut une classification non supervisée des pixels dans le but d'aider à la création de la documentation. Malgré leur efficacité, ces solutions présentent quelques inconvénients. Les traitements appliqués par Dstretch, ainsi que leur paramétrisation sont parfois mystérieux, et peu décrits dans la notice d'utilisation. Il devient alors difficile d'atteindre un résultat

particulier ou de le reproduire. La méthode PyDRA a l'avantage d'être bien mieux documentée, mais son application nécessite d'être familiarisé avec le langage Python. Le but de l'étude qui suit est d'introduire un logiciel exécutable de traitement d'image pour la mise en valeur des peintures rupestres : Extraction of Rock Art, *i.e.* ERA. La solution ici proposée se veut claire dans l'exposé des mathématiques appliquées, et suffisamment simple pour être utilisée par tous. Ce programme possède en outre une option de dessin automatique des motifs peints, basée sur une classification des pixels par apprentissage automatique supervisé.

Journal of Cultural Heritage 58 (2022) 91–101

Contents lists available at ScienceDirect

Journal of Cultural Heritage

journal homepage: www.elsevier.com/locate/culher

Original article

ERA: A new, fast, machine learning-based software to document rock paintings

Fabrice Monna[a,*], Tanguy Rolland[a], Jérôme Magail[b], Yury Esin[c], Benjamin Bohard[d], Anne-Caroline Allard[e], Josef Wilczek[e,f], Carmela Chateau-Smith[g]

[a] ARTEHIS, UMR CNRS 6298, Université de Bourgogne–Franche Comté, 6 Boulevard Gabriel, Bat. Gabriel, Dijon 21000, France
[b] Musée D'anthropologie Préhistorique de Monaco, 56, boulevard du Jardin exotique, MC 98000, Monaco
[c] Archaeological Research Center of the National University of Mongolia, n°202, 2nd Building, 1 Ikh Surguuli Str., Baga Toiruu, Ulaanbaatar 14200, Mongolia
[d] Cadoles, 29 bis rue de l'Arquebuse, Dijon 21000, France
[e] Centre André Chastel, UMR CNRS 8150, Faculté des Lettres de Sorbonne Université, 2, rue Vivienne, Paris 75002, France
[f] Department of Archaeology, University of Hradec Králové, Rokitanského 62, Hradec Králové 50003, Czech Republic
[g] CPTC, EA4178, Université de Bourgogne, 4, boulevard Gabriel, Dijon 21000, France

ARTICLE INFO

Article history:
Received 16 September 2021
Accepted 16 September 2022

Keywords:
Colour channel
Machine learning
Whitening transformation
Colour space
Open source

ABSTRACT

The present study proposes a new software program to help researchers identify rock paintings from digital images, rapidly producing high-quality documentation, in a user-friendly way. The three RGB colour channels of the digital image are first decorrelated and then stretched, a well-known technique used by remote-sensing specialists for over thirty years. In contrast with the approaches previously developed specifically for rock art, several data-whitening algorithms are used at this step: (regular) principal component analysis, zero-phase component analysis, Cholesky decomposition, and independent component analysis. These transformations produce different arrangements of the colour information, which nevertheless share some important properties (e.g. the covariance matrix of the new channels equals the identity matrix). The decorrelated data, previously stretched and scaled to fit the RGB space, are then converted into various colour spaces (selected from among the most popular): XYZ, HLS, HSV, LAB (CIELAB), Luv, CMY(K), YCrCb, and YUV. The most subtle colour variations will be better perceived in some of these newly produced, contrasted, false-coloured images. The researcher can then take advantage of supervised machine learning algorithms to isolate painted figures. At this step, binary pixel classification is performed either by logistic regression, support vector machine, or *k*-nearest neighbours, possibly including confident learning. There is no need for complex tuning at any point during the procedure, which lasts a few minutes at most, while *a posteriori* cleaning of the produced document is minimal. The software, written in Python, is provided as a stand-alone executable program for Windows, for broader diffusion, and as open-source code, which can therefore be adapted to the evolving needs of the community.

1. Introduction

One of the main difficulties encountered in the study of rock painting is that of clearly seeing painted patterns with the naked eye. This problem is particularly true when pigments have suffered from decay and fading over time [1]. Colour contrast between paintings and background may have almost completely vanished, so that recognition of shape, texture, contour, and position (i.e., elements essential for analysis) becomes problematic. The introduction of consumer-grade digital CMOS cameras in the late 1990s was a game-changer, as these tools rapidly became popular for the non-invasive documentation of rock paintings (see [2] for a summary of method evolution). Common 24-bit colour images produced by cameras and processed by computers are basically built from three channels: red (R), green (G), and blue (B). Each is encoded in 8 bits, resulting in 256 integers (i.e. 2^8). This colour model is commonly represented by a cube [3], where each axis is a colour channel (with integer values ranging from 0 to 255), and where black and white, respectively correspond to the (0, 0, 0) and (255, 255, 255) triplets. The additive combination of these three channels forms a palette containing 16.7 million colours. Even though this colour palette is vast enough to cover the full range of human colour perception, estimated at 10 million different colours, the close examination of a raw digital image displaying a rather homogeneous painted panel, which may, in addition, have suffered

* Corresponding author.
E-mail address: Fabrice.Monna@u-bourgogne.fr (F. Monna).

https://doi.org/10.1016/j.culher.2022.09.018
1296-2074/

from weathering, does not provide more information than a close inspection of the scene itself. Researchers have therefore taken advantage of the post-processing capabilities offered by raster graphics editors (e.g. rescaling colour, manipulating saturation, etc.) to artificially enhance the contrast between the painted figures and the background [4] (note that a similar approach that has recently been applied to rock art carving by manipulating 3D geometry in place of colour [5,6]). In 2005, the introduction by Jon Harman of DStretch® [7] led to a key breakthrough in methods for recognizing and recording painted rock art [8]. This software program benefitted from decorrelation stretching procedures previously developed by remote-sensing specialists to analyse satellite images [9,10]. Its underlying principle is quite simple: in the RGB space, colour channels tend to show high levels of correlation, so that the pixels composing the image occupy a reduced space in the RGB cube model. The goal is therefore to expand the volume of this envelope in order to artificially enhance the colour richness of the image. Such a boost is expected to facilitate differentiation of the painted parts from the background. According to the DStretch® documentation [7], the colour enhancement of the images operates in four steps. The first step relies on the decorrelation of the colour channels using a Karhunen-Loève transformation, also known as KLT or Hotelling transform, which is in fact a principal component analysis (PCA) [11], based on the covariance matrix [12], although the correlation matrix may also be used at this step [7]. The resulting variables are therefore uncorrelated in a new orthonormal basis in $\mathbb{R}^3$. The second step is stretching, which rescales each component by normalizing the variances of the eigenvectors. The third step is a rotation of the coordinate system, which brings the transformed data back into their original (RGB) vector space. At this point, the transformed RGB values, remapped on to a 0–255 range, are converted into other colour spaces, including new ones specifically designed to emphasize yellow, red, or blue/black pigments. Once the painted figures appear, they can be isolated semi-automatically using a colour-picker tool, together with an appropriate tolerance value to determine how closely the pixels composing the entire image must match the colour picked in order to be finally selected [2]. They can also be traced manually with the help of a raster or vector graphics editor, using the false-coloured image thus produced as a background layer. The DStretch® program is distributed as a plugin compiled for ImageJ, an open-source multiplatform software for image processing [13]. More recently, Rogerio-Candelera and co-workers [14] used only a PCA to produce a false-colour image with three uncorrelated bands. These bands correspond to the three principal components (PCs) obtained after shifting and rescaling the values in a range compatible with 8-bit encoding (see also [1] for an example of PCA application). As the amount of information accumulated by the PCs decreases from the first to the last component, PC1 is expected to represent most of the variation contained within the original three bands. After close examination of several experiments, both Rogerio-Candelera and co-workers [14] and Domingo and co-workers [1] concluded that the minority components PC2 and PC3 are the most informative for rock art studies. Cerrillo-Cuenca and co-workers [15] took advantage of these observations and developed PyDRA, a distributable, open-source application, which later evolved by including a finely tunable, selective intensification of saturation or intensity [16]. Interestingly, these authors also introduced unsupervised pixel classification by applying a K-means algorithm that is expected to facilitate documentation.

Although no statistical analysis has investigated how rock art specialists preferentially process images, it is reasonable to affirm that DStretch® has been extensively adopted by the community [7,17–24], while a minority of scientists use a non-standard method based on empirical image manipulation with raster graphics editors, such as Adobe Photoshop® (see [25], and references in [2]). Yet, as noted by Cerrillo-Cuenca and Sepúlveda [16], although DStretch® is generally efficient, its data treatment remains somewhat opaque. This is true not only for the decorrelation stretching phase, but also during the elaboration of new colour spaces. Numerous options are available during the workflow, but the reasons why and when they should be applied and tuned are not always sufficiently well explained. The plugin can be obtained on request from the author under a compiled form, so that any further inspection of the code requires a certain level of expertise.

The PyDRA application possesses several attractive features. Its mathematical basis is clearly described in two published papers [15,16], and the snippets written in Python 2.7 are readily available at Github (https://github.com/ecerrillo/PyDRA), under an open-source form. However, as no standalone version is provided, its use implies the installation of a Python interpreter, together with the necessary libraries, which is detrimental to dissemination among a broader audience. Furthermore, the 2.7 version of Python used for its development has now been discontinued; modifications will thus be required to run the code on the current Python version.

2. Research aim

In this study, we aim to provide the community with software (for Extraction of Rock Art, i.e. ERA), to identify rock paintings from digital images, and to produce high-quality documentation very quickly, using the information-retrieval capabilities of machine learning algorithms. Interestingly, the software is provided as a standalone executable for Windows, and as open-source snippets for Python 3.7 (and above). In contrast with previous approaches, decorrelation of the RGB channels uses four different whitening transformations. Once rescaled for 8-bit encoding, and reshaped in colour raster form, images are converted into a variety of colour spaces, selected from among those most commonly used. Optional tunings were carefully limited to a strict minimum, to simplify the process while maintaining high-level outputs. These options should efficiently counteract the deleterious effect of some particular distributions of colour channels on colour enhancement. Fundamental principles are also discussed, because a better understanding of the underlying concepts will help the researcher to optimize the production workflow from image capture to final documentation. The quality of outputs produced by supervised machine learning is evaluated.

3. Material and methods

3.1. Whitening the RGB channels

Principles. Whitening (or sphering) transformations belong to a family of methods for decorrelating and standardizing a set of variables [26]. They are applied, in our case, to enhance the colour richness of the image. An image can be seen as a data matrix, $\mathbf{X} \in \mathbb{R}^{n\times p}$, where each row, n, corresponds to a pixel, and $p = 3$ because there are three colour channels (RGB). Note, however, that pixel colour is encoded using a combination of integers. The first step is to centre the data:

$$\mathbf{X}_c = \mathbf{X} - \boldsymbol{\mu}, \tag{1}$$

where μ corresponds to the vector mean of each channel. The resulting data matrix, $\mathbf{X}_c \in \mathbb{R}^{n\times p}$, possesses a zero mean and has a covariance matrix, $\mathrm{cov}(\mathbf{X}_c) = \Sigma \in \mathbb{R}^{p\times p}$:

$$\boldsymbol{\Sigma} = \frac{1}{n-1}\mathbf{X}_c\mathbf{X}_c^{T} \tag{2}$$

with n, the number of data samples (i.e. pixels). The goal is then to find a p × p whitening matrix, namely **W**, satisfying:

$$\mathbf{Z} = \mathbf{W}\mathbf{X}_c, \tag{3}$$

with:

$$\mathrm{cov}(\mathbf{Z}) = \mathbf{I}_p, \tag{4}$$

where $\mathbf{I}_p$ is a p × p identity matrix, in other words a situation where all variables are decorrelated and possess a unit variance, and where **Z** is the new, transformed data matrix. It can be demonstrated that the expressions above are equivalent to:

$$\mathbf{W}^T\mathbf{W} = \mathbf{\Sigma}^{-1} \tag{5}$$

The **W** matrix is not unique, as any p × p orthogonal matrix **Q**, with $\mathbf{Q}^T\mathbf{Q} = \mathbf{I}_p$, produces:

$$\mathbf{W} = \mathbf{Q}\,\mathbf{\Sigma}^{-1/2}, \tag{6}$$

where the **W** matrix satisfies Eq. (5) above. Geometrically, this involves a multivariate rescaling by $\mathbf{\Sigma}^{-1/2}$, followed by a rotation by **Q**. To go further, the **W** matrix can be rewritten using the eigendecomposition of the covariance matrix, **Σ**, in the eigenvector matrix, **U**, and the eigenvalue matrix, **Λ**:

$$\mathbf{\Sigma} = \mathbf{U}\mathbf{\Lambda}\mathbf{U}^T \tag{7}$$

Eq. (6) can be rewritten as:

$$\mathbf{W} = (\mathbf{QU})\,\mathbf{\Lambda}^{-1/2}\,\mathbf{U}^T \tag{8}$$

Finally, one obtains:

$$\mathbf{Z} = \mathbf{W}\mathbf{X}_c \;=\; (\mathbf{QU})\Lambda^{-1/2}\,\mathbf{U}^T(\mathbf{X} - \boldsymbol{\mu}) \tag{9}$$

To summarize, the data, centred using their vector mean μ, are rotated by $\mathbf{U}^T$ to align with the eigenbasis, scaled by $\mathbf{\Lambda}^{-1/2}$, and (possibly) rotated again by **QU**. Note that without this final rotational step by **QU**, the data are already whitened as they are decorrelated, and each dimension possesses a unit variance.

Algorithms. The issue is therefore to find relevant configurations of **W**, and thus an appropriate value for **Q**. Five possible (natural) sphering procedures have been discussed [26]. The most common procedure, PCA whitening, simply uses $\mathbf{W} = \mathbf{\Lambda}^{-1/2}\,\mathbf{U}^T$. Note that, for PCA whitening, **W** is not unique, as **U** suffers from sign ambiguity. The ZCA whitening (aka Mahalanobis whitening, [27]) is unique and implies the use of $\mathbf{W} = \mathbf{\Sigma}^{-1/2}$; in other words, $\mathbf{Q} = \mathbf{I}_p$. In contrast with the above method, the data are rotated back by **U** to their original coordinate system. The Cholesky whitening uses Cholesky factorization, well known in numerical computation [28]. It decomposes a positive-definite matrix into the product of a lower triangular matrix and its conjugate component. Here, the precision matrix, another name for the inverse of the covariance matrix, $\mathbf{\Sigma}^{-1}$, is decomposed as: $\mathbf{\Sigma}^{-1} = \mathbf{L}\mathbf{L}^T$. In this case, the whitening matrix **W** is unique and equals $\mathbf{L}^T$. Two additional procedures were presented by Kessy and co-workers (2018) [26], which either maximally compress the original variables (PCA-cor) or are maximally similar to them (ZCA-cor). They were nevertheless discarded here, as both produced almost identical results to either PCA or ZCA whitening for all images tested. One other algorithm was considered: independent component analysis (ICA), as it was recently and successfully applied to rock paintings [29]. It starts from data whitened with PCA, which are rotated to maximize the non-gaussianity of their projection on to 3 new axes, thus producing a new space where the data are maximally independent (see [30] for more details). This transformation can be accomplished using the FastICA algorithm, here following the implementation found in [31]. As a final step, and whatever the procedure applied, the $\mathbf{Z} \in \mathbb{R}^{n\times p}$ matrix is converted into the shape of the original raster, and the values are scaled to an integer 8-bit format to fit the 0 - 255 range.

Optional further colour enhancement. Two different approaches, which are not mutually exclusive, can be applied to further enhance colour distribution. The first consists in rapidly selecting a part of the image by hand, taking care to focus on the area of interest. The vector $\boldsymbol{\mu}$ and the **Σ** and **W** matrices are computed from this subset of selected pixels, $\mathbf{X}_S$, and upon this basis **Z** is drawn for the entire image. Importantly, the remapping of **Z** in 8 bits takes into account the minimum and maximum values found in the subset, and not in the entire image, which is subsequently clipped of its values below 0 or above 255. The second approach consists in a linear contrast stretching with saturation, also known as percentage linear contrast stretch [32], where **Z** is rescaled to include all values that fall within an interval corresponding to the $(\alpha/2)^{th}$ and $(100\text{-}\alpha/2)^{th}$ percentiles (with α configurable).

3.2. Converting the whitened data to other colour spaces

The four resulting images (one for each whitening procedure) are then converted into each of the eight following colour spaces: XYZ, HLS, HSV, LAB (i.e. CIE L*a*b), Luv (i.e. CIE L*u*v), CMY(K), YCrCb, and YUV, which were specifically chosen as they are among those most commonly used. Describing each of these colour spaces and their respective properties is outside the scope of the present study, but the reader will find this information in the vast specialized literature (e.g. [33,34]), while the mathematical description of the transformations performed by OpenCV is available at https://docs.opencv.org/3.4/de/d25/imgproc_color_conversions.html. As a result, 36 colour images are produced: 4 whitening procedures × 9 colour spaces (i.e. one whitened RGB image plus its conversion into 8 other colour spaces). The reason for this abundance is to supply a large set of false-coloured images, through which the operator can easily navigate to identify the painted areas, without any fastidious manual tuning.

3.3. Machine learning for the automatic delineation of painted areas

Underlying idea. The integration of machine learning aims to produce documentation close to the best standards of publication, with minimum intervention by the operator. Rather than the unsupervised method previously applied [16], a supervised approach was preferred here, because the operator can train the model very specifically to fit the desired objective [35]. Note that Lerma [36] previously tested a similar form of supervised classification, taking as feature input the three visible spectral bands of an image plus one near infrared. In the present study, a simple binary classification (painted *vs* non-painted) is presented first, while situations with multi-coloured paintings will be discussed later.

Supervision. This step consists in labelling two classes: pixels belonging to the painted areas, and those belonging to the substrate. Ideally, supervision should be at pixel level to minimize the risk of erroneous labelling [37]. This pixel-wise task would be quite tedious, particularly since good representativity is sought. Consequently, supervision is performed by drawing two groups of curves (of adjustable thickness) on the image, each at best corresponding to one class. However, such rough-and-ready supervision will inevitably lead to some errors (i.e. pixels erroneously included in both classes).

Additional feature engineering and feature selection. To each pixel coordinate corresponds a vector containing 108 values (36 images × 3 colour channels). Processing this entire dataset as input is certainly not the best option, as it includes variables without any discriminating power (i.e., channels where no difference can be noticed between painted areas and substrate). It would considerably slow down the training and prediction phases, and might even have a deleterious effect on output quality. Automatic preselection therefore retains the *n* most discriminating variables, possessing the *n* highest values of the *t*-statistic (*n* is configurable, with $n = 30$ channels as default value). It is worth mentioning that even if the distribution within each group is non-normal, variable-by-variable, the two-sample *t*-test can be used at this step, as the central limit theorem applies when sampling is sufficiently large

[38]. Using thick curves for supervision will always produce thousands of labelled pixels. The n variables thus retained are nevertheless strongly correlated, so that a PCA must be performed. This reduces the number of (decorrelated) principal components to m ($m<n$), allowing the total variance to be expressed at a given level (also configurable by the operator, with 97% as default value).

Algorithms. At this point, the aim is to build a mathematical model (i.e. a decision rule) allowing binary pixel classification. In other words, the two categories: y_c, (with $c \in \{0;1\}$ for background and painted pixels, respectively) must be predicted from $\mathbf{x}$, a vector describing the set of m previously built features, $\mathbf{x} = \{PC_1,...,PC_m\}$. There are several different techniques for solving such a classification problem, among them naïve Bayes, k-nearest neighbours, logistic regression, linear and quadratic discriminant analysis, artificial neural network, and random forest, to cite only the most popular. They can also be combined using voting classifiers. Many competitions open to both researchers and enthusiasts seek to find the technique producing the highest performance for a specific problem, using a given dataset. The winning workflow generally involves complex algorithms, fine hyperparameter tuning, and heavy calculation load. Even though its performance will formally surpass that of more classical algorithms, the gain is often modest. Here, the idea is not to find the best algorithm through a long and complex optimization process (as manual cleaning of the resulting image will undoubtedly be necessary at the end), but to provide good results quickly. This is particularly true in our case, since the best algorithm is likely to vary with the dataset (i.e. the image processed) and the choices made by the operator during supervision. For these reasons, only three of the simplest approaches are implemented in the software: logistic regression (LR), support-vector machine (SVM), and k-nearest neighbours (KNN).

For logistic regression, a new variable, z, is built from a linear combination of weights, $\mathbf{w}$, and sample features: $z = \mathbf{w}^T\mathbf{x}$. The probability of belonging to a particular class is provided by the logistic sigmoid function: $\Phi(z) = 1/(1+e^{-z})$, with $\Phi(z) \in [0;1]$; weights are optimized using the L-BFGS algorithm; regularisation is operated using an L2 penality. The support-vector machine algorithm aims to maximize the margin between the decision boundary hyperplane and the closest training samples with the goal of separating the two classes. The SVM can also manage data that are not linearly separable using the so-called "kernel trick", which transforms the data into a higher dimensional space. Here, a radial basis function (RBF) is applied. The algorithm provides the probabilities of belonging to each class. Finally, the KNN algorithm is a non-parametric machine learning technique, which determines the k-nearest neighbours (here k= 31) and simply assigns a class after majority voting.

For more details about these methods, the reader is invited to refer to the abundant specialized literature, e.g. [39–41]. Once the classifier is trained, in other words once the mapping function $f(\mathbf{x}) \rightarrow y_c$ is optimized, the model is applied to the entire image, and predictions are made for each of the pixels composing the image to identify its class: background or painted pixel? For the sake of speed, the traditional split into training and test datasets (the first used to train the model, and the second for performance evaluation), possibly including a grid search for hyperparameters, was not applied. Since the supervised dataset is very large and the complexity of classifiers low, models do not suffer from overfitting, and thus, from difficulties in successfully generalizing to unseen data [42]. Assessing performance scores would also be pointless in our case, since outputs are visually evaluated. By default, the LR model is applied to the entire set of supervised pixels. This model generally produces good results quite quickly. Its outputs may thus rapidly provide valuable information about how the operator could improve final documentation quality: e.g., by increasing the number of supervised pixels, thus focusing on a specific area of the image, or by changing the default settings used for feature engineering (e.g., number of best channels retained, variance expressed by PCs, etc.).

Confident learning. Recent methods have been specifically developed to identify potential noise in the labelling mentioned above, and to integrate dealing with this common issue into the learning process (see [43] for more details). Noisy data are pruned using probabilistic thresholds, the level of noise is estimated, and examples to train the models are ranked with confidence. This confident learning approach is integrated into the ERA software to complement the more conventional learning processes.

Image blurring. In the output images, a few pixels may erroneously stray beyond the segmentation borders of painted areas. Applying a Gaussian blur to images may help to eliminate such false positives, by smoothing out image noise, but at the expense of detail. By default, a square 5 × 5 px kernel is applied, but its size can be modified.

3.4. Practical implementation

The pixel envelope volume within the RGB cube was calculated using the free R programming language (https://www.r-project.org/), with the tiff, misc3d, oce, and RGL libraries, using a three-dimension kernel density estimate, with a cut-off of 99.9%. The ERA software itself is written in Python 3.7, with the numpy, scipy, scikit-learn, qimage2ndarray (https://github.com/hmeine/qimage2ndarray), OpenCV, and PyQt5 (or PySide) libraries, together with the whiten function (modified after https://gist.github.com/joelouismarino/ce239b5601fff2698895f48003f7464b). It is made available, together with a standalone executable version for Windows, as Supplementary Material SM1, at the following internet address: https://gitlab.huma-num.fr/fmonna/era-extraction-from-rock-art/-/tree/Paper_Supp_Mat. Fig. 1 depicts the layout of the page dedicated to data preparation. General principles, options, and workflow are discussed in detail below, and in the accompanying user manual, included in Supplementary Material SM1.

3.5. Visual evaluation

During the elaboration of the ERA software, dozens of images were processed. Outputs were evaluated visually, by rock art experts, based on the time required in post-processing to attain the highest standards of archaeological documentation.

4. Results and discussion

4.1. Basic workflow

The rock art painting used here as the first example belongs to the Okunev culture, which existed in the South Siberian steppe during the Bronze Age (2600–1800 BC). It represents the face of a deity on a brownish rock, with orange lichen colonizing some parts of the surface, and dark cracks. The image (3888 × 2592 px, saved in high-quality JPG format) was captured at Tarpig Mountain, as orthogonally as possible to the panel surface, using a DSLR CANON EOS 400D camera (Fig. 2a). The 3 channels composing the image are strongly inter-correlated, as illustrated by their projection in the RGB cube (Fig. 2a). The envelope of the input picture occupies only about 7% of the full RGB colour space, explaining why the image appears so homogeneous. When whitening is applied, the envelope increases considerably, occupying more than 21% of the cube, whatever the procedure (Fig. 2b), with slight differences because stretching is performed after the rotational step. Colour richness is basically the same in all cases, but the resulting images are not all equally useful to identify the painted areas.

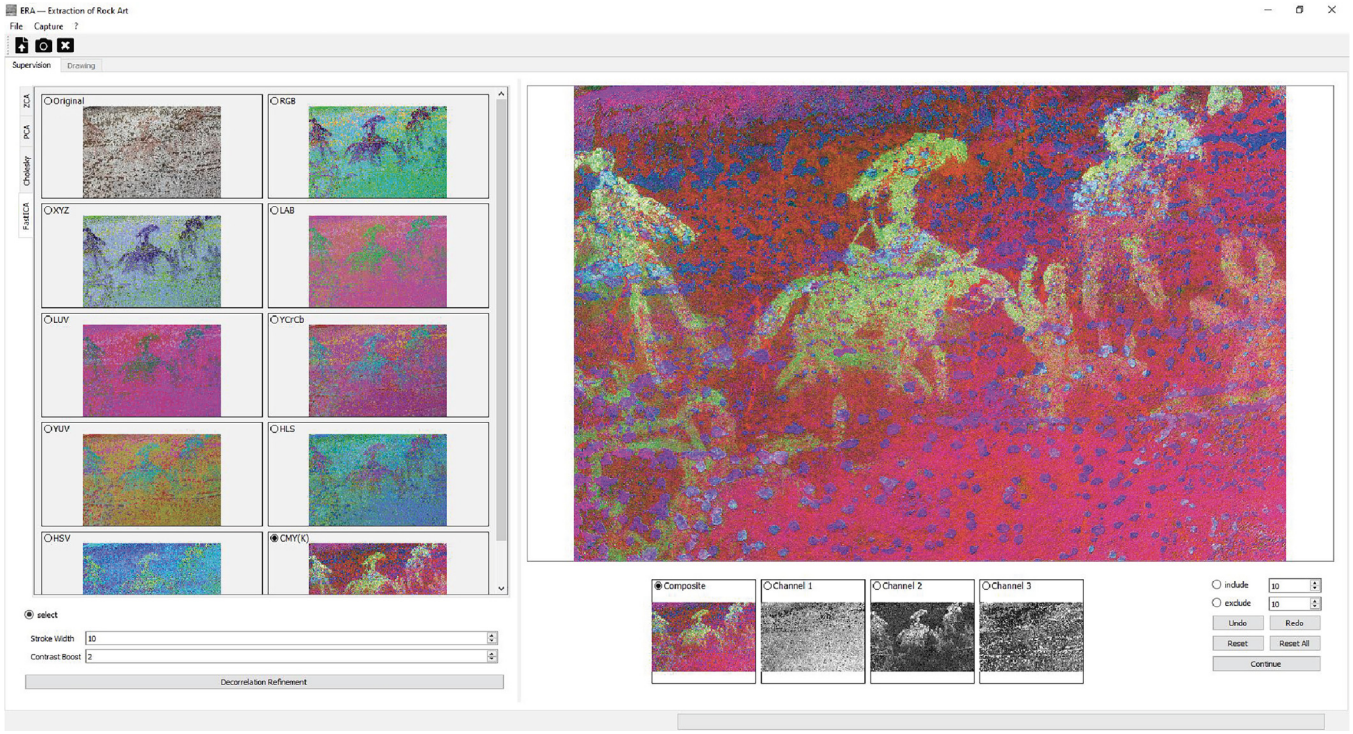

Fig. 1. Layout of the ERA software. The processed image represents several images of the Xiongnu - Xianbei period; in the middle, a rider with an eagle over an earlier image of an animal in a different shade of red (original colour). The image was captured at Kavkazskoe, South Siberia, Russia.

Here, the Cholesky and FastICA transforms seem to be the most appropriate. Note that FastICA produces results visually different at each run, due to its stochastic nature, but that the data structure remains unchanged (i.e. the three channels are sometimes rearranged and/or the values reversed). Interestingly, Cerrillo Cuenca and co-workers (2021) reported that decorrelation by FastICA often isolates paintings more sharply than PCA, probably because ICA seeks to separate superimposed components, while principal components are computed in order, according to the amount of variation they represent [29]. After colour conversion, the operator can rapidly identify the best colour image(s) and/or one specific grey channel by toggling between images, and can also supervise pixel labelling, with black for painted areas, and red for background (Fig. 2c). Features corresponding to the values of supervised pixels for each channel are extracted, the best channels are identified and selected, PCA is computed, and the machine learning model is trained. For the Okunev painting, applying the trained LR model to the entire set of pixels composing the image produces good results. The painted areas are emphasized in black or in their true colour with no (i.e. white) background, or in black on the original colour image (Fig. 2d). Another output is systematically produced using confident learning (not shown in Fig. 2). Most of the time, no great difference was observed between results with or without confident learning. In some situations, however, confident learning clearly produced better results, probably because the training set contained too many mislabelled pixels. During these tests, it was also noticed that the slower KNN model generally produced outputs similar to LR. The SVM model often provided outputs with a little bit less noise, but such improvements require more computation time (several minutes may be necessary). As each image possesses its own characteristics, the final choices are left to the researcher's appreciation, based on visual evaluation by the expert, for more versatility. The default parameters are nonetheless appropriate as a first guess, in most situations.

4.2. Optional colour enhancement

Depending on the distribution of the input pixels, the beneficial effect of the sphering transformation described above may be modest. Just a handful of pixels falling close to the corners or the edges of the RGB cube (unrelated to the painted area) would be sufficient to impair the colour enhancement of the entire image. The presence of outliers may have a drastic impact on the mean, the covariance matrix, and thus subsequently on the PCA transformation, but above all on the final rescaling in 8-bit format, which linearly remaps the **Z** matrix by making the minimum value coincide with 0, and the maximum with 255.

The Okunev painting from the Tarpig Mountain is used again here to show the effect of the two options available for further colour enhancement (Fig. 3), in comparison with the default processing depicted in Fig. 3a, all using the Cholesky whitening procedure. For subset-based enhancement, the operator needs to manually select areas covering both the painted areas and the substrate around the figure of interest (Fig. 3b). In other words, the orange lichen growing on the rock must be set aside, as must the cracks and vegetation behind the painted panel. As whitening and stretching parameters applied to the entire image are computed on the basis of this selection alone, the influence of troublesome elements in the rest of the image is somewhat minimized. Consequently, the pixels occupy a larger volume, ~33% of the RGB cube (versus ~23% for default processing). The painted figure is slightly better identified (Fig. 3b). However, although manual selection was performed carefully, some pixels were incorrectly included (e.g., tiny patches of lichen), and the contrast between the figure and its substrate is not optimally increased. Contrast boosting using linear stretching with saturation produces a much better output, at least in this example (Fig. 3c). With $\alpha = 2\%$, the deleterious effects of (outlier) pixels below the 1st and above the 99th percentiles are removed within each RGB channel. Since these troublesome pix-

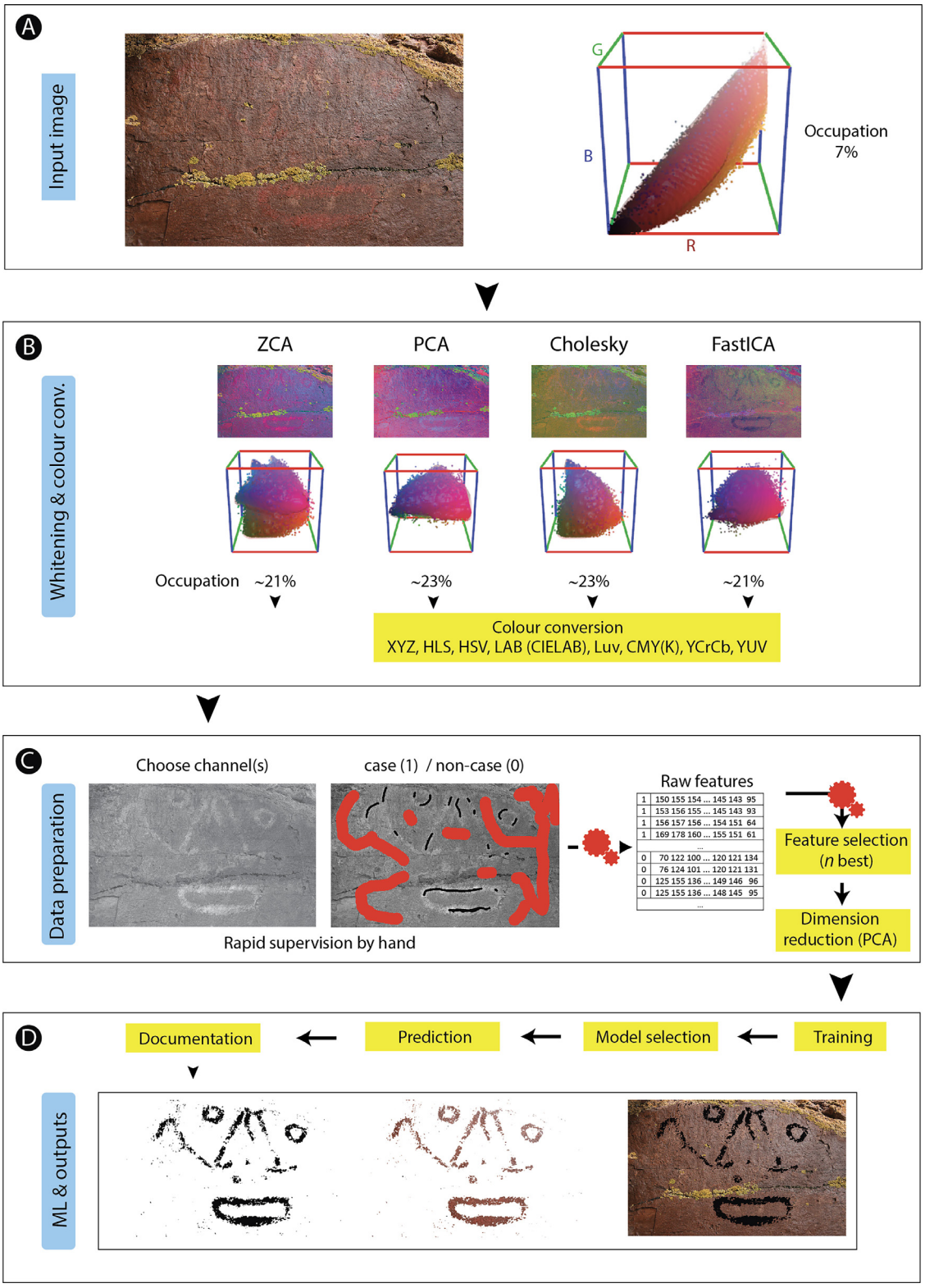

Fig. 2. Typical workflow with the ERA software. (a) Original image of an early Bronze Age rock painting from Tarpig Mountain (South Siberia, Russia), and the position of the pixels composing the image in the RGB cube; (b) whitening and colour conversion step, with the projection of pixels in the RGB colour space; (c) data preparation, including selection of one or several channels from which the supervision is operated; manual supervision on the image (painted areas in black, and substrate/background in red); feature engineering; (d) training, prediction, and production of the final documentation. Occupation, expressed as a percentage, represents the part of the RGB cube filled with image pixels.

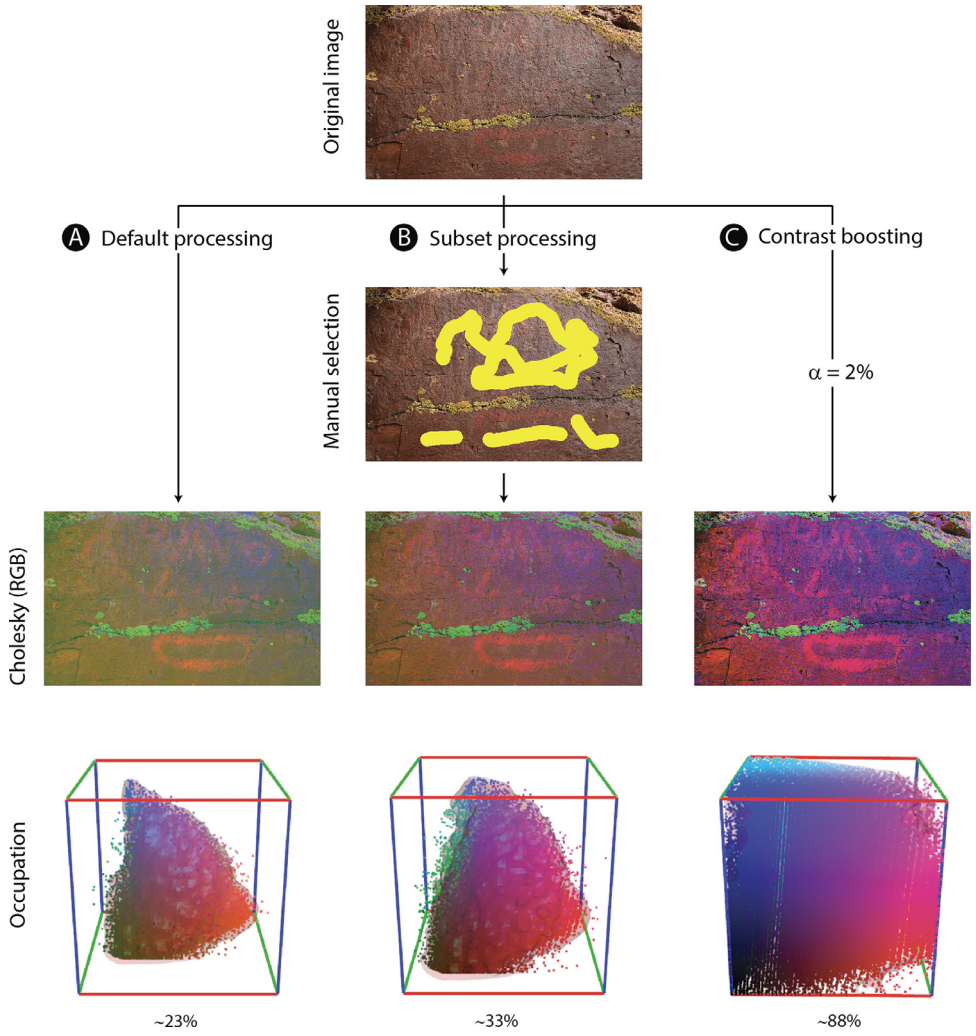

Fig. 3. The effect of optional further colour enhancement compared to the standard procedure. (a) default settings; (b) manual selection of pixels on which whitening parameters are computed; (c) contrast boosting by linear stretching with saturation. For each processing method, the resulting projection of the pixels in the RGB cube is provided, as well as the volume of their envelope, expressed as a percentage of the whole.

els are not very numerous, $\alpha = 2\%$ is sufficient to increase the pixel envelope in the RGB cube to 88%. The figure can then be seen much more clearly (Fig. 3c).

A synthetic image was constructed to investigate which colour enhancement method should be applied in a challenging context, where extraneous elements are included in the scene (Fig. 4a, left). The background was first filled with a pinkish RGB colour, set to (155, 85, 102). Two texts written in similar colours were then added in the foreground: 'ERA' in the bottom left using (151, 90, 100), and 'Rock Art' in the top right using (155, 86, 105). Noise was then added to the image to mask the contours of the letters, making the texts barely or even not at all distinguishable, especially for 'Rock Art', where the colour is very close to that of the background. Finally, four uniform relatively large rectangles were also added to mimic the possible presence of lichen (yellow), shadows (black), and bird droppings (whitish) on the rock substrate, or the inclusion of some sky (light blue) in the image. Note that such a configuration also takes into account the possible presence of a black and white scale, often integrated in field photographs. The pixels constituting the original image only take up ca. 1% of the RGB cube (Fig. 4a, left). The situation does not improve with the default processing, because the presence of the four coloured rectangles ruins the effect of the whitening procedure (Fig. 4b, left). The text 'ERA' is however distinguishable in several channels (e.g., the HSV channel 2 after Cholesky whitening; Fig. 4b, right), making manual supervision and extraction of the text possible, with only a low amount of noise. The 'Rock Art' text cannot be perceived. The same observations are made when linear stretching with saturation is applied. In fact, $\alpha = 2\%$ is not sufficient to remove the deleterious influence of the coloured rectangles, which cover too large a part of the image (Fig. 4c). Increasing α would be tempting, but not appropriate, since this would lead to saturation (and loss of information) of the pinkish pixels falling close to the cube edge, which remain of interest. Operating whitening from only a selected subset of pixels within the pinkish area is the best choice here. The pixel volume within the RGB cube increases dramatically to $\sim$ 59% (Fig. 4d, left), 'ERA' is better seen, and interestingly, 'Rock Art' becomes visible on several channels (Fig. 4d, right). Extracting both inscriptions is straightforward, using two separate supervisions (one for each text): 'ERA' is isolated with the same level of precision as previously, while 'Rock Art' is now clearly visible, together with an unavoidable amount of noise, due to the colour proximity of the text with the background. Both isolated inscriptions can then be combined (e.g., in false colour) in a single image using a raster graphics editor (Fig. 4d, right). Superimposition of figures of different colours, such as those described in [44], can therefore be tackled with the ERA software by processing each painting independently.

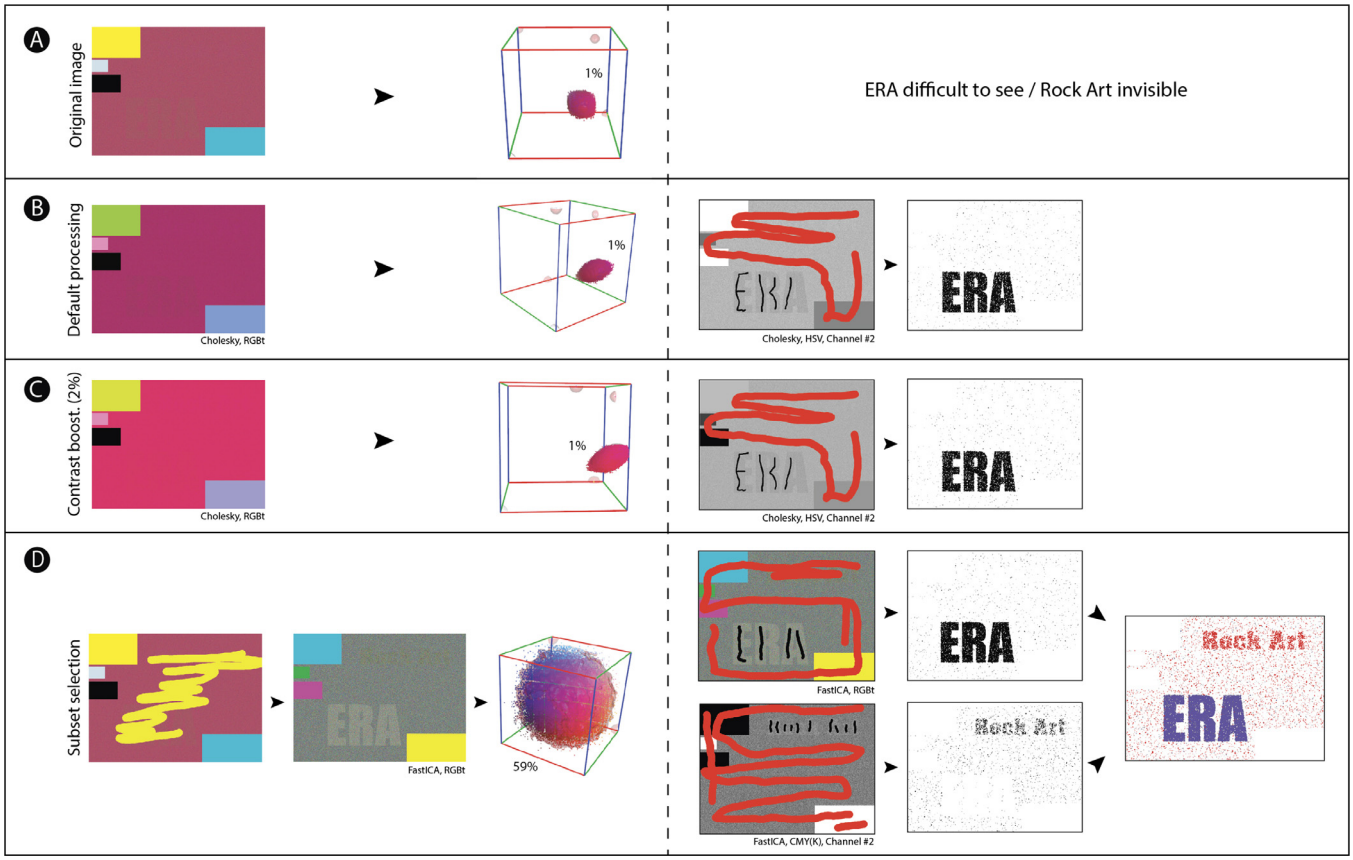

Fig. 4. Colour enhancement of a synthetically produced image, with extraneous elements. (a) the original image and its pixels in the RBG cube (text barely visible or completely invisible); (b) default processing (left); 'ERA' is visible and can be extracted by supervised machine learning algorithm (right); (c) contrast boosting (2%, left), and subsequent extraction of 'ERA' (right); (d) subset selection of pixels (left), and extraction of 'ERA' and 'Rock Art' by two different supervisions (right). The values, expressed as a percentage of the RGB cube, represent the volume of the pixel envelope.

4.3. Guidelines for fast and efficient processing

The aim here is not to offer a recipe that could be used in all circumstances, but rather to provide general guidelines to help the researcher obtain the most appropriate results rapidly. During the shooting step, care should be taken to seek the most homogeneous lighting for the scene, because the whitening procedure will be much more efficient in such a situation. Following the same principle, a colour chart, a scale, or anything that has nothing to do with the area to be treated should not be included in the image; such elements introduce outlier pixels. As an example, Fig. 5a was captured at the Shalabolino rock art site, South Siberia, Russia. This rock painting depicts a human-like face, with an oblique cross between eyes and mouth, which overlies a pre-existing rock carving representing a bovid animal. Fig. 5b demonstrates how the presence of a colour chart, which by nature integrates a large spectrum of colours, can ruin any colour enhancement of the painted panel, to such an extent that the original RGB photograph is more informative than the processed version. In such a case, the best choice is to focus on the area of interest, trying to eliminate any worrying elements, as in Fig. 5c. Unfortunately, it was not possible to eliminate the dark area behind the targeted substrate without cropping part of the painted zone. A subset of pixels was therefore selected, as well as contrast boosting, with α set to 1% (Fig. 5d). The face is clearly seen, for example with the ZCA whitening, transformed into the CMY(K) colour space (cf. Fig. 5e). Switching from one channel to another (e.g., those displayed in Fig. 5f–g) will avoid misinterpreting the painted parts and the background during the supervision phase (Fig. 5h). The result is obtained within seconds (Fig. 5i). Unfortunately, it is difficult to compare this black and white output with that obtained with DStretch® and an associated raster graphics editor, as the rendered quality depends in great part on the operator's skill in tuning the numerous settings of the DStretch® software, but also in handling the colour picker tool and its associated tolerance value to produce the final binary picture. The face will be as clearly visible with DStretch® (especially with the YRE colour space) as with ERA. However, despite several attempts to isolate the painted figure, the level of noise with DStretch® remained much higher than that observed with ERA. This result is probably due to the use of a single channel, or at best a combination of three (if working on a colour image), whereas ERA applies its machine learning algorithms to an array containing a very large set of carefully selected channels. With PyDRA, the problem is rather that classification is unsupervised, so that models are not designed for tasks as specific as those requiring supervision.

5. Limitations

Poor-quality JPEG images should be avoided whenever possible. It is well known that this popular lossy compression, based on a block-coding scheme, introduces visible artefacts in pixels and at block boundaries, together with notable loss of detail in lowly contrasted, homogeneous areas [45]. These artefacts will appear on several channels after processing, undoubtedly reducing recognition. Ideally, the photographs should therefore be captured in RAW format, and later saved in uncompressed TIF format before processing. If this is not possible for any reason, a high-quality camera should be used, and the photographs should be saved in the

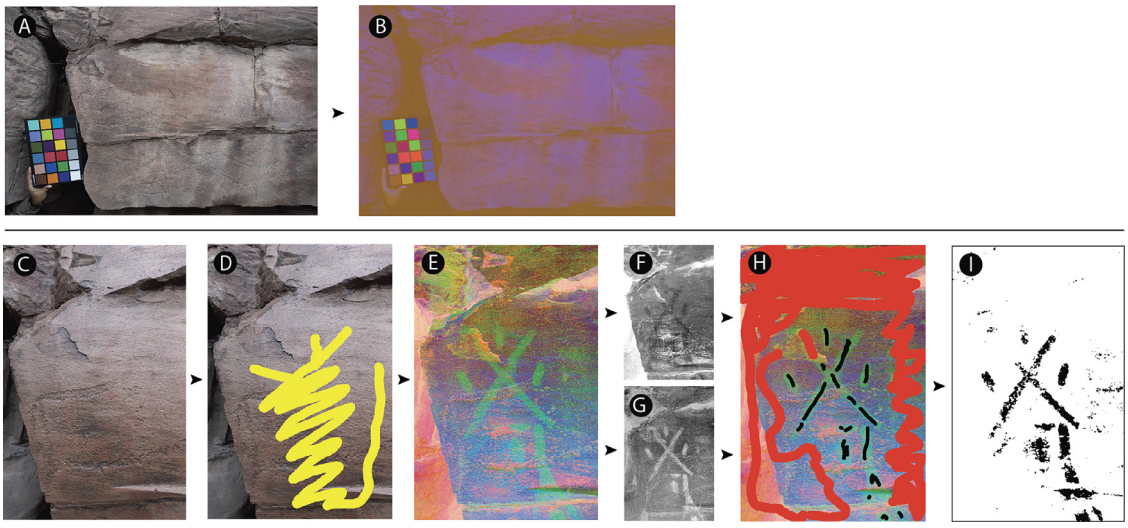

Fig. 5. Processing early Bronze Age rock art paintings from the Shalabolino site, South Siberia, Russia. Pictures were captured in RAW format with a SONY RX100M3, resized to 1500 px for the largest side and saved in TIF format, before processing. (a) extended view of a painted panel, including an X-RITE colour chart, and (b) its processing (Cholesky whitening, RGB); (c) a new picture, taken closer to the rock, avoiding troublesome elements; (d) pixels manually selected, from which the whitening parameters are computed, and (e) then applied to the whole image (ZCA whitening, CMY(K)); the two first channels of this colour image (f,g) are used for supervision (h); the final output using logistic regression (i).

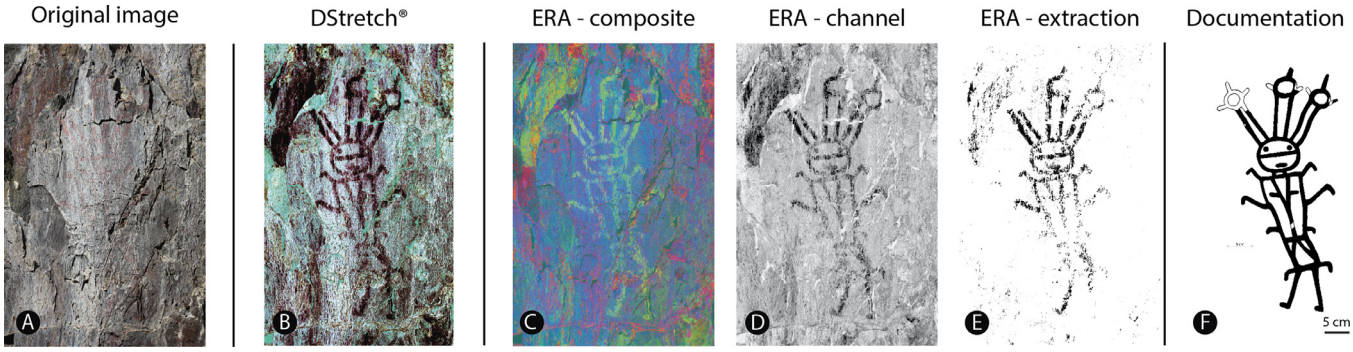

Fig. 6. Processing of an image representing an early Bronze Age human figure. It was captured with a Canon EOS 5D Mark II, at Oya river, South Siberia, Russia. The original picture was 3744 × 5616 px in size and was saved in high-quality JPEG format. For further treatment, it was rescaled to 2000 × 3000 px. (a) original image; (b) DStretch® processing with the YRE colour space; (c) false-coloured image produced by ERA using Cholesky decomposition and YCrCb colour space; (d) channel 1 of the CMY(K) colour space after Cholesky decomposition by ERA; (e) attempt to extract the figure after supervision with the LR algorithm of ERA; (f) final documentation produced manually from ERA outputs. ERA images were produced with a contrast boost of 2%.

highest possible JPEG quality. The ERA software is not demanding in terms of computational resources, since it can run on a consumer-grade computer, delivering outputs within seconds, or at most within a few minutes. Depending on the amount of memory installed, however, resizing very large pictures may be necessary, as more than 100 one-channel images are produced from a single RGB photograph.

The ERA software cannot accomplish miracles: results will depend above all on the degree of pigment alteration. Elements lost over the course of time will never be recoverable. The machine does not seek to replace the expert eye, as many crucial choices must still be made, in particular in terms of interpretation, and hence in the supervision, cleaning, and adjustments of the outputs. For example, when applying machine learning, one should be aware that the quality of the training set used for supervision is of vital importance: it must be truly representative of the whole, as otherwise the classification results will be poor. The noise present on the final documentation can be reduced by manual cleaning, or by increasing the blur radius, but at the price of lower recognition of the pixels composing the painted figure. Note that extraction by machine learning is always an optional step. The operator will often encounter situations where pigments have almost completely or partially faded, or where superimpositions are so complex that machine learning algorithms implemented in ERA will provide improper or incomplete results. In such cases, documentation can still be prepared with a raster/vector graphics editor, from an appropriate selection of RGB images or individual channels produced by ERA, perhaps by manually completing or cleaning the images. To illustrate such situations, two additional examples are reported, where ERA partly fails to produce adequate documentation by machine learning extraction. The first concerns an early Bronze Age human figure captured at Oya, South Siberia, Russia (Fig. 6). On the original image, the figure is almost invisible (Fig. 6a). Both DStretch® and ERA succeeded in enlightening the painted parts (Fig. 6b, c); they become even clearer when an appropriate single ERA channel is selected (e.g. channel 1 of the CMY(K) colour space after Cholesky decomposition, Fig. 6d). Unfortunately, painting has to some extent vanished over time and most of the pixels composing the figure are disconnected, so that the training set contains too many mislabelled pixels. As a result, the extraction is only partial (Fig. 6e), unusable for the final documentation, which must be performed by manual tracing (Fig. 6f). The second example is an image representing a part of a herd, captured in Oued In Djaren, Tadrat region, Tassili N'Ajjer National Park, Al-

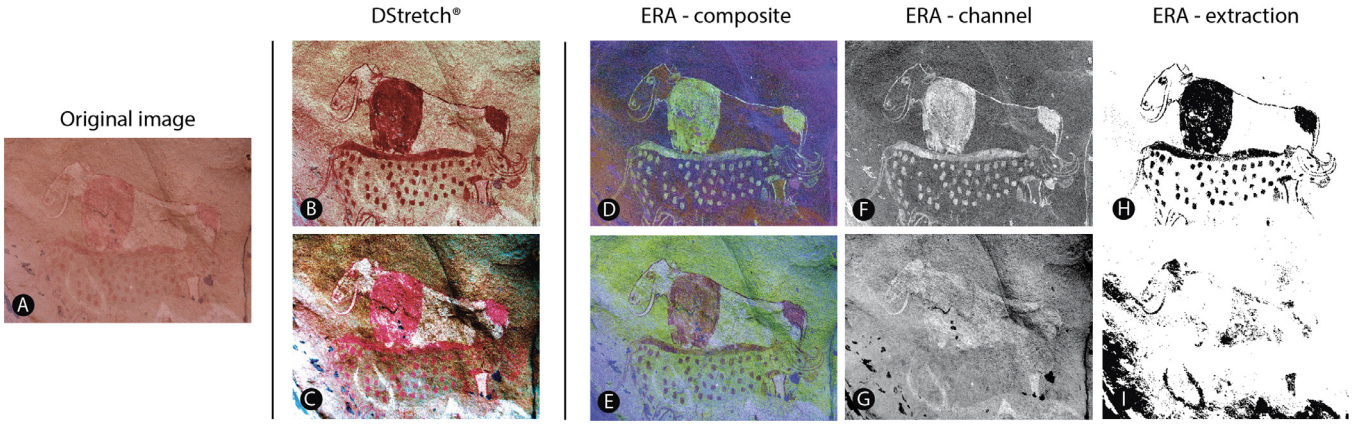

Fig. 7. Processing of an image representing a part of a herd, Oued In Djaren, Tadrat region, Tassili N'Ajjer National Park, Algeria. The picture captured with a SONY DSC-F828 in RAW format, at a resolution of 3264 × 2448 px, was converted into TIF. (a) original image; (b) DStretch® processing with the YRE colour space; (c) DStretch® processing with the LWE colour space; (d) false-coloured image produced by ERA using FastICA and XYZ colour space; (e) false-coloured image produced by ERA using FastICA and CMY(K) colour space; (f) channel 2 of the CMY(K) colour space after ZCA decorrelation by ERA; (g) channel 3 of the CMY(K) colour space after FastICA decomposition by ERA; (h) extraction of parts of the figures after supervision with the LR algorithm; (i) attempt to extract the bovid in the foreground after supervision with the LR algorithm. ERA images were produced with a contrast boost of 2%.

geria (Fig. 7). Three bovids organized on three distinct planes are distinguishable in some way on the original image (Fig. 7a). Again, processing by both DStretch® and ERA allows the figures to be much more clearly recognised. This is true for the YRE option of DStretch® (Fig. 7b) and the combination FastICA and XYZ colour space of ERA (Fig. 7d), for the two bovids in the background. The bovid present in the foreground is visible with the LWE option of DStretch® (Fig. 7c), as well as with the combination FastICA and CMY(K) colour space of ERA, which interestingly also marks the two other bovids. At least two groups of tints, reddish and whitish, with different shades, are present on this panel. The bovid in the foreground is whitish, the one in the middle is reddish, and the one in the background is composed of both tints. Using channel 2 of the CMY(K) colour space after ZCA decorrelation (Fig. 7f) for supervision, the reddish painting can be successfully extracted by machine learning (Fig. 7h). Note that the contours of the animals are well marked, even if they are thin. The whitish bovid in the foreground and inner parts of the one in the background are reasonably well rendered using channel 3 of the CMY(K) colour space after FastICA decomposition (Fig. 7g), but the automatic extraction of these areas falls short, except for one leg of the bovid in the background and parts of the bovid body in the foreground, where the whitish areas are very pronounced. This poor result comes with a number of undesired pixels. In such complex circumstances, when figures have partly and irregularly faded, when they overlap, and/or when they are drawn with different pigments, manual tracing from images produced by ERA remains a possible solution.

6. Conclusions

We demonstrate that the ERA software can be used easily, rapidly, and efficiently to identify painted areas in a rock art context presenting various colour schemes. The principles of whitening procedures that enhance colour are described comprehensively, as are the two options for boosting contrast between paintings and substrate. Tuning options are limited, to facilitate the integration of ERA in a routine workflow by researchers unfamiliar with image processing. The ERA software is made freely available in a compiled, straightforwardly executable version for Windows, and as an open-source Python snippet for those who want to improve the code (for example by integrating the unsupervised PyDRA procedure), or simply for those who desire complementary information about calculations. Interestingly, the Python version also runs on Android, provided that a Python IDE (such as Pydroid 3, available on Google Play) and appropriate libraries are installed. Tests performed with a Samsung S5e tablet were conclusive. The images were processed quickly without any issues related to memory limitation, which can be a decisive asset in the field. Guidelines follow easy-to-understand principles, even without extensive knowledge of linear algebra, because they mainly rely on visual inspection and analysis of the elements composing the scene. Machine learning algorithms act as a background process, taking as input features a large set of channels, and not merely three (for RGB colour images), or even only one (for greyscale images). This is why the models trained by rough-and-ready supervision are often so efficient at producing documentation close to current standards in archaeology, with a low amount of noise (depending, of course, on the preservation of the painting and the quality of the training set used for supervision). In any case, if machine learning extraction of rock painting fails, manual tracing from images produced by ERA remains a potential option. Interestingly, panoramas or orthomosaics produced by photogrammetry can be seamlessly processed by ERA. Nothing prevents the integration of enhanced images produced by ERA into a photogrammetrical workflow to tackle the question of the relationship between rock art and rock surface, as previously proposed [46]. Finally, for the sake of traceability, it is advised to report details concerning the workflow applied and, if possible, to make available the original set of images used to produce the documentation. Such good practices would not only allow researchers to replicate the entire process, but also to compare existing and future technical solutions seeking to bring to light rock paintings.

Appendix A. Supplementary data

Supplementary material related to this article can be found, at https://gitlab.huma-num.fr/fmonna/era-extraction-from-rock-art/-/tree/Paper_Supp_Mat.

Acknowledgements

This research was funded by the Joint mission Mongolia – Monaco and the project ROSAS (uB-FC and RNMSH), and by the Observatoire des Patrimoines Sorbonne Université (A.-C. A. Ph.D. grant). We are grateful for comments by the anonymous reviewers, which have greatly improved the manuscript.

Supplementary materials

Supplementary material associated with this article can be found, in the online version, at doi:10.1016/j.culher.2022.09.018. https://gitlab.huma-num.fr/fmonna/era-extraction-from-rock-art/-/tree/Paper_Supp_Mat.

References

[1] I. Domingo, B. Carrión, S. Blanco, J.L. Lerma, Evaluating conventional and advanced visible image enhancement solutions to produce digital tracings at el Carche rock art shelter, DAACH 2 (2015) 79–88.
[2] I.D. Sanz, Rock art recording methods: from traditional to digital, in: C. Smith (Ed.), Encyclopedia of Global Archaeology, Springer, New York, 2014.
[3] W. Burger, M.J. Burge, in: Digital Image Processing: An Algorithmic Introduction Using Java, Springer, 2016, p. 811.
[4] L.M. Brady, Documenting and analyzing rock paintings from Torres Strait, NE Australia, with digital photography and computer image enhancement, J. Field Archaeol. 31 (2006) 363–379.
[5] C. Horn, O. Ivarsson, C. Lindhé, R. Potter, A. Green, J. Ling, Artificial intelligence, 3D documentation, and rock art – approaching and reflecting on the automation of identification and classification of rock art images, J. Archaeol. Method Theory 29 (2022) 188–213.
[6] T. Rolland, F. Monna, J.F. Buoncristiani, J. Magail, Y. Esin, B. Bohard, C. Chateau–Smith, Volumetric obscurance as a new tool to better visualize relief from digital elevation model, Remote Sens. 14 (2022) 941.
[7] J. Harman, 2008. DStretch Algorithm description. Available at http://www.dstretch.com/ (Accessed 30 June 2021).
[8] N. Cortón Noya, Á. López García, F. Carrera Ramírez, Combining photogrammetry and photographic enhancement techniques for the recording of megalithic art in north-west Iberia, DAACH 2 (2015) 89–101.
[9] A.R. Gillespie, A.B. Kahle, R.E. Walker, Color enhancement of highly correlated images. I. Decorrelation and HIS contrast stretch, Remote Sens. Environ. 20 (1986) 209–235.
[10] R.E. Alley, Algorithm Theoretical Basis Document for Decorrelation Stretch, Version 2.2, 1996. NASA Jet Propulsion Laboratory, Pasadena California. http://eospso.gsfc.nasa.gov/sites/default/files/atbd/ASTER_ATBD_99-2010.pdf.
[11] I.T. Jolliffe, in: Principal Component Analysis, 2nd ed., Springer, New York, 2002, p. 488.
[12] R.D. Dony, Karhunen-Loève transform, in: K.R. Rao, P.C. Yip (Eds.), The Transform and Data Compression Handbook, CRC Press LLC, Boca Raton, 2001.
[13] Rasband W, ImageJ - Image processing and analysis in Java. http://rsb.info.nih.gov/ij/.
[14] M.A. Rogerio-Candelera, V. Jurado, L. Laiz, C. Saiz-Jimenez, Laboratory and in situ assays of digital image analysis based protocols for biodeteriorated rock and mural paintings recording, J. Archaeol. Sci. 38 (2011) 2571–2578.
[15] E. Cerrillo-Cuenca, P. Ortiz-Coder, J. Á, Martínez-del-Pozo, Computer vision methods and rock art: towards a digital detection of pigments, Archaeol. Anthropol. Sci. 6 (2014) 227–239.
[16] E. Cerrillo-Cuenca, M. Sepúlveda, An assessment of methods for the digital enhancement of rock paintings: the rock art from the precordillera of Arica (Chile) as a case study, J. Archaeol. Sci. 55 (2015) 197–208.
[17] D. Caldwell, U. Botzojorns, An historic sign, possible Mesolithic menhir, DStretch, and problems in dating rock art to the Sauveterrian in the Massif de Fontainebleau, J. Archaeol. Sci. 42 (2014) 140–151.
[18] E. Kotoula, D.W. Robinson, C. Bedford, Interactive relighting, digital image enhancement and inclusive diagrammatic representations for the analysis of rock art superimposition: The main Pleito cave (CA, USA), J. Archaeol. Sci. 93 (2018) 26–41.
[19] C. Defrasne, Digital image enhancement for recording rupestrian engravings: applications to an alpine rockshelter, J. Archaeol. Sci. 50 (2014) 31–38.
[20] J.L. Le Quellec, J. Harman, C.I. Defrasne, F. Duquesnoy, D-Stretch® et l'amélioration des images numériques: applications à l'archéologie des images rupestres, Les Cahiers de l'AARS 16 (2013) 177–198.
[21] E. Rodríguez González, S. Carbonell Pastor, J.R. Casals, Lost colours: Photogrammetry, image analysis using the DStretch plugin, and 3-D modelling of post–firing painted pottery from the south west Iberian Peninsula, DAACH 13 (2019) e00093.
[22] E. Quesada, J. Harman, A step further in rock art digital enhancements. DStretch on Gigapixel imaging, DAACH 13 (2019) e00098.
[23] L. Evans, A.L. Mourad, DStretch® and Egyptian tomb paintings: a case study from beni hassan, J. Archaeol. Sci. Rep. 18 (2018) 78–84.
[24] E. Robert, S. Petrognani, E. Lesvignes, Applications of digital photography in the study of Paleolithic cave art, J. Archaeol. Sci. Rep. 10 (2016) 847–858.
[25] L.M. Brady, A different look: comparative rock-art recording from the Torres Strait using computer enhancement techniques, Aust. Aboriginal Stud. 1 (2007) 98–115.
[26] A. Kessy, A. Lewin, K. Strimmer, Optimal whitening and decorrelation, Am. Stat. 72 (2018) 309–314.
[27] A.J. Bell, T.J. Sejnowski, The "Independent Components" of scenes are edge filters, Vision Res. 37 (1997) 3327–3338.
[28] G.H. Golub, C.F. Van Loan, in: Matrix computations, 4th ed., Johns Hopkins University Press, 2013, p. 784.
[29] E. Cerrillo Cuenca, M. Sepúlveda, Z. Guerrero-Bueno, Independent component analysis (ICA): a statistical approach to the analysis of superimposed rock paintings, J. Archaeol. Sci. 125 (2021) 105269.
[30] A. Hyvärinen, Independent component analysis: recent advances, Philos. Trans. A Math. Phys. Eng. Sci. 371 (2013) 20110534.
[31] A. Hyvärinen, E. Oja, Independent component analysis: algorithms and applications, Neural Netw. 13 (2000) 411–430.
[32] S.S. Al-Amri, N.V. Kalyankar, S.D. Khamitkar, Linear and non-linear contrast enhancement image, IJCSNS 10 (2010) 139–143.
[33] S.E. Han, B. Tao, T. Cooper, I. Tastl, Comparison between different color transformations for JPEG 2000, in: Proceedings of the IS&T's 2000 PICS Conference, 2000.
[34] K. Dawson-Howe, in: A Practical Introduction to Computer Vision with OpenCV, Willey, 2014, p. 235.
[35] A.A. Patel, Hands-on unsupervised learning using Python, in: How to Build Applied Machine Learning Solutions from Unlabeled Data, O'Reilly, 2019, p. 400.
[36] J.L. Lerma, Documentation and recovery of rupestrian paintings: an automatic approach, in: J. Albertz (Ed.), Proceedings of the XVIII International Symposium of CIPA 2001 Postdam, (Germany), 2002.
[37] F. Monna, J. Magail, T. Rolland, N. Navarro, J. Wilczek, J.O. Gantulga, Y. Esin, L. Granjon, A.C. Allard, C. Chateau-Smith, Machine learning for rapid mapping of archaeological structures made of dry stones – example of burial monuments from the Khirgisuur culture, Mongolia –, J. Cult. Herit. 43 (2020) 118–128.
[38] T.K. Kim, T test as a parametric statistic, Korean J. Anesthesiol. 68 (2015) 540–546.
[39] S.Y. Kung, in: Kernel Methods and Machine Learning, Cambridge University Press, 2014, p. 572.
[40] C.M. Bishop, in: Pattern Recognition and Machine Learning, Springer-Verlag NewYork Inc., 2006, p. 738.
[41] B. Lantz, in: Machine Learning With R, 2nd ed., Packt Publishing, 2015, p. 452.
[42] A. Géron, in: Hands-on Machine Learning with Scikit-Learn, Keras & Tensorflow. Concepts, Tools, and Techniques to Build Intelligent Systems, 2nd ed., O'Reilly, 2019, p. 600.
[43] C.G. Northcutt, L. Jiang, I.L. Chuang, Confident Learning: estimating uncertainty in dataset labels, J. Artif Intell. Res. 70 (2021) 1373–1411.
[44] R.G. Gunn, C.L. Ogleby, D. Lee, R.L. Whear, A method to visually rationalize superimposed pigment motifs, Rock Art Res. (2010) 27–2.
[45] A. Bovik, in: Handbook of Image and video Processing, Academic Press Inc., 2000, p. 891.
[46] I. Domingo, V. Villaverde, E. López-Montalvo, J.L. Lerma, M. Cabrelles, Latest developments in rock art recording: towards an integral documentation of Levantine rock art sites combining 2D and 3D recording techniques, J. Archaeol. Sci. 40 (2013) 1879–1889.

Chapitre 4. Etude typologique des khirigsuurs

Ce chapitre consiste en un article en préparation (voir ci-après)

Tanguy Rolland, Fabrice Monna, Jérôme Magail, Yury Esin, Carmela Chateau-Smith. Unsupervised classification of burial structures applied to the Mongolian Bronze Age monuments: the khirigsuurs.

Article

Unsupervised classification of burial structures applied to Mongolian Bronze Age monuments: the khirigsuurs

Tanguy Rolland[1,*], Fabrice Monna[1], Jérôme Magail[2], Yury Esin[3], Carmela Chateau-Smith[4]

[1]ARTEHIS, UMR CNRS 6298, Université de Bourgogne–Franche Comté, 6 Boulevard Gabriel, Bat. Gabriel, 21000 Dijon, France
[2]Musée d'Anthropologie préhistorique de Monaco, 56 bis, boulevard du Jardin exotique, 98000 MC, Monaco
[3]Archaeological Research Center of the National University of Mongolia, n °202, 2nd Building, 1 Ikh Surguuli Str., Baga Toiruu, Ulaanbaatar 14200, Mongolia
[4]CPTC, EA4178, Université de Bourgogne–Franche Comté, 4, boulevard Gabriel, 21000 Dijon, France

*: tanguy.rolland@u-bourgogne.fr, tel: +33 (0) 3 80 39 57 97

1. Introduction

The Late Bronze Age (ca. 1400-700 cal BC) is a pivotal time in Mongolia because it corresponds to the spread of nomadic pastoralism and the emergence of a new social order. For archaeologists, however, the main issues are the low number of artefacts found during excavations, and the difficulty of recognizing settled sites. Fortunately, despite this artefact scarcity, the region is extremely rich in funeral monuments, named khirigsuurs, dating from the period studied. Khirigsuurs are found over a very large geographical area, from north-west China to southern Siberia, and from eastern Kazakhstan to central Mongolia. They are not homogeneously distributed across this space, but are found grouped in geographically limited regions (Frohlich, 2010; Jacobson et al., 2001; Allard and Erdenebaatar, 2005; Erdenebaatar, 2004; Volkov, 1981). They have been at the heart of archaeological investigations since the nineteenth century, as they are almost the only remains left by nomadic populations (Allard and Erdenebaatar, 2005; Wright, 2007, 2014, 2017; Frohlich et al., 2008; Houle, 2010; Fitzhugh, 2009; Fitzhugh and Bayarsaikhan, 2011; Littleton et al., 2012; Zazzo et al., 2019). A khirigsuur consists of several architectural elements made of dry stones, forming mounds, rings, platforms, alignments, fences, etc., which are organized around a central tumulus containing a funeral chamber. Several typologies have previously been established. Tsybiktarov (1995) defined 9 types of khirigsuurs (Wright, 2014). Frohlich et al. (2008) proposed to divide the khirigsuurs into three classes, characterized by the value of the terrain slope on which the monument was built. Wright (2007) established a method of classification based on the architectural elements constituting the khirigsuurs, defining 3 types governed by the complexity of the monuments. Finally, Houle (2009) divided khirigsuurs into two groups: monuments either with or without deposit structures (the latter are associated with the vicinity of habitation sites). The designs of khirigsuurs may vary widely, from a simple tumulus surrounded by a fence to a large funeral structure including thousands of elements. At the regional scale, discrepancies probably result from the presence of different communities and the evolution of funeral practices over time. At the very large scale of the present study, however, all khirigsuurs can be seen to follow the same construction rules, in terms of the nature and organization of architectural elements, indicating a certain degree of cultural coherence among these communities. Studying these questions with existing typologies is problematic, as such classifications are rarely based on the same features. Design complexity is not always sufficiently taken into account, while the criteria used to categorize monuments are not always described with the precision necessary to allow their application to other sites. Although previous studies have identified many interesting elements, several important aspects for deeper understanding of the organization of ancient societies still remain unexplored.

Several objective classification methods, gathered under the name of 'cluster analysis', have been developed to solve similar problems in numerous scientific fields, such as biology, psychology, geography, marketing, and archaeology (Everitt et al., 2011). In archaeology, cluster analysis is commonly used to group artefacts on the basis of their similarity according to a set of selected features. This approach, used since the 1960s, has been largely adopted during the past few decades (Hodson

et al., 1966; Hodson, 1971; Philip and Ottaway, 1983; Sutton and Reinhard, 1995; Mallory-Greenough and Greenough,1998; Baxter, 2006; Blinkhorn and Grove, 2018; Bellanger et al., 2021, Wilczek et al., 2015). One of the main assets of cluster analysis is that it provides near optimal reproducible results. It is also able to deal with large datasets, where numerous variables are recorded.

The aim of this study is therefore to propose a new approach, which is (i) more inclusive in terms of features, (ii) established from a larger set of items, and (iii) based on unsupervised classification. As the Mongolian territory is vast, with tens of thousands of khirigsuurs, the present study focused mainly on two large valleys in central Mongolia, supplemented by some sites distributed northwards, up to the Siberian border. The first step consists in selecting a set of features best describing the monuments. Here, these features include intrinsic (e.g. size and monument elements) and extrinsic (e.g. slope and aspect) variables, which are either determined from aerial pictures obtained by unmanned aerial vehicles (UAVs), or calculated from available digital elevation models (DEMs). As such a dataset is composed of both quantitative and qualitative variables, the similarity matrix (qualifying the proximity between all pairs of individuals) is produced using intrinsic features and the Gower metric, as this metric is able to handle mixed data. An objective classification of khirigsuurs is then computed using an unsupervised clustering algorithm. Results are analysed in relation to field characteristics (geographical position, slope, and aspect). The two neighbouring valleys are compared to evaluate the spatial coherence of khirigsuur culture.

2. Material and methods

2.2 Corpus

Most of the khirigsuurs studied here are located in two neighbouring valleys in the Arkhangai region, central Mongolia: the Khoid Tamir and the Khunuin Gol river valleys (Fig. 6); the remainder are situated on several well-known sites, from the centre to the north of Mongolia (Fig. 1). The Khoid Tamir valley is an area that has been extensively studied for several years (Gantulga et al., 2016; Esin et al., 2021; Zazzo et al., 2019; Lepetz et al., 2019; Baroni et al., 2016), where dating is available at least for some khirigsuurs, at ca. 1050 cal BC (Zazzo et al., 2019). The Khunuin river valley is mostly known for the famous khunuu necropolis of Gol Mod dating from the Iron Age, a period more recent than our object of study. Nevertheless, several necropolises from the Bronze Age, composed of numerous burial structures are also found in the surrounding area. Structures from the following sites are also included in the corpus: Ulaan Uushig, Orkhon, Zunii gol, Zulegtyn gol, Ulaan Tolgoi, Jargalant, Urt Bulag, Durujiim am, and Shuuregtein uvur.

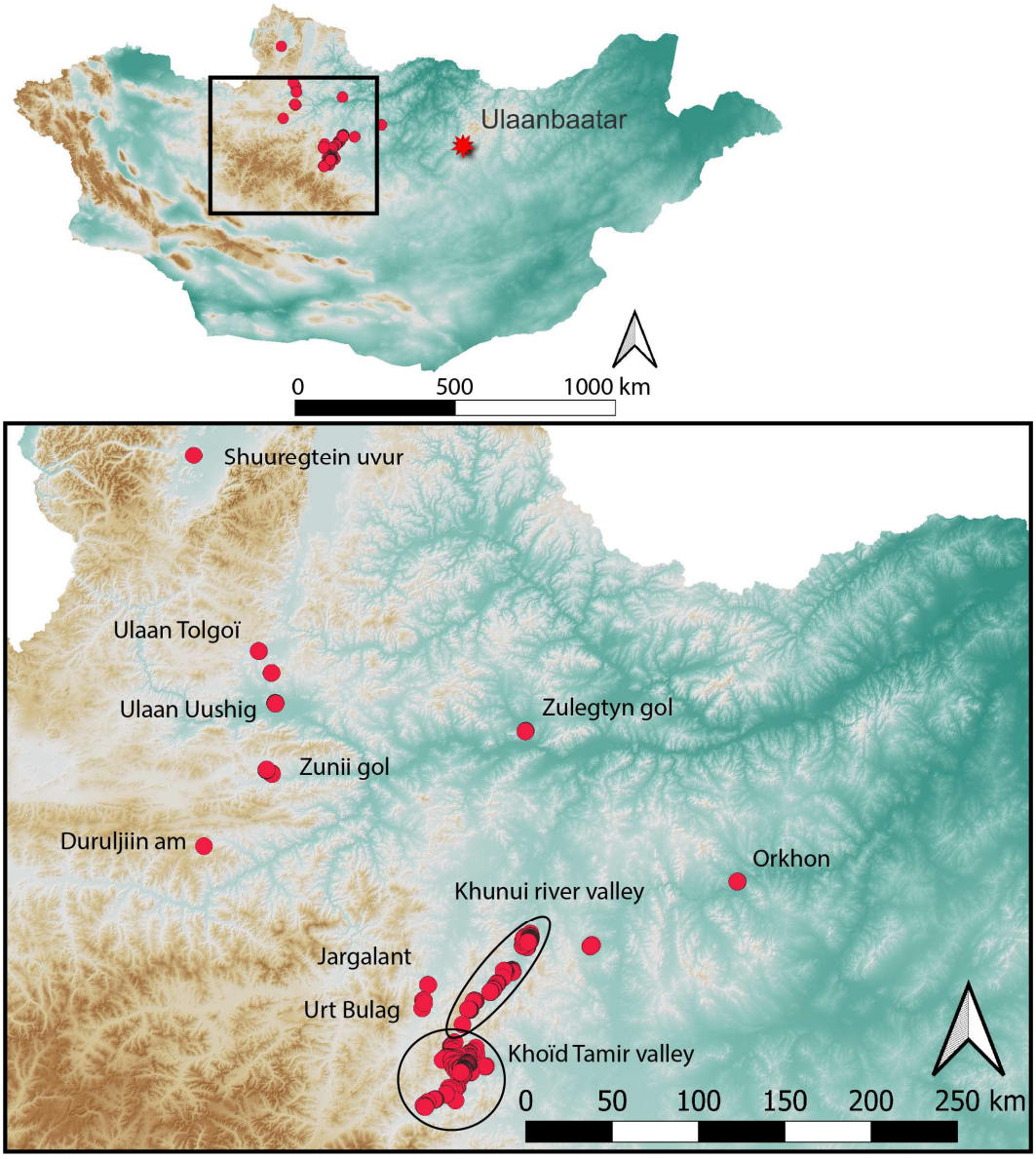

Fig. 1 Distribution of the khirigsuurs studied.

2.1 Definition of a khirigsuur

A khirigsuur (Fig. 2) is composed of multiple elements such as a central mound (2–50 m in diameter) under which lies the funerary chamber. The central mound (also named tumulus) is surrounded by a fence, a quadrangular or circular stone alignment, which can cover a few hundred square metres to several hectares. Outside the fence, there are several structures, the most common of which are mounds and stone rings. Both are deposit structures. The first are heaps of stones (1–5 m in diameter), under which horse heads have been deposited, sometimes accompanied by the first vertebrae and hooves. The second deposits are composed of about ten stones forming a ring of about 1 m in diameter. Generally, calcinated ovi-caprine bones are found there. The number of mounds and rings ranges from a few elements to more than a thousand for the largest khirigsuurs. Some rarer elements, such as platforms, alleys,

associated deer stone structures, and stone alignments, can be present near the fence.

The precise definition of a khirigsuur is not uncontroversial. For some authors (Houle, 2010; Allard and Erdenebaatar, 2005), a khirigsuur requires a tumulus, a fence, and deposit structures, while for others (e.g. Wright, 2007), deposit structures are not necessary. In the following, the second definition is retained.

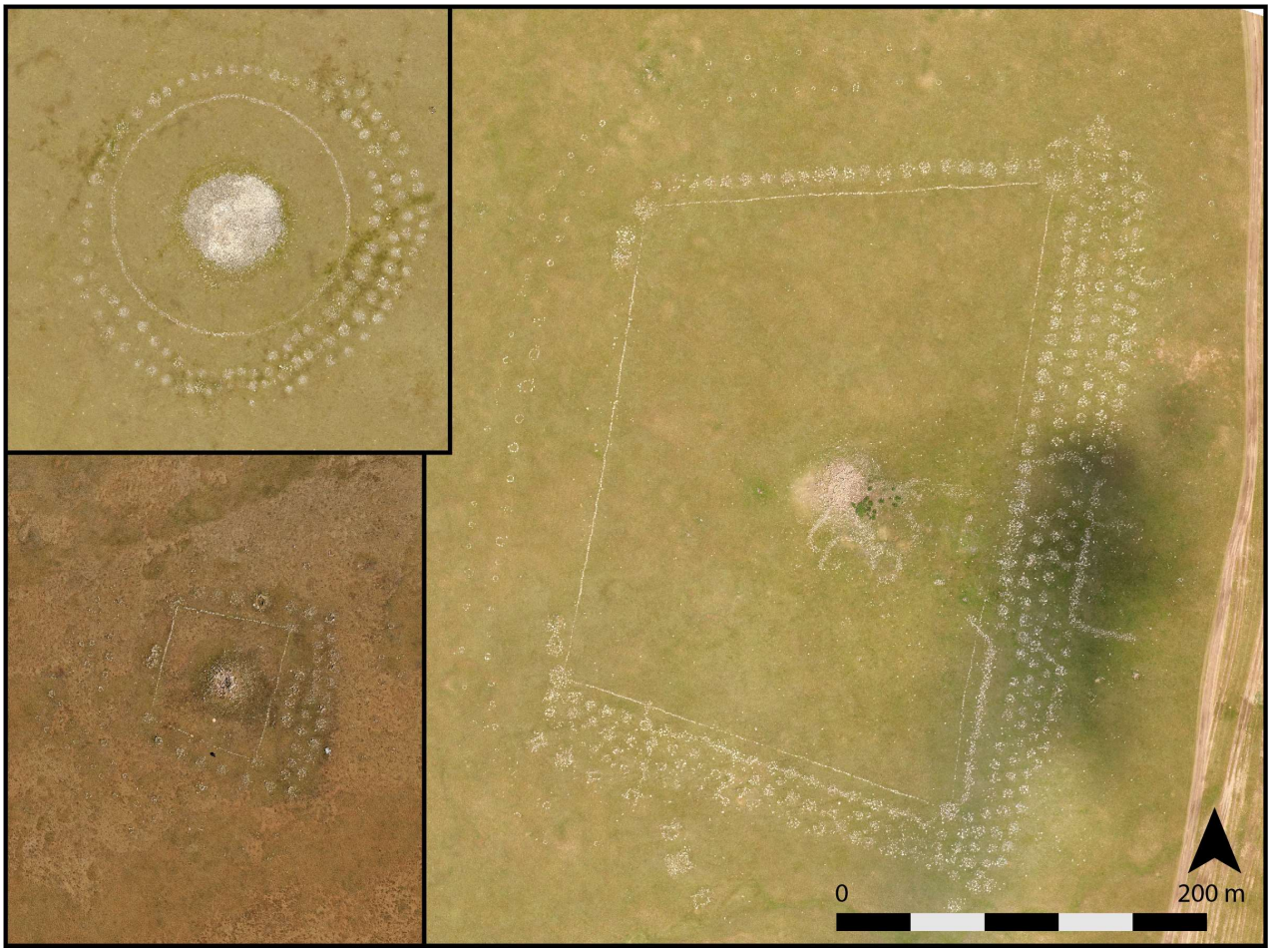

Fig. 2 Example of different shapes and size of khirigsuurs. Here, one circular and two trapezoidal khirigsuurs with the same organization and elements: tumuli, fence, rings, and mounds.

2.2. Orientation of khirigsuur

The elements of the khirigsuur are not evenly distributed in space. When an imbalance is identified in the design (e.g. more rings on a particular side), it is possible to orient the monument, provided that a common orientation system is established for all khirigsuurs (Fig. 3). The criteria follow a priority order.

i) For trapezoidal khirigsuurs, the longest side corresponds to the front of the monument.
ii) When there is an imbalance between the number of mounds and rings on opposite sides of the monument, the side with the greater number of mounds is considered as the front.
iii) Alignments inside the fence, linking the burial mound to the fence, indicate the front of the monument.
iv) In the other cases, the orientation cannot be defined.

Once the orientation has been defined, the space is divided into four areas, corresponding to 1) the back, 2) the left, 3) the front, and 4) the right sides of the monument (Fig. 3). These areas are used for spatialization of architectural elements.

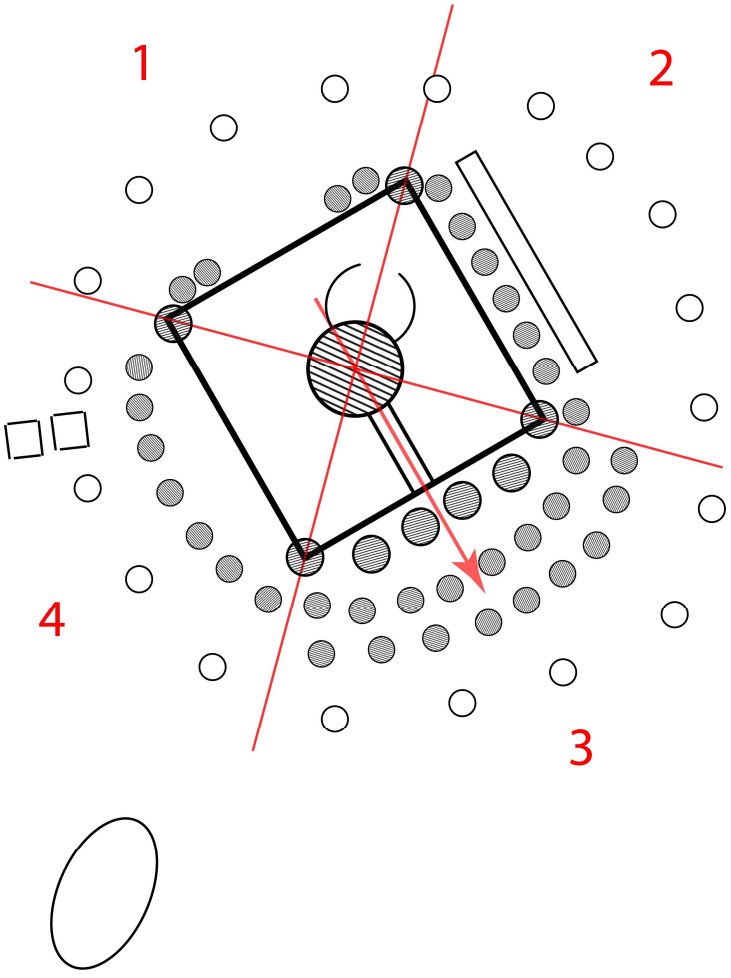

Fig. 3 Orientation of a khirigsuur divided into four areas corresponding to 1) the back, 2) the left, 3) the front, and 4) the right.

2.3. Quantification of rings and mounds

The number of rings or mounds varies widely, from zero to thousands of items, making any precise recording tedious. In addition, depending on the state of conservation of the monument, some structures

may be very difficult to identify. This is especially true for rings, the smallest structures, which are prone to vanish over time. Simply counting items cannot adequately record the complexity of the structure's organization. For example, a small khirigsuur can have about thirty mounds forming several rows, which are distributed over three of its sides, whereas a larger one can possess the same number of mounds distributed as a single row, along only one side. The alternative proposed here is rather to count the rows formed by both rings and mounds in each of the four zones, as defined above. This solution records the full pattern of the structure in terms of number of elements and organization, while advantageously simplifying the information thus recorded.

2.4. Recorded features

The encoding proposed here includes more variables than those used by Wright (2014). It is based on intrinsic features related to the nature, the position, and the number of elements constituting the monument.

Descriptors	Modality	Clarification
1) Shape of the fence	Circular Square Rectangular Trapezoidal Oval Mixed	
2) Surface enclosed by the fence	Quantitative variable expressed in m²	Area allows size comparison for all shapes
3) Diameter of the central mound	Measurement in m	
4) Lane inside the fence	Presence /Absence	
5) Arms inside the fence	Presence /Absence	
6) Fence surrounding the central mound	Presence /Absence	
7) Other structures inside the fence	Presence /Absence	
8) Front mounds	Presence /Absence	Mounds aligned in the front of the monument, generally bigger than the other surrounding mounds, distorting the row behind them.
9) Back mounds	Absent Corners Centre Corners + Centre Corners + Centre + Interval Complete	Mounds aligned at the back of the monument. The alignment is regularly punctuated by empty space. Different layouts exist.
10) Mounds in zone 2	Number of rows	
11) Mounds in zone 3	Number of rows	
12) Mounds in zone 4	Number of rows	
13) Rings in zone 1	Number of rows	
14) Rings in zone 2	Number of rows	
15) Rings in zone 3	Number of rows	
16) Rings in zone 4	Number of rows	
17) Supplementary structures	Presence /Absence	
18) Structures associated with deer stones	Presence /Absence	Soil mounds, surrounded by deposit structures, where deer stones are installed.
19) Corner structures	Absence/Heap of stones/ Vertical stone	Usually, placed in the corners of the fence if quadrangular, or positioned at the four main directions if the fence is circular
20) External platform	Number of the zone	
21) Khirigsuur orientation	Angle from North, between 0° and 360°	Orientation of the monument

Table 1. List of the descriptors used for khirigsuur classification.

A total of 21 variables is recorded. They are listed in Table 1 and illustrated in Fig. 4. The first descriptor, #1, qualifies the fence shape. Descriptors #2 and #3 are directly related to size: the area of the fence, and the diameter of the central mound. Descriptors #4 to #7 designate the presence or absence of features inside the fence. These features are generally stone alignments. Descriptors #8 to #16 relate to the position and quantity of deposit structures around the fence. Front mounds and back mounds are two particular cases of mound position (Fig. 5). Descriptors #17 to #20 illustrate the presence or absence of features outside the fence. Finally, Descriptor #21 corresponds to the orientation of the khirigsuur, as described above.

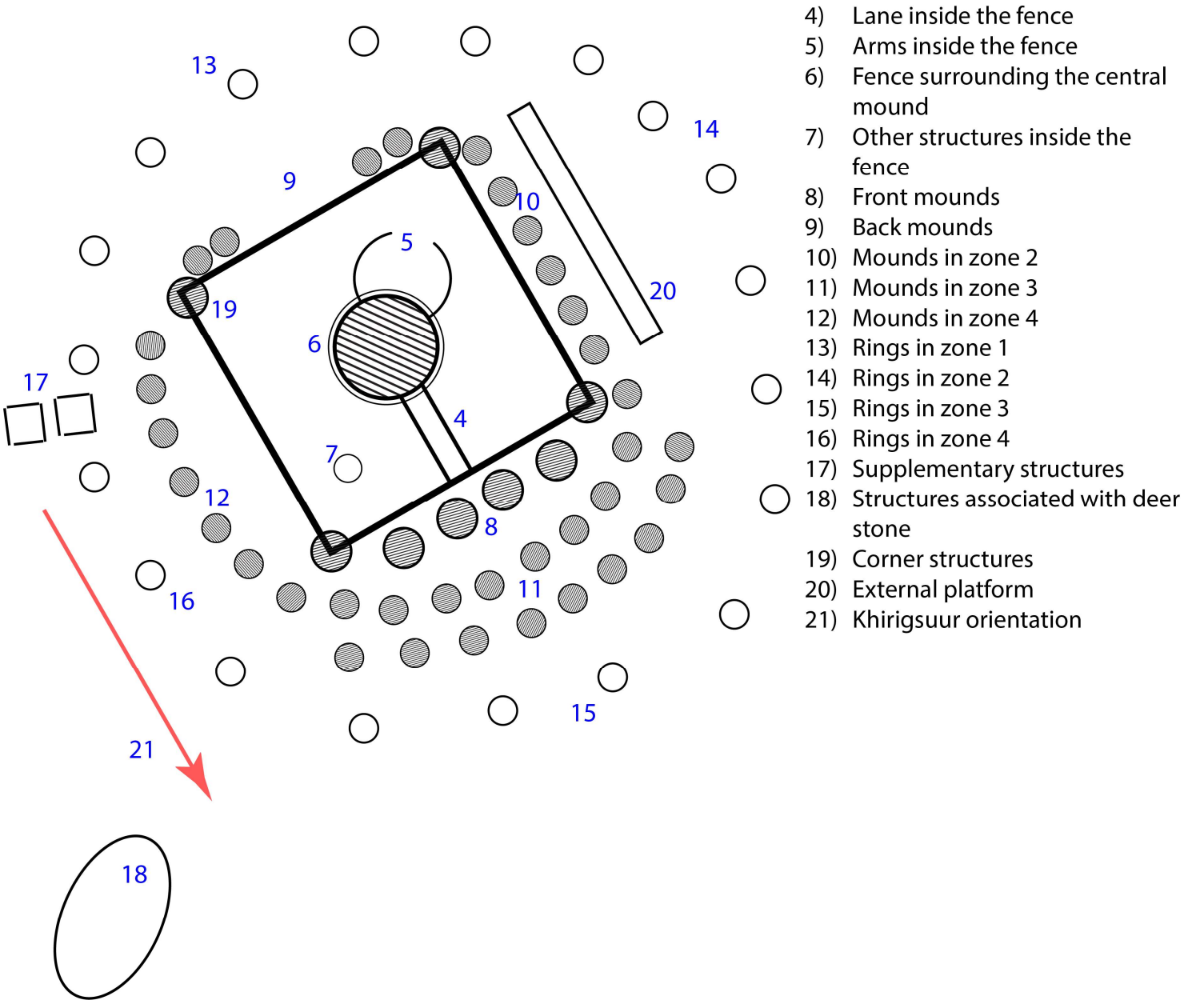

Fig. 4 Illustration of the elements constituting a khirigsuur used as descriptors. Each number on the diagram refers to the number in Table 1.

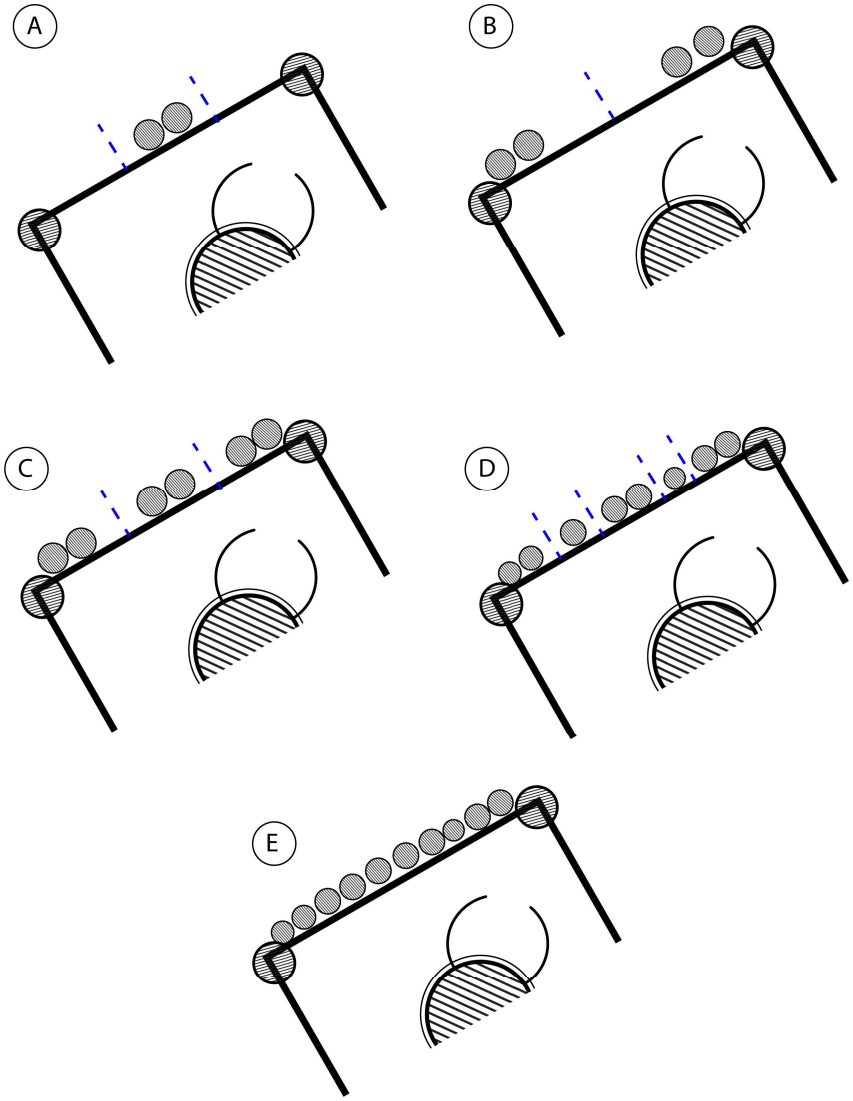

Fig. 5. Example of configuration for the position of the "back mounds". A-Corners, B-Centre, C-Corners+Centre, D-Corners+Centre+Interval, E-Complete (Absent not depicted)

2.3 Clustering

2.3.1 Principle

Clustering is a mathematical method that aims to reveal structures by grouping similar data into common classes. The notion of similarity between two individuals means proximity according to a particular metric, such as Euclidian distance, for example. Numerous methods of clustering and metrics have been developed over the past few decades. Algorithms have been specifically designed to handle numerical data (Macqueen, 1967), with others for categorical features (Khan and Kant, 2007).

2.3.2 Metric

The Gower distance is a coefficient of similarity (Gower, 1971). This metric has the advantage of handling both quantitative and qualitative variables seamlessly, while also permitting missing values. These characteristics make this metric appropriate for the problem at hand. The similarity S_{ij} between individuals i and j is given by:

$$S_{ij} = \sum_{k=1}^{n} s_{ijk} \; / \sum_{k=1}^{n} \delta_{ijk}$$

where S_{ij} is the score of similarity between i and j pertaining the variable k. It is equal to 0 if the individuals are different, equal to 1 if they are identical, and can take values within this range; δ_{ijk} represents the possibility of comparing i and j. It is equal to 1 when comparison is possible, and 0 otherwise; n is the number of parameters compared.

The calculation rules of the score s_{ijk} depends on the nature of the variable k:

i) When k is qualitative, $s_{ijk} = 1$ if $k_i = k_j$ and 0 otherwise.
ii) When k is quantitative, $s_{ijk} = 1 - |k_i - k_j| / R_k$, where R_k is the range of the k variable.

For the circular azimuthal variable (expressed in degrees from North), the second rule cannot apply, as the upper value (360°) is the same as the lower one (0°). A third rule was therefore applied.

iii) When k is the azimuth, $s_{ijk} = 1 - \min(|k_i - k_j|, 360 - |k_i - k_j|) / 180$

Calculations of Gower's distances between each couple of samples produces a similarity matrix, which is then used as input in clustering algorithms.

2.3.3 Hierarchical clustering

Hierarchical classification is a step-by-step method dividing a unique cluster (the whole dataset), into subgroups until the result obtained is n clusters with a single individual in each. This family of algorithms is called 'divisive'. Another alternative, namely agglomerative, consists in merging clusters, starting from n clusters to reach a single cluster. The decision to agglomerate (or to divide) individuals or groups is based on a linkage criterion. Among the numerous algorithms that exist, the agglomerative Ward method has often been identified as the most appropriate in circumstances similar to those exposed here, especially in archaeology (Baxter, 2015; Duflou and Maenhaur, 1990; Everitt et al., 2011), which is why it is the approach retained here. Hierarchical classifications are generally illustrated as dendrograms, which depict each step of the process.

2.3.4 Optimal number of clusters

For each of the methods described above, the number of clusters, k, need to be set a priori. Finding this optimal value may be problematic, so that several approaches have been proposed to help the researcher with

this task. In this study, two methods were applied. The underlying idea is to cluster with various values of *k*, to calculate associated indices, and to determine the optimal number of clusters on the basis of a visual inspection of how these indices evolve with *k*. The elbow method computes the within sum, and the presence of an elbow or bend is considered as a good indicator for finding the optimal value of *k*. The silhouette method uses the average silhouette width, and its higher value corresponds to an optimal value of *k*. These methods must be considered only as recommendations: they help in the decision process, but they are not strict rules. It should always be kept in mind that the grouping obtained must, at the end, make sense for the problem at hand.

2.3.5 Validation

Clustering quality is assessed by two indices: the silhouette coefficient and the Dunn index. For each individual, the silhouette coefficient measures how close the individuals belonging to the other clusters are. This index, generally displayed on a silhouette plot, is comprised between 1 and -1. A value equal to 1 indicates that the individual is well assigned, while -1 suggests that it might be misplaced (Rousseeuw, 1987, Kassambara, 2017; Everitt et al., 2011). The Dunn index (Dunn, 1973) is the ratio between the minimum distance between two individuals belonging to different clusters and the maximum distance between two individuals belonging to the same cluster. The higher the index, the better the clustering. Like the methods described above to find the optimal number of clusters, these indices are decision support tools. They do not provide definitive answers.

The coherence of the computed clusters was also checked using a non-linear projection of the data on self-organizing maps (SOMs). This unsupervised machine learning method, introduced by Teuvo Kohonen (Kohonen, 1997), is used for pattern recognition in many scientific disciplines (Liu, 2005; Lin, 2008; Wilczek, 2015). It is able to reduce a high dimensional dataset to a lower one, often making the data more readable. Its typical 2D representation consists of an artificial neural network, where the nodes form a grid. Each node possesses associated weights (as many as there are dimensions to start with), which are adjusted step by step to fit the data topology as close as possible, so that the relation between individuals is preserved (two similar individuals are close to each other on the grid). A hexagonal grid-shaped network is generally recommended because nodes have more neighbours than with a square-shaped network. The dimension of the grid depends on the number of observations in the dataset and on the first principal dimensions (here 2) in which the variances of the data are the largest (Kohonen, 2014). Here, considering the number of individuals and variables, a 24 × 6 hexagonal grid was found appropriate.

2.3. Acquisition and post processing

The data used in this study come from UAV acquisition campaigns in the framework of the Monaco-Mongolia joint mission. Two different UAVs were used: a DJI Phantom 3 PRO with a 12 Mpix camera and a 20 mm lens (equivalent 35 mm), and a DJI MAVIC AIR with a 12 Mpix camera and a 24 mm lens (equivalent 35 mm). The principle is to take a series of overlapping photos (fixed at 80%) covering the area of interest. The relief can then be reconstructed by photogrammetry using Metashape

(https://www.agisoft.com/), allowing the computation of orthomosaics and DEMs (Fig. 6). The flight height was set between 70 m and 100 m for a ground resolution of about 3 cm/px, a value sufficient to distinguish the decimetric stones constituting the khirigsuurs. Flights were planned *via* the free application Pix4Dcapture (https://www.pix4d.com/).

The orthomosaics and DEMs were then processed with a pixel classifier based on machine learning (Monna et al., 2020) to obtain images where only stones are visible (Fig. 6C). Such an output allows better identification of the elements constituting the khirigsuurs. Finally, orthomosaics and DEMs were input into a geographical information system (QGIS, https://www.qgis.org) to manually describe and record in a database all the anthropogenic structures visible in the images.

The registration strategy sought to obtain a satisfactory corpus for statistical applications. Several areas were entirely covered for exhaustive records, the largest being a 700 ha zone in the Khoid Tamir valley and a 260 ha zone in the Khunui river valley. From about 236 orthomosaics (each covering 2–9 ha), a total of 1527 structures was recognized, among which 907 were identified as khirigsuurs. A total of 117 khirigsuurs was however removed from this database, because they appeared to be severely damaged. Classification was therefore finally performed on 790 monuments.

Data were processed using scripts written in R (https://www.r-project.org/), with the help of the functions included in the dendextend (Galili, 2022), fpc (Hennig, 2020), gglpot2 (Wickham et al., 2022), cluster (Maechler, 2022), circular (Lund e al., 2022), ecodist (Goslee et Urban, 2007), and factoextra (Kassambara et Mundt, 2020) packages. The computation of slope and aspect was performed on the 30 m Shuttle Radar Topography Mission (SRTM) data.

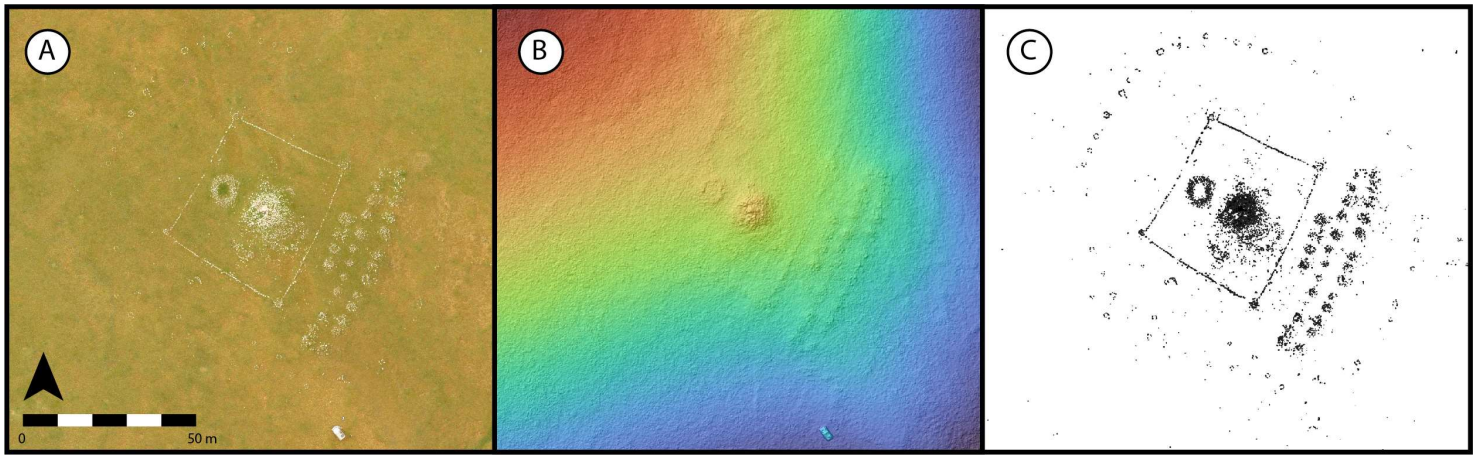

Fig. 6 Steps of the process of stone detection for khirigsuurs. A) orthomosaic; 2) coloured hillshaded DEM; 3) extraction of dry stones by machine learning.

3. Results

3.1 Descriptive statistics

All khirigsuur shapes are well represented in the dataset, except for the oval (Fig. 7A), but more than 60% are quandrangular. The diameter of the tumulus is correlated with the area enclosed by the fence ($R_{Spearman}$ = 0.898, *p*-value = $<10^{-6}$). Several authors (Wright, 2014; Frohlich et al., 2008, Houle, 2009) also empirically noted that khirigsuur size is related to the number of constituent elements. To examine the possible dependence of size on other qualitative descriptors, U Mann-Whitney or Kruskal-Wallis tests (depending on the number of modalities) were performed. The results, all significant (Appendix 3), indicate that all

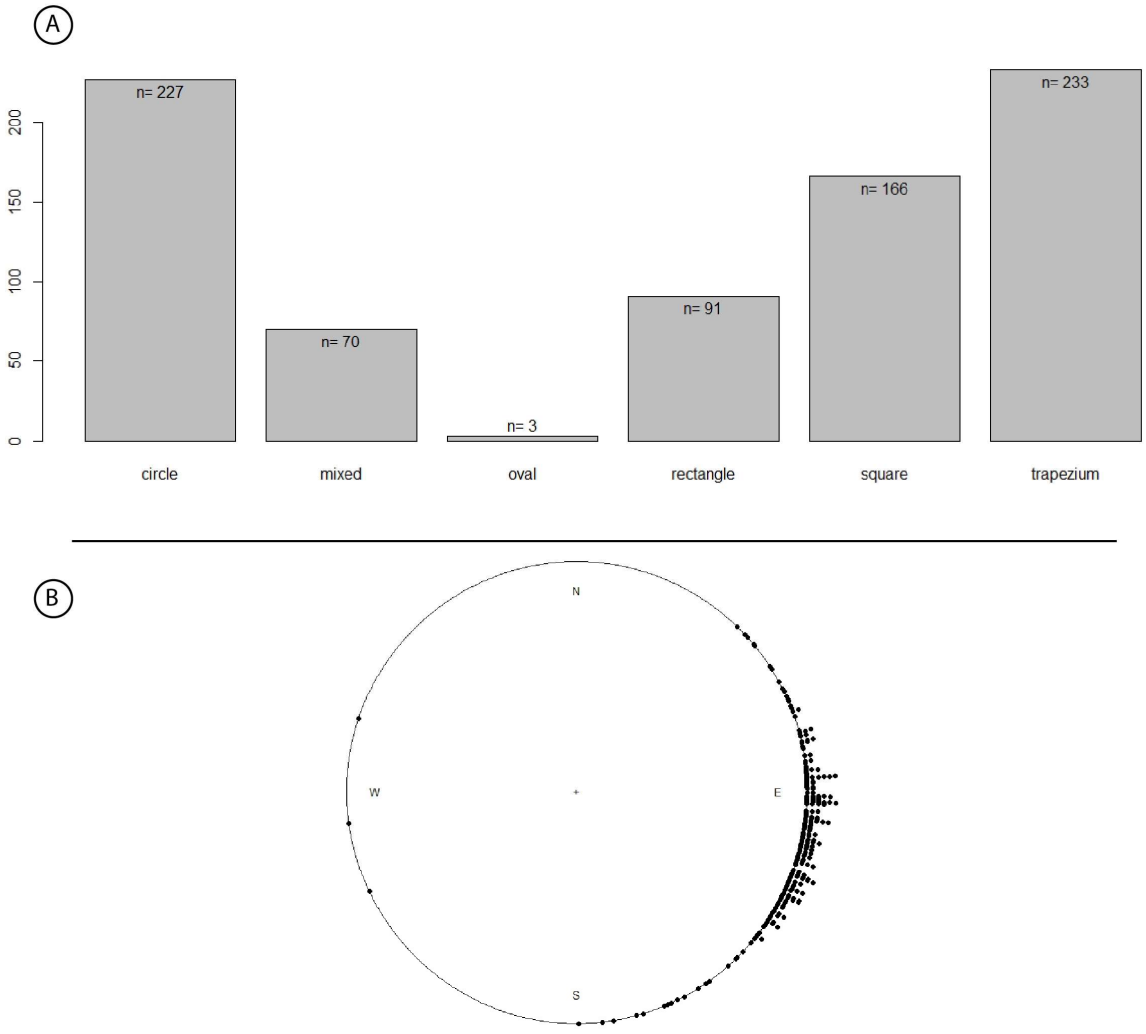

Fig. 7 A) Fence shape distribution for the khirigsuurs studied. B) circular plot of khirigsuur orientation (n=244)

features are not independent of size parameters (i.e. fence area and tumulus diameter). It is also noted that, among the orientable khirigsuurs (*n* = 244), the majority of the front sides face East (Fig. 7B).

3.2 Clustering

The optimal number of clusters was estimated as between 6 or 7 clusters using the elbow method, as well as the average silhouette width. The Dunn index could not be used to decide between these values, as both configurations produce the same index value. Nevertheless, the number of possibly misplaced individuals is slightly higher with 6 clusters (34 items) than with 7 clusters (24 items), encouraging the use of 7 clusters.

3.2.1 Cluster validation

The silhouette plot (Fig. 8A) shows that the individuals are generally well assigned, except for the 24 individuals mentioned above, which fall in clusters 1,3,5,6,7. These individuals have a negative silhouette width, warning us about possible wrong assignment. It remains possible to reassign them to the closest clusters in view of improving classification performance. However, after applying such a correction, the Dunn index decreases notably, suggesting a drop in classification quality. The projection of individuals on a SOM (Fig. 8B) shows that each type occupies

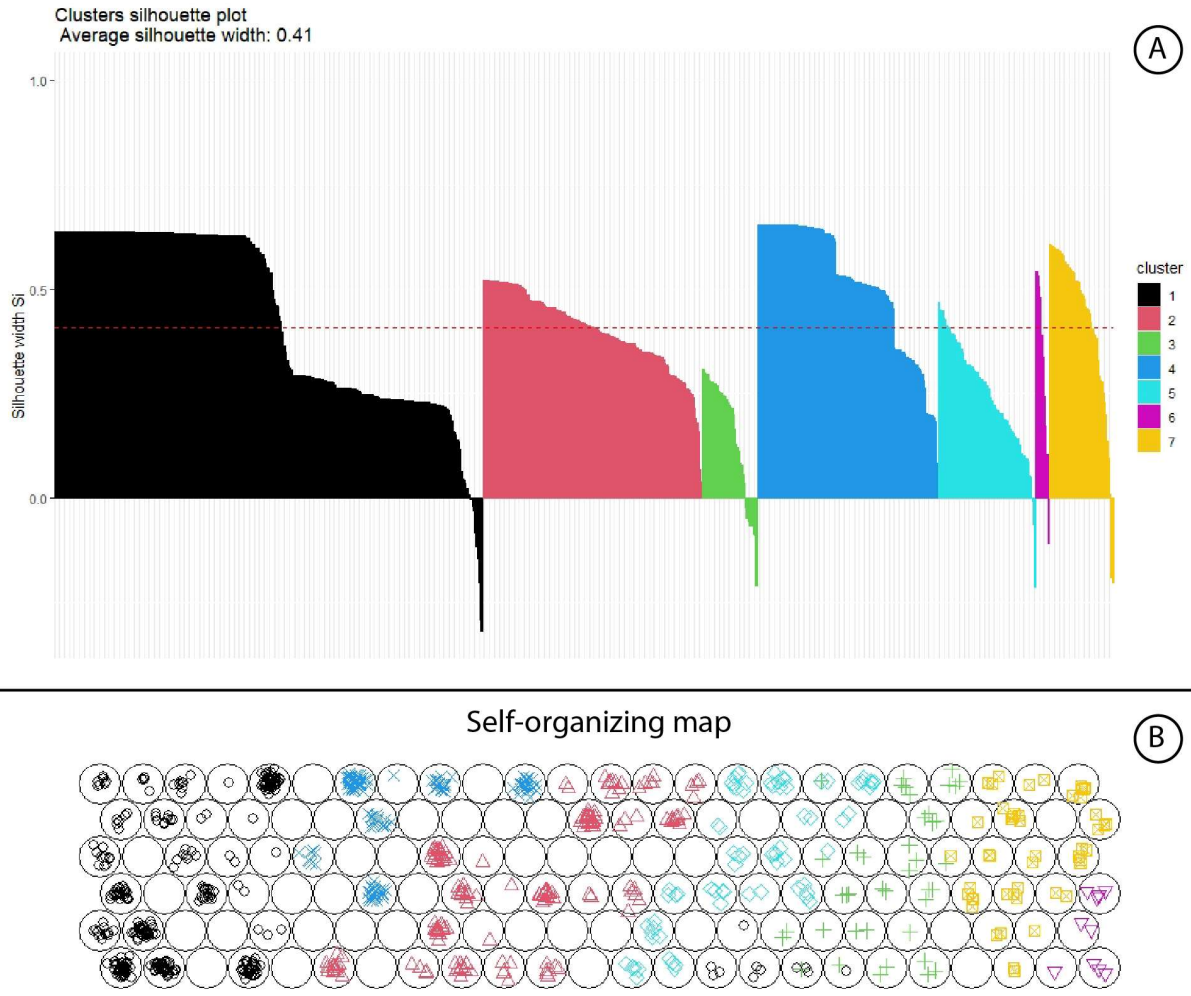

Fig. 8 A) Silhouette plot of the k=7 clusters. B) projection of the 790 individuals on the Self-organizing map. The clusters 1-7 are depicted with different colours and symbols. 1) black circles; 2) pink triangles; 3) green plus signs; 4) blue crosses; 5) light blue diamonds; 6) purple inverted triangles; 7) yellow squares.

a distinct region, except for a few individuals in cluster 1 (black circle) found between cluster 3 (green cross) and cluster 5 (light blue diamond). Some of these individuals were also misplaced in the silhouette plot. The classification obtained using the Ward algorithm with 7 classes is generally good, whatever the validation method applied, with no need for any item reassignment.

3.2.2 Groups of khirigsuurs

The groups provided by the Ward classification have been renamed and ordered from Type I to Type VII, according to the median tumulus diameter, to facilitate their description. The characteristics of the groups are summarized in Table 2, and detailed in the Appendix 4. The first group, Type I, contains only 10 monuments. It gathers the gigantic khirigsuurs in the dataset, with a tumulus diameter of ~26 m and a fence encompassing ~1 ha. All khirigsuurs in this group are trapezoidal, with corners accentuated by mounds. The presence of front mounds is systematic, whereas back mounds and platforms are only present in half of these khirigsuurs. They possess numerous rows of rings and mounds. Zone 2 has fewer mounds (0 - 4 rows) than zones 3 and 4 (3 - 30 rows).

Type II groups 48 individuals, generally smaller than those of Type I. The diameter of the tumulus is around 14 m, and the area enclosed by the fence around 2500 m². The trapezoidal form is predominant and, as with Type I, all fences are highlighted by mounds. The front mounds are present in most cases, while the platform and back mounds are observed in half of them. Type II has from 1 to 2 rows of rings and/or mounds surrounding the fence.

Type III groups 41 individuals. The tumulus diameter is around 12 m and a median fence surface of 990 m². All shapes are represented, but the trapezium remains the most common, accounting for ~50%. One third of the khirigsuurs of this type possesses front mounds. Back mounds (3 occurrences) and platforms (7 occurrences) are even rarer. As with Type II, Type III monuments are generally surrounded by one row of rings and possess one row of mounds in zone 3. The presence of mound rows in the other zones is less common. One third of the fences is not highlighted, while the others possess mounds, and one item possesses vertical stones.

Type IV groups 73 individuals. The tumulus diameter is around 9.5 m and the fence surface ~690 m². The trapezium is the most common shape, but other shapes can also be found. Except for one unique case, no back mounds are observed in Type IV khirigsuurs. Both platform and front mounds represent one seventh of cases. The majority of the fences is highlighted by mounds. Less than half of the items are surrounded by rows of rings or mounds.

Type V groups 164 individuals. The tumulus diameter is around 7.3 m and the fence surface is around 244 m². No internal or external structures are associated with this type. Only 10-20 % of the monuments possess rows of rings or mounds. The fence has no predominant shape, but all are highlighted by mounds.

Type VI groups 319 individuals. The tumulus diameter is around 5.4 m and the fence surface is around 103 m². The fence shape is diverse, but more than 50 percent have the circular form, and none of them are highlighted. No internal or external structures are associated with this type. Less than 10% of the khirigsuurs in this type possess a row of rings or mounds.

Type VII groups 135 individuals. The tumulus diameter is around 4.3 m and the fence surface is around 89 m². This type is associated with no internal or external structures, nor with a row of mounds, but approximately 1 % of individuals possess one row of rings. The fence is mostly quadrilateral, mostly with a square shape. All of them are highlighted by vertical stones.

Type I (*n* = 10)	**Diameter**: 18.6 m to 35.0 m (median = 26.0 m) **Area**: 2340 m² to 44675 m² (median = 10000 m²) **Shape**: trapezium **Internal structure**: no arms, but possibly other structures **External structure**: front mounds (always), platform and back mounds (present in about half of the cases) **Fence highlighting**: mounds
Type II (n = 48)	**Diameter**: 9.4 m to 24.0 m (median = 14.0 m) **Area**: 832 m² to 16192 m² (median = 2504 m²) **Shape**: mostly trapezoidal **Internal structure**: rare **External structure**: 1-2 rows and front mounds (always), platform and back mounds (present in about half of the cases) **Fence highlighting**: mounds
Type III (n = 41)	**Diameter**: 5.9 m to 26.5 m (median = 11.8 m) **Area**: 141 m² to 6412 m² (median = 991 m²) **Shape**: diverse **Internal structure**: rare **External structure**: very rare back mounds, front mounds and platform uncommon, average of 1 row of rings and mounds, mostly present in zone 3 **Fence highlighting**: mostly mounds
Type IV (n = 73)	**Diameter**: 3.3 m to 14.8 m (median = 9.5 m) **Area**: 51 m² to 4392 m² (median = 688 m²) **Shape**: mostly trapezoidal **Internal structure**: very rare **External structure**: no back mounds, rare front mounds and platform, rare rows. **Fence highlighting**: mostly mounds
Type V (n = 164)	**Diameter**: 2.9 m to 13.8 m (median = 7.3 m) **Area**: 44 m² to 4736 m² (median = 244 m²) **Shape**: diverse **Internal structure**: none **External structure**: no back mounds, no platform, no front mounds, very rare rows **Fence highlighting**: mound
Type VI (n = 319)	**Diameter**: 1.8 m to 26.1 (median = 5.4 m) **Area**: 10 m² to 3966 m² (median = 103 m²) **Shape**: mostly circular **Internal structure**: none **External structure**: no back mounds, very rare platforms, no front mounds, very rare rows **Fence highlighting**: none
Type VII (n = 135)	**Diameter**: 1.8 m to 10.6 m (median = 4.3 m) **Area**: 16 m² to 509 m² (median = 89 m²) **Shape**: diverse **Internal structure**: none **External structure**: none **Fence highlighting**: vertical stones

Table 2. List of the seven types of khirigsuurs and description of their main features. Each type is associated with n, the number of individuals it contains.

Although the order in which the types appear is governed by the median of the tumulus diameter, it is necessary to determine whether the differences between each pair of groups are statistically significant. The same approach can be undertaken with the fence area, even though has been demonstrated that these two variables evolve monotonically. This is done using non-parametric Kruskal-Wallis tests (p-values < 10^{-6} for both variables), followed by post-hoc pairwise Wilcoxon tests. The results indicate that all groups are significantly different from each other for tumulus diameter, except for Type VI and Type VII, which cannot be distinguished. The fence area is less discriminating, because it is not significantly different between Type VI and Type VII, or Type III and Type IV.

The second variable that seems to drive the construction of the groups is fence highlighting. Except for Type III and Type IV, the other types possess only one modality: mounds for Types I, II, and V, vertical stones for Type VII, and nothing for Type VI.

Trapezoidal fences are predominant in Type I–IV, while other shapes are more frequent in Types V–VII. Type VI groups 85% of the observed circular fences. Except for Type I, which counts only 10 individuals, the fence shape does not appear to define any group categorically.

3.1.2 Spatial distribution of groups

Figure 9A shows the spatial distribution of khirigsuurs according to group in the Khoid-Tamir valley. Types IV, V, VI, and VII are

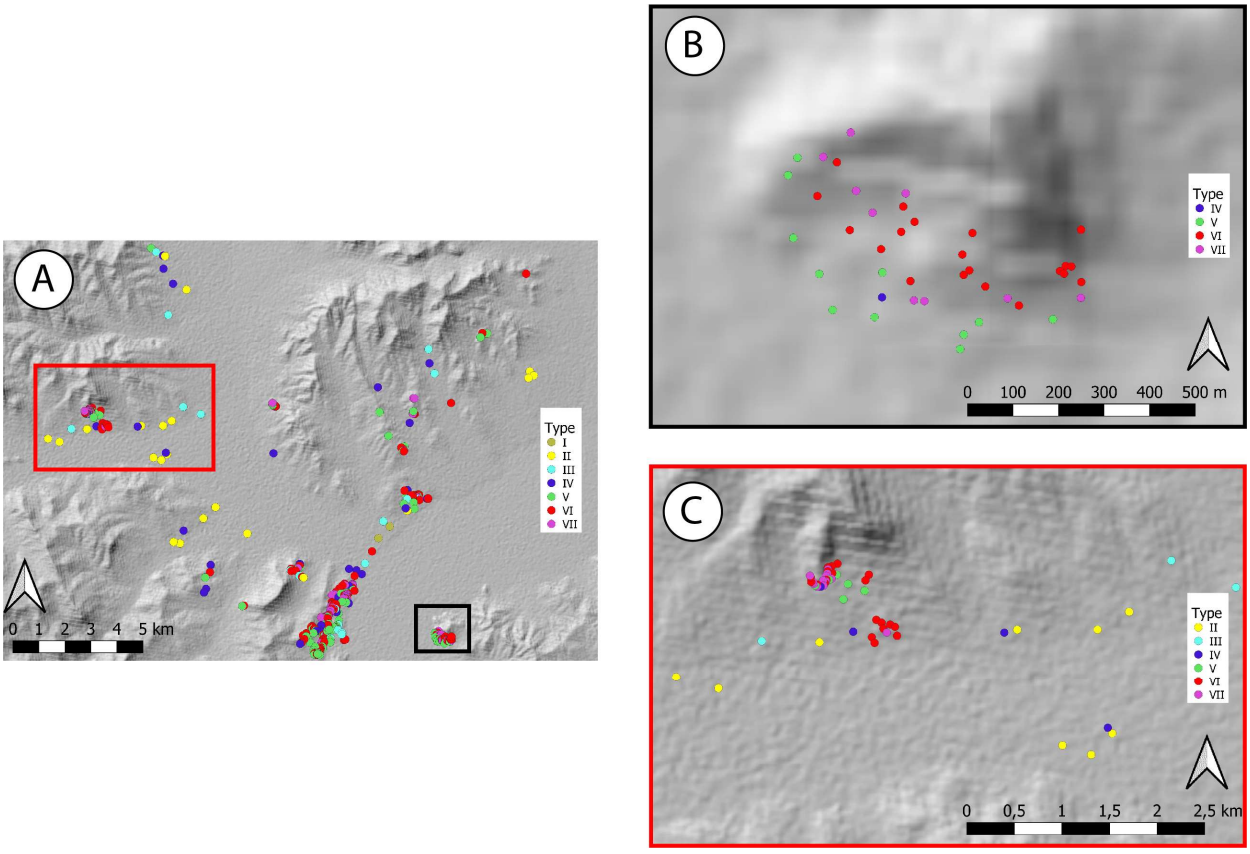

Fig. 9 Distribution of the khirigsuur types over part of the Khoïd Tamir valley. A) general view; B) and C) show details of two different necropolises in the valley.

agglomerated around the relief, forming a funerary complex. In contrast, Types I, II and III are spread out over the valley. Figure 9B zooms in on the complex located in the South-East of Fig. 9A. The organization of the different types is clear. Types VI and VII are in the centre of the complex, while Types IV and V are in the periphery. The same organization can be observed in the North-West of the valley (Fig9C). Here, two complexes are close to each other, with a core composed of Types VI and VII, and again, the Type IV and V in the surrounding area. Even further away are the khirigsuurs belonging to Types II and III.

The complexes of the Khunui river valley possess a similar organization (Appendix 5). This organization resembles the classification proposed by Frohlich, who categorized the khirigsuurs into 3 classes, according to the terrain slope where they stand. To check if the automatically categorized groups are slope-dependent, a Kruskal-Wallis test was performed. The p-value $<10^{-6}$ demonstrates that at least one group is different with regard to the slope. Post-hoc pairwise Wilcoxon tests indicate that Types I and II cannot be distinguished from each other, but are significantly different from the other five groups. The same can be noted for Types I and IV, Types III and IV, and for Types VI and VII (average slope of each type on first row, Table 3). So the grouping proposed in this study has a geographical meaning in terms of slope, echoing Frohlich's classification with the presence of type on specific slopes.

The same reasoning was conducted with regard to the aspect parameter. It is commonly said that khirigsuurs are installed on the southern side of the relief. As Aspect is a circular variable (values in Table 3), the Watson large-sample non-parametric test is adopted to compare mean directions. No significant difference appears between types (p-value> 0.05).

Type	I (n=10)	II (n=48)	III (n=41)	IV (n=73)	V (n=164)	VI (n=319)	VII (n=135)
Slope (in degrees)	1.55	2.82	4.65	5.48	8.76	11.05	11.84
Aspect (in degrees from North)	195.8	154.2	151.9	146.4	155.7	158.9	155.2

Table 3. Means of slope and aspect for each type of khirigsuur.

3.2 Comparison between the two valleys

A total of 415 khirigsuurs was identified in the Khoïd Tamir valley, with 326 in the Khunui river valley. Their respective distribution in terms of type is depicted in Fig 10. A Chi-square test of homogeneity was used to compare these distributions. As the number of Type I khirigsuurs is low, they are agglomerated with those of Type II, which possesses the closest characteristics. Interestingly, no significant difference between the Khoïd Tamir and Khunui river valleys was observed (p-value > 0.05). This

suggests that the nomad Bronze Age populations occupying these neighbouring valleys shared common burial practices.

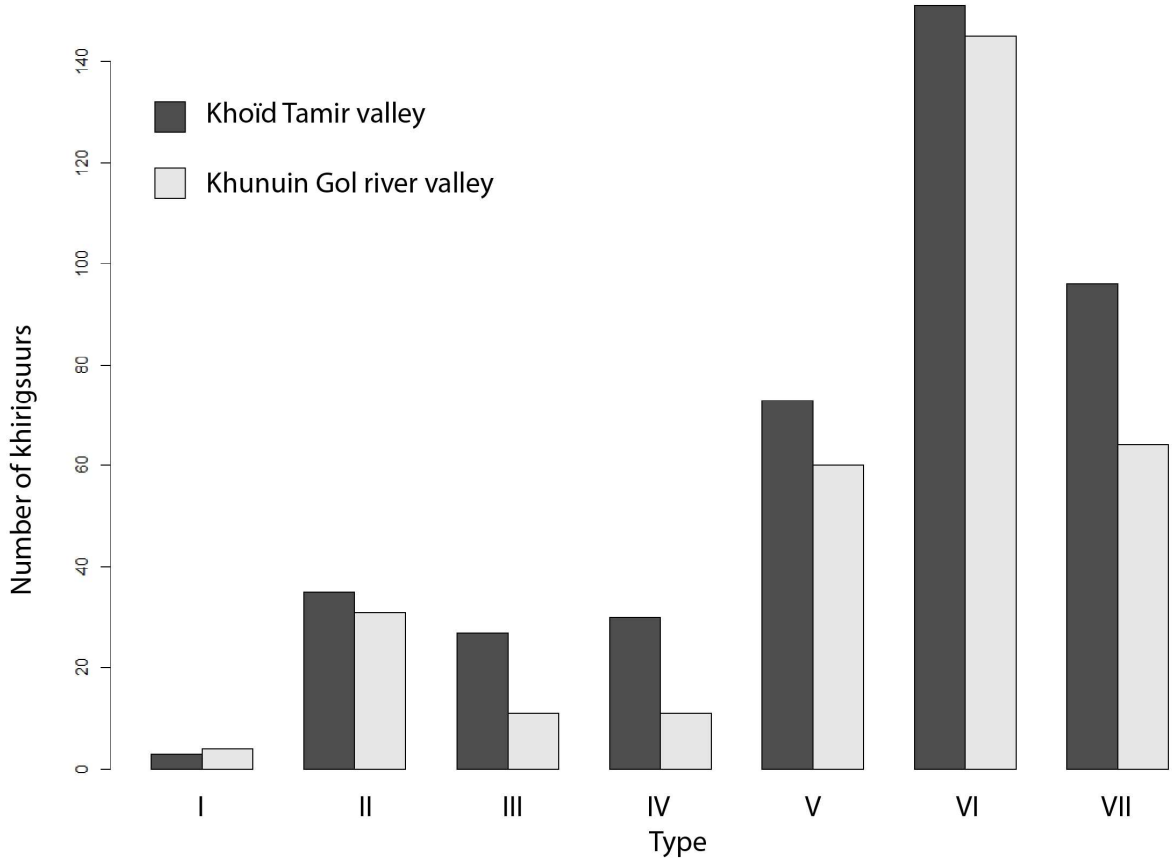

Fig. 10 Comparison of khirigsuur type distributions in the Khoïd Tamir and Khunui gol river valleys.

4. Conclusion

This study introduces a new khirigsuur typology. This typology is based on a set of intrinsic parameters describing the constituent elements of a khirigsuur, together with their position. The descriptors are built to be applicable in any other khirigsuur study and to depict the design of the monument with great precision. Note, however, that the set descriptors has been selected only from the items observed, so that this list is susceptible to be amended by the addition of other architectural elements observable in new, previously unstudied khirigsuurs. Beyond that, this study provides a new approach for quantifying rings and mounts, and the spatial organization of elements, following the monument orientation.

The unsupervised clustering methods used here provide an objective classification, able to deal with a mixed dataset, with versatility. A total of seven types has been defined. The size of the monuments appears to be an important parameter for the definition of these types. Nevertheless, other elements, such as fence highlighting or fence shape, are also important. This new classification supports statistically the empirical

findings presented in previous classifications, which were based on monument complexity, slope value, and the presence/absence of different elements. These new types support the idea that the khirigsuurs evolve in size with the slope. Unfortunately, there are not enough available data to assess the relationship between the types built and their chronology. However, the lack of difference in terms of khirigsuur composition between the neighbouring river valleys of Khoïd Tamir and Khunui may indicate that, in both valleys, the same funeral traditions were followed.

The unsupervised method does not provide only one classification. That proposed here is considered the best, but it is not set in stone. Indeed, the defined types result from several choices. The number of clusters was set according to a mathematical optimization, making sense when taking field data into account. Other numbers of clusters could have been chosen, leading to a slightly different classification where subgroups or supergroups of the current types could also be meaningful. This classification may well change with the addition of new individuals to the dataset. These drawbacks do not diminish the strengths of this method, which is able to provide an objective and reproducible classification of a dataset containing hundreds of individuals, characterized by tens of parameters. This study shows the great potential of unsupervised clustering methods associated with a large corpus for the spatial study of the khirigsuurs over a vast area. Its implementation in new areas should leads to better understanding of khirigsuur culture and its development in the Mongolian territory.

Chapitre 5. Etude typologique des pierres à cerfs

5.1) Organisation des motifs sur les stèles

Les nombreuses études sur les pierres à cerfs ont conduit à la définition de certaines tendances générales quant à l'organisation des motifs gravés (e.g. division de la stèle en trois espaces, cercles au sommet des stèles qui apparaissent par paires). L'organisation des éléments sur la stèle et les associations des symboles les uns par rapports aux autres sont potentiellement porteurs de sens ; un sens qui témoignerait d'une façon de faire ou d'un code dictant la conception d'une pierre à cerfs. L'esprit humain est capable de concevoir les schémas les plus simples à partir de quelques stèles, mais sa limite de perception est vite atteinte lorsqu'on considère des centaines d'objets comportant des dizaines de motifs. Les motifs gravés à la surface des stèles ne sont pas réguliers, et de multiples variants du même objet existent sur l'ensemble des stèles (Fig. 17), ce qui complique considérablement la découverte de règles d'organisation. Tout l'enjeu est donc de développer des méthodes permettant de confirmer ou d'infirmer les schémas pressentis, et d'identifier des schémas plus fins, qui utilisent l'ensemble des données disponibles.

Plusieurs méthodes existant dans d'autres domaines, comme l'économie ou le marketing peuvent être appliquées au cas des pierres à cerfs. L'une d'entre elles consiste à analyser le panier de la ménagère (market basket analysis). Souvent utilisée par les supermarchés, cette méthode permet de déterminer des schémas dans les achats des consommateurs en créant des règles d'associations (Lantz, 2015). Ces règles impliquent deux objets ou deux groupes d'objets. Elles énoncent que l'achat d'un objet A implique de façon probabiliste l'achat d'un objet B. Par exemple l'achat d'une voiture télécommandée implique dans une certaine mesure l'achat de piles, tandis que l'achat de piles n'implique que très rarement l'achat d'une voiture télécommandée. Un très grand nombre de règles

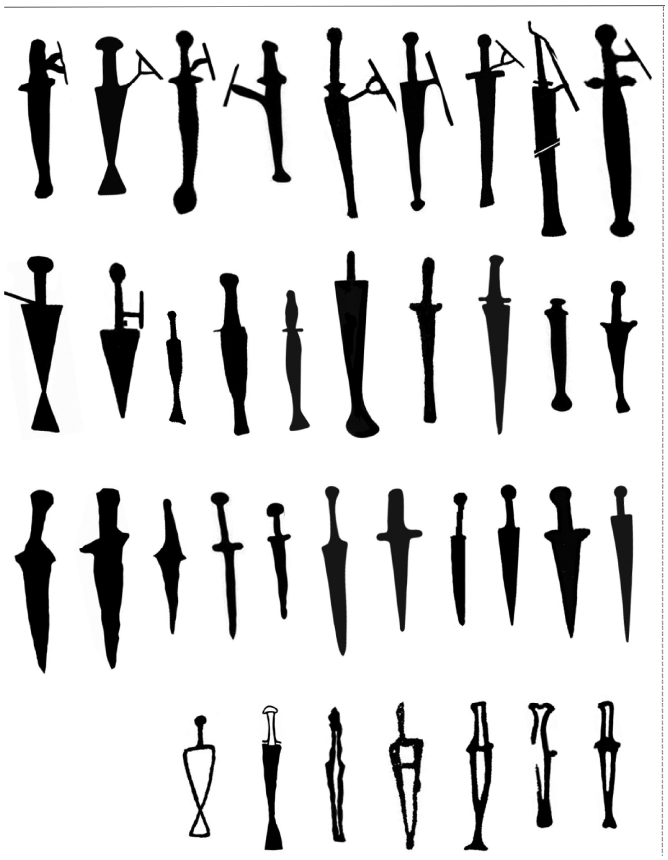

Fig. 17 Exemple de poignards retrouvés sur les pierres à cerfs (d'après Turbat et al., 2021)

peuvent être ainsi créées, et pour chacune d'entre elles, un indice nommé *confidence* en anglais est calculé. Cet indice traduit la puissance de la règle en question. Il représente la probabilité d'acheter des piles quand une voiture télécommandée vient d'être achetée. Plus cet indice est grand, plus la règle se vérifie. La *confidence* est égale à P(B|A), soit la probabilité de réalisation de B sachant que A est déjà réalisé. Un autre indicateur peut être calculé, le *lift* (Lantz, 2015). On trouve cette valeur en divisant la *confidence* d'une règle par la probabilité de croiser l'objet attendu. Cet indice équivaut à calculer P(B|A)/P(B). Cet indice montre l'importance d'une règle et le lien fort entre les objets de cette règle. C'est ainsi que des schémas d'achats peuvent être trouvés à partir des milliers de factures produites par les grands magasins. Il est possible de faire un parallèle avec les pierres à cerfs pour identifier les schémas d'organisation les plus forts parmi les motifs gravés. Ce ne sont plus des achats qui sont considérés, mais des stèles. Les produits sont remplacés par les motifs gravés. Contrairement à un panier où tous les produits achetés sont dissociés les uns des autres, les motifs gravés sont

liés à leurs voisins adjacents dans l'espace que représente la stèle. Ce sont ces liaisons qui seront étudiées ici et qui donneront lieu à des règles d'association. Les règles pourront être énoncées comme suit : la présence du motif A implique une très forte probabilité d'adjacence avec le motif B. Les mêmes indices d'évaluation peuvent être calculés, définissant la probabilité d'existence d'un lien associé à sa *confidence*, ainsi que la sur-représentation ou non de ce lien en fonction d'un cas aléatoire. Une différence demeure cependant entre marketing et archéologie. Si le marketing ne s'intéresse qu'aux règles sur-représentées, désignant l'association fréquente entre deux produits, pour l'archéologue un lien sous-représenté possède tout autant de sens. En effet, des liens forts ou presque inexistants qui s'éloignent d'une organisation des motifs aléatoire, sont symptomatiques d'un choix effectué par l'artiste.

Lier les symboles présents à la surface d'une stèle à leurs voisins adjacents revient à créer un réseau ayant pour nœuds les éléments gravés. Une telle représentation (Fig. 18) ouvre sur tout un domaine d'analyse statistique des réseaux (parfois appelé analyse des graphes). Il devient possible par exemple d'identifier

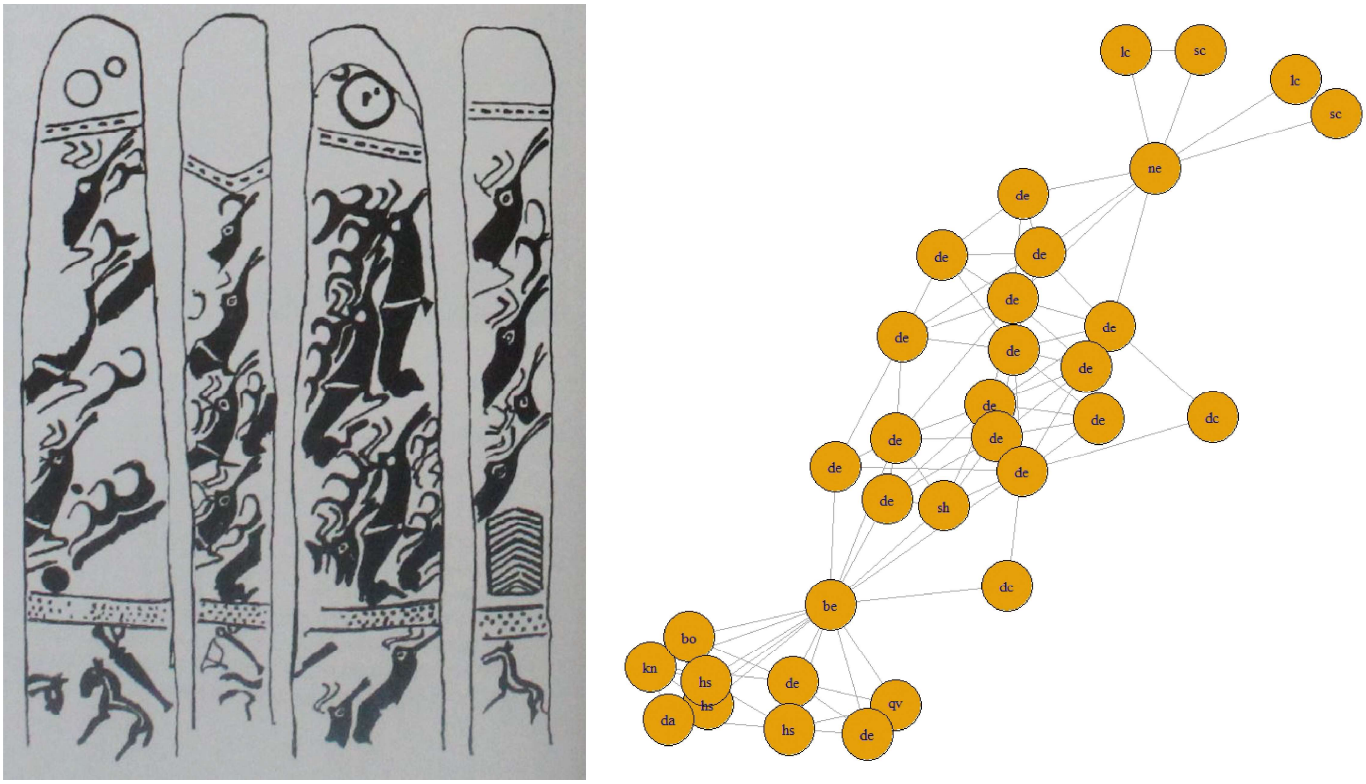

Fig. 18 Relevé de la pierre à cerfs n°2 du site de Daagan del (à gauche) et le réseau obtenu après encodage (à droite).

des points de ruptures, des motifs servant de séparateurs pour deux groupes d'éléments, ou bien d'analyser les chemins reliant différents éléments (nœuds). De nombreux paramètres caractérisent les réseaux, et donc par la même occasion les stèles représentées, apportant des éléments de comparaison entre les pierres à cerfs. Ces caractéristiques peuvent être utilisées pour construire une classification.

5.2. Thésaurus pour l'encodage des stèles

L'approche par les réseaux nécessite la mise en place de descripteurs capables de synthétiser la forme des variants pour l'ensemble des motifs. Malgré les nombreux inventaires montrant les différentes possibilités associées à un type de motif, il n'existe pas de base commune pour la description et la caractérisation des gravures des pierres à cerfs. Il a donc été nécessaire de créer ce lexique descriptif. Le thesaurus proposé ici (établi en collaboration avec Anne Caroline Allard) (version complète annexe 6) se divise en deux niveaux. Le premier désigne le type d'objet concerné : cerf, bouclier, arc, cercle, etc. Le second niveau est associé aux variables décrivant la forme des motifs. Elles sont adaptées pour chaque type et définies en fonction des éléments variants de ce type (Fig. 19). Ces variables qualitatives nominales associent une liste de modalités exclusives entre elles, de sorte qu'un objet ne peut pas être décrit par deux modalités différentes. L'encodage proposé tente d'être le plus exhaustif possible, tout en s'inspirant des travaux de Volkov (1981), de Novgorodova (1989), et de Gantulga et al. (2018). Au total, 31 types d'objets sont différenciés dans ce thesaurus possédant 1 variable descriptive (i.e. présence) pour les formes les plus simples tels que le disque ou la spirale, et 7 variables descriptives pour les cerfs.

Parmi l'ensemble des objets, seuls le bouclier et la ceinture sont décorés. Ces décorations sont le plus souvent composées d'un ensemble de figures géométriques pouvant dessiner des motifs complexes, difficilement descriptibles (Fig. 20). L'approche systémique introduit par vanBerg (1994) pour l'étude des décors de la céramique rubanée fine d'Alsace présente une solution attirante dans

Spirale : spiral	**SP**			
Disque : disc	**DQ** **DC**			
Grand cercle = large circle	**GC** **LC**	**Rayon**		
		Absence	**0**	
		Un	**1**	
		Deux	**2**	
		Trois	**3**	
		Quatre et plus	**4**	
		Ornement		
		Absence	**0**	
		Présence	**1**	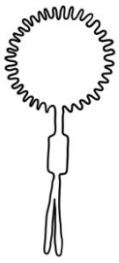
		Remplissage		
		Aucun	**0**	
		Points	**1**	
		Animaux	**2**	
		Autres	**3**	

Fig. 19 Exemple de l'organisation du thésaurus avec le type de motif, les variables descriptives associées et les modalités de ces variables.

notre cas. Dans cette méthode, le décor des céramiques est le résultat de l'association de décors principaux et secondaires (Fig. 21). Ces décors sont eux-mêmes constitués d'unités graphiques élémentaires, ou composants (traits, points,

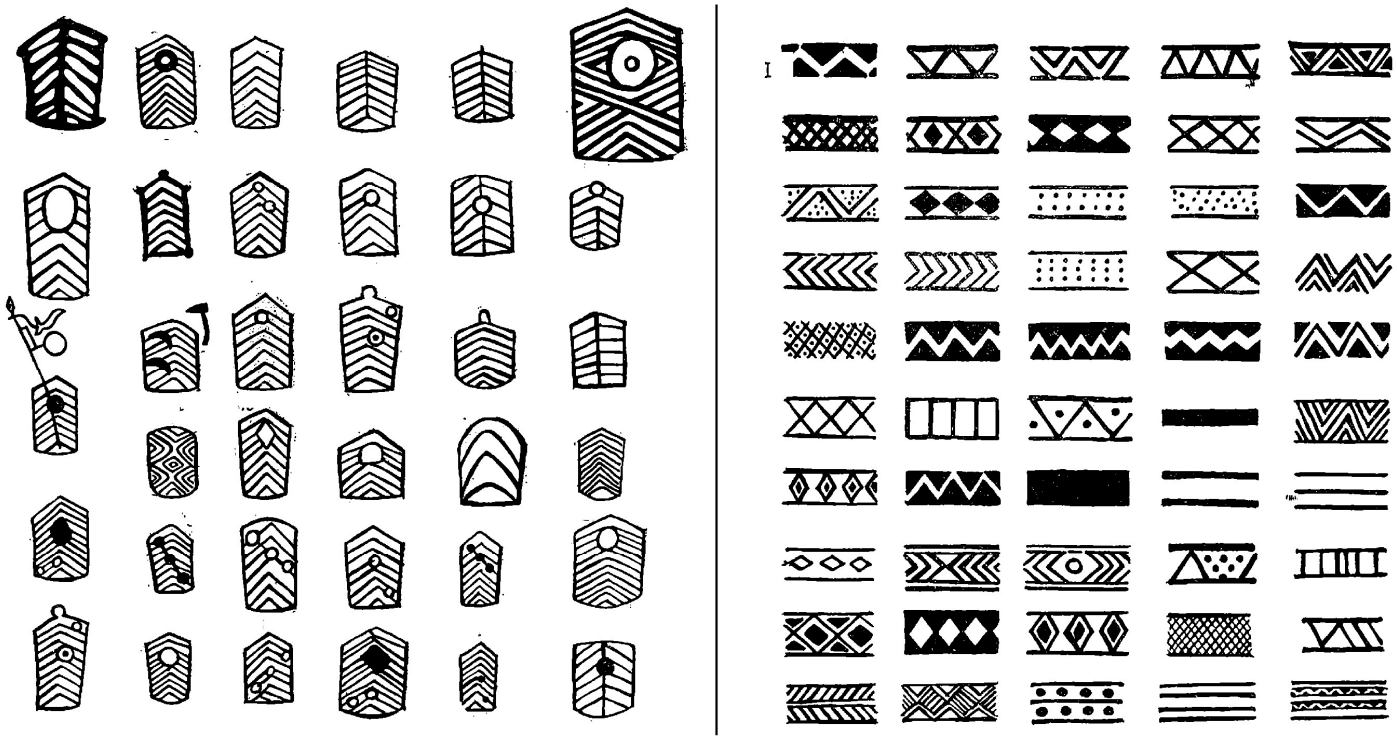

Fig. 20 Exemple de décorations pour les boucliers (à gauche) et les ceintures (à droite) gravés sur les pierres à cerfs (d'après Novgorodova, 1989)

angles), organisées suivant des règles de transformations géométriques (e.g. translation, rotation, homothétie, répétition). Des motifs élémentaires peuvent s'ajouter à cet ensemble, ce sont les élargissements. L'approche systémique caractérise le décor au travers des différentes étapes qui ont permis de passer de l'unité graphique élémentaire au motif final. Les décors sur les pierres à cerfs sont moins sophistiqués que ceux du Rubanée, avec une plus faible variété de motifs élémentaires (angles, triangle, vague, point, trait). De plus, le bouclier et la ceinture définissent des espaces limités qui ne permettent qu'une faible évolution du décor : horizontale pour la ceinture et verticale pour le bouclier (Fig. 20). Le nombre de transformations possibles est donc restreint. Au final, trois étapes sont définies comme variables descriptives pour ces objets : la forme, le remplissage et l'embellissement. Le remplissage correspond à l'association des unités graphiques ayant pour certaines subi une transformation. Ces cas étant assez rares, il a été décidé de les associer avec les unités graphiques élémentaires.

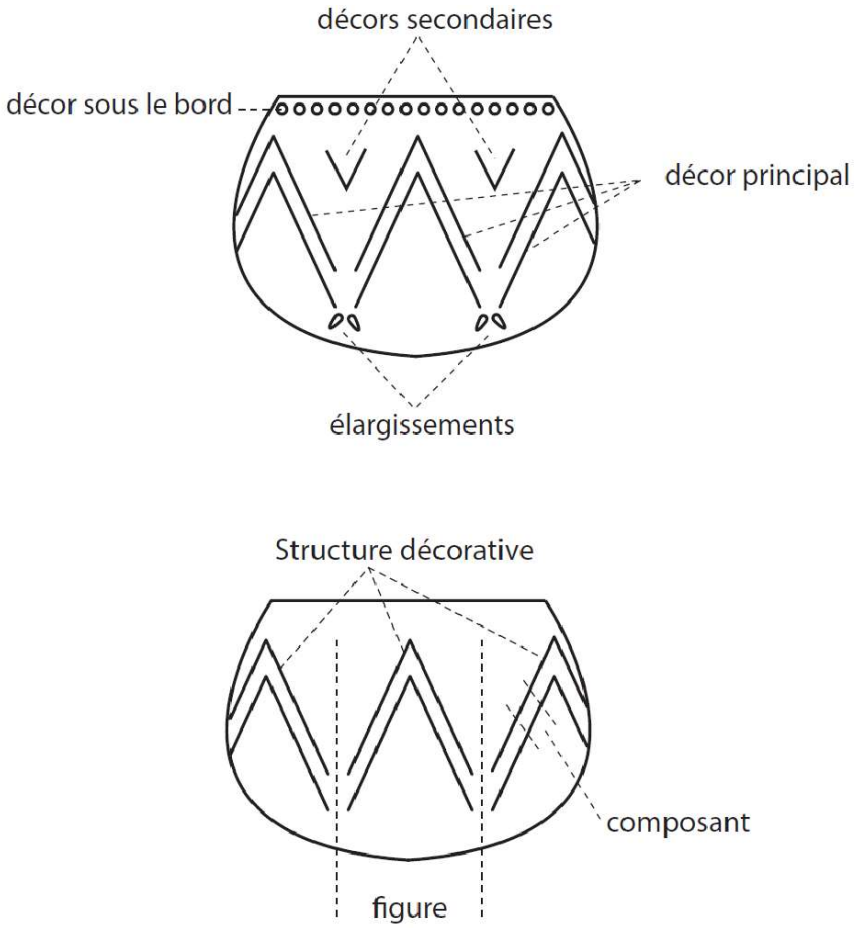

Fig. 21 Vocabulaire associé à la méthode systémique pour la description des décors de la céramique Rubanée (d'après Houbre,2013)

La définition de l'élargissement pour le Rubanée correspond ici à l'embellissement.

Chaque modalité d'une variable est associée à un facteur (0, 1, 2, …) qui ne doit pas être considérée comme numérique. La forme d'un motif est encodée *via* deux lettres indiquant le type de motif auquel on se réfère, suivies des facteurs associés aux modalités de ce type (Fig. 22) ; la chaine de caractères produite étant le résultat de la combinaison de plusieurs variables. Cet encodage peut être simplifié à loisir en ôtant les éléments correspondants aux variables non désirées.

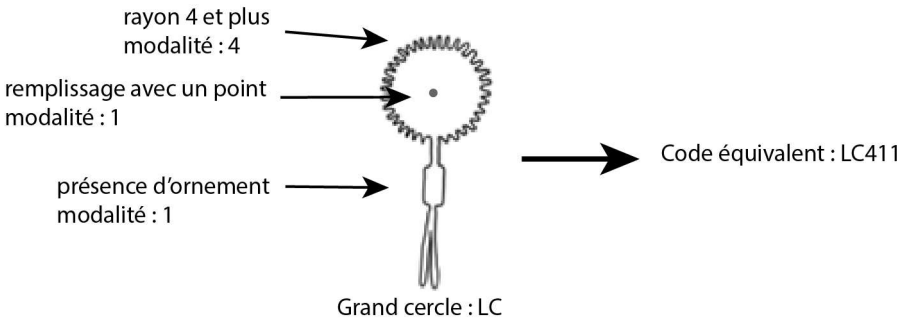

Fig. 22 Exemple d'application du thésaurus pour encoder un symbole

5.3) Premiers résultats

Une étude préliminaire a été menée sur un échantillon de 314 pierres à cerfs dont la répartition par type est : 111 eurasiennes, 187 mongol-transbaikales et 17 sayan-altai. L'enregistrement des stèles sous forme de réseau a été effectué à partir de relevés présents dans Turbat et al. (2018). Au total 4941 motifs et 11774 ont été encodés dans le cadre du travail de Master 2 ASA de Elodie Maronat. Les premiers essais utilisent une description minimale des iconographies qui se limite à la nature des objets. Le cerf domine largement, avec près de 55% de l'effectif total (Fig. 23A) ; vient ensuite, loin derrière, le grand cercle qui représente 6.5% des motifs. Si en revanche on s'intéresse aux stèles présentant au moins un représentant d'un type, la distribution est toute autre (Fig. 23B). Dix types sont présents sur au moins un tier des pierres à cerfs, tandis que le poisson, la masse, le char, et le yack ne dépassent pas 2 occurrences dans le corpus. La *confidence* des liens montre clairement que le cerf domine l'organisation de la stèle avec la présence de 18 liens cerf-objet parmi les 20 plus fortes valeurs de *confidence*. La multiplication d'un motif a de fortes chances d'augmenter naturellement le nombre de liens avec les autres motifs, et par la même occasion la probabilité de rencontrer ce lien sur une stèle. Le *lift* pondère cet effet avec la probabilité de rencontrer les objets. Cette pondération met en avant les liens (ou l'absence de liens) vraiment porteurs de sens, pour lesquels l'association entre

les deux motifs était un choix (ou un interdit).

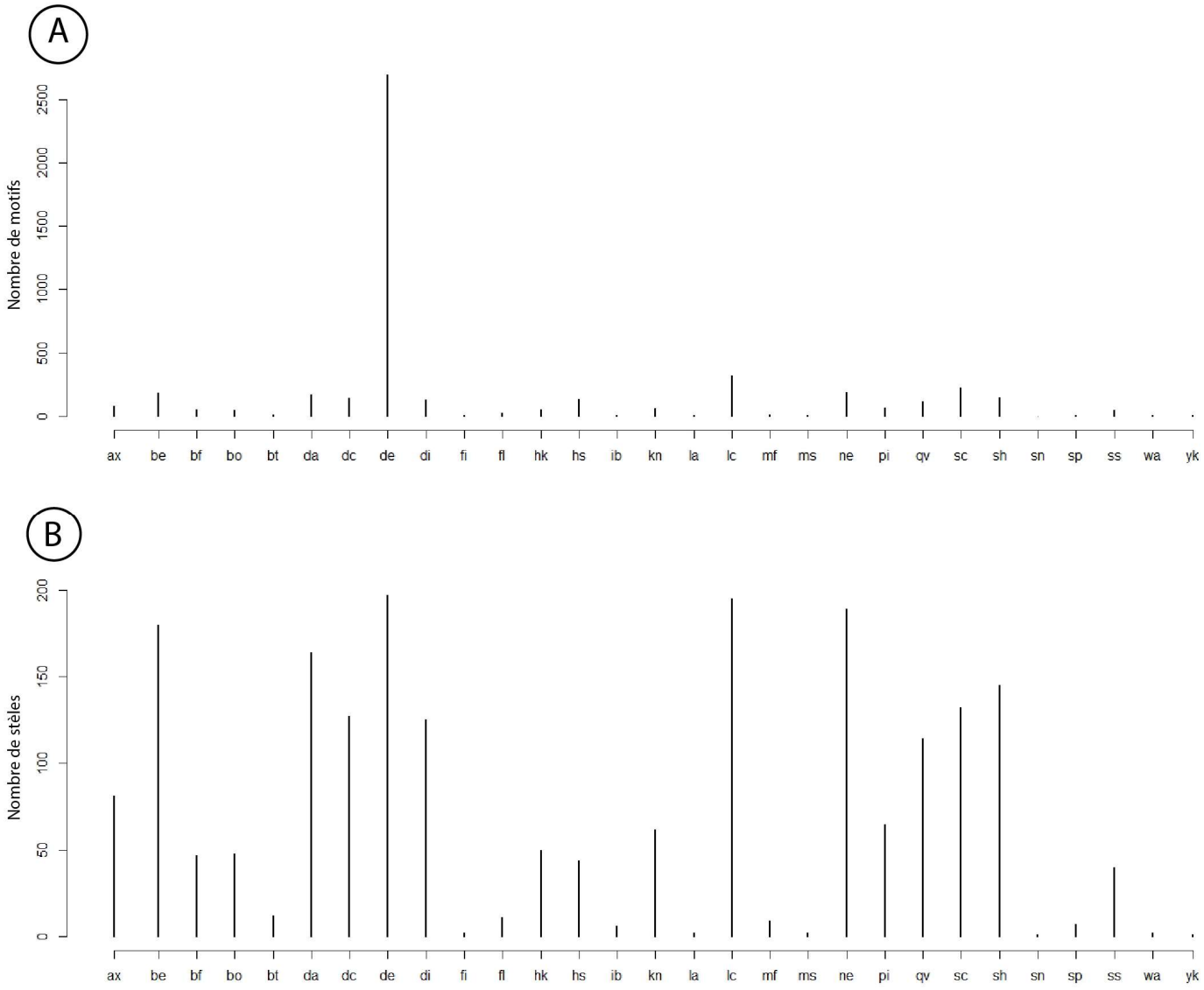

Fig. 23 A) Représentation du nombre d'individus par types. B) Nombre de stèles contenant au moins un exemplaire du type concerné. De gauche à droite les types de motif sont : Hache, Ceinture, Bandeau, Sanglier, Matraque, Poignard, Disque, Cerfs, Obliques, Poisson, Félin, Crochet, Cheval, Bouquetin, Couteau, Lance, Grand disque, Visage, Masse, Collier, Pic, Carquois, Petit cercle, Bouclier, Spiral, Pierre à aiguiser, Char, Yack.

Il est possible de caractériser une stèle par les liens qu'elle possède. La proximité entre deux stèles peut alors être envisagée en comparant leur composition en termes de liens. Utiliser la distance euclidienne risquerait de donner trop de poids aux liens avec des cerfs car ces derniers sont très nombreux. La distance du chi2 proposée par Catherine Labruère-Chazal et Ahmed Jébrane

est une métrique ayant l'avantage d'éliminer l'effet généré par le grand nombre de cerfs. La distance entre deux stèles A et B, d_{AB}, est calculée par :

$$d_{AB} = \sum_{i=1}^{k} (\frac{1}{n.i})(f_{Ai} - f_{Bi})^2$$

Où k est le nombre total de types de lien différents dans l'échantillon. $n.i$ représente le nombre total de lien du type i dans l'échantillon. f_{Ai} correspondent à la proportion de liens de type i sur la stèle A.

Il est alors possible de calculer, avec cette métrique, une matrice de distances décrivant la proximité entre chaque stèle avec laquelle il est possible d'appliquer un algorithme de classification. La figure 24 montre le dendrogramme obtenu par classification hiérarchique suivant la méthode de Ward (c'est-à-dire, la même que celle utilisée pour la classification des khirigsuurs). Cinq groupes semblent se détacher dont trois de tailles similaires, un plus petit et un plus conséquent ; un certain nombre de stèles se séparent très haut dans l'arbre, notamment sur la gauche du dendrogramme. Ces dernières sont très différentes de l'ensemble du corpus et se comportent comme individus hors normes. Ce sont des stèles possédant très peu de gravures (une ou deux seulement). Les groupes identifiés correspondent plutôt bien à la typologie en vigueur (Eurasien, Sayan-Altaï, Mongol-Transbaïkal), repérable par un code couleur. Le plus grand groupe correspond aux stèles du type Mongol-Transbaikal, trois des groupes sont constitués de pierres à cerfs du type Eurasien, et le dernier, à droite, rassemble majoritairement des stèles eurasiennes et sayan-altai.

Cette étude préliminaire montre qu'une classification des stèles basée sur l'organisation des motifs est envisageable. Les premiers résultats obtenus avec la méthode hiérarchique sont cohérents avec la classification actuelle et semblent indiquer la possibilité de définir des sous-groupes, au moins dans le type Eurasien. Il serait intéressant d'effectuer une classification en prenant en compte davantage de variables descriptives qualifiant les motifs. Il pourrait être également envisagé de diviser au préalable le corpus en fonction de la classification actuelle afin de rechercher spécifiquement la présence de sous-groupes potentiels. Une caractérisation plus poussée des réseaux formés par les stèles avec des paramètres tel que la centralité, la modularité ou la densité, par

exemple, pourrait intégrer la classification.

Il pourrait être judicieux d'augmenter le nombre de variables utilisées dans la description des cerfs. Ceci créerait des catégories d'objets avec de plus faibles effectifs, ce qui pourrait affiner les règles d'associations, voire de confronter ces dernières avec la distribution spatiale des différents groupes constitués.

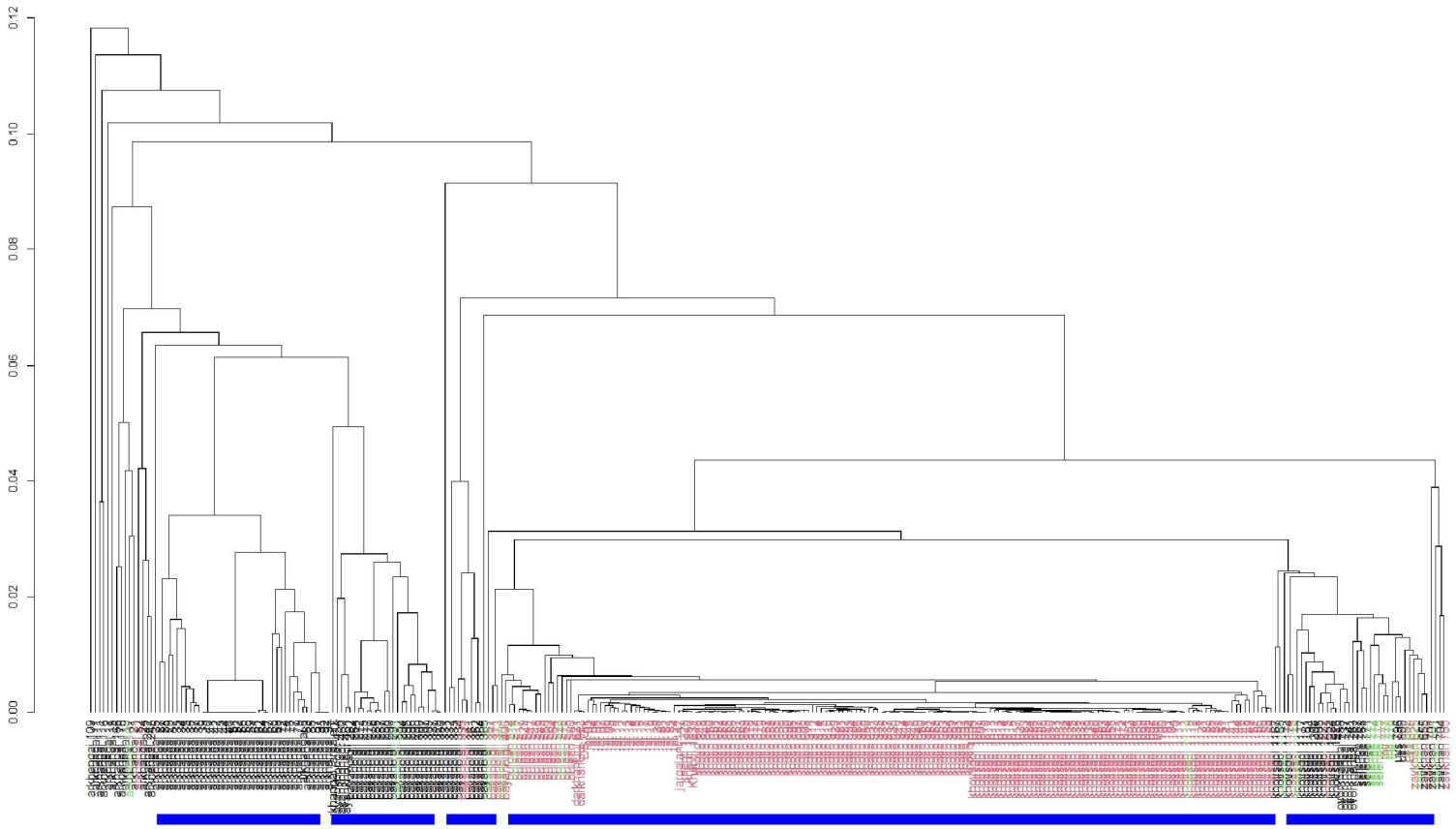

Fig. 24 Dendrogramme obtenu par la méthode Ward. Les segments bleus désignent cinq groupes potentiels. En rouge le type Mongol-Transbaïkal ; en noir le type Eurasien ; en vert le type Sayan-Altaï.

Chapitre 6. Valorisation et sauvegarde des données

6.1) Valorisation des données

La valorisation des données archéologiques est un aspect de la recherche qui ne doit pas être négligé. Il est important de rendre accessible les découvertes, non seulement aux autres chercheurs, mais également au grand public. Cette communication hors cadre académique se fait au travers de nombreux supports : posters, films, expositions, etc. L'avènement de l'utilisation de la 3D en archéologie à quelque peu changé la donne, puisqu'il a fallu s'adapter à ce type de données. De nouveaux supports de médiation ont donc vu le jour, ou se sont démocratisés. L'impression 3D des modèles d'objets permet de passer du virtuel au réel, facilitant ainsi leur manipulation par le grand public ou les étudiants. L'exposition d'objets uniques devient possible, sans aucun déplacement depuis leur lieu de conservation. Les scènes virtuelles, quant à elles, permettent l'intégration des modèles 3D dans des films, des visites virtuelles, des jeux, etc. Un certain format de visite virtuelle ne s'appuie pas sur des rendus 3D mais sur des photos 360° ou photosphères qui procurent au spectateur un sentiment d'immersion dans la scène d'origine. Celui-ci est particulièrement fort lorsqu'un casque de réalité virtuelle (VR) est utilisé. Ces visites sont généralement interactives, incluant vidéos, images, textes, sons, et éventuellement augmentations de la scène observée. Le travail qui suit porte sur une méthode de projection de données, 2D et 3D, sur une photosphère, afin d'y inclure directement les informations apportées par la documentation archéologique, et d'augmenter ainsi l'immersion des utilisateurs dans l'environnement de la visite virtuelle. Cette immersion a pour but de faciliter la compréhension de ces données et de leur contexte. C'est un outil didactique très utile pour les chercheurs qui ont aussi besoin de se replonger dans un terrain éloigné ou difficile d'accès.

sustainability

MDPI

Article

Contextualization of Archaeological Information Using Augmented Photospheres, Viewed with Head-Mounted Displays

Fabrice Monna [1,*], Nicolas Navarro [2,3], Jérôme Magail [4], Rodrigue Guillon [5], Tanguy Rolland [1], Josef Wilczek [1,6], Yury Esin [7] and Carmela Chateau [8]

1 ARTEHIS, UMR 6298 CNRS, Université de Bourgogne Franche-Comté, 21000 Dijon, France
2 Biogéosciences, UMR CNRS EPHE 6282, Université Bourgogne Franche-Comté, 21000 Dijon, France
3 EPHE, PSL University, 75014 Paris, France
4 Musée d'Anthropologie Préhistorique de Monaco, MC 98000, Monaco
5 Archéologies Sciences de l'Antiquité, UMR 7041 CNRS Université de Paris 1, 92023 Nanterre, France
6 Department of Archaeology, University of Hradec Králové, 50003 Hradec Králové, Czech Republic
7 Khakassian Research Institute of Language, Literature and History, 655017 Abakan, Russia
8 UFR SVTE, Université de Bourgogne Franche-Comté, 21000 Dijon, France
* Correspondence: fabrice.monna@u-bourgogne.fr; Tel.: +33-038-0396360

Received: 19 May 2019; Accepted: 8 July 2019; Published: 17 July 2019

Abstract: Photospheres, or 360° photos, offer valuable opportunities for perceiving space, especially when viewed through head-mounted displays designed for virtual reality. Here, we propose to take advantage of this potential for archaeology and cultural heritage, and to extend it by augmenting the images with existing documentation, such as 2D maps or 3D models, resulting from research studies. Photospheres are generally produced in the form of distorted equirectangular projections, neither georeferenced nor oriented, so that any registration of external documentation is far from straightforward. The present paper seeks to fill this gap by providing simple practical solutions, based on rigid and non-rigid transformations. Immersive virtual environments augmented by research materials can be very useful to contextualize archaeological discoveries, and to test research hypotheses, especially when the team is back at the laboratory. Colleagues and the general public can also be transported to the site, almost physically, generating an authentic sense of presence, which greatly facilitates the contextualization of the archaeological information gathered. This is especially true with head-mounted displays, but the resulting images can also be inspected using applications designed for the web, or viewers for smartphones, tablets and computers.

Keywords: virtual reality; archaeology; scientific mediation; visualization; cultural heritage; registration; thin-plate spline; Procrustes; projection; computer graphics

1. Introduction

In archaeology, as well as in other scientific fields where information derived from the environment is of primary importance, the physical presence of researchers at the site under investigation is often beneficial for the quality of interpretations. Knowledge of the environmental context (e.g., topography, vegetation cover, presence of anthropogenic structures, geomorphological or geological peculiarities, etc.) beyond the zone studied generally contributes to better understanding of the processes and potential interactions that have presided over the development of the site. Archaeologists therefore seek to describe context, far beyond the restricted geographical extent of excavated areas. Despite these attempts, without physical presence at the site, it is often difficult to apprehend space (by fixing references, and estimating scales, distances, and volumes), since spatial perception is closely related

to personal sensory experience [1]. For example, Henri Poincaré stated that locating an object in space is simply figuring out the physical movements that would be necessary to reach it [2]. Even the best photographs, which incorporate scale, can only convey some of the relationships that exist between objects and/or structures, because perceived distances and angles cannot be fully described by a single perspective [3]. The field of view covered by photographs is limited by the focal length of the lens, and the world is generally rendered at eye level (i.e. from one to two meters above the ground). Geographical information systems (GIS) are efficient for the manipulation and analysis of spatial information layers [4], but generally fail when attempting to render any physical sensation of space. Innovative solutions can nowadays be found in the field of virtual reality (VR). The concept of virtual archaeology was first proposed by Paul Reilly in 1990 [5], when he originally referred to the use of three-dimensional models of buildings and artefacts for documentation purposes. The considerable advancements in the field of computer graphics during the past few decades have led to the development of virtual tours staging archaeological information in virtual worlds. These tours are often based on web viewers, where 360° photos (also known as spherical panoramas or photospheres) are used for navigation, while trigger buttons provide access to specific archaeological information in 2D (plans, etc.) or 3D form [6–10]. Three-dimensional models may also be rendered in interactive virtual 3D scenes, enhancing the feeling of presence [11], or for research purposes, such as testing hypotheses [12]. The interest of such virtual tours, integrating informational modeling, is obvious for heritage preservation [13]. Virtual environments can thus be created, providing documentation, interpretation, and information about the conservation state of the archaeological remains [6]. Interestingly, virtual tours also convey valuable information for education [14,15]. As suggested by Barcelo [16], scientific visualization should no longer be restricted to "presentation" techniques, but should also include explanatory tools. Incorporating archaeological documentation directly into the 360° scene (and separately as often the case) is expected to reinforce the feeling of immersion, more particularly when tours are experienced via wide field-of-view, immersive, head-mounted displays (HMDs) [17,18]. Such devices provide a better sense of scale and depth than any printed document or image displayed with standard monitors and projectors [19], even though absolute egocentric distances may be slightly underestimated by HMDs, compared to the real world [1]. Given an interpupillary distance of about 6 cm, we are not able to apprehend a 3D scene solely by stereoscopic vision for objects further away than 10–20 m [20]. To estimate depth and scale, our brain therefore uses the presence of familiar objects, assumed to be of normal size, interprets the possible overlay of object contours, and the distribution of highlights and shadows, and analyzes linear perspectives [21]. Therefore, a full 3D rendering (i.e., the production of two different, shifted images, one for each eye) is not always necessary, and simple 2D photospheres may suffice to apprehend space. The ability to augment, on demand, 2D representation as a photosphere of an archaeological site with pertinent information (e.g., maps, 3D models, virtual reconstruction, etc.) would be advantageous for research purposes, for disseminating discoveries to a broader audience, and even to promote tourism. For scenes modelled entirely in 3D, registering any additional 3D models is relatively easy, using specialized game engines, such as Unity, Blender, or others [22,23], because 3D coordinates on which new documents must be attached are available. After registration, the scene can then be rendered using a virtual 360° camera. Projecting the same documents on 2D photospheres may be much more problematic. Photospheres acquired from the air or from the ground are neither georeferenced nor oriented, nor do they contain information about depth. Equirectangular projection also suffers from polar deformation (e.g., North and South Poles are stretched over the entire width of the image, at the top and bottom edges, respectively). Accurate registration of objects close to polar regions may be far from straightforward, as these regions appear highly distorted. Some authors therefore simply place the 3D model inside a rendered virtual scene, and then manually translate, rotate, and scale-up, to reach the appropriate alignment [24]. When integrating 2D documents produced by orthoprojection, severe visual mismatches with the photosphere may occur due to parallax issues. In such cases, there is no chance that good results will be achieved manually, even after many attempts. To the best of our

knowledge, there is no simple procedure available nowadays for accurate registration of 2D or 3D archaeological information on equirectangular projections, whether in game engines, or in packages or libraries of the main programming languages. The aim of this study is therefore to propose practical workflows to overcome these drawbacks, with data from the archaeological sites of Loropéni (Burkina Faso) and Tsatsiin Ereg (Mongolia).

2. Materials and Methods

2.1. Study Sites

The photospheres and archaeological information presented here were acquired from two archaeological sites. The first is the Loropéni ruins, in Burkina Faso, probably dating from the fifteenth century [25], and listed as a World Heritage site by UNESCO since 2009 [26,27]. This imposing enclosure, with laterite stone walls up to 6 m high, built to protect buildings, courtyards, and alleys, covers about 1 ha, and is surrounded by wooded savanna. The second site, at Tsatsiin Ereg, Mongolia, is composed of large burial structures, with decorated stelae belonging to the Khereksuur and Deer Stone cultures [28]. These stelae were raised at the end of the second to early first millennium BC. Standing about 0.5–5 m tall, these megaliths were hand-carved with graceful symbols, including stylized deer [29].

2.2. Photosphere Assembly

The ground-based spherical panoramas were acquired using a Roundabout-NP Deluxe II 5R panoramic tripod head (Roundabout-NP, Rosenheim, Deutschland), to which was attached a DSLR Nikon D800 (Nikon Corporation, Tokyo, Japan), equipped with a NIKKOR 24 mm prime lens (Nikkor, Tokyo, Japan); see Supplementary Materials, Text S1 for more details about principles of equirectangular projection. The use of a panoramic head allows the nodal point of the lens to be maintained on the rotation axis, avoiding stitching failure, in particular for the nearest objects. Two sets of 12 pictures, using a horizontal rotation of 30° between pictures, were taken at +30° and −30° from the horizontal plane. Two additional pictures were acquired, one for nadir and one for zenith. For aerial views, a Phantom 3 PRO from DJI was used, in combination with the Litchi application for Android. This combination allows the seamless automatic acquisition of a set of pictures, covering slightly more than the entire southern hemisphere. Three rows of 13 pictures with different inclinations were necessary for appropriate coverage and overlapping. The images were stitched together with Autopano Giga Pro 4, Kolor/Gopro (Kolor, Francin, France), a software program also used to produce the final equirectangular images, limited here to 6000 × 3000 pixels. The northern hemisphere, depicting the sky, which cannot be captured by drone, contained no archaeological information. It was therefore manually completed for natural rendering. For ground acquisition, the tripod visible at the nadir was simply patched with a logo.

2.3. Programming

The code snippets allowing the registration of archaeological information were written, for images, in Python 3.6, with the help of the opencv, numpy, png, and matplotlib libraries, and a set of functions written for the CellTool software [30]. For 3D models, the script used the R language [31] in combination with the Morpho, mesheR, rgl, Rvcg, and png packages. Codes are provided as Supplementary Materials (Codes S1 and S2).

3. Method Implementation

3.1. Registration of Planar Documentation on Approximately Horizontal Surfaces

With aerial photospheres taken at a sufficient elevation above the ground, there is a good chance that an archaeological structure located close to the South Pole can be considered to be approximately

horizontal. This approximation means that its projection from the position where the viewer stands, on any horizontal plane situated below the viewer, produces an image of the structure possessing the same shape as the orthographic map to be registered (Figure 1). In this case, registration can easily be accomplished by Procrustes transformation, using the sum of errors between input and target landmark coordinates as a goodness-of-fit criterion [32–34]. Expressed more formally, let **P** and **Q** be two configurations of n points on input and target images. The aim is to find a rigid-body transformation **T** so that:

$$\min_{\boldsymbol{T}} \|\boldsymbol{PT} - \boldsymbol{Q}\| \quad (1)$$

with **T** a matrix corresponding to translation, orthogonal rotation, and uniform scaling (see [29] for details of optimization methods).

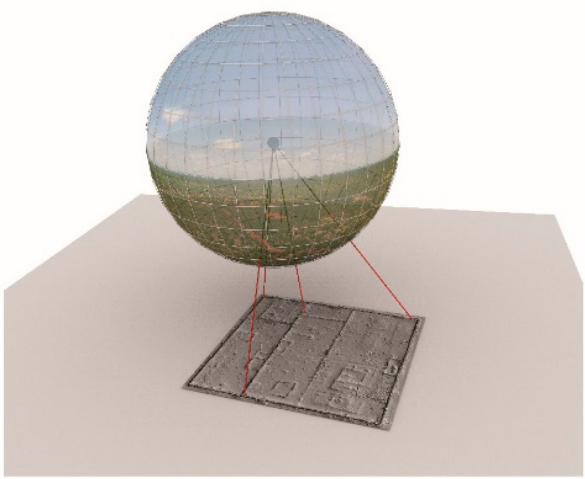

Figure 1. Registration of planar archaeological information on the horizontal plane.

Once registered, the image can be projected onto the sphere, and then transformed by equirectangular projection. The problem is how to select with precision at least three (preferentially more) unambiguous and not collinear landmarks on the equirectangular image, given that the area of interest lies in the distorted part of the southern hemisphere with aerial photospheres. For this step, the sphere is first rotated to make the region of interest coincide with the South Pole. The southern hemisphere is then stereographically projected from the North Pole (0, 0, 1) onto a plane below the sphere, here tangent at the South Pole (0, 0, −1) [35]. Such a projection is not recommended for mapping large parts of the southern hemisphere due to the high distortion appearing close to the equator, but it performs well close to the South Pole [36], where the site of interest lies. Archaeological structures become clearly visible and landmarks can be precisely positioned. Note that the workflow would have been simplified if the first stereographic projection used to define the landmark's position had been performed directly from the center of the sphere, instead of from the North Pole. Tests nonetheless proved that, for large structures, a projection from the sphere center produces more distortion, increasing further from the nadir, and making landmark positioning more difficult. The example presented here uses an aerial view of Loropéni, on which is projected a high-resolution hill-shaded digital elevation model (DEM), produced by photogrammetry from more than 4000 pictures taken at eye level (Figure 2).

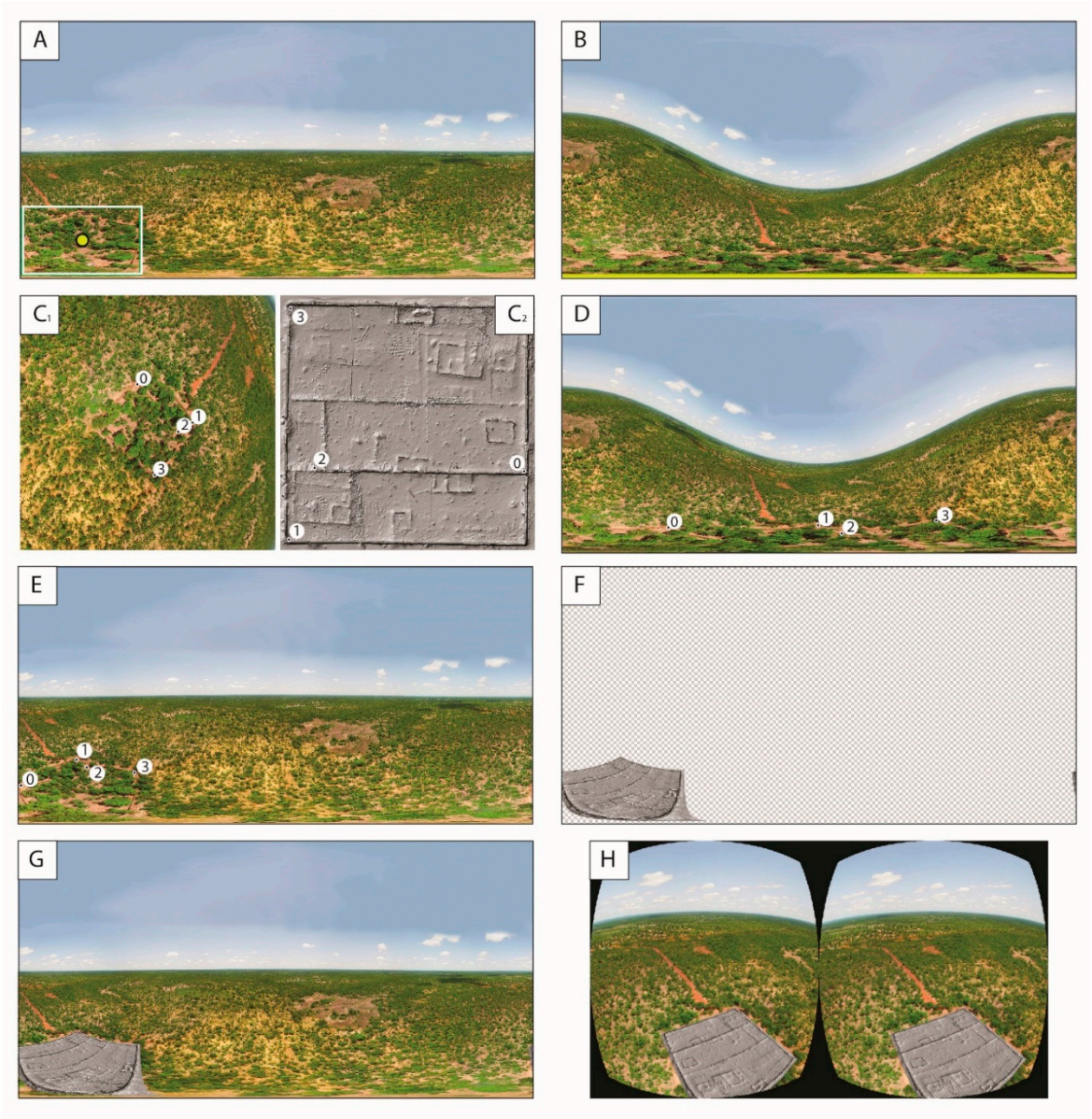

Figure 2. Workflow for registering planar documentation (horizontal structures). (**A**) Original equirectangular image with the center of interest marked (yellow dot); (**B**) the photosphere is rotated in order to place the center of interest at the South Pole; (**C_1**) stereographic projection (target image) with four landmarks positioned (0–3); (**C_2**) input image (here digital elevation model (DEM) acquired by photogrammetry from pictures taken from the ground, represented as shaded relief) with the four corresponding landmarks (0–3); (**D**) projection of the landmarks onto the photosphere; (**E**) rotation of the photosphere back to its original position, including landmarks; (**F**) projection onto the unit sphere of the registered input image, after Procrustes transformation and equirectangular projection; (**G**) incorporation of the deformed input image into the original photosphere; and (**H**) binocular rendering for head-mounted display (HMD).

The workflow is summarized below:

1. Determine the coordinates of the center of the area of interest on the equirectangular image (Figure 2A).
2. Rotate the sphere in order to place the center of interest at the South Pole (Figure 2B).
3. Project the area surrounding the South Pole stereographically on a tangent plane, using the North Pole as reference (Figure 2C_1).

4. Position a set of landmarks manually on the document to be registered (input) and on the stereographic projection (target) (Figure 2C_1,C_2).
5. Back-project the target landmarks onto the unit sphere (North Pole as reference) (Figure 2D).
6. Rotate the landmarks together with the unit sphere to return to the sphere's original position (Figure 2E).
7. Project the landmarks on a plane tangent to the South Pole, taking the center of the unit sphere as reference.
8. Calculate the rotation matrix, scaling factor, and translation vector, from input to target coordinates by rigid Procrustes registration (cf. Equation (1)).
9. Position the transformed input image in the tangent plane coordinate system.
10. Back-project the registered image onto the unit sphere (sphere center as reference).
11. Perform an equirectangular projection of the image to be registered (Figure 2F), and add as background the original image (Figure 2G).
12. The final image is ready to be seen in HMD (Figure 2H).

The registered image perfectly fits the archaeological structures (Figure 2G,H; see also in Supplementary Material, Figures S1 and S2 for the original and augmented jpeg images), strengthening the feeling of immersion for the viewer, particularly when the augmented image is viewed with the HMD. Note that any other map could be projected following the same procedure.

3.2. Registration of Planar Documentation on Irregular Surfaces

It is also quite common for the topographical surface to be irregular, or for the viewpoint not to be elevated enough to consider this surface as reasonably horizontal. Figure 3 illustrates the problems related to parallax when points of interest are located on an irregular surface. Let A′, B′, C′ be the apparent position on the horizontal plane of points A, B, C from viewpoint 1, and A″, B″, C″ from viewpoint 2, while A‴, B‴, C‴ are the orthographic projection of A, B, C (e.g., a map of the area). The distances between points of interests A′, B′, C′ and A″, B″, C″ projected onto the plane are no longer proportionate to their counterparts, A‴, B‴, C‴, on the map to be registered (cf. Figure 3). This is especially true from viewpoint 1: B′ appears much closer to C′ than to A′, while B‴ is approximately in mid-position between A‴ and C‴. Note that from viewpoint 2, the ratios of distances between points are in greater conformity with those observed on the map, because of the approximately zenithal position of viewpoint 2, and its high elevation in relation to variations in relief. In such circumstances, especially for the scene observed from viewpoint 1, any rigid registration of the map is not recommended, because serious mismatches are expected if the map is registered using the Procrustes procedure described above. Practical solutions can rather be found in non-rigid techniques, such as thin plate splines (TPS), a method popularized by image morphing. This technique is based on surface interpolation, using a curve-smoothing spline function over scattered control points. As constraints, the input surface is deformed using minimal bending, and all landmark pairs belonging to both input and target must coincide [37]. Warping with TPS requires more point placements than Procrustes registration, because deformation may produce some mismatches, especially close to the edges (if not well constrained by several control points). In practice, the proposed workflow is comparable to the one described above, except that TPS warping is applied in place of Procrustes registration, and that the stereographic projection from the center of the sphere is unnecessary, since TPS accounts for all deformation. The example provided here concerns the burial structures of Tsatsiin Ereg. An orthomosaic was produced from aerial images over a 16 ha area, very rich in funeral monuments made of dry stones. A supervised machine-learning algorithm was applied to delineate the stones automatically on the basis of RGB channels, texture parameters, and elevation (more details about the procedure will be provided in [38]). The aim is to project this information onto the photosphere, to make the structures more visible for the spectator.

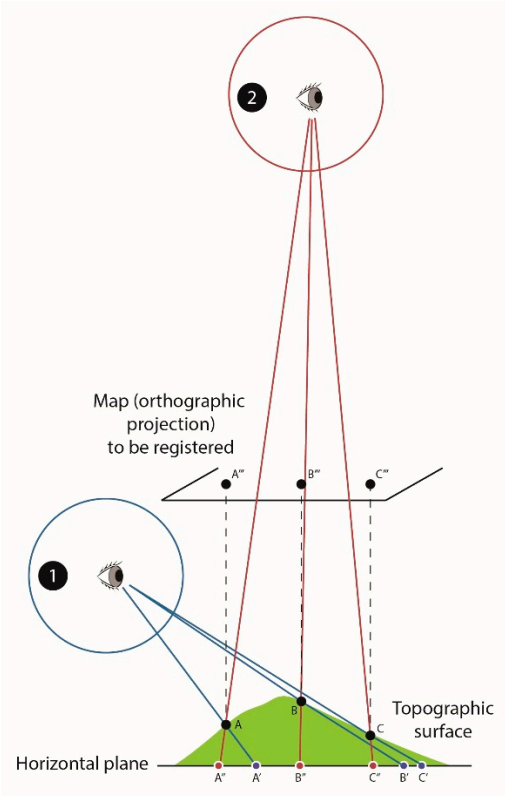

Figure 3. Problems related to parallax when points of interest A, B, C, are located on an irregular surface. A′, B′, C′ and A″, B″, C″ correspond to the projection of A, B, C on the horizontal plane from viewpoint 1 and viewpoint 2, respectively. The distance ratios between A′, B′, C′, or between A″, B″, C″ are not proportionate to those between A‴, B‴, C‴, corresponding to the orthographic projection of A, B, and C on the map to be registered.

A total of 87 control points were therefore placed on both input and target images. The workflow is as follows:

1. Determine the center of the area of interest on the equirectangular image.
2. Rotate the unit sphere in order to place the center of interest at the South Pole (Figure 4B).
3. Project the area surrounding the South Pole stereographically onto a tangent plane, using the North Pole as reference (Figure 4B_1).
4. Place a set of control points manually on the stereographic projection (target), and on the document to be registered (input) (Figure 4B_1,B_2).
5. Perform TPS deformation of the input image (Figure 4C)
6. Project the deformed input image onto the unit sphere.
7. Rotate the sphere to return it to its original position.
8. Perform equirectangular projection (Figure 4D), and add the original image as background (Figure 4E).
9. The final image is ready to be seen in HMD (Figure 4F).

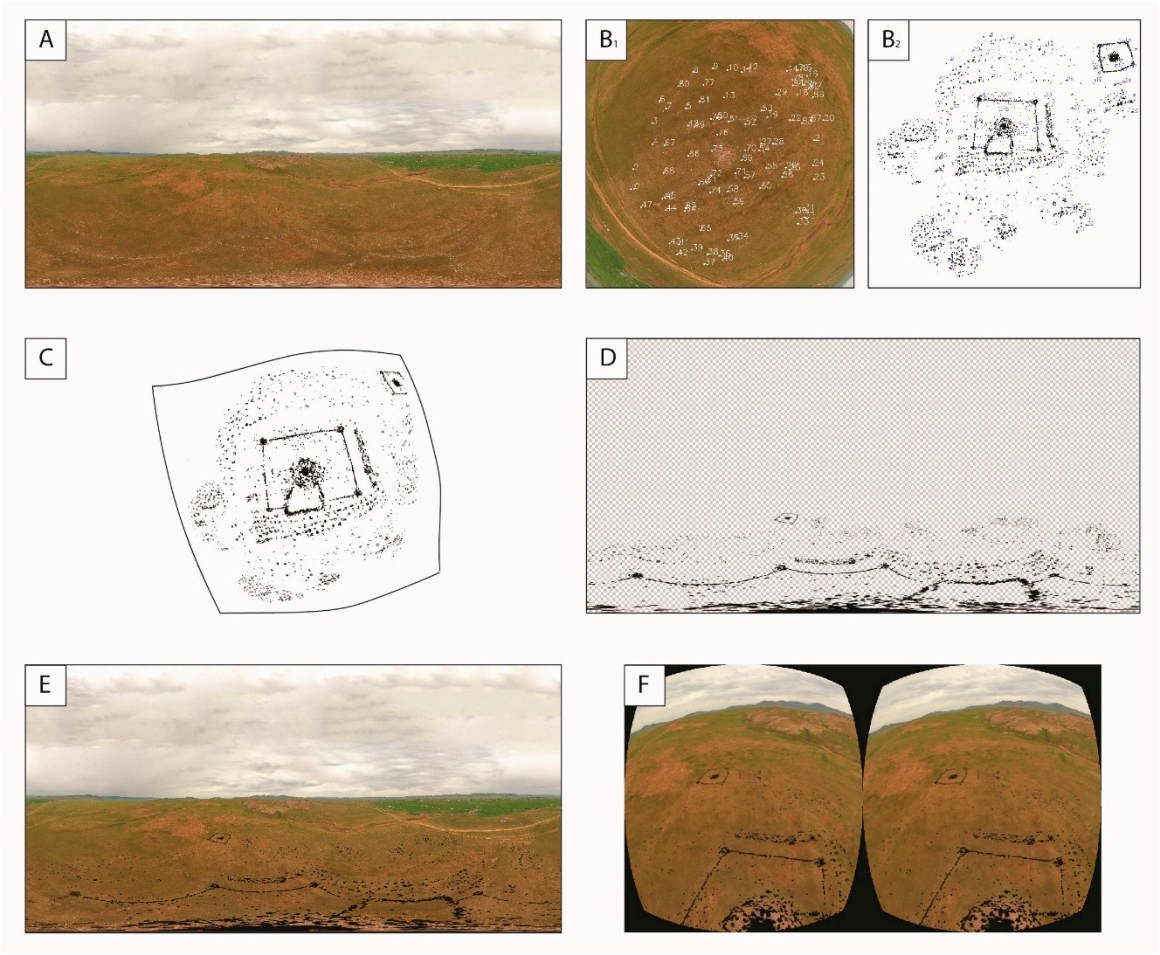

Figure 4. Workflow for registering planar documentation on irregular surfaces. (**A**) Original equirectangular image with the center of interest at the South Pole; (**B_1**) stereographic projection (target image) with 87 control points (0–86); (**B_2**) input image (here an automatic delineation of stones forming the monument) with the 87 corresponding control points (0–86); (**C**) deformation of the input image by thin plate splines (TPS); (**D**) projection onto the unit sphere of the registered input image after TPS transformation, and equirectangular projection; (**E**) incorporation of the deformed input image into the original photosphere; and (**F**) binocular rendering for HMD.

As expected, the image resulting from TPS deformation appears to fit the archaeological structures well, except perhaps close to the edges (Figure 4E; see also in Supplementary Material, Figures S3 and S4 for the original and augmented jpeg images). The results are much more accurate than those obtained by Procrustes (not shown here), because the topography of the surface on which the monument lies is somewhat irregular.

3.3. Registration of 3D Models on the Photosphere

Advances in acquiring 3D models and the treatment of their geometry have also been adapted for archaeological and cultural heritage purposes [39–43]. Such information might also efficiently augment photospheres. The alignment of the 3D model can easily be achieved by first positioning two sets of landmarks on both the equirectangular image and the 3D model (Figure 5).

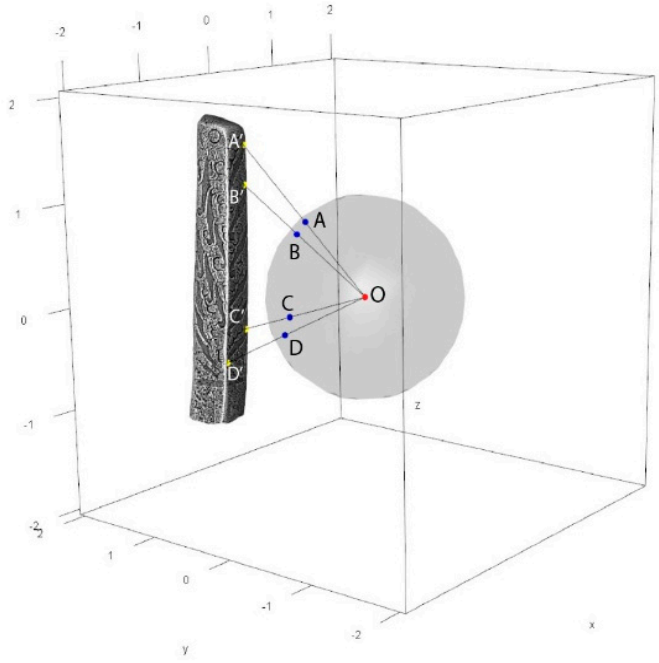

Figure 5. Optimal position of the #22 stela showing landmarks on the model (A′, B′, C′, D′) and their counterparts on the photosphere (A, B, C, D), with O as the center of the sphere.

The optimal position of the 3D model is obtained by minimizing the sum of squared distances, d_i, between landmarks placed on the models and the lines linking their corresponding counterparts on the photosphere to the sphere center:

$$\min_{a,b,c,\varphi,\theta,\rho} \sum d_i^2, \tag{2}$$

with

$$d_i = \frac{\|\vec{OP'_i} \times \vec{OP_i}\|}{\|\vec{OP_i}\|}, \tag{3}$$

where O is the center of the sphere; P_i and P'_i the landmarks on the photosphere and their counterparts on the 3D model; a, b, c the translation parameters; and φ, θ, ρ the rotation parameters around the three axes. Note that the size is fixed. The visible parts of the 3D model are then projected onto the sphere and transformed by equirectangular projection. The funeral stela #22 from Tsatsiin Ereg, decorated with symbols including many deer, is used to illustrate the projection capabilities of 3D models on photospheres (Figure 6A). The carved parts of the rock are not clearly visible to the naked eye in the original image, but they become clearer after applying an algorithm of ambient occlusion, which darkens the areas with difficult access to light (for an application in archaeology, see [44]). The aim here is to project this artificial texture obtained from the 3D model onto the photosphere. The complete projection workflow is summarized below:

1. Place a set of landmarks manually on the 3D model and on the equirectangular image (if possible, otherwise use appropriate rotation and projection, as described above).
2. Translate and rotate the 3D model to minimize the cost function (Equation (2)).
3. Determine the part of the 3D model visible from the sphere center.
4. Project the color of visible vertices onto the unit sphere (sphere center as reference).
5. Perform an equirectangular projection of the sphere (Figure 6B).

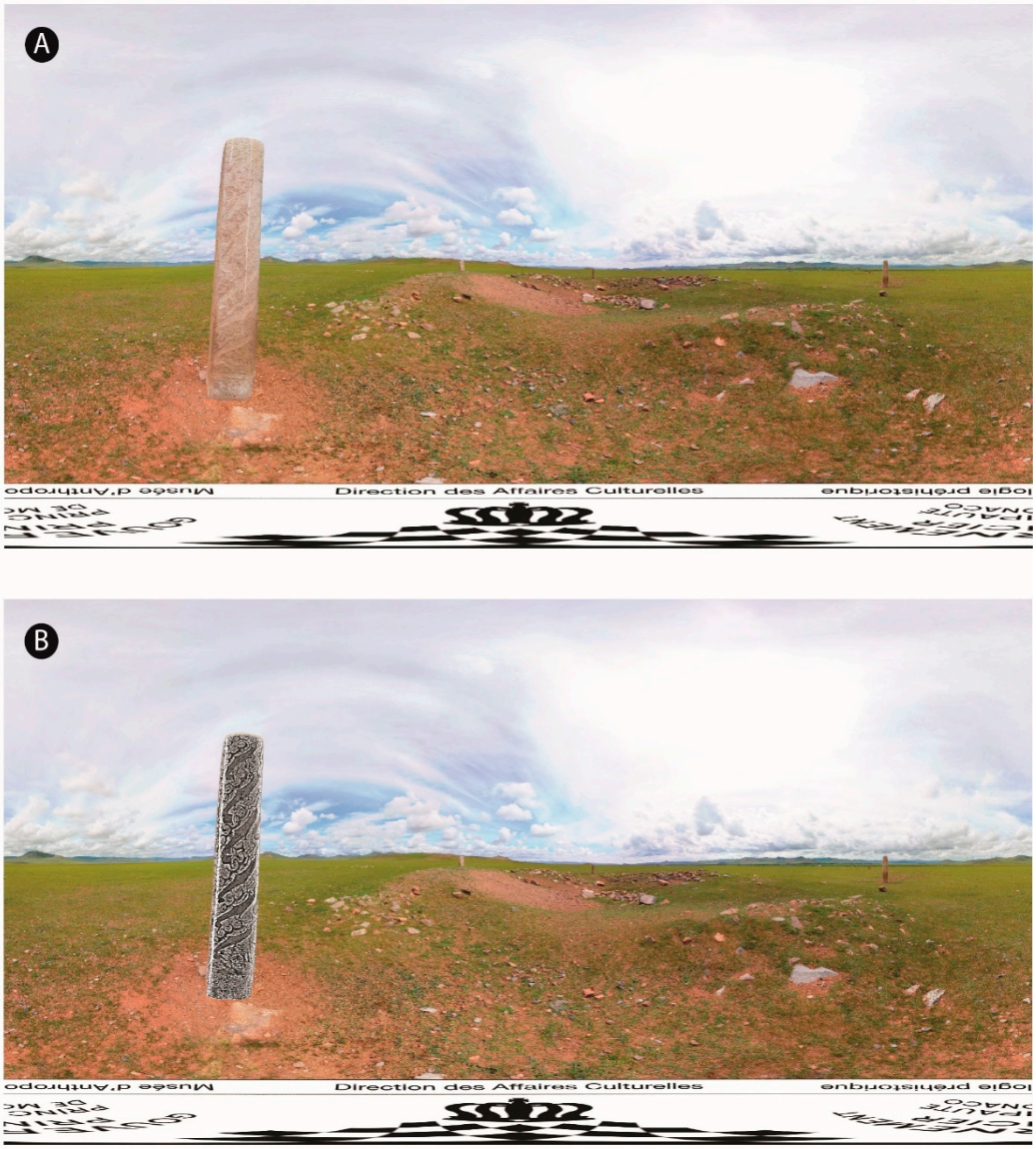

Figure 6. (**A**) Original equirectangular image displaying the S22 stela in the Tsatsiin Ereg landscape; (**B**) equirectangular image obtained after orientating the S22 stela, and projecting the parts visible after treatment by ambient occlusion.

The augmentation of the photosphere is undoubtedly effective for better understanding of the monument, especially for apprehending the spatial organization of symbols at the surface of the stela (Figure 6A,B; see also in Supplementary Material, Figures S5 and S6 for the original and augmented jpeg images). Note that several photospheres could have been captured to cover the other sides of the stela, allowing visitors to change their point of view, while maintaining their perception of environmental scale and space.

4. Concluding Remarks

Simple procedures are provided to project different types of materials onto 2D photospheres, whether plane (maps, orthomosaics, etc.) or 3D meshes. To the best of our knowledge, although common mathematical tools based on Procrustes registration, thin plate splines, and simple optimization are involved, such implementations were not available in popular game engines, or in packages and libraries of the main programming languages. The final equirectangular images can be used as supplementary layers over the original photospheres, and incorporated into virtual archaeological

tours [45,46], or rendered individually by dedicated web viewers, or stand-alone VR browsers for Windows, Mac, and Linux, and for tablets and smartphones based on Android or iOS (Photo Sphere Viewer, Panorama Viewer, Insta360 Player, PhotoSphere Viewer). The HMDs should; however, be privileged for better immersion, almost real-life experiences, greatly enhancing spatial perception. An Android application, build using Unity and designed for Google Daydream HDMs and compatible smartphones, is provided as Supplementary Material (see Supplementary Materials). It displays the three examples described in this paper, including interaction, and presents photospheres with and without augmentation. Note that it could easily be ported to other popular systems, such as Samsung Gear VR (Facebook technologies LCC, Irvine, USA), Oculus GO (Facebook technologies LCC, Irvine, USA), Google Cardboard (Google LCC, Mountain View, USA), etc. In most virtual tours, photospheres are simply used for navigating, and the documentation is presented separately, using trigger buttons, so that the feeling of immersion, or at least of contextualization, is broken. By contrast, augmented versions of photospheres maintain this feeling, especially with HDMs. The general public can be transported to the site almost physically, with a real sense of being there, which greatly enhances the contextualization of archaeological information. Augmented photospheres may facilitate interpretations by research teams, especially for remote sites, where repeated access on demand may be impossible, due to cost, schedules, seasonal constraints, etc. In rescue archaeology, this new medium could be very valuable to preserve a visual record of interpreted remains, after their destruction. Augmented photospheres are therefore expected to be beneficial for the sustainability of archaeological information, including documentation, visualization, and interpretation, and more generally for scientific mediation. They may also be an asset for tourism and for education, by improving learning performance. Although the entire 3D modeling of a site offers extended capability, such as to build a virtual world, and to allow physical walking through it via a virtual camera, implementation in the field and later in the laboratory is complex, costly, time-consuming, and demanding in terms of storage and computing resources [6]. The acquisition of 2D photospheres does not suffer from these handicaps, as it takes only a few minutes in the field and is inexpensive. Considering the numerous advantages already mentioned above, archaeological use of photospheres should be encouraged, especially when they are augmented by the abundant documentation produced by research, all the more in that the proposed workflow can easily be reproduced for almost every archaeological site.

Supplementary Materials: The following are available online at http://www.mdpi.com/2071-1050/11/14/3894/s1, Text S1: Principles of equirectangular projection, Figure S1: Original photosphere of the Loropéni ruins, Figure S2: Augmented photosphere of the Loropéni ruins, Figure S3: Original photosphere of an archaeological complex at Tsatsiin Ereg, Figure S4: Augmented photosphere of an archaeological complex at Tsatsiin Ereg, Figure S5: Original photosphere of the #22 stela at Tsatsiin Ereg, Figure S6: Augmented photosphere of the #22 stela at Tsatsiin Ereg. Code S1: Python scripts for Procrustes and TPS registrations. Code S2: R script for 3D model registration. Application S1: application with the three examples provided for Google Daydream (Google LCC, Mountain View, USA).

Author Contributions: Conceptualization: F.M., J.M., R.G., T.R. and J.W.; methodology: F.M., N.N., J.W., T.R. and Y.E.; funding: J.M., R.G. and F.M.; acquisition: J.W., J.M., T.R. and F.M.; all the authors contributed to the manuscript.

Funding: This research was funded by the Joint Mission Mongolia–Monaco, Lobi-or-fort (MEAE), and the project ROSAS (uB-FC and RNMSH).

Acknowledgments: We are grateful to the anonymous reviewers whose judicious comments have improved the manuscript.

Conflicts of Interest: The authors declare no conflicts of interest.

References

1. Creem-Regehr, S.H.; Stefanucci, J.K.; Thompson, W.B. Perceiving absolute scale in virtual environments: How theory and application have mutually informed the role of body-based perception. *Psychol. Learn. Motiv.* **2015**, *62*, 195–224.

2. Berthoz, A. Fondements cognitifs de la perception de l'espace. In Proceedings of the 1st International Congress on Ambiances, Grenoble, France, 10–12 September 2008; pp. 121–132.
3. Erkelens, C.J. Perspective space as a model for distance and size perception. *i-Perception* **2017**, *8*, 1–20. [CrossRef] [PubMed]
4. Connolly, J.; Lake, M. *Geographical Information Systems in Archaeology*; Cambridge University Press: Cambridge, UK, 2006; 358p.
5. Reilly, P. Towards a Virtual Archaeology. In *Computer Applications in Archaeology 1990*; Bar International, Series; Lockyear, K., Rahtz, S., Eds.; BAR Publishing: Oxford, UK, 1991; Volume 565, pp. 133–139.
6. Napolitano, R.K.; Scherer, G.; Glisic, B. Virtual tours and informational modeling for conservation of cultural heritage sites. *J. Cult. Herit.* **2018**, *29*, 123–129. [CrossRef]
7. Koehl, M.; Brigand, N. Combination of virtual tours 3D model and digital data in a 3D archaeological knowledge and information system. *Int. Arch. Photogramm. Remote Sens. Spat. Inf. Sci.* **2012**, *39*, 439–444. [CrossRef]
8. Castagnetti, C.; Giannini, M.; Rivola, R. Image-based virtual tours and 3D modeling of past and current ages for the enhancement of archaeological parks: The Visualversilia 3D project. *Int. Arch. Photogramm. Remote Sens. Spat. Inf. Sci.* **2017**, *XLII-5/W1*, 639–645. [CrossRef]
9. Fiorillo, F.; Fernández-Palacios, B.J.; Remondino, F.; Barba, S. 3D surveying and modelling of the archaeological area of Paestum, Italy. *Virtual Archaeol. Rev.* **2013**, *4*, 55–60. [CrossRef]
10. Koeva, M.; Luleva, M.; Maldjanski, P. Integrating spherical panoramas and maps for visualization of cultural heritage objects using virtual reality technology. *Sensors* **2017**, *17*, 829. [CrossRef]
11. Gonizzi Barsanti, S.; Caruso, G.; Micoli, L.L.; Covarrubias Rodriguez, M.; Guidi, G. 3D visualization of cultural heritage artefacts with virtual reality devices. *Int. Arch. Photogramm. Remote Sens. Spat. Inf. Sci.* **2015**, *XL-5/W7*, 165–172. [CrossRef]
12. Katsouri, I.; Tzanavari, A.; Herakleous, K.; Poullis, C. Visualizing and Assessing Hypotheses for Marine Archaeology in a VR CAVE Environment. *J. Comput. Cult. Herit.* **2015**, *8*, 10. [CrossRef]
13. Guttentag, D.A. Virtual reality: Applications and implications for tourism. *Tour. Manag.* **2010**, *31*, 637–651. [CrossRef]
14. Roussou, M. Virtual Heritage: From the Research Lab to the Broad Public. In *Virtual Archaeology, Proceedings of the VAST Euroconference, Arezzo, Italy, 24–25 November 2000*; Bar International Series; Niccolucci, F., Ed.; BAR Publishing: Oxford, UK, 2002; Volume 1075, pp. 93–100.
15. Christofi, M.; Kyrlitsias, C.; Michael-Grigoriou, D.; Anastasiadou, Z.; Michaelidou, M. A Tour in the Archaeological Site of Choirokoitia Using Virtual Reality: A Learning Performance and Interest Generation Assessment. In *Advances in Digital Cultural Heritage*; Lecture Notes in Computer Science; Ioannides, M., Martins, J., Žarnić, R., Lim, V., Eds.; Springer: Berlin/Heidelberg, Germany, 2018; Volume 10754, pp. 208–217.
16. Barceló, J.A. Virtual Reality for Archaeological Explanation: Beyond 'picturesque' reconstruction. *Archeologia e Calcolatori* **2001**, *12*, 221–244.
17. Mihelj, M.; Novak, D.; Beguš, S. *Virtual Reality Technology and Applications*; Series: Intelligent Systems, Control and Automation: Science and Engineering 68; Springer: Berlin/Heidelberg, Germany, 2014; 231p.
18. Linowes, J. *Unity Virtual Reality Projects: Learn Virtual Reality by Developing more than 10 Engaging Projects with Unity 2018*, 2nd ed.; Packt Publishing: Birmingham, UK, 2018; 492p.
19. Ruddle, R.A.; Payne, S.J.; Jones, D.M. Navigating large-scale virtual environments: What differences occur between helmet-mounted and desk-top displays? *Presence* **1999**, *8*, 157–168. [CrossRef]
20. Renner, R.S.; Velichkovsky, B.M.; Helmert, J.R. The perception of egocentric distances in virtual environments—A review. *ACM Comput. Surv.* **2013**, *46*. [CrossRef]
21. Ronfard, R.; Taubin, G. *Image and Geometry Processing for 3-D Cinematography (Geometry and Computing)*; Springer: Berlin/Heidelberg, Germany, 2010; 305p.
22. Michiels, N.; Jorissen, L.; Put, J.; Philippe, B. Interactive augmented omnidirectional video with realistic lighting. In *Augmented and Virtual Reality*; Lecture Notes in Computer Science; De Paolis, L., Mongelli, A., Eds.; Springer: Cham, Switzerland, 2014; Volume 8853.
23. Fernández-Palacios, B.J.; Morabito, D.; Remondino, F. Access to complex reality-based 3D models using virtual reality solutions. *J. Cult. Herit.* **2017**, *23*, 40–48. [CrossRef]
24. Gheisari, M.; Sabzevar, M.F.; Chen, P.; Irizzary, J. Integrating BIM and panorama to create a semi-augmented-reality experience of a construction site. *Int. J. Constr. Educ. Res.* **2016**, *12*, 303–316. [CrossRef]

25. Guillon, R.; Simporé, L. *Les Forts du Pays Lobi et L'activité Aurifère au Sud-Ouest du Burkina Faso, 11^{e}–18^{e} Siècles: Origine, Rôle Social et Réseau D'échange Associés Aux Ruines de Loropéni (Site UNESCO) Projet de Recherche Franco-Burkinabè*; Ministère des Affaires Etrangères: Paris, France, 2018; p. 80.
26. Simporé, L. The ruins of Loropeni, the first mankind worldwide patrimony Burkinabe site. *J. Egyptol. Afr. Civiliz.* **2011**, *18–20*, 255–279.
27. Simporé, L.; Guillon, R.; Camerlynck, C.; Farma, H.; Kouassi, S.K.; Monna, F.; Mégret, Q. The Pre-Colonial Enclosure of Loropéni (Southwestern Burkina Faso): Preliminary Results of the Lobi-Or-Fort Project's Archaeological Excavation. In Proceedings of the SAFA 2016, Toulouse, France, 26 June–2 July 2016.
28. Magail, J. Tsatsiin Ereg, site majeur du début du 1er millénaire en Mongolie. *Bull. Mus. Anthrop. Prehist. Monaco* **2008**, *48*, 107–120.
29. Magail, J. Les stèles ornées de Mongolie dites « pierres à cerfs », de la fin de l'âge du Bronze. In Proceedings of the Actes du 3e Colloque de Saint-Pons-de-Thomières, Saint-Pons-de-Thomières, France, 16 September 2012; Direction Régionale des Affaires Culturelles Languedoc-Roussillon: Montpellier, France, 2015; pp. 89–101.
30. Pincus, Z. CellTool: Command-Line Tools for Statistical Analysis of Shapes, Particularly Cell Shapes from Micrographs. 2014. Available online: https://github.com/zpincus/celltool/blob/master/celltool/numerics/image_warp.py (accessed on 10 July 2019).
31. R Core Team. *R: A Language and Environment for Statistical Computing*; R Foundation for Statistical Computing: Vienna, Austria, 2019; Available online: https://www.R-project.org/ (accessed on 10 July 2019).
32. Dryden, I.L.; Mardia, K.V. *Statistical Shape Analysis*; John Wiley & Sons: Chichester, NY, USA, 1998; 376p.
33. Zelditch, L.; Swiderski, D.L.; Sheets, D. *Geometric Morphometrics for Biologists: A Primer*, 2nd ed.; Academic Press: Cambridge, MA, USA, 2012; 488p.
34. Gower, J.C.; Dijksterhuis, D.B. *Procrustes Problems*; Oxford University Press: Oxford, UK, 2004; 248p.
35. Coxeter, H.S.M. *Introduction to Geometry*, 2nd ed.; Wiley: New York, NY, USA, 1989; 492p.
36. Lapaine, M.; Usery, E.L. *Choosing a Map Projection*; Springer: Berlin/Heidelberg, Germany, 2017; 360p.
37. Bookstein, F.L. Principal warps: Thin plate splines and the decomposition of deformations. *IEEE Trans. Pattern Anal. Mach. Intell.* **1989**, *11*, 567–585. [CrossRef]
38. Monna, F.; Magail, J.; Rolland, T.; Navarro, N.; Wilczek, J.; Gantulga, J.-O.; Esin, Y.; Granjon, L.; Chateau, C. Machine learning for rapid mapping of archaeological structures made of dry stones—Example of burial monuments from the Khirgisuurs culture, Mongolia. *J. Cult. Herit.* submitted.
39. Pavlidis, G.; Koutsoudis, A.; Arnaoutoglou, F.; Tsioukas, V.; Chamzas, C. Methods for 3D digitization of cultural heritage. *J. Cult. Herit.* **2007**, *8*, 93–98. [CrossRef]
40. Yastikli, N. Documentation of cultural heritage using digital photogrammetry and laser scanning. *J. Cult. Herit.* **2007**, *8*, 423–442. [CrossRef]
41. Remondino, F.; Rizzi, A. Reality-based 3D documentation of natural and cultural heritage sites—Techniques, problems, and examples. *Appl. Geomat.* **2010**, *2*, 85–100. [CrossRef]
42. Domingo, I.; Villaverde, V.; Lopez-Montalvo, E.; Lerma, J.L.; Cabrelles, M. Latest developments in rock art recording: Towards an integral documentation of Levantine rock art sites combining 2D and 3D recording techniques. *J. Archaeol. Sci.* **2013**, *40*, 1879–1889. [CrossRef]
43. Monna, F.; Esin, Y.; Magail, J.; Granjon, L.; Navarro, N.; Wilczek, J.; Saligny, L.; Couette, S.; Dumontet, A.; Chateau, C. Documenting carved stones by 3D modelling—Example of Mongolian deer stones. *J. Cult. Herit.* **2018**, *34*, 116–128. [CrossRef]
44. Rolland, T.; Monna, F.; Magail, J.; Esin, Y.; Navarro, N.; Wilczek, J.; Chateau, C. Documenting carved stones from 3D models. Part II—Ambient occlusion to reveal carved parts. *J. Cult. Herit.* In prep.
45. Kiourt, C.; Koutsoudis, A.; Arnaoutoglou, F.; Petsa, G.; Markantonatou, S.; Pavlidis, G. A dynamic web-based 3D virtual museum framework based on open data. In Proceedings of the 2015 Digital Heritage, Granada, Spain, 28 September–2 October 2015; pp. 647–650.
46. Barreau, J.B.; Gaugne, R.; Bernard, Y.; Le Cloirec, G.; Gouranton, V. Virtual reality tools for the West digital conservatory of archaeological heritage. In Proceedings of the VRIC 2014, Laval, France, 9–11 April 2014; ACM: New York, NY, USA, 2014; pp. 1–4.

6.2. Diffusion et archivage des données

Le problème du partage des données, et de l'état d'avancement de leur traitement, à l'ensemble partenaires, a fait partie des nombreux défis rencontrés durant ce travail de thèse. Une simple visualisation des données peut parfois suffire pour partager et discuter sur les problématiques rencontrées. L'idée a donc été de trouver une solution pratique pour : i) visualiser de manière claire les données disponibles puis ii) accéder facilement aux données qui nous intéresse. Cette solution prend la forme d'une cartographie en ligne. Elle se base sur des projets QGIS mis en ligne *via* le logiciel open-source Lizmap (https://www.lizmap.com/). Le principe est assez simple : les données sont stockées sur un serveur et elles sont ensuite moissonnées afin de créer des cartes dans un système d'information géographique. Il est possible d'y afficher l'emplacement des stèles modélisées, tout comme les zones couvertes par les acquisitions aux drones. Chaque objet sur la carte peut être associé à une table d'attributs fournissant des informations recueillies, mais aussi des visuels comportant images, ou modèles 3D (Fig. 25). Cet outil, développé en collaboration avec Ludovic Granjon du pôle géomatique de la MSH de Dijon, en est au premier stade de sa création.

Une fois terminée, cette cartographie en ligne sera un outil de partage efficace entre chercheurs, parfois très éloignés géographiquement. Elle rassemblera l'ensemble des données acquises dans le cadre de ce projet. L'objectif n'est pas de créer une cartographie figée. L'accessibilité en ligne devra permettre, par la suite, une mise à jour régulière de la carte, avec l'apport de nouvelles données. Le logiciel Lizmap donne la possibilité de gérer les accès aux projets SIG, les rendant accessibles uniquement à certaines personnes choisies. On peut alors imaginer une solution à deux niveaux. Certains projets destinés aux chercheurs, contenant l'ensemble des données de l'étude, et d'autres destinés au grand public, contenant des informations limitées. Ces projets deviennent alors des supports pour la valorisation du patrimoine et le tourisme archéologique. Il serait même possible d'envisager d'y associer un aspect de science participative en permettant à toutes personnes intéressées d'informer l'équipe de la présence d'un nouveau site, d'un nouveau monument, ou d'une nouvelle stèle, par le biais de photos géoréférencées. Touristes et locaux participeraient ainsi à la difficile

mais indispensable étape de prospection. Une sauvegarde des données recueillies durant ce travail est présente au conservatoire national des données 3D. Ce dernier offre une solution d'archivage assuré par la TGIR Huma-Num garantissant la pérennité de la donnée numérique.

Fig. 25 Capture du logiciel lizmap montrant les capacités de la cartographie en ligne.

Chapitre 7. Conclusions

Ce travail de thèse propose de nouvelles méthodes d'acquisition, de préparation et d'analyse de la donnée, avec pour objectif de créer et de gérer un échantillon d'objets qui se veut significatif pour aborder le problème posé : ici la cohérence sociale des populations nomades de l'époque. La prospection et l'enregistrement des complexes funéraires par drone convient parfaitement aux grands espaces ouverts de la steppe mongole. Cette méthode permet de prendre facilement de la hauteur par rapport aux sites et d'en appréhender toute la complexité spatiale, ce qui peut être difficile voire impossible depuis le sol, en particulier lorsque que les sites étudiés couvrent plusieurs hectares. La quantité d'informations recueillies sur un laps de temps court est énorme. La prospection aérienne a permis l'élaboration d'un inventaire des structures de la vallée de la Khoïd Tamir et de la rivière Khunui. Celui-ci vient enrichir notablement les connaissances des vestiges du patrimoine mongol.

Les résultats des traitements des modèles 3D par occlusion ambiante rivalisent avec les meilleures méthodes de relevé de gravures actuelles. Le traitement 3D possède également des avantages indéniables : la possibilité de manipuler l'objet dans un espace virtuel, l'absence de déformation due au support papier utilisé lors des relevés traditionnels, la mise en valeur, non seulement des gravures, mais aussi de l'état de conservation des surfaces, avec toujours la possibilité de produire une documentation 2D classique. Cette méthode a fait ses preuves pour la mise en valeur des gravures sur les pierres à cerfs, mais peut être utilisée dans n'importe quelle étude où il s'agit de souligner les reliefs d'un modèle 3D.

L'apprentissage automatique et l'apprentissage profond automatisent efficacement une partie du processus de préparation des données. Ces méthodes sont utilisées dans quasiment tous les domaines scientifiques pour

notamment répondre à des problèmes de détection d'objets ou de classification. Le présent travail a conduit à leur adaptation pour résoudre des problèmes archéologiques spécifiques (e.g. production de plan des khirigsuurs à partir de l'isolation des pierres qui le composent). La détection d'objets par apprentissage profond se développe de plus en plus en archéologie, notamment pour la détection de structures anthropiques à partir de MNE produits lors des grandes campagnes d'acquisition LIDAR. Au final, ces méthodes ont pour but d'assister le chercheur dans ces tâches lentes et répétitives. Il se libère ainsi pour entreprendre celles qui nécessitent plus son expertise que son temps.

La typologie des khirigsuurs proposée s'insère parfaitement dans les travaux antérieurs. Sans révolutionner la façon d'appréhender un khirigsuur, elle confirme statistiquement ce qui a pu être pressenti jusqu'alors : (i) l'évolution conjointe de la complexité avec la taille des monuments et (ii) l'évolution typologique suivant la valeur de la pente.

La possibilité d'appliquer les méthodes et les protocoles développés ici à d'autres problématiques, sujets, ou terrains a été au cœur de ce travail de thèse. De l'acquisition, à la préparation des données et jusqu'à leur analyse, toutes les solutions proposées sont directement applicables à d'autres domaines. Les applications développées sont en libre accès et sous la forme d'exécutables pour faciliter leur diffusion et leur utilisation au sein de la communauté scientifique. Les codes et les scripts sont écrits en langage R ou Python qui sont des langages informatiques libres également.

Les études actuelles sur les monuments de l'âge du Bronze en Mongolie se font le plus souvent à des échelles locales. Elles permettent de mieux comprendre les populations nomades de l'époque au sein d'une aire géographique excédant rarement la vallée. Il apparait pourtant nécessaire d'élargir cette vision afin d'appréhender la culture ayant bâti les khirigsuurs et érigé les pierres à cerfs, dont les marqueurs se retrouvent sur un territoire de plusieurs milliers de kilomètres carrés. Les fenêtres ouvertes sur cet espace sont trop restreintes et empêchent de voir le tableau dans sa globalité. Il ne faut pas seulement étudier les monuments d'une nécropole ou d'une vallée, mais comparer les vallées et même les régions entre elles. Pour

atteindre cette vision à large échelle, il serait intéressant d'étendre la zone étudiée dans ce travail de thèse ; dans un premier temps, en s'intéressant aux autres vallées autour de celles de la Khoid Tamir et de la rivière Khunui, puis sur la province de l'Akhangaï, pour finir sur plusieurs provinces, et le territoire mongol dans son ensemble. Une étude à une telle échelle implique nécessairement une perte drastique de précision dans l'information recueillie par rapport aux précédentes études. Il s'agirait en contrepartie de gagner en exhaustivité et en représentativité. Les fouilles resteront bien entendu indispensables car elles offrent un cadre temporel, et plus généralement contraignent les modèles établis à plus grande échelle.

Les travaux présentés ici démontrent en partie la faisabilité d'une telle étude puisque les outils conceptuels et technologiques existent. Bien qu'il n'existe pas de carte répertoriant l'ensemble des khirigsuurs sur une province, elles sont désormais envisageables grâce à l'apprentissage profond appliqué aux photos aériennes / satellitaires. Le seul frein réside pour le moment dans l'accessibilité à des images suffisamment définie (celles disponibles à l'heure actuelle ont une résolution trop faible). Nul doute que ce verrou sautera dans les prochaines années ; l'important est d'avoir défini le concept de l'étude depuis l'analyse des images jusqu'au traitement de l'information.

L'étude des khirigsuurs apparait indissociable de celle des pierres à cerfs puisqu'il semble impossible de pleinement comprendre l'un sans comprendre l'autre. Bien que moins nombreuses, les pierres à cerfs sont des marqueurs culturels forts de l'âge du Bronze mongol. Au-delà du simple inventaire iconographique, le décryptage de la syntaxe cachée dans la composition et l'organisation des motifs gravés pourrait bien s'avérer être une piste prometteuse dans la compréhension des populations nomades de l'époque.

Bibliographie

Abdullah, C. I., Rampnoux, J.-P., Bellon, H., Maury, R. C., & Soeria-Atmadja, R. (2000). The evolution of Sumba Island (Indonesia) revisited in the light of new data on the geochronology and geochemistry of the magmatic rocks. Journal of Asian Earth Sciences, 18(5), 533-546. https://doi.org/10.1016/S1367-9120(99)00082-6

Abolt, C. J., Young, M. H., Atchley, A. L., & Wilson, C. J. (2019). Brief communication : Rapid machine-learning-based extraction and measurement of ice wedge polygons in high-resolution digital elevation models. The Cryosphere, 13(1), 237-245. https://doi.org/10.5194/tc-13-237-2019

Adams, R. L., & Kusumawati, A. (2010). 2 The Social Life of Tombs in West Sumba, Indonesia : The Social Life of Tombs in West Sumba, Indonesia. Archeological Papers of the American Anthropological Association, 20(1), 17-32. https://doi.org/10.1111/j.1551-8248.2011.01025.x

Agarwal, S., Terrail, J. O. D., & Jurie, F. (2018). Recent Advances in Object Detection in the Age of Deep Convolutional Neural Networks. https://doi.org/10.48550/ARXIV.1809.03193

Ahmad, A., & Dey, L. (2007). A k-mean clustering algorithm for mixed numeric and categorical data. Data & Knowledge Engineering, 63(2), 503-527. https://doi.org/10.1016/j.datak.2007.03.016

Ahmad, A., & Khan, S. S. (2019). Survey of State-of-the-Art Mixed Data Clustering Algorithms. IEEE Access, 7, 31883-31902. https://doi.org/10.1109/ACCESS.2019.2903568

Aicardi, I., Chiabrando, F., Maria Lingua, A., & Noardo, F. (2018). Recent trends in cultural heritage 3D survey : The photogrammetric computer vision approach. Journal of Cultural Heritage, 32, 257-266. https://doi.org/10.1016/j.culher.2017.11.006

Al-amri, S. S., Kalyankar, N. V., & Khamitkar, S. D. (2010). Linear and non-linear contrast enhancement image. International Journal of Computer Science and Network Security, 10(2), 139-143.

Allard, F., & Erdenebaatar, D. (2005). Khirigsuurs, ritual and mobility in the Bronze Age of Mongolia. Antiquity, 79(305), 547-563. https://doi.org/10.1017/S0003598X00114498

Alley, R. E. (1996). Algorithm Theoretical Basis Document for : Decorrelation Stretch. NASA propulsion laboratory.

Baiarsaïkhan, Z., & Ėrdėnėbat, U. (2017). Mongolyn umard nutgiĭn bugan khėshėėd. « Interpress » KhKhK-d khėvlėv.

Barceló, J. A. (2001). Virtual reality for archaelogical explanation. Beyond « picturesque » reconstruction. Archeologia e calcolatori, 12, 221-244.

Barone, G., Mazzoleni, P., Spagnolo, G. V., & Raneri, S. (2019). Artificial neural network for the provenance study of archaeological ceramics using clay sediment database. Journal of Cultural Heritage, 38, 147-157. https://doi.org/10.1016/j.culher.2019.02.004

Baroni, I., Gantulga, J.-O., Magail, J., & Yeruul-Erdene, C. (2016). Three Thousand Years of Nomadism on the Tsatsyn Ereg Site in the Heart of Mongolia. In S. Biagetti & F. Lugli (Éds.), The Intangible Elements of Culture in Ethnoarchaeological Research (p. 151-159). Springer International Publishing. https://doi.org/10.1007/978-3-319-23153-2_10

Barreau, J.-B., Gaugne, R., Bernard, Y., Le Cloirec, G., & Gouranton, V. (2014). Virtual reality tools for the west digital conservatory of archaeological heritage. Proceedings of the 2014 Virtual Reality International Conference, 1-4. https://doi.org/10.1145/2617841.2617845

Baxter, M. J. (2006). A REVIEW OF SUPERVISED AND UNSUPERVISED PATTERN RECOGNITION IN ARCHAEOMETRY. Archaeometry, 48(4), 671-694. https://doi.org/10.1111/j.1475-4754.2006.00280.x

Baxter, M. J. (2015). Exploratory multivariate analysis in archaeology. Percheron Press, a division of Eliot Werner Publications, Inc.

Bell, A. J., & Sejnowski, T. J. (1997). The “independent components” of natural scenes are edge filters. Vision Research, 37(23), 3327-3338. https://doi.org/10.1016/S0042-6989(97)00121-1

Bellanger, L., Coulon, A., & Husi, P. (2021). PerioClust : A Simple Hierarchical Agglomerative Clustering Approach Including Constraints. In T. Chadjipadelis, B. Lausen, A. Markos, T. R. Lee, A. Montanari, & R. Nugent (Éds.), Data Analysis and Rationality in a Complex World (p. 1-8). Springer International Publishing. https://doi.org/10.1007/978-3-030-60104-1_1

Berthoz, A. (2008). Fondements cognitifs de la perception de l’espace. 121-132.

Bishop, C. M. (2016). Pattern Recognition and Machine Learning (Softcover reprint of the original 1st edition 2006 (corrected at 8th printing 2009)). Springer New York.

Blinkhorn, J., & Grove, M. (2018). The structure of the Middle Stone Age of eastern Africa. Quaternary Science Reviews, 195, 1-20. https://doi.org/10.1016/j.quascirev.2018.07.011

Bokšanský, J., Pospíšil, A., & Bittner, J. (2017). VAO++ : Practical Volumetric Ambient Occlusion for Games. Eurographics Symposium on Rendering - Experimental Ideas & Implementations, 9 pages. https://doi.org/10.2312/SRE.20171192

Bookstein, F. L. (1989). Principal warps : Thin-plate splines and the decomposition of deformations. IEEE Transactions on Pattern Analysis and Machine Intelligence, 11(6), 567-585. https://doi.org/10.1109/34.24792

Borovka, G. I. (1927). Arkheologicheskoye obsledovaniye srednego techeniya r. Toly. Predvaritel’nyye otchoty lingvisticheskoy i arkheologicheskoy ekspeditsiy o rabotakh, 43-88.

Bottou, L. (2010). Large-Scale Machine Learning with Stochastic Gradient Descent. In Y. Lechevallier & G. Saporta (Éds.), Proceedings of COMPSTAT'2010 (p. 177-186). Physica-Verlag HD. https://doi.org/10.1007/978-3-7908-2604-3_16

Bourgeois, J., & Meganck, M. (Éds.). (2005). Aerial photography and archaeology 2003 : A century of information ; papers presented during the conference held at the Ghent University, December 10th - 12th, 2003. Academia Press.

Bovik, A. C. (Éd.). (2000). Handbook of image and video processing. Academic Press.

Boyd, D. S., & Danson, F. M. (2005). Satellite remote sensing of forest resources : Three decades of research development. Progress in Physical Geography: Earth and Environment, 29(1), 1-26. https://doi.org/10.1191/0309133305pp432ra

Brady, L. M. (2006). Documenting and Analyzing Rock, Paintings from Torres Strait, NE Australia, with Digital Photography and Computer Image Enhancement. Journal of Field Archaeology, 31(4), 363-379. https://doi.org/10.1179/009346906791071837

Brady, L. M. (2007). A different look : Comparative rock-art recording from the Torres Strait using computer enhancement techniques. Australian Aboriginal Studies, 98-115.

Burger, W., & Burge, M. J. (2016). Digital Image Processing : An Algorithmic Introduction Using Java (2nd ed. 2016). Springer London : Imprint: Springer. https://doi.org/10.1007/978-1-4471-6684-9

Caldwell, D., & Botzojorns, U. (2014). An historic sign, possible Mesolithic menhir, DStretch, and problems in dating rock art to the Sauveterrian in the Massif de Fontainebleau. Journal of Archaeological Science, 42, 140-151. https://doi.org/10.1016/j.jas.2013.09.023

Campana, S. (2017). Drones in Archaeology. State-of-the-art and Future Perspectives : Drones in Archaeology. Archaeological Prospection, 24(4), 275-296. https://doi.org/10.1002/arp.1569

Carrero-Pazos, M., Vázquez-Martínez, A., & Vilas-Estévez, B. (2016). AsTrend : Towards a new method for the study of ancient carvings. Journal of Archaeological Science: Reports, 9, 105-119. https://doi.org/10.1016/j.jasrep.2016.06.044

Carrero-Pazos, M., Vilas-Estévez, B., & Vázquez-Martínez, A. (2018). Digital imaging techniques for recording and analysing prehistoric rock art panels in Galicia (NW Iberia). Digital Applications in Archaeology and Cultural Heritage, 8, 35-45. https://doi.org/10.1016/j.daach.2017.11.003

Caspari, G. (2020). Mapping and Damage Assessment of "Royal" Burial Mounds in the Siberian Valley of the Kings. Remote Sensing, 12(5), 773. https://doi.org/10.3390/rs12050773

Caspari, G., & Crespo, P. (2019). Convolutional neural networks for archaeological site detection – Finding "princely" tombs. Journal of Archaeological Science, 110, 104998. https://doi.org/10.1016/j.jas.2019.104998

Cassen, S., & Grimaud, V. (2017). Enregistrements, représentations et analyse structurale d'une stèle néolithique gravée dans l'ouest de la France. Kermaillard à Sarzeau (Morbihan, France). Bolletino del Centro camuno di Studi Preistorici, 43, 33-56.

Cassen, S., Lescop, L., Grimaud, V., & Robin, G. (2014). Complementarity of acquisition techniques for the documentation of Neolithic engravings : Lasergrammetric and photographic recording in Gavrinis passage tomb (Brittany, France). Journal of Archaeological Science, 45, 126-140. https://doi.org/10.1016/j.jas.2014.02.019

Castagnetti, C., Giannini, M., & Rivola, R. (2017). IMAGE-BASED VIRTUAL TOURS AND 3D MODELING OF PAST AND CURRENT AGES FOR THE ENHANCEMENT OF ARCHAEOLOGICAL PARKS : THE VISUALVERSILIA 3D PROJECT. The International Archives of the Photogrammetry, Remote Sensing and Spatial Information Sciences, XLII-5/W1, 639-645. https://doi.org/10.5194/isprs-archives-XLII-5-W1-639-2017

Cerrillo-Cuenca, E., Ortiz-Coder, P., & Martínez-del-Pozo, J.-Á. (2014). Computer vision methods and rock art : Towards a digital detection of pigments. Archaeological and Anthropological Sciences, 6(3), 227-239. https://doi.org/10.1007/s12520-013-0147-2

Cerrillo-Cuenca, E., & Sepúlveda, M. (2015). An assessment of methods for the digital enhancement of rock paintings : The rock art from the precordillera of Arica (Chile) as a case study. Journal of Archaeological Science, 55, 197-208. https://doi.org/10.1016/j.jas.2015.01.006

Cerrillo-Cuenca, E., Sepúlveda, M., & Guerrero-Bueno, Z. (2021). Independent component analysis (ICA) : A statistical approach to the analysis of superimposed rock paintings. Journal of Archaeological Science, 125, 105269. https://doi.org/10.1016/j.jas.2020.105269

Chan, T.-H., Jia, K., Gao, S., Lu, J., Zeng, Z., & Ma, Y. (2014). PCANet : A Simple Deep Learning Baseline for Image Classification? https://doi.org/10.48550/ARXIV.1404.3606

Chlenova, N. L. (1956). Neskol'ko pisanits Yugo-Zapadnoy Tuvy (Vol. 4).

Chlenova, N. L. (1962). Ob Olennykh Kamnyakh Mongolii i Sibiri. Mongolski Arkheologicheskii Sbornik, 27-35.

Christofi, M., Kyrlitsias, C., Michael-Grigoriou, D., Anastasiadou, Z., Michaelidou, M., Papamichael, I., & Pieri, K. (2018). A Tour in the Archaeological Site of Choirokoitia Using Virtual Reality : A Learning Performance and Interest Generation Assessment. In M. Ioannides, J. Martins, R. Žarnić, & V. Lim (Éds.), Advances in Digital Cultural Heritage (Vol. 10754, p. 208-217). Springer International Publishing. https://doi.org/10.1007/978-3-319-75789-6_15

Conolly, J., & Lake, M. (2006). Geographical Information Systems in Archaeology (1re éd.). Cambridge University Press. https://doi.org/10.1017/CBO9780511807459

Cortes, C., & Vapnik, V. (1995). Support-vector networks. Machine Learning, 20(3), 273-297. https://doi.org/10.1007/BF00994018

Cowley, D., Moriarty, C., Geddes, G., Brown, G., Wade, T., & Nichol, C. (2017). UAVs in Context : Archaeological Airborne Recording in a National Body of Survey and Record. Drones, 2(1), 2. https://doi.org/10.3390/drones2010002

Coxeter, H. S. M. (1989). Introduction to geometry (2. ed). Wiley.

Creem-Regehr, S. H., Stefanucci, J. K., & Thompson, W. B. (2015). Perceiving Absolute Scale in Virtual Environments : How Theory and Application Have Mutually Informed the Role of Body-Based Perception. In Psychology of Learning and Motivation (Vol. 62, p. 195-224). Elsevier. https://doi.org/10.1016/bs.plm.2014.09.006

Cybiktarov, A. B. (2003). Central Asia in the Bronze and Early Iron ages. Archaeology, Ethnology and Anthropology of Eurasia, 1, 80-97.

Dachsbacher, C., & Kautz, J. (2009). Real-time global illumination for dynamic scenes. ACM SIGGRAPH 2009 Courses on - SIGGRAPH '09, 1-217. https://doi.org/10.1145/1667239.1667258

Dai, J., Li, Y., He, K., & Sun, J. (2016). R-FCN : Object Detection via Region-based Fully Convolutional Networks. https://doi.org/10.48550/ARXIV.1605.06409

Dalal, N., & Triggs, B. (2005). Histograms of Oriented Gradients for Human Detection. 2005 IEEE Computer Society Conference on Computer Vision and Pattern Recognition (CVPR'05), 1, 886-893. https://doi.org/10.1109/CVPR.2005.177

Davis, D. S. (2020). Geographic Disparity in Machine Intelligence Approaches for Archaeological Remote Sensing Research. Remote Sensing, 12(6), 921. https://doi.org/10.3390/rs12060921

Dawson, J. B. (2008). The Gregory Rift Valley and neogene-recent-volcanoes of Northern Tanzania. Geological Soc.

Dawson-Howe, K. (2014). A practical introduction to computer vision with OpenCV. John Wiley & Sons., Inc.

De Reu, J., Bourgeois, J., Bats, M., Zwertvaegher, A., Gelorini, V., De Smedt, P., Chu, W., Antrop, M., De Maeyer, P., Finke, P., Van Meirvenne, M., Verniers, J., & Crombé, P. (2013). Application of the topographic position index to heterogeneous landscapes. Geomorphology, 186, 39-49. https://doi.org/10.1016/j.geomorph.2012.12.015

Defrasne, C. (2014). Digital image enhancement for recording rupestrian engravings : Applications to an alpine rockshelter. Journal of Archaeological Science, 50, 31-38. https://doi.org/10.1016/j.jas.2014.06.010

del Barrio, E., Cuesta-Albertos, J. A., Carlos, M., & Jesus M., R.-R. (1999). TESTS OF GOODNESS OF FIT BASED ON THE L2-WASSERSTEIN DISTANCE. The Annals of Statistics, 27(4), 1230-1239.

Delvet, E. (2012). Recent rock art studies in northern Eurasia, 2005-2009 (p. 124-148). Oxbow ; David Brown Book Company [distributor].

Denaire, A., Jeunesse, C., Monna, F., & Waldvogel, L. (2019). Quelques remarques sur les enceintes en pierre sèche des habitats traditionnels actuels de l'île de Sumba (Indonésie). le phénomène des enceintes dans le Néolithique du nord- ouest de l'Europe, 33e colloque interrégional sur le Néolithique, Saint-Dié-des- Vosges.

Devanastya, M. (2020). The Transformation of Form and Discourse of Identity in Sumbanese Houses and Settlements: Proceedings of the 3rd International Conference on Dwelling Form (IDWELL 2020). 3rd International Conference on Dwelling Form (IDWELL 2020), Sanur, Bali, Indonesia. https://doi.org/10.2991/assehr.k.201009.016

Devereux, B. J., Amable, G. S., & Crow, P. (2008). Visualisation of LiDAR terrain models for archaeological feature detection. Antiquity, 82(316), 470-479. https://doi.org/10.1017/S0003598X00096952

Díaz-Guardamino, M., García Sanjuán, L., Wheatley, D., & Rodríguez Zamora, V. (2015). RTI and the study of engraved rock art : A re-examination of the Iberian south-western stelae of Setefilla and Almadén de la Plata 2 (Seville, Spain). Digital Applications in Archaeology and Cultural Heritage, 2(2-3), 41-54. https://doi.org/10.1016/j.daach.2015.07.002

Diaz-Guardamino, M., & Wheatley, D. (2013). Rock art and digital technologies : The application of Reflectance Transformation Imaging (RTI) and 3D laser scanning to the study of Late Bronze Age Iberian stelae. Journal of Andalusian Prehistory, 4, 187-203.

Dikov, N. N. (1958). Bronzovyi vek Zabaikal'ya.

Domingo, I., Carrión, B., Blanco, S., & Lerma, J. L. (2015). Evaluating conventional and advanced visible image enhancement solutions to produce digital tracings at el Carche rock art shelter. Digital Applications in Archaeology and Cultural Heritage, 2(2-3), 79-88. https://doi.org/10.1016/j.daach.2015.01.001

Domingo, I., Villaverde, V., López-Montalvo, E., Lerma, J. L., & Cabrelles, M. (2013). Latest developments in rock art recording : Towards an integral documentation of Levantine rock art sites combining 2D and 3D recording techniques. Journal of Archaeological Science, 40(4), 1879-1889. https://doi.org/10.1016/j.jas.2012.11.024

Domingos, P., & Pazzani, M. (1997). On the Optimality of the Simple Bayesian Classifier under Zero-One Loss. Machine Learning, 29(2/3), 103-130. https://doi.org/10.1023/A:1007413511361

Doneus, M. (2013). Openness as Visualization Technique for Interpretative Mapping of Airborne Lidar Derived Digital Terrain Models. Remote Sensing, 5(12), 6427-6442. https://doi.org/10.3390/rs5126427

Dozier, J., & Frew, J. (1990). Rapid calculation of terrain parameters for radiation modeling from digital elevation data. IEEE Transactions on Geoscience and Remote Sensing, 28(5), 963-969. https://doi.org/10.1109/36.58986

Dryden, I. L., & Mardia, K. V. (1998). Statistical shape analysis. John Wiley & Sons.

Duffy, S. M. (2010). Polynomial texture mapping at roughint linn rock art site. nternational Archives of Photogrammetry, Remote Sensing and Spatial Information Sciences, . XXXVIII(5), 213-217.

Duflou, H., Maenhaut, W., & De Reuck, J. (1990). Application of principal component and cluster analysis to the study of the distribution of minor and trace elements in normal human brain. Chemometrics and Intelligent Laboratory Systems, 9(3), 273-286. https://doi.org/10.1016/0169-7439(90)80078-K

Dunn, J. C. (1973). A Fuzzy Relative of the ISODATA Process and Its Use in Detecting Compact Well-Separated Clusters. Journal of Cybernetics, 3(3), 32-57. https://doi.org/10.1080/01969727308546046

Emmert-Streib, F., Yang, Z., Feng, H., Tripathi, S., & Dehmer, M. (2020). An Introductory Review of Deep Learning for Prediction Models With Big Data. Frontiers in Artificial Intelligence, 3, 4. https://doi.org/10.3389/frai.2020.00004

Erdenebaatar, D. (2004). Burial materials related to the history of the Bronze Age in the territory of Mongolia. In Metallurgy in ancient eastern Eurasia from the Urals to the Yellow River (Vol. 31, p. 189-222).

Ergün Hatir, M., & İnce, İ. (2021). Lithology mapping of stone heritage via state-of-the-art computer vision. Journal of Building Engineering, 34, 101921. https://doi.org/10.1016/j.jobe.2020.101921

Erkelens, C. J. (2017). Perspective Space as a Model for Distance and Size Perception. I-Perception, 8(6), 204166951773554. https://doi.org/10.1177/2041669517735541

Esin, Y., Magail, J., Gantulga, J.-O., & Yeruul-Erdene, C. (2021). Chariots in the Bronze Age of Central Mongolia based on the materials from the Khoid Tamir river valley. Archaeological Research in Asia, 27, 100304. https://doi.org/10.1016/j.ara.2021.100304

Esin, Y., Magail, J., Yeruul-Erdenne, C., & Gantulga, J.-O. (2018). Au sujet des traces de peintures sur les stèles ornées de Mongolie de la fin de l'âge du Bronze et du début de l'âge du Fer. Bulletin du Musée d'Anthropologie Préhistorique de Monaco, 58, 145-156.

Esin, Y. N., Magail, J., Yeruul-Erdene, C., & Gantulga, J. (2017). Paint on Deer Stones of Mongolia. Archaeology, Ethnology & Anthropology of Eurasia, 45(3), 79-89. https://doi.org/10.17746/1563-0110.2017.45.3.079-089

Ester, M., Kriegel, H.-P., Sander, J., & Xu, X. (1996). A density-based algorithm for discovering clusters in large spatial databases with noise. 226-231.

Evans, L., & Mourad, A.-L. (2018). DStretch® and Egyptian tomb paintings : A case study from Beni Hassan. Journal of Archaeological Science: Reports, 18, 78-84. https://doi.org/10.1016/j.jasrep.2018.01.011

Everitt, B. (Éd.). (2011). Cluster analysis (5th ed). Wiley.

Filion, D., & McNaughton, R. (2008). Effects & techniques. ACM SIGGRAPH 2008 Classes on - SIGGRAPH '08, 133. https://doi.org/10.1145/1404435.1404441

Fiorillo, F., Jiménez Fernández-Palacios, B., Remondino, F., & Barba, S. (2015). 3d Surveying and modelling of the Archaeological Area of Paestum, Italy. Virtual Archaeology Review, 4(8), 55. https://doi.org/10.4995/var.2013.4306

Fitzhugh, W., & Bayarsaikhan, J. (2010). American-Mongolian Deer Stone Project : Field Report 2009. Washington DC and Ulaanbaatar: Arctic Studies Center, Smithsonian Institution, and National Museum of Mongolia.

Fitzhugh, W., & Bayarsaikhan, J. (Éds.). (2011). 8. Mapping Ritual Landscapes in Bronze Age Mongolia and Beyond : Interpreting the Ideoscape of the Deer Stone-Khirigsuur Complex. In Mapping Mongolia (p. 166-192). University of Pennsylvania Press. https://doi.org/10.9783/9781934536315.166

Fitzhugh, W. W. (2009a). The Mongolian Deer Stone-Khirigsuur Complex : Dating and Organiation of a Late Bronze Age Menagerie. Current Archaeological Research in Mongolia, 183-199.

Fitzhugh, W. W. (2009b). Pre-Scythian Ceremonialism, Deer Stone Art, and Cultural Intensification in Northern Mongolia. In B. K. Hanks & K. M. Linduff (Éds.), Social Complexity in Prehistoric Eurasia (1re éd., p. 378-412). Cambridge University Press. https://doi.org/10.1017/CBO9780511605376.021

Fitzhugh, W. W. (2017). Mongolian Deer Stones, European Menhirs, and Canadian Arctic Inuksuit : Collective Memory and the Function of Northern Monument Traditions. Journal of Archaeological Method and Theory, 24(1), 149-187. https://doi.org/10.1007/s10816-017-9328-0

Freitag, G., Czado, C., & Munk, A. (2007). A nonparametric test for similarity of marginals—With applications to the assessment of population bioequivalence. Journal of Statistical Planning and Inference, 137(3), 697-711. https://doi.org/10.1016/j.jspi.2006.06.003

Freund, Y., & Schapire, R. E. (1997). A Decision-Theoretic Generalization of On-Line Learning and an Application to Boosting. Journal of Computer and System Sciences, 55(1), 119-139. https://doi.org/10.1006/jcss.1997.1504

Frohlich, B., Amgalantögs, T., Littleton, J., Erdene, B., Hunt, D., Nittler, E., Karstens, S., Frohlich, T., & Galdan, G. (2010). An overview of theories and hypothesis pertaining to Mongolian Bronze Age khirgisuurs in the Hovsgol Aimag, Mongolia. Studia Archaeologica Instituti Archaeologici Academiae Scientiarum Mongolicae, IX(XXIX).

Frohlich, B., Amgalantögs, T., Littleton, J., Hunt, D., Hinton, J., Batchatar, E., Dickson, M., Frohlich, T., & Goler, K. (2008). Bronze Age burial mounds (Khirigsuurs) in the Hovsgol aimag, Mongolia : A reconstruction of biological and social histories. Studia Archaeologica Instituti Archaeologici Academiae Scientiarum Mongolicae, 6, 92-114.

Galili, T. (2022). Dendextend. http://talgalili.github.io/dendextend/,

Gallwey, Eyre, Tonkins, & Coggan. (2019). Bringing Lunar LiDAR Back Down to Earth : Mapping Our Industrial Heritage through Deep Transfer Learning. Remote Sensing, 11(17), 1994. https://doi.org/10.3390/rs11171994

Gansell, A. R., Meent, J.-W. van de, Zairis, S., & Wiggins, C. H. (2014). Stylistic clusters and the Syrian/South Syrian tradition of first-millennium BCE Levantine ivory carving : A machine learning approach. Journal of Archaeological Science, 44, 194-205. https://doi.org/10.1016/j.jas.2013.11.005

Gantulga, J., Bayarkhuu, N., Batsukh, D., Erdene-Ochir, N., Batbold, N., Enkhbayar, G., Omirbek, B., Iderkhangai, T., & Turbat, T. (2018). Mongol ba bùs nutgiĭn bugan khòshòòniĭ soël : Ėrdėm shinzhilgėėniĭ katalog (Vol. 2). « Admon Print » KhKhK.

Gantulga, J.-O., Yeruul-Erdene, C., Magail, J., & Esin, Y. (2013). Khoid Tamiryn khundiy dekh bugan chuluun khushuuniy sudalgaany zarim ur dyn. Studia Archaeologica Instituti Archaeologici Academiae Scientiarum Mongolicae, XXXIII(1), 95-119.

Gantulga, Z., Bayarkhuu, N., Batsukh, D., Erdene-Ochir, N., Batbold, N., Enkhbayar, G., Omirbek, B., Iderkhangai, T., & Turbat, T. (2018). Mongol ba bùs nutgiĭn bugan khòshòòniĭ soël : Ėrdėm shinzhilgėėniĭ katalog (Vol. 1). « Admon Print » KhKhK.

Gantulga, Z., Eròòl-Ėrdėnė, C., Magail, J., & T͡Sėvėėndorzh, D. (2016). Khoĭd Tamiryn bugan khòshòò. Admon Print KhKhK-d khėvlėv.

Gantulga, Ž.-O. (2021). DEER STONE CULTURE OF MONGOLIA AND NEIGHBORING REGIONS (T. Turbat & D. Cėvėėndorž, Éds.; Nėg dėh hėvlėl). « Mönhijn Üsėg » HHK.

Géron, A. (2017). Hands-on machine learning with Scikit-Learn and TensorFlow : Concepts, tools, and techniques to build intelligent systems (First edition). O'Reilly Media.

Géron, A., & Soulard, H. (2020). Deep learning avec Keras et TensorFlow : Mise en oeuvre et cas concrets (2e ed). Dunod.

Gheisari, M., Foroughi Sabzevar, M., Chen, P., & Irizzary, J. (2016). Integrating BIM and Panorama to Create a Semi-Augmented-Reality Experience of a Construction Site. International Journal of Construction Education and Research, 12(4), 303-316. https://doi.org/10.1080/15578771.2016.1240117

Gillespie, A. R., Kahle, A. B., & Walker, R. E. (1986). Color enhancement of highly correlated images. I. Decorrelation and HSI contrast stretches. Remote Sensing of Environment, 20(3), 209-235. https://doi.org/10.1016/0034-4257(86)90044-1

Golub, G. H., & Van Loan, C. F. (2013). Matrix computations (Fourth edition). The Johns Hopkins University Press.

Gonizzi Barsanti, S., Caruso, G., Micoli, L. L., Covarrubias Rodriguez, M., & Guidi, G. (2015). 3D Visualization of Cultural Heritage Artefacts with Virtual Reality devices. The International Archives of the Photogrammetry, Remote Sensing and Spatial Information Sciences, XL-5/W7, 165-172. https://doi.org/10.5194/isprsarchives-XL-5-W7-165-2015

Goodfellow, I., Bengio, Y., & Courville, A. (2016). Deep learning. The MIT Press.

Goslee, S. C., & Urban, D. L. (2007). The ecodist Package for Dissimilarity-based Analysis of Ecological Data. Journal of Statistical Software, 22(7). https://doi.org/10.18637/jss.v022.i07

Goupy, J. (1993). Methods for experimental design : Principles and applications for physicists and chemists. Elsevier.

Gower, J. C. (1971). A General Coefficient of Similarity and Some of Its Properties. Biometrics, 27(4), 857. https://doi.org/10.2307/2528823

Gower, J. C., & Dijksterhuis, G. B. (2004). Procrustes problems. Oxford University Press.

Grosse-Brauckmann, K. (2012). Triply periodic minimal and constant mean curvature surfaces. Interface Focus, 2(5), 582-588. https://doi.org/10.1098/rsfs.2011.0096

Gullì, A., Kapoor, A., & Pal, S. (2019). Deep learning with TensorFlow 2 and Keras : Regression, ConvNets, GANs, RNNs, NLP, and more with TensorFlow 2 and the Keras API (Second edition). Packt.

Gunn, R. G., Ogleby, C. L., & Whear, R. L. (2010). A METHOD TO VISUALLY RATIONALISE SUPERIMPOSED PIGMENT MOTIFS. Rock Art Research, 27(2), 131-136.

Gupta, R. P. (2018). Remote Sensing Geology (3rd ed. 2018). Springer Berlin Heidelberg : Imprint: Springer. https://doi.org/10.1007/978-3-662-55876-8

Guttentag, D. A. (2010). Virtual reality : Applications and implications for tourism. Tourism Management, 31(5), 637-651. https://doi.org/10.1016/j.tourman.2009.07.003

Hall-Beyer, M. (2017). Practical guidelines for choosing GLCM textures to use in landscape classification tasks over a range of moderate spatial scales. International Journal of Remote Sensing, 38(5), 1312-1338. https://doi.org/10.1080/01431161.2016.1278314

Han, S.-E., Tao, B., Cooper, T., & Tastl, I. (2000). Comparison between Different Color Transformations for JPEG 2000. IS&T's 2000 PICS Conference.

Haralick, R. M., Shanmugam, K., & Dinstein, I. (1973). Textural Features for Image Classification. IEEE Transactions on Systems, Man, and Cybernetics, SMC-3(6), 610-621. https://doi.org/10.1109/TSMC.1973.4309314

Harman, J. (2005). DStretch. http://www.dstretch.com/

Hastie, T., Tibshirani, R., & Friedman, J. H. (2009). The elements of statistical learning : Data mining, inference, and prediction (2nd ed). Springer.

Hatir, M. E., Barstuğan, M., & İnce, İ. (2020). Deep learning-based weathering type recognition in historical stone monuments. Journal of Cultural Heritage, 45, 193-203. https://doi.org/10.1016/j.culher.2020.04.008

Hay, R. L. (1976). Geology of the Olduvai Gorge : A study of sedimentation in a semiarid basin. Univ. of California Pr.

Hay, R. L., & Kyser, T. K. (2001). Chemical sedimentology and paleoenvironmental history of Lake Olduvai, a Pliocene lake in northern Tanzania. GSA Bulletin, 113(12), 1505-1521. https://doi.org/10.1130/0016-7606(2001)113<1505:CSAPHO>2.0.CO;2

He, K., Gkioxari, G., Dollár, P., & Girshick, R. (2017). Mask R-CNN. https://doi.org/10.48550/ARXIV.1703.06870

He, K., Zhang, X., Ren, S., & Sun, J. (2015). Deep Residual Learning for Image Recognition. https://doi.org/10.48550/ARXIV.1512.03385

Hennig, C. (2020). Flexible Procedures for Clustering. L https://www.unibo.it/sitoweb/christian.hennig/en/

Hesse, R. (2010). LiDAR-derived Local Relief Models—A new tool for archaeological prospection. Archaeological Prospection, n/a-n/a. https://doi.org/10.1002/arp.374

Hinton, G. E., Osindero, S., & Teh, Y.-W. (2006). A Fast Learning Algorithm for Deep Belief Nets. Neural Computation, 18(7), 1527-1554. https://doi.org/10.1162/neco.2006.18.7.1527

Hobbs, K. F. (1999). An investigation of RGB multi-band shading for relief visualisation. International Journal of Applied Earth Observation and Geoinformation, 1(3-4), 181-186. https://doi.org/10.1016/S0303-2434(99)85011-9

Hodson, F. R. (1971). Numerical typology and prehistoric archaeology. In Mathematics in the Archaeological and Historical Sciences (p. 30-45). Edinburgh University Press.

Hodson, F. R., Sneath, P. H. A., & Doran, J. E. (1966). Some Experiments in the Numerical Analysis of Archaeological Data. Biometrika, 53(3/4), 311. https://doi.org/10.2307/2333638

Hofmann, M. (2006). Support Vector Machines—Kernels and the Kernel Trick.

Holden, D., Saito, J., & Komura, T. (2016). Neural network ambient occlusion. SIGGRAPH ASIA 2016 Technical Briefs, 1-4. https://doi.org/10.1145/3005358.3005387

Honeychurch, W., & Amartuvshin, C. (2006). States on Horseback:The Rise of Inner Asian Confederations and Empires. In M. T. Stark (Éd.), Archaeology of Asia (p. 255-278). Blackwell Publishing Ltd. https://doi.org/10.1002/9780470774670.ch12

Honeychurch, W., Wright, J., & Amartuvshin, C. (2009). Re-writing Monumental Landscapes as Inner Asian Political Process. In B. K. Hanks & K. M. Linduff (Éds.), Social Complexity in Prehistoric Eurasia (1re éd., p. 330-357). Cambridge University Press. https://doi.org/10.1017/CBO9780511605376.019

Horn, B. K. P. (1981). Hill shading and the reflectance map. Proceedings of the IEEE, 69(1), 14-47. https://doi.org/10.1109/PROC.1981.11918

Horn, C., Ivarsson, O., Lindhé, C., Potter, R., Green, A., & Ling, J. (2022). Artificial Intelligence, 3D Documentation, and Rock Art—Approaching and Reflecting on the Automation of Identification and Classification of Rock Art Images. Journal of Archaeological Method and Theory, 29(1), 188-213. https://doi.org/10.1007/s10816-021-09518-6

Horning, N. (Éd.). (2010). Remote sensing for ecology and conservation : A handbook of techniques. Oxford University Press.

Hörr, C., Lindinger, E., & Brunnett, G. (2014). Machine learning based typology development in archaeology. Journal on Computing and Cultural Heritage, 7(1), 1-23. https://doi.org/10.1145/2533988

Hosmer, D. W., Lemeshow, S., & Sturdivant, R. X. (2013). Applied logistic regression (Third edition). Wiley.

Houbre, A. (2013). La grammaire des décors céramiques du Néolithique ancien danubien des bassins du Rhin, de la Meuse et de la Seine : Entre norme et transgression. Bulletin de la Société préhistorique française, 110(1), 77-103. https://doi.org/10.3406/bspf.2013.14230

Houle, J.-L. (2009). Socially Integrative Facilities and the Emergence of Societal Complexity on the Mongolian Steppe. In B. K. Hanks & K. M. Linduff (Éds.), Social Complexity in Prehistoric Eurasia (1re éd., p. 358-377). Cambridge University Press. https://doi.org/10.1017/CBO9780511605376.020

Houle, J.-L. (2010). Emergent Complexity on the Mongolian Steppe : Mobility, Territoriality, and the Development of Early Nomadic Polities [Doctoral Dissertation]. University of Pittsburgh.

Houle, J.-L. (2016). Bronze Age Mongolia. In Oxford Handbooks Editorial Board (Éd.), Online Only—Archaeology (1re éd.). Oxford University Press. https://doi.org/10.1093/oxfordhb/9780199935413.013.20

Hu, G., Dai, W., Li, S., Xiong, L., Tang, G., & Strobl, J. (2021). Quantification of terrain plan concavity and convexity using aspect vectors from digital elevation models. Geomorphology, 375, 107553. https://doi.org/10.1016/j.geomorph.2020.107553

Hudzietz, B. P., & Saripalli, S. (2012). AN EXPERIMENTAL EVALUATION OF 3D TERRAIN MAPPING WITH AN AUTONOMOUS HELICOPTER. The International Archives of the Photogrammetry, Remote Sensing and Spatial Information Sciences, XXXVIII-1/C22, 137-142. https://doi.org/10.5194/isprsarchives-XXXVIII-1-C22-137-2011

Hyvärinen, A. (2013). Independent component analysis : Recent advances. Philosophical Transactions of the Royal Society A: Mathematical, Physical and Engineering Sciences, 371(1984), 20110534. https://doi.org/10.1098/rsta.2011.0534

Hyvärinen, A., & Oja, E. (2000). Independent component analysis : Algorithms and applications. Neural Networks, 13(4-5), 411-430. https://doi.org/10.1016/S0893-6080(00)00026-5

Jacobson, E. (1993). The deer goddess of ancient Siberia : A study in the ecology of belief. E.J. Brill.

Jacobson-Tepfer, E. (2001). Cultural Riddles : Stylized Deer and Deer Stones of the Mongolian Altai. Bulletin of the Asia Institute, 15, 31-56.

James, G., Witten, D., Hastie, T., & Tibshirani, R. (2021). An introduction to statistical learning : With applications in R (Second edition). Springer. https://doi.org/10.1007/978-1-0716-1418-1

Jasiewicz, J., & Stepinski, T. F. (2013). Geomorphons—A pattern recognition approach to classification and mapping of landforms. Geomorphology, 182, 147-156. https://doi.org/10.1016/j.geomorph.2012.11.005

Jeunesse, C. (2019a). Dualist socio-political systems in South East Asia and the interpretation of late prehistoric European societies. 181-213.

Jeunesse, C. (2019b). Sacrifice et partage dans l'île de Sumba (Indonésie). L'Archéologie, 150, 66-69.

Jiménez Fernández-Palacios, B., Morabito, D., & Remondino, F. (2017). Access to complex reality-based 3D models using virtual reality solutions. Journal of Cultural Heritage, 23, 40-48. https://doi.org/10.1016/j.culher.2016.09.003

Jolliffe, I. T. (2002). Principal component analysis (2nd ed). Springer.

Kassambara, A. (2017). Practical guide to cluster analysis in R : Unsupervised machine learning (Edition 1). STHDA.

Kassambara, A., & Mundt, F. (2020). Package 'factoextra'. http://www.sthda.com/english/rpkgs/factoextra

Katsouri, I., Tzanavari, A., Herakleous, K., & Poullis, C. (2015). Visualizing and Assessing Hypotheses for Marine Archaeology in a VR CAVE Environment. Journal on Computing and Cultural Heritage, 8(2), 1-18. https://doi.org/10.1145/2665072

Kennelly, P. J. (2008). Terrain maps displaying hill-shading with curvature. Geomorphology, 102(3-4), 567-577. https://doi.org/10.1016/j.geomorph.2008.05.046

Kennelly, P. J., & Stewart, A. J. (2014). General sky models for illuminating terrains. International Journal of Geographical Information Science, 28(2), 383-406. https://doi.org/10.1080/13658816.2013.848985

Kessy, A., Lewin, A., & Strimmer, K. (2015). Optimal whitening and decorrelation. https://doi.org/10.48550/ARXIV.1512.00809

Khan, S. S., & Kant, S. (2007). Computation of initial modes for k-modes clustering algorithm using evidence accumulation. 2784-2789.

Kim, T. K. (2015). T test as a parametric statistic. Korean Journal of Anesthesiology, 68(6), 540. https://doi.org/10.4097/kjae.2015.68.6.540

Kiourt, C., Koutsoudis, A., Arnaoutoglou, F., Petsa, G., Markantonatou, S., & Pavlidis, G. (2015). A dynamic web-based 3D virtual museum framework based on open data. 2015 Digital Heritage, 647-650. https://doi.org/10.1109/DigitalHeritage.2015.7419589

Kobler, A., Džeroski, S., & Keramitsoglou, I. (2006). Habitat mapping using machine learning-extended kernel-based reclassification of an Ikonos satellite image. Ecological Modelling, 191(1), 83-95. https://doi.org/10.1016/j.ecolmodel.2005.08.002

Koehl, M., & Brigand, N. (2012). COMBINATION OF VIRTUAL TOURS, 3D MODEL AND DIGITAL DATA IN A 3D ARCHAEOLOGICAL KNOWLEDGE AND INFORMATION SYSTEM. The International Archives of the Photogrammetry, Remote Sensing and Spatial Information Sciences, XXXIX-B4, 439-444. https://doi.org/10.5194/isprsarchives-XXXIX-B4-439-2012

Koeva, M., Luleva, M., & Maldjanski, P. (2017). Integrating Spherical Panoramas and Maps for Visualization of Cultural Heritage Objects Using Virtual Reality Technology. Sensors, 17(4), 829. https://doi.org/10.3390/s17040829

Koga, Y., Miyazaki, H., & Shibasaki, R. (2020). A Method for Vehicle Detection in High-Resolution Satellite Images that Uses a Region-Based Object Detector and Unsupervised Domain Adaptation. Remote Sensing, 12(3), 575. https://doi.org/10.3390/rs12030575

Kohonen, T. (1997). Self-organizing maps (2nd ed). Springer.

Kohonen, T. (2014). MATLAB Implementations and Applications of the Self-Organizing Map (Unigrafia Oy).

Kokalj, Ž., & Somrak, M. (2019). Why Not a Single Image? Combining Visualizations to Facilitate Fieldwork and On-Screen Mapping. Remote Sensing, 11(7), 747. https://doi.org/10.3390/rs11070747

Kotoula, E., Robinson, D. W., & Bedford, C. (2018). Interactive relighting, digital image enhancement and inclusive diagrammatic representations for the analysis of rock art superimposition : The main Pleito cave (CA, USA). Journal of Archaeological Science, 93, 26-41. https://doi.org/10.1016/j.jas.2018.02.012

Krizhevsky, A., Sutskever, I., & Hinton, G. E. (2017). ImageNet classification with deep convolutional neural networks. Communications of the ACM, 60(6), 84-90. https://doi.org/10.1145/3065386

Kuhn, M., & Johnson, K. (2013). Applied predictive modeling. Springer.

Kulldorff, M. (1999). Spatial Scan Statistics : Models, Calculations, and Applications. In J. Glaz & N. Balakrishnan (Éds.), Scan Statistics and Applications (p. 303-322). Birkhäuser Boston. https://doi.org/10.1007/978-1-4612-1578-3_14

Kung, S. Y. (2014). Kernel Methods and Machine Learning (1re éd.). Cambridge University Press. https://doi.org/10.1017/CBO9781139176224

Lachenbruch, P. A., & Goldstein, M. (1979). Discriminant Analysis. Biometrics, 35(1), 69. https://doi.org/10.2307/2529937

Lambers, K., Verschoof-van der Vaart, W., & Bourgeois, Q. (2019). Integrating Remote Sensing, Machine Learning, and Citizen Science in Dutch Archaeological Prospection. Remote Sensing, 11(7), 794. https://doi.org/10.3390/rs11070794

Langer, M. S., & Zucker, S. W. (1994). Shape-from-shading on a cloudy day. Journal of the Optical Society of America A, 11(2), 467. https://doi.org/10.1364/JOSAA.11.000467

Lantz, B. (2015). Machine learning with R : Discover how to build machine learning algorithms, prepare data, and dig deep into data prediction techniques with R (2. ed). Packt Publ.

Lapaine, M., & Usery, E. L. (Éds.). (2017). Choosing a Map Projection (1st ed. 2017). Springer International Publishing : Imprint: Springer. https://doi.org/10.1007/978-3-319-51835-0

Lawrence, S., Giles, C. L., Ah Chung Tsoi, & Back, A. D. (1997). Face recognition : A convolutional neural-network approach. IEEE Transactions on Neural Networks, 8(1), 98-113. https://doi.org/10.1109/72.554195

Le Quellec, J.-L., Harman, J., Defrasne, C., & Duquesnoy, F. (2013). D-Stretch® et l'amélioration des images numériques : Applications à l'archéologie des images rupestres. Les Cahiers de l'AARS, 16, 177-198.

Leachtenauer, J. C., & Driggers, R. G. (2001). Surveillance and reconnaissance imaging systems : Modeling and performance prediction. Artech House.

LeCun, Y., Bengio, Y., & Hinton, G. (2015). Deep learning. Nature, 521(7553), 436-444. https://doi.org/10.1038/nature14539

Lepetz, S., Zazzo, A., Bernard, V., de Larminat, S., Magail, J., & Gantulga, J.-O. (2019). Customs, rites, and sacrifices relating to a mortuary complex in Late Bronze Age Mongolia (Tsatsyn Ereg, Arkhangai). Anthropozoologica, 54(1), 151. https://doi.org/10.5252/anthropozoologica2019v54a15

Lerma, J. L., Navarro, S., Seguí, A. E., & Cabrelles, M. (2014). Range-Based Versus Automated Markerless Image-Based Techniques For Rock Art Documentation. The Photogrammetric Record, 29(145), 30-48. https://doi.org/10.1111/phor.12054

Lin, T.-Y., Dollár, P., Girshick, R., He, K., Hariharan, B., & Belongie, S. (2016). Feature Pyramid Networks for Object Detection. https://doi.org/10.48550/ARXIV.1612.03144

Lin, T.-Y., Maire, M., Belongie, S., Hays, J., Perona, P., Ramanan, D., Dollár, P., & Zitnick, C. L. (2014). Microsoft COCO : Common Objects in Context. In D. Fleet, T. Pajdla, B. Schiele, & T. Tuytelaars (Éds.), Computer Vision – ECCV 2014 (Vol. 8693, p. 740-755). Springer International Publishing. https://doi.org/10.1007/978-3-319-10602-1_48

Lin, W. (2008). Earthquake‐induced landslide hazard monitoring and assessment using SOM and PROMETHEE techniques : A case study at the Chiufenershan area in Central Taiwan. International Journal of Geographical Information Science, 22(9), 995-1012. https://doi.org/10.1080/13658810801914458

Linowes, J. (2018). Unity virtual reality projects : Learn virtual reality by developing more than 10 engaging projects with Unity 2018 (Second Edition). Packt Publishing.

Littleton, J., Floyd, B., Frohlich, B., Dickson, M., Amgalantögs, T., Karstens, S., & Pearlstein, K. (2012). Taphonomic analysis of Bronze Age burials in Mongolian khirigsuurs. Journal of Archaeological Science, 39(11), 3361-3370. https://doi.org/10.1016/j.jas.2012.06.004

Liu, L., Ouyang, W., Wang, X., Fieguth, P., Chen, J., Liu, X., & Pietikäinen, M. (2020). Deep Learning for Generic Object Detection : A Survey. International Journal of Computer Vision, 128(2), 261-318. https://doi.org/10.1007/s11263-019-01247-4

Liu, Q., Cheng, W., Yan, G., Zhao, Y., & Liu, J. (2019). A Machine Learning Approach to Crater Classification from Topographic Data. Remote Sensing, 11(21), 2594. https://doi.org/10.3390/rs11212594

Liu, W., Anguelov, D., Erhan, D., Szegedy, C., Reed, S., Fu, C.-Y., & Berg, A. C. (2015). SSD : Single Shot MultiBox Detector. https://doi.org/10.48550/ARXIV.1512.02325

Liu, Y. (2005). Patterns of ocean current variability on the West Florida Shelf using the self-organizing map. Journal of Geophysical Research, 110(C6), C06003. https://doi.org/10.1029/2004JC002786

Longley, P. (Éd.). (2011). Geographic information systems & science (3. ed., fully updated). Wiley.

Loos, B. J., & Sloan, P.-P. (2010a). Volumetric obscurance. Proceedings of the ACM SIGGRAPH Symposium on Interactive 3D Graphics and Games - I3D 10, 151. https://doi.org/10.1145/1730804.1730829

Loos, B. J., & Sloan, P.-P. (2010b). Volumetric obscurance. Proceedings of the ACM SIGGRAPH Symposium on Interactive 3D Graphics and Games - I3D 10, 151. https://doi.org/10.1145/1730804.1730829

Lund, U., Agostinelli, C., Arai, H., Gagliardi, A., García-Portugué, E., Giunchi, D., Irisson, J.-O., Pocernich, M., & Rotolo, F. (2022). Package ‘circular’.

Lundstedt, T., Seifert, E., Abramo, L., Thelin, B., Nyström, Å., Pettersen, J., & Bergman, R. (1998). Experimental design and optimization. Chemometrics and Intelligent Laboratory Systems, 42(1-2), 3-40. https://doi.org/10.1016/S0169-7439(98)00065-3

Luo, L., Wang, X., Guo, H., Lasaponara, R., Zong, X., Masini, N., Wang, G., Shi, P., Khatteli, H., Chen, F., Tariq, S., Shao, J., Bachagha, N., Yang, R., & Yao, Y. (2019). Airborne and spaceborne remote sensing for archaeological and cultural heritage applications : A review of the century (1907–2017). Remote Sensing of Environment, 232, 111280. https://doi.org/10.1016/j.rse.2019.111280

MacQueen, J. (1967). Some methods for classification and analysis of multivariate observations. Proc. of the fifth Berkeley Symposium on Mathematical Statistics and Probability, 5, 281-297.

Maechler, M., Rousseeuw, P. J., Struyf, A., Hubert, M., Hornik, K., Studer, M., Roudier, P., Gonzalez, J., Kozlowski, K., & Murphy, K. (2022). Package ‘cluster’. https://svn.r-project.org/R-packages/trunk/cluster/

Magail, J. (2008). Tsatsiin Ereg, site majeur du début du 1er millénaire en Mongolie. Bulletin du Musée d’Anthropologie Préhistorique de Monaco, 48, 107-121.

Magail, J. (2015). Les stèles ornées de Mongolie dites « pierres à cerfs », de la fin de l’âge du Bronze. In Statues-menhirs et pierres levées du Néolithique à aujourd’hui (p. 89-101). Direction régionale des affaires culturelles Languedoc-Roussillon Groupe archéologique du Saint-Ponais.

Magail, J., Gantulga, J.-O., Yeruul-Erdenne, C., & Tsengel, M. (2010). Inventaire et relevésdes pierres à cerfs de Tsatsiin Ereg. Bulletin du Musée d’Anthropologie Préhistorique de Monaco, 77-114.

Magail, J., Monna, F., Esin, Y., Wilczek, J., & Yeruul-Erdenne, C. (2017). Application de la photogrammétrie à la documentation de l’art rupestre, des chantiers de fouilles et du bâti. Bulletin du Musée d’Anthropologie préhistorique de Monaco, 56, 69-92.

Mallory-Greenough, L. M., Greenough, J. D., & Owen, J. V. (1998). New Data For Old Pots : Trace-Element Characterization of Ancient Egyptian Pottery Using ICP-MS. Journal of Archaeological Science, 25(1), 85-97. https://doi.org/10.1006/jasc.1997.0202

Masita, K. L., Hasan, A. N., & Shongwe, T. (2020). Deep Learning in Object Detection : A Review. 2020 International Conference on Artificial Intelligence, Big Data, Computing and Data Communication Systems (icABCD), 1-11. https://doi.org/10.1109/icABCD49160.2020.9183866

Maxwell, A. E., Pourmohammadi, P., & Poyner, J. D. (2020). Mapping the Topographic Features of Mining-Related Valley Fills Using Mask R-CNN Deep Learning and Digital Elevation Data. Remote Sensing, 12(3), 547. https://doi.org/10.3390/rs12030547

McGuire, M., Osman, B., Bukowski, M., & Hennessy, P. (2011). The alchemy screen-space ambient obscurance algorithm. Proceedings of the ACM SIGGRAPH Symposium on High Performance Graphics - HPG ’11, 25. https://doi.org/10.1145/2018323.2018327

Michiels, N., Jorissen, L., Put, J., & Bekaert, P. (2014). Interactive Augmented Omnidirectional Video with Realistic Lighting. In L. T. De Paolis & A. Mongelli (Éds.), Augmented and Virtual Reality (Vol. 8853, p. 247-263). Springer International Publishing. https://doi.org/10.1007/978-3-319-13969-2_19

Mihelj, M., Novak, D., & Beguš, S. (2014). Virtual reality technology and applications. Springer.

Miller, G. (1994). Efficient algorithms for local and global accessibility shading. Proceedings of the 21st Annual Conference on Computer Graphics and Interactive Techniques - SIGGRAPH ’94, 319-326. https://doi.org/10.1145/192161.192244

Minár, J., Evans, I. S., & Jenčo, M. (2020). A comprehensive system of definitions of land surface (topographic) curvatures, with implications for their application in geoscience modelling and prediction. Earth-Science Reviews, 211, 103414. https://doi.org/10.1016/j.earscirev.2020.103414

Mittring, M. (2007). Finding next gen : CryEngine 2. ACM SIGGRAPH 2007 Courses on - SIGGRAPH '07, 97. https://doi.org/10.1145/1281500.1281671

Miyamoto, K., Adachi, T., Amgalantgus, T., Batbold Natsag, Delgermaa, L., Funahashi, K., Ito, S., Nakano, N., Okazaki, K., Omori, T., Osanai, Y., Ozaki, H., Tajiri, Y., Yoneda, M., & Yonemoto, S. (2017). Excavations at Bor Ovoo and Khyar Kharaach Sites : The second Report on Joint Mongolian-Japanese Excavations in Outer Mongolia. 九州大学大学院人文科学研究院考古学教室. https://doi.org/10.15017/1812330

Monna, F., Esin, Y., Magail, J., Granjon, L., Navarro, N., Wilczek, J., Saligny, L., Couette, S., Dumontet, A., & Chateau, C. (2018). Documenting carved stones by 3D modelling – Example of Mongolian deer stones. Journal of Cultural Heritage, 34, 116-128. https://doi.org/10.1016/j.culher.2018.04.021

Monna, F., Magail, J., Rolland, T., Navarro, N., Wilczek, J., Gantulga, J.-O., Esin, Y., Granjon, L., Allard, A.-C., & Chateau-Smith, C. (2020). Machine learning for rapid mapping of archaeological structures made of dry stones – Example of burial monuments from the Khirgisuur culture, Mongolia –. Journal of Cultural Heritage, 43, 118-128. https://doi.org/10.1016/j.culher.2020.01.002

Monna, F., Navarro, N., Magail, J., Guillon, R., Rolland, T., Wilczek, J., Esin, Y., & Chateau, C. (2019). Contextualization of Archaeological Information Using Augmented Photospheres, Viewed with Head-Mounted Displays. Sustainability, 11(14), 3894. https://doi.org/10.3390/su11143894

Monna, F., Rolland, T., Denaire, A., Navarro, N., Granjon, L., Barbé, R., & Chateau-Smith, C. (2021). Deep learning to detect built cultural heritage from satellite imagery. - Spatial distribution and size of vernacular houses in Sumba, Indonesia -. Journal of Cultural Heritage, 52, 171-183. https://doi.org/10.1016/j.culher.2021.10.004

Montserrat, D. M., Lin, Q., Allebach, J., & Delp, E. J. (2017). Training Object Detection And Recognition CNN Models Using Data Augmentation. Electronic Imaging, 29(10), 27-36. https://doi.org/10.2352/ISSN.2470-1173.2017.10.IMAWM-163

Mross, J. W. (2000). Cultural and architectural transitions of Southwestern Sumba island, Indonesia. 260-265.

Nair, V., & Hinton, G. E. (2010). Rectified linear units improve restricted boltzmann machines. 801-814.

Napolitano, R. K., Scherer, G., & Glisic, B. (2018). Virtual tours and informational modeling for conservation of cultural heritage sites. Journal of Cultural Heritage, 29, 123-129. https://doi.org/10.1016/j.culher.2017.08.007

Northcutt, C. G., Jiang, L., & Chuang, I. L. (2019). Confident Learning : Estimating Uncertainty in Dataset Labels. https://doi.org/10.48550/ARXIV.1911.00068

Novgorodova, E. A. (1989). Drevniaia Mongoliya [Ancient Mongolia].

Noya, N. C., García, Á. L., & Ramírez, F. C. (2015). Combining photogrammetry and photographic enhancement techniques for the recording of megalithic art in north-west Iberia. Digital Applications in Archaeology and Cultural Heritage, 2(2-3), 89-101. https://doi.org/10.1016/j.daach.2015.02.004

Oke, T. R. (2006). Boundary layer climates (2nd ed). Routledge.

Okladnicov, A. P. (1954). Olennyy kalen s reki lvolgi: Vol. XIX.

Olkhovsky, V. S. (2005). Monumentalnaya skulptura naseleniya zapadnoi chasti evraziyskikh stepei epokhi rannego zheleza.

Palma, G., Corsini, M., Cignoni, P., Scopigno, R., & Mudge, M. (2010). Dynamic shading enhancement for reflectance transformation imaging. Journal on Computing and Cultural Heritage, 3(2), 1-20. https://doi.org/10.1145/1841317.1841321

Parcak, S. H. (2009). Satellite remote sensing for archaeology. Routledge.

Patel, A. A. (2019). Hands-on unsupervised learning using Python : How to build applied machine learning solutions from unlabeled data (First edition). O'Reilly Media.

Pavlidis, G., Koutsoudis, A., Arnaoutoglou, F., Tsioukas, V., & Chamzas, C. (2007). Methods for 3D digitization of Cultural Heritage. Journal of Cultural Heritage, 8(1), 93-98. https://doi.org/10.1016/j.culher.2006.10.007

Pedregosa, F., Varoquaux, G., Gramfort, A., Michel, V., Thirion, B., Grisel, O., Blondel, M., Müller, A., Nothman, J., Louppe, G., Prettenhofer, P., Weiss, R., Dubourg, V., Vanderplas, J., Passos, A., Cournapeau, D., Brucher, M., Perrot, M., & Duchesnay, É. (2012). Scikit-learn : Machine Learning in Python. https://doi.org/10.48550/ARXIV.1201.0490

Pertuz, S., Puig, D., & Garcia, M. A. (2013). Analysis of focus measure operators for shape-from-focus. Pattern Recognition, 46(5), 1415-1432. https://doi.org/10.1016/j.patcog.2012.11.011

Philip, G., & Ottaway, B. S. (1983). MIXED DATA CLUSTER ANALYSIS : AN ILLUSTRATION USING CYPRIOT HOOKED-TANG WEAPONS. Archaeometry, 25(2), 119-133. https://doi.org/10.1111/j.1475-4754.1983.tb00671.x

Phong, B. T. (1975). Illumination for computer generated pictures. Communications of the ACM, 18(6), 311-317. https://doi.org/10.1145/360825.360839

Piragnolo, M., Masiero, A., & Pirotti, F. (2017). Open source R for applying machine learning to RPAS remote sensing images. Open Geospatial Data, Software and Standards, 2(1), 16. https://doi.org/10.1186/s40965-017-0033-4

Plets, G., Gheyle, W., Verhoeven, G., De Reu, J., Bourgeois, J., Verhegge, J., & Stichelbaut, B. (2012). Three-dimensional recording of archaeological remains in the Altai Mountains. Antiquity, 86(333), 884-897. https://doi.org/10.1017/S0003598X00047980

Plets, G., Verhoeven, G., Cheremisin, D., Plets, R., Bourgeois, J., Stichelbaut, B., Gheyle, W., & De Reu, J. (2012). The deteriorating preservation of the altai rock art : Assessing three-dimensional image-based modelling in rock art research and management. Rock Art Research, 29(2), 139-156.

Pyatkin, B. N. (1998). The Shalabolino petroglyphs on the river Tuba (middle Yenisei). International newsletter on rock art, 20, 26-30.

Pyatkin, B. N., & Martinov, A. I. (1985). Shalabolinskie petroglify.

Quesada, E., & Harman, J. (2019). A step further in rock art digital enhancements. DStretch on Gigapixel imaging. Digital Applications in Archaeology and Cultural Heritage, 13, e00098. https://doi.org/10.1016/j.daach.2019.e00098

Ramdas, A., Trillos, N., & Cuturi, M. (2017). On Wasserstein Two-Sample Testing and Related Families of Nonparametric Tests. Entropy, 19(2), 47. https://doi.org/10.3390/e19020047

Rao, K. R., & Yip, P. C. (Éds.). (2001). The transform and data compression handbook. CRC Press.

Raschka, S. (2016). Python machine learning : Unlock deeper insights into machine learning with this vital guide to cutting-edge predictive analytics. Packt Publishing open source.

Raschka, S., & Mirjalili, V. (04). Python machine learning : Machine learning and deep learning with Python, scikit-learn, and TensorFlow (Second edition, fourth release,[fully revised and updated]). Packt Publishing.

Rathore, S., Hussain, M., Aksam Iftikhar, M., & Jalil, A. (2014). Ensemble classification of colon biopsy images based on information rich hybrid features. Computers in Biology and Medicine, 47, 76-92. https://doi.org/10.1016/j.compbiomed.2013.12.010

Reilly, P. (1991). Towards a virtual archaeology. 565, 132-139.

Reitberger, J., Krzystek, P., & Stilla, U. (2008). Analysis of full waveform LIDAR data for the classification of deciduous and coniferous trees. International Journal of Remote Sensing, 29(5), 1407-1431. https://doi.org/10.1080/01431160701736448

Remondino, F., & Rizzi, A. (2010). Reality-based 3D documentation of natural and cultural heritage sites—Techniques, problems, and examples. Applied Geomatics, 2(3), 85-100. https://doi.org/10.1007/s12518-010-0025-x

Ren, S., He, K., Girshick, R., & Sun, J. (2015). Faster R-CNN : Towards Real-Time Object Detection with Region Proposal Networks. https://doi.org/10.48550/ARXIV.1506.01497

Ren, Y., Zhu, C., & Xiao, S. (2018). Small Object Detection in Optical Remote Sensing Images via Modified Faster R-CNN. Applied Sciences, 8(5), 813. https://doi.org/10.3390/app8050813

Renner, R. S., Velichkovsky, B. M., & Helmert, J. R. (2013). The perception of egocentric distances in virtual environments—A review. ACM Computing Surveys, 46(2), 1-40. https://doi.org/10.1145/2543581.2543590

Rezatofighi, H., Tsoi, N., Gwak, J., Sadeghian, A., Reid, I., & Savarese, S. (2019). Generalized Intersection over Union : A Metric and A Loss for Bounding Box Regression. https://doi.org/10.48550/ARXIV.1902.09630

Riley, D. N. (1944). The Technique of Air-Archaeology. Archaeological Journal, 101(1), 1-16. https://doi.org/10.1080/00665983.1944.10853775

Robert, E., Petrognani, S., & Lesvignes, E. (2016). Applications of digital photography in the study of Paleolithic cave art. Journal of Archaeological Science: Reports, 10, 847-858. https://doi.org/10.1016/j.jasrep.2016.07.026

Rodríguez González, E., Pastor, S. C., & Casals, J. R. (2019). Lost colours : Photogrammetry, image analysis using the DStretch plugin, and 3-D modelling of post-firing painted pottery from the south west Iberian Peninsula. Digital Applications in Archaeology and Cultural Heritage, 13, e00093. https://doi.org/10.1016/j.daach.2019.e00093

Rogerio-Candelera, M. A., Jurado, V., Laiz, L., & Saiz-Jimenez, C. (2011a). Laboratory and in situ assays of digital image analysis based protocols for biodeteriorated rock and mural paintings recording. Journal of Archaeological Science, 38(10), 2571-2578. https://doi.org/10.1016/j.jas.2011.04.020

Rogerio-Candelera, M. A., Jurado, V., Laiz, L., & Saiz-Jimenez, C. (2011b). Laboratory and in situ assays of digital image analysis based protocols for biodeteriorated rock and mural paintings recording. Journal of Archaeological Science, 38(10), 2571-2578. https://doi.org/10.1016/j.jas.2011.04.020

Ronfard, R., & Taubin, G. (2010). Image and Geometry Processing for 3-D Cinematography. Springer-Verlag Berlin Heidelberg Springer e-books.

Rousseeuw, P. J. (1987). Silhouettes : A graphical aid to the interpretation and validation of cluster analysis. Journal of Computational and Applied Mathematics, 20, 53-65. https://doi.org/10.1016/0377-0427(87)90125-7

Roussou, M. (2002). Virtual Heritage : From the Research Lab to the Broad Public. 1075, 93-100.

Ruddle, R. A., Payne, S. J., & Jones, D. M. (1999). Navigating Large-Scale Virtual Environments : What Differences Occur Between Helmet-Mounted and Desk-Top Displays? Presence: Teleoperators and Virtual Environments, 8(2), 157-168. https://doi.org/10.1162/105474699566143

Sanz, I. D. (2014). Rock Art Recording Methods : From Traditional to Digital. In C. Smith (Éd.), Encyclopedia of Global Archaeology (p. 6351-6357). Springer New York. https://doi.org/10.1007/978-1-4419-0465-2_1277

Schmugge, T. J., Kustas, W. P., Ritchie, J. C., Jackson, T. J., & Rango, A. (2002). Remote sensing in hydrology. Advances in Water Resources, 25(8-12), 1367-1385. https://doi.org/10.1016/S0309-1708(02)00065-9

Sébastien, L. (2013). Les restes de chevaux issus des tertres des structures B10, PAC 38 et KTS 01 (Tsatsyn Ereg). Rapport d'étude.

Seong, H., Son, H., & Kim, C. (2018). A Comparative Study of Machine Learning Classification for Color-based Safety Vest Detection on Construction-Site Images. KSCE Journal of Civil Engineering, 22(11), 4254-4262. https://doi.org/10.1007/s12205-017-1730-3

Shorten, C., & Khoshgoftaar, T. M. (2019). A survey on Image Data Augmentation for Deep Learning. Journal of Big Data, 6(1), 60. https://doi.org/10.1186/s40537-019-0197-0

Simporé, L. (2011). The ruins of Loropeni, the first mankind worldwide patrimony Burkinabe site. J. Egyptol. Afr. Civiliz., 255-279.

Simpson, A., Clogg, P., Díaz-Andreu, M., & Larkman, B. (2004). Towards three-dimensional non-invasive recording of incised rock art. Antiquity, 78(301), 692-698. https://doi.org/10.1017/S0003598X00113328

Smith, M., Goodchild, M. F., & Longley, P. A. (2009). Geospatial analysis : A comprehensive guide to principles, techniques and software tools. Matador.

Smith, N. G., Passone, L., al-Said, S., al-Farhan, M., & Levy, T. E. (2014). Drones in Archaeology : Integrated Data Capture, Processing, and Dissemination in the al-Ula Valley, Saudi Arabia. Near Eastern Archaeology, 77(3), 176-181. https://doi.org/10.5615/neareastarch.77.3.0176

Soh, L.-K., & Tsatsoulis, C. (1999). Texture analysis of SAR sea ice imagery using gray level co-occurrence matrices. IEEE Transactions on Geoscience and Remote Sensing, 37(2), 780-795. https://doi.org/10.1109/36.752194

Solecki, R. S. (1957). Practical Aerial Photography for Archaeologists. American Antiquity, 22(4), 337-351. https://doi.org/10.2307/276132

Soroush, M., Mehrtash, A., Khazraee, E., & Ur, J. A. (2020). Deep Learning in Archaeological Remote Sensing : Automated Qanat Detection in the Kurdistan Region of Iraq. Remote Sensing, 12(3), 500. https://doi.org/10.3390/rs12030500

Sural, S., Gang Qian, & Pramanik, S. (2002). Segmentation and histogram generation using the HSV color space for image retrieval. Proceedings. International Conference on Image Processing, 2, II-589-II-592. https://doi.org/10.1109/ICIP.2002.1040019

Sutton, M. Q., & Reinhard, K. J. (1995). Cluster analysis of the coprolites from antelope house : Implications for anasazi diet and cuisine. Journal of Archaeological Science, 22(6), 741-750. https://doi.org/10.1016/0305-4403(95)90004-7

Szegedy, C., Liu, W., Jia, Y., Sermanet, P., Reed, S., Anguelov, D., Erhan, D., Vanhoucke, V., & Rabinovich, A. (2014). Going Deeper with Convolutions. https://doi.org/10.48550/ARXIV.1409.4842

Takahama, S., Hayashi, T., Kawamata, M., Matsubara, R., & Erdenebaatar, D. (2003). Preliminary Report on Archaeological Investigations in Mongolia 2003.

Takahama, S., Hayashi, T., Kawamata, M., Matsubara, R., & Erdenebaatar, D. (2006). Preliminary Report of the Archaeological Investigations in Ulaan Uushig I (Uushigiin Övör) in Mongolia.

Tishkin, A. A. (2013). Vyyavleniye, dokumentirovaniye i izucheniye "olennykh,'kamnei v doline Buyanta (Mongolskiy Altai) . Teoriya i praktika arkheologicheskikh issledovaniy, 1(7), 73-90.

Traviglia, A., & Torsello, A. (2017). Landscape Pattern Detection in Archaeological Remote Sensing. Geosciences, 7(4), 128. https://doi.org/10.3390/geosciences7040128

Tsybiktarov, A. D. (1998). Kul'tura plitochnykh mogil Mongolii i Zabaikal'ia [Culture of the slab burials of Mongolia and Zabaikal].

Turbat, T., Bayarsaikhan, J., Batsukh, D., & Bayarkhuu, N. (2011). DEER STONES of the JARGALANTYN AM (Mongolian Tangible Heritage Association NGO).

Turbat, T., Gantulga, J., Bayarkhuu, N., Batsukh, D., Turbayar, N., Erdene-Ochir, N., Batbold, N., & Tselkhagarav, T. (2021). Mongol ba bùs nutgiĭn bugan khòshòòniĭ soël : Ėrdėm shinzhilgėėniĭ katalog (Vol. 3). « Admon Print » KhKhK.

Van Berg, P.-L. (1994). Grammaire des styles céramiques du rubané d'Alsace. Association pour la promotion de la recherche archéologique en Alsace.

Vardis, K., Papaioannou, G., & Gaitatzes, A. (2013). Multi-view ambient occlusion with importance sampling. Proceedings of the ACM SIGGRAPH Symposium on Interactive 3D Graphics and Games - I3D '13, 111. https://doi.org/10.1145/2448196.2448214

Vavulin, M., Nevskaya, I., & Tybykova, L. (2019). DIGITAL MACRO-PHOTOGRAMMETRY IN DOCUMENTATION OF OLD TURKIC RUNIFORM INSCRIPTIONS IN THE ALTAI MOUNTAINS. https://doi.org/10.5281/ZENODO.3239053

Veeranampalayam Sivakumar, A. N., Li, J., Scott, S., Psota, E., J. Jhala, A., Luck, J. D., & Shi, Y. (2020). Comparison of Object Detection and Patch-Based Classification Deep Learning Models on Mid- to Late-Season Weed Detection in UAV Imagery. Remote Sensing, 12(13), 2136. https://doi.org/10.3390/rs12132136

Velios, A., & John P, H. (2001). Laser Scanning and Digital Close Range Photogrammetry for Capturing 3-d Archaeological Objects : A Comparison of Quality and Practicality. In Archaeological Informatics : Pushing the Envelope CAA2001. Computer Applications and Quantitative Methods in Archaeology Proceedings ofthe 29th Conference, Gotland, April 2001 (Vol. 1016, p. 567-574).

Verhoeven, G. (2011). Taking computer vision aloft—Archaeological three-dimensional reconstructions from aerial photographs with photoscan. Archaeological Prospection, 18(1), 67-73. https://doi.org/10.1002/arp.399

Volkov, V. V. (1981). Olennye Kamni Mongolii (Pierres à cerfs de Mongolie).

Volkov, V. V., & Novgorodova, E. A. (1975). Olennye kamni Ushkiin Uvera (Mongoliya). Pervobytnaya arkheologiya Sibiri, 78-84.

Vrbik, I., Van Nest, S. J., Meksiarun, P., Loeppky, J., Brolo, A., Lum, J. J., & Jirasek, A. (2019). Haralick texture feature analysis for quantifying radiation response heterogeneity in murine models observed using Raman spectroscopic mapping. PLOS ONE, 14(2), e0212225. https://doi.org/10.1371/journal.pone.0212225

Wang, N., Zhao, X., Zhao, P., Zhang, Y., Zou, Z., & Ou, J. (2019). Automatic damage detection of historic masonry buildings based on mobile deep learning. Automation in Construction, 103, 53-66. https://doi.org/10.1016/j.autcon.2019.03.003

Wehrens, R., & Kruisselbrink, J. (2022). Package 'kohonen'. https://CRAN.R-project.org/package=kohonen

Weiss, A. D. (2001). Topographic Position and Landforms Analysis [Poster]. ESRI user conference, San Diego, California.

Weiss, K., Khoshgoftaar, T. M., & Wang, D. (2016). A survey of transfer learning. Journal of Big Data, 3(1), 9. https://doi.org/10.1186/s40537-016-0043-6

Wickham, H., Chang, W., Henry, L., Takahashi, K., Wilke, C., Woo, K., Yutani, H., & Dunnington, D. (2022). Create Elegant Data Visualisations Using the Grammar of Graphics. https://ggplot2.tidyverse.org

Wilczek, J., Monna, F., Gabillot, M., Navarro, N., Rusch, L., & Chateau, C. (2015). Unsupervised model-based clustering for typological classification of Middle Bronze Age flanged axes. Journal of Archaeological Science: Reports, 3, 381-391. https://doi.org/10.1016/j.jasrep.2015.06.030

Wilson, J. P., & Gallant, J. C. (Éds.). (2000). Terrain analysis : Principles and applications. Wiley.

Wood, J. (1996). The Geomorphological Characterisation of Digital Elevation Models. University of Leicester.

Wright, J. (2007). Organizational principles of Khirigsuur monuments in the lower Egiin Gol valley, Mongolia. Journal of Anthropological Archaeology, 26(3), 350-365. https://doi.org/10.1016/j.jaa.2007.04.001

Wright, J. (2014). Grammars of design : Tools for reading khirigsuurs. 34(12), 142-163.

Wright, J. (2017). The honest labour of stone mounds : Monuments of Bronze and Iron Age Mongolia as costly signals. World Archaeology, 49(4), 547-567. https://doi.org/10.1080/00438243.2017.1360791

Xiao, Y., Tian, Z., Yu, J., Zhang, Y., Liu, S., Du, S., & Lan, X. (2020). A review of object detection based on deep learning. Multimedia Tools and Applications, 79(33-34), 23729-23791. https://doi.org/10.1007/s11042-020-08976-6

Yan, J., Wang, H., Yan, M., Diao, W., Sun, X., & Li, H. (2019). IoU-Adaptive Deformable R-CNN : Make Full Use of IoU for Multi-Class Object Detection in Remote Sensing Imagery. Remote Sensing, 11(3), 286. https://doi.org/10.3390/rs11030286

Yastikli, N. (2007). Documentation of cultural heritage using digital photogrammetry and laser scanning. Journal of Cultural Heritage, 8(4), 423-427. https://doi.org/10.1016/j.culher.2007.06.003

Yokoyama, R., Shirasawa, M., & Pike, R. J. (2002). Visualizing Topography by Openness : A New Application of Image Processing to Digital Elevation Models. Photogrammetric Engineering & Remote Sensing, 68(3), 257-265.

Zakariya Jasim, O. (2019). Using of machines learning in extraction of urban roads from DEM of LIDAR data : Case study at Baghdad expressways, Iraq. Periodicals of Engineering and Natural Sciences (PEN), 7(4), 1710. https://doi.org/10.21533/pen.v7i4.914

Zakšek, K., Oštir, K., & Kokalj, Ž. (2011a). Sky-View Factor as a Relief Visualization Technique. Remote Sensing, 3(2), 398-415. https://doi.org/10.3390/rs3020398

Zakšek, K., Oštir, K., & Kokalj, Ž. (2011b). Sky-View Factor as a Relief Visualization Technique. Remote Sensing, 3(2), 398-415. https://doi.org/10.3390/rs3020398

Zarit, B. D., Super, B. J., & Quek, F. K. H. (1999). Comparison of five color models in skin pixel classification. Proceedings International Workshop on Recognition, Analysis, and Tracking of Faces and Gestures in Real-Time Systems. In Conjunction with ICCV'99 (Cat. No.PR00378), 58-63. https://doi.org/10.1109/RATFG.1999.799224

Zazzo, A., Lepetz, S., Magail, J., & Gantulga, J.-O. (2019). High-precision dating of ceremonial activity around a large ritual complex in Late Bronze Age Mongolia. Antiquity, 93(367), 80-98. https://doi.org/10.15184/aqy.2018.175

Zelditch, M. (Éd.). (2004). Geometric morphometrics for biologists : A primer. Elsevier Academic Press.

Zhang, X., Cui, J., Wang, W., & Lin, C. (2017). A Study for Texture Feature Extraction of High-Resolution Satellite Images Based on a Direction Measure and Gray Level Co-Occurrence Matrix Fusion Algorithm. Sensors, 17(7), 1474. https://doi.org/10.3390/s17071474

Zhao, Z.-Q., Zheng, P., Xu, S., & Wu, X. (2019). Object Detection with Deep Learning : A Review. arXiv:1807.05511 [cs]. http://arxiv.org/abs/1807.05511

Zotkina, L. V. (2019). On the Methodology of Studying Palimpsests in Rock Art : The Case of the Shalabolino Rock Art Site, Krasnoyarsk Territory. Archaeology, Ethnology & Anthropology of Eurasia, 47(2), 93-102. https://doi.org/10.17746/1563-0110.2019.47.2.093-102

Zotkina, L. V., & Kovalev, V. S. (2019). Lithic or metal tools : Techno-traceological and 3D analysis of rock art. Digital Applications in Archaeology and Cultural Heritage, 13, e00099. https://doi.org/10.1016/j.daach.2019.e00099

Zou, Z., Zhao, X., Zhao, P., Qi, F., & Wang, N. (2019). CNN-based statistics and location estimation of missing components in routine inspection of historic buildings. Journal of Cultural Heritage, 38, 221-230. https://doi.org/10.1016/j.culher.2019.02.002

Annexes

Annexe 1.

Magail, Jérôme & Esin, Yury & Jamiyan-Ombo, Gantulga & Monna, Fabrice & Rolland, Tanguy & Allard, Anne-Caroline. (2022). Bronze Age and Iron Age decorated megaliths and funerary complexes in Mongolia and Southern Siberia Megaliths from Central and East Asia.

35

Jérôme MAGAIL, Yuri ESIN,
Jamiyan-Ombo GANTULGA, Fabrice MONNA,
Tanguy ROLLAND, Anne-Caroline ALLARD

Bronze Age and Iron Age decorated megaliths and funerary complexes in Mongolia and Southern Siberia

Abstract: Mongolia and southern Siberia are rich in funerary, ceremonial and iconographic remains of Bronze Age and Iron Age nomadic civilizations. Part of this archaeological heritage, in a cultural and funerary context, could be classified as megaliths. Among the oldest menhirs (2500-1800 BC), the stelae of the Okuniev culture are found across most of the territory of the Republic of Khakassia. Russian archaeologists have catalogued nearly 600 monuments, the largest of which was reused in the Iron Age in the large Tagar tomb at the site of Salbik. Other more recent megaliths appear in the Bronze Age, mainly in Mongolian territory, where about 1240 decorated stelae have been recorded by the Archaeological Institute of Ulaanbaatar. One of the stelae from the Ulan Tolgoi site is almost 5 m high. During the Final Bronze Age, High Asian populations erected granite menhirs, called 'deer stones' on account of their deer carvings. This megalithism is associated with highly codified funerary complexes, consisting of individual aristocratic tombs in the form of large tumuli surrounded by hundreds of mounds, each of which contains the deposit of a horse's head. The joint Monaco-Mongolian archaeological mission is carrying out research in the Upper Tamir Valley, where abundant remains of this culture are found. This valley lies in the centre of the country and has more than 800 tombs, 115 deer stone stelae and a rock art site with more than a thousand petroglyphs. At the beginning of the Iron Age, a new type of megalithic structure emerged in Southern Siberia: aristocratic burial mounds delimited by large standing stones and enormous retaining slabs. Tomb no. 1 of the Royal Necropolis of Salbik contains a 50-ton retaining slab.

Keywords: *adorned stelae, petroglyphs, menhir, Bronze Age, Iron Age, deer stone, Tagar, Okuniev, Mongolia, Siberia*

Fig. 1 – Distribution map of the Okuniev stelae and the deer stones (J. Magail).

1. Introduction

Since 2006, the Museum of Prehistoric Anthropology of Monaco has conducted archaeological missions to investigate the Bronze Age and Early Iron Age nomadic populations of High Asia. Agreements have been signed with the Mongolian Academy of Sciences, Research Institute for Language, Literature, and History of the Republic of Khakassia, the Institute of Social Sciences of the Republic of Tuva and the Museum of Minusinsk. Some of the studied remains can be classified as megaliths and menhir statues. These are essentially stelae which are either constituent elements of tombs or elements implanted in sacred and/or funerary sites. Thanks to a partnership with the ARTEHIS laboratory of the University of Burgundy, a corpus of about 100 3D models of menhirs and a substantial number of digital terrain models and orthophotographs have been produced (Magail *et al.* 2017; Monna *et al.* 2018, 2020; Rolland *et al.* 2019). This article, which does not claim to be exhaustive, deals with objects from a period that begins with the Okuniev culture in the 3rd millennium BC, continues into the Bronze Age with the deer stone' stelae culture and ends in the 5th century BC with the Tagar culture. The majority of these menhirs bear engraved or even sculpted – sometimes painted – iconography (**Fig. 1**).

2. The Okuniev stelae

Between 2500 and 1800 BC, a society of sheep, cattle and horse breeders erected the oldest menhirs in High Asia. The Okuniev archaeological sites are mainly funerary and religious places, so the documentation of daily life is still very partial. Copper and bronze objects, ceramics and representations of chariots attest to the inclusion of these items in the cultural assemblage following the earlier Afanasyev culture. The singularity of the Okuniev stelae is to be found in the carved and engraved art on surfaces that were often pre-prepared (Leontiev 1976; Leontiev *et al.* 2006). These monoliths are mainly located in the Khakassia Republic; very few

are found in a primary context (Kyzlasov 1986; Esin 2010). They were often reused and eventually moved during the development of agricultural land during the 20th century. During the long Okuniev period, communities sometimes reused their own stelae and subsequent cultures continued this practice (Lazaretov & Poliakov 2018). The Tagar culture took Okuniev menhirs from sites of worship to integrate them into the construction of their princely tombs in the 5th century BC. One monolith, for example, was embedded in the passageway of aristocratic Tomb no. 1 at Salbik. The most exceptional of the 600 listed Okuniev stelae, in terms of size and iconography, are displayed in museums in the towns of the region, in Abakan, Minusinsk and Poltakov. Some are also curated at the State Historical Museum in Moscow and the Hermitage Museum in St. Petersburg. The iconographies observed on the menhirs are also recorded on more than 40 engraved and painted rocks. Not only is there an 'Okuniev style', but a codification of the figures and their combinations is also found on each monument. The aim here is to present an overview of the different types of Okuniev monoliths through a very succinct selection.

Some monoliths, such as that from the commune of Shira village, display rich iconographic groups of sculptures and engravings. On the narrowest side, the Shira menhir bears a representation of a chimeric half-animal, half-human creature with an anthropomorphic face (**Fig. 2a, b**). The engraved head of the animal at the base of the wider sides illustrates the chimeric composition of the represented being. Its eyes and muzzle correspond to the chest and belly of the anthropomorph. The legs of the beast are also

Fig. 2 – Stele of Shira: a. Photo Y. Esin; b-c. Survey of the stele with details of the iconography of the upper section, drawing by N. Leontiev and Y. Esin. Preserved in the Khakassia National Museum of Regional Research (Abakan). Reddish-brown sandstone, size: 290 x 80 x 25 cm.

the arms of the anthropomorph. Its open mouth, with sharp teeth and a pointed tongue, reinforces the mythological character of this wild beast, overhanging a circular Okuniev symbol with four triangular rays. The iconographic themes of the main side unfold in three parts, one above the other. In the central section, the large, ovoid, sculpted anthropomorphic face is divided into three parts by horizontal lines. Above this, in the top part of the stele, the vertical headdress of the creature is engraved, enhanced by the sculpture of a small, very realistic human face. All the images of this monument can be interpreted as the body and clothing of a single deity whose face is located in the centre of the stele. The vertical headdress schematically repeats the tripartite iconographic structure of the stele (**Fig. 2c**).

Another type of stele, often a thin slab, depicts an anthropomorphic figure evoking a solar deity together with animals. One of the broad sides of the stele in the village of Ankhakov (2.5 m high) depicts a being whose head is encircled by a halo of rays and whose body is surrounded by snakes (**Fig. 3a, b**). It was found in two pieces, reused in the structure of a Tagar culture tomb. The pieces were subsequently reassembled and the stele is currently displayed in the Abakan Museum. Traces of red paint are preserved on the engraved side. The entire surface of the stele seems to have been painted with ochre in the Okuniev period. A reconstruction of the monument in its context has been proposed (**Fig. 3a**) (Esin *et al.* 2014). A radiant face associated with snakes, but also with the head of a wild animal, is a theme also developed on a stele fragment discovered near the Tibik River (**Fig. 3c**). The open mouth with sharp teeth of the Okuniev mythological beast is placed under the anthropomorph's rounded head, echoing the themes engraved on the Shira menhir described above (**Fig. 2a, b**). Note that its bestial tongue touches the chin of the solar being, either to suggest its engulfment or regurgitation. On this stele, schematic representations of snakes contribute to forming the mouth of the beast. The reptiles seem to transmit their strength to the animal by suggesting a fatal bite. The number of five snakes appears

Fig. 3 – Stele from the village of Ankhakov: a. Reconstruction in its context; b. Drawing of the stele by Y. Esin. Preserved in the National Museum of Regional Research in Khakassia (Abakan). Reddish-brown sandstone size: 250 x 130 x 25 cm; c. Drawing of the Tibik stele by Y. Esin. Grey-green aleurolite, size: 55 x 38 x 12 cm.

to be significant as the same number of snakes are observed on the Ankhakov stele.

The record of representations of chimeric creatures is considerably enriched by a stele from the Askiz River, on which two animal figures are endowed with a bear's head, a snake's tongue, an ox's torso and horns, and finally with hawk's talons (**Fig. 4**). Is this the same Okuniev beast observed on the monuments of Shira and Tilbik? In **Fig. 4b** the chimeras are shown in black and overlie a representation of a typical Okuniev three-eyed anthropomorphic face (in blue), also with a large mouth and nostrils. A similar superimposition is found on the Kurgan stele of Chernovaya VIII, where the chimera has an elk torso and legs associated with a long feline tail, different from that of the stele of Askiz. The overlapping of iconographies from the same culture seems to be part of the syntactic code.

The iconographies of mythological predators in Okuniev art are distinguished from other themes by their wide variety of representations (Lazaretov 1997). In one category, the animal has the silhouette of an elk, bull, bear, wolf or dog. In another category, the beings are standing on their hind limbs and have a human figure. Despite the large number of variations, the images retain a coherence around a set of symbols. The oral tradition that transmits mythological stories from generation to generation

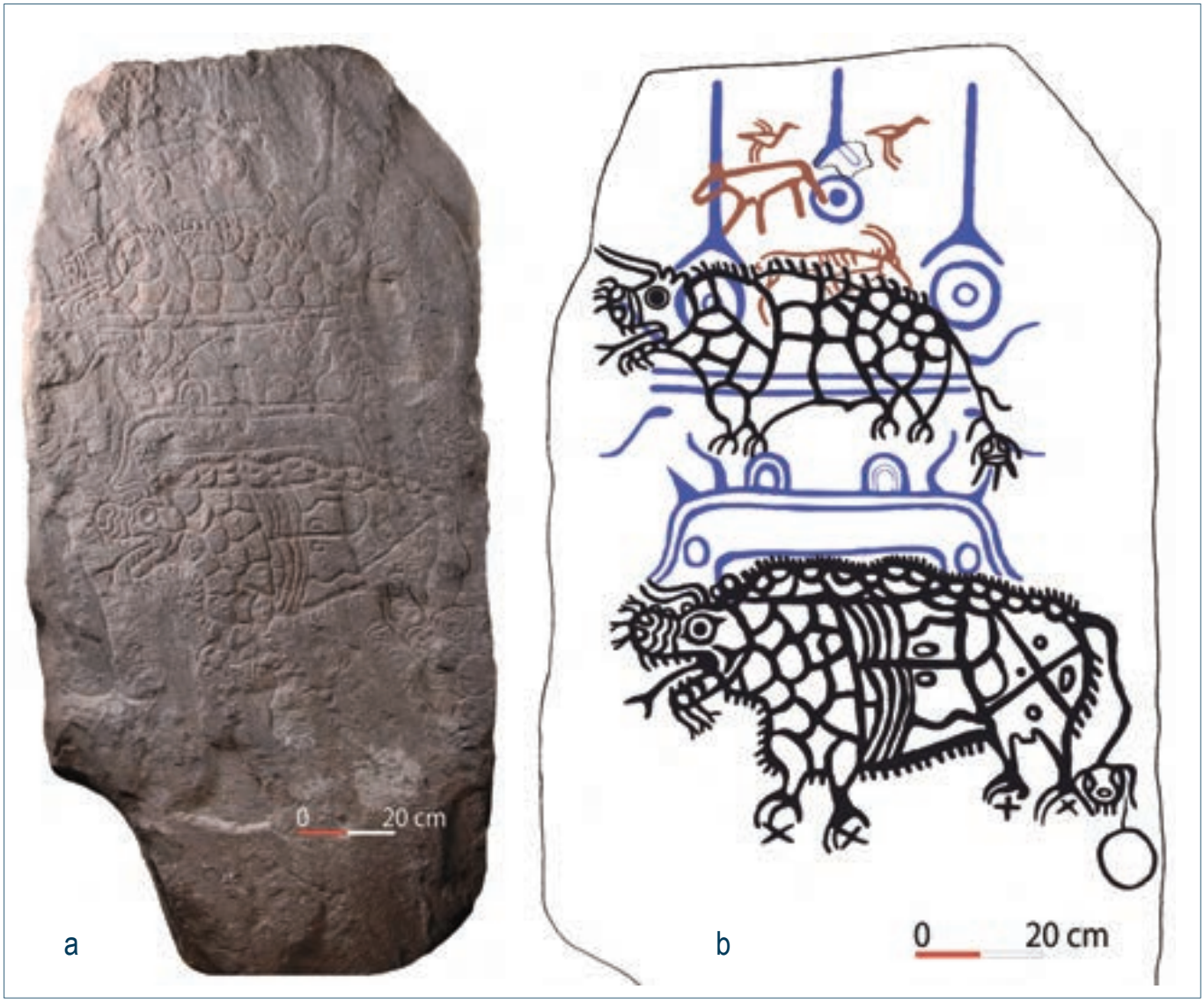

Fig. 4 – Askiz stele: a. Photo by B. Dolinin; b. Drawing by Y. Esin. Preserved in the National Museum of Regional Research in Khakassia (Abakan). Reddish brown sandstone, Size: 210 x 105 cm.

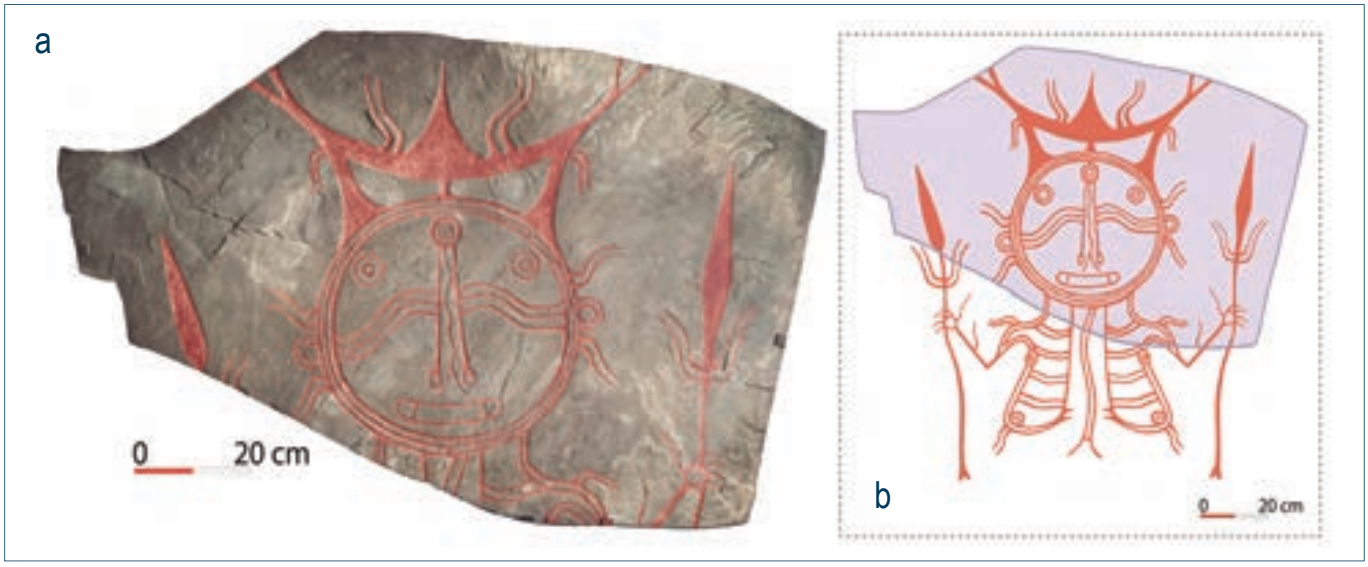

Fig. 5 – Stele from Chernovaya VIII (fragment) preserved in the Hermitage Museum in St. Petersburg: a. Photo with reconstruction of the pigments by Y. Esin; b. Drawing and proposed reconstruction by Y. Esin. Reddish brown sandstone, size: 130 x 85 cm.

could explain all these nuances around the same theme.

A whole image has been reconstructed from a fragment of stele found in the tomb of Chernovaya VIII (**Fig. 5**). On the preserved upper part, the representation of a deity holds, in each hand, an unknown type of weapon consisting of a spear point, curved bull horns and a serpentine handle. The details of the deity's face correspond to symbols that represent the different domains of the universe (Esin 2010). The three eyes could, for example, correspond to the positions of the sun during the day. Red ochre was found inside the hollowed and polished parts (Esin *et al.* 2014). The deity was therefore painted after being engraved onto the block of sandstone.

In the commune of Erbinskiy village, an archaeological excavation of an Okuniev sanctuary carried out in 1971 by L.R. Kyzlasov provided a better understanding of the religious context of the stelae (Kyzlasov 1986). Two stelae and two pits, intended to hold the blood of sacrificed animals, were discovered on the site, which extends along a north-south axis (**Fig. 6a, b**). Stele no. 1, of grey granite and 1.30 m high, was unearthed with its front side facing the rising sun. Stele no. 2, of pink granite, was found broken into two pieces, one overturned to the north of the site, the other covering the sacrificial pit to the south. The lower part of this stele has an ovoid carved shape without facial details (i.e., eyes and mouth), and relief evoking the shape of breasts. The two pieces together show that its original height was 3.16 m. The two sacrificial pits, elliptical in shape and 1.20 m and 1.48 m deep respectively, were filled with white limestone stones. Animal bones were found in the upper part of these pits and in the vicinity of the stele. These consisted mainly of horse bones, but also the remains of horned cattle and birds. This sanctuary was completely excavated; the stelae are kept in the Museum of History and Cultures of Siberian and Far Eastern Peoples in Novosibirsk.

A stele curated in the Poltakov open-air Museum is a sandstone slab 2.5 m high and 1.2 m wide, decorated with the largest known radiating Okuniev face (**Fig. 7**). In the middle of this face, a large triangle corresponds to the nose of the deity. The eyes and mouth are deeply carved into the rock. Different types of small faces and cup marks are engraved behind the large face. This monument was found in a Tagar culture tomb in a context of reuse. Traces of ochre were found on its surface, as on the Ankhakov stele. Archaeologists took a moulding of the entire surface of the stele and made two resin casts to show the public its present appearance and how it looked 4500 years ago when it was painted with red ochre (**Fig. 7a**) (Esin *et al.* 2014).

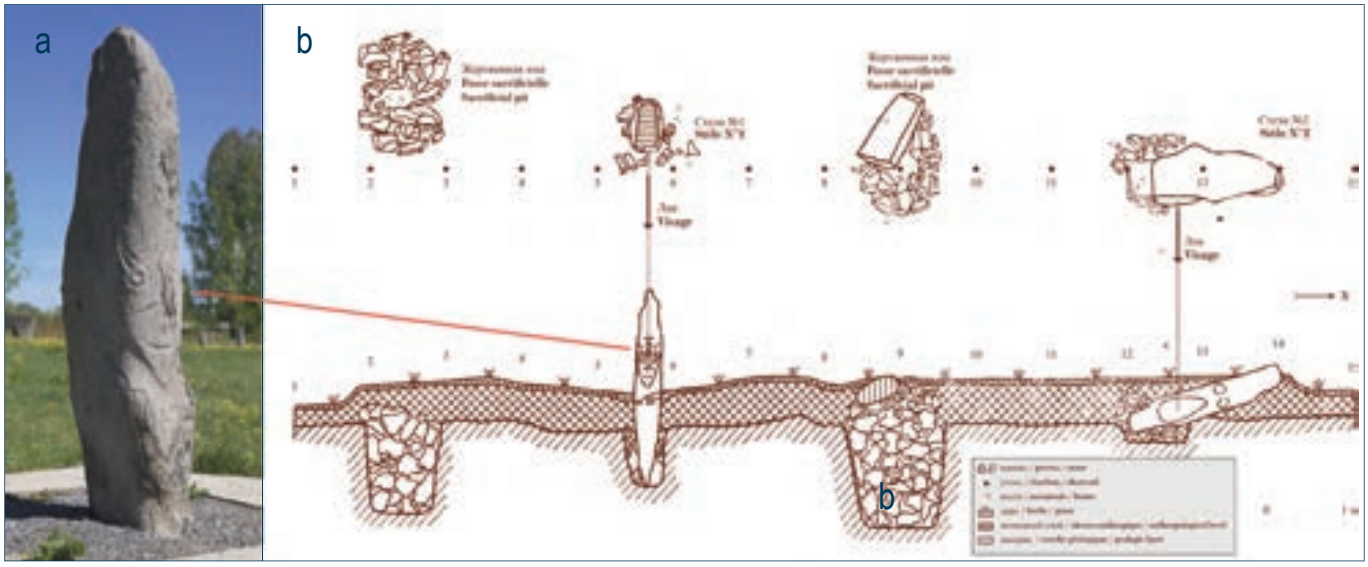

Fig. 6 – a. Stele no. 1 from the Erbinskiy sanctuary preserved in the Museum of History and Cultures of the Peoples of Siberia and the Far East in Novosibirsk. Grey granite, size: 130 x 55 x 27 cm (Photo: Y. Esin); b. Plan and cross-section of the Erbinskiy sanctuary (From the drawing by L.R. Kyzlasov).

Fig. 7 – Stele from the Poltakov Museum. Reddish brown sandstone, size: 250 x 120 cm: a. Photo of the cast of the stele, painted with the original colours; b. Photograph of the painted stele by J. Magail; c. Drawing by Y. Esin.

The surfaces of the most sophisticated Okuniev stelae were generally worked before the sculpture and engraving of the iconography. The 'sabre-shaped' stele in the village of Tazmin shows evidence of such surfaceworking (**Fig. 8**). The sculpted face at the base of the monument is fine and elongated and is of exceptional finesse. The Khakas called it *Apsakh oba*, 'the Old Stone Man'.

Fig. 8 – Anisim Kyrzanovich Tazmin, a villager, is standing next to the stele now kept in the Ethnographic Museum in St. Petersburg. The photograph, kept in the archives of the Minusinsk Regional History Museum, was taken in 1910 by N. Fyodorov. Reddish brown sandstone, size: 360 x 70 x 15 cm.

Sculpted faces are a recurring theme on Okuniev menhirs. In the region of the village of Beltyry, a menhir reused in the construction of the enclosure of a kurgan (tomb) of the Tagar culture bears three realistic faces carved one above the other on an angle of the stele. On the widest side of the monument, schematic human figures were added by Tagar artists.

3. Deer stone stelae

The decorated stelae known as deer stones have a distribution centred on Mongolia and extending over China, Kazakhstan and Russia (**Fig. 1**). The earliest studies of their engravings of leaping deer and weapons compared them to images from the Karasuk culture of the South Siberian Bronze Age (Okladnikov 1954; Novgorodova 1989). Numerous ^{14}C datings of animal deposits directly related to the erection of these menhirs confirm that they were made by a pre-Scythian culture existing between the 2nd and 1st millennia BC (Fitzhugh 2009). Indeed, the Saka, the Eastern Scythians of Siberia and Altai, inherited some of the weapons and art of these populations. The typology of the leaping deer, engraved in around 1200 BC on the Mongolian stelae, is known in the form of gold appliques among the West Scythians in the 4th century BC in Ukraine and Hungary. Approximately 85% of the 1500 deer stone monuments are in Mongolia. The Institute of Archaeology of the Mongolian Academy of Sciences lists 1240 examples (Turbat 2018), about 100 in southern Siberia in the republics of Altai, Tuva and Buryatia, and a few dozen in the north of the Chinese province of Xinjiang and in eastern Kazakhstan. The stones have been known since the end of the 19th century thanks to Grigory and Alexandra Potanin who took part in the expeditions of the Russian Geographical Society to Siberia, Mongolia, China and Tibet. During their visits to Mongolia in 1876 and 1877, they surveyed stelae and structures from the Bronze Age (Potanin 1881, vol. 2). Ten years later, Vassily Radlov, a famous Turkologist, included deer stones in his *Atlas of Mongolian Antiquities* (Radlov 1892). It should be noted that Bronze Age stelae were sometimes used as a support for Turkish runic writings in the 7th and 8th centuries of our era. The same phenomenon occurred with the Okuniev stelae discussed in the previous section. By documenting the runes inscribed

on the menhirs, Turkish scholars made the first surveys of the decorated stelae. After the Second World War, authors such as Alexei Okladnikov and Natalia Chlenova drew attention to deer stones by analysing the typology of their iconography as objects of Scythian culture (Okladnikov 1954; Chlenova 1962, 1984). Over the last 40 years, study of the stones has developed thanks to increasingly easy access to archaeological sites. Due to the vast steppe areas to be prospected, with no roads, and accessible only during the summer season, isolated sites remained hidden for a long time. The fall of the Soviet Union then contributed to the arrival of foreign archaeological missions which enriched discoveries, including the corpus of deer stones. In 1994, the number of stones was estimated at 700 (Savinov 1994). When a joint Monaco-Mongolian mission arrived in 2006 in the sector of the Upper Tamir Valley (province of Arkhangai), only about 40 stelae were listed. Today, 115 deer stones have been found and almost every survey leads to the discovery of new examples. In 2019, for example, the team uncovered three new menhirs. Some sites are particularly spectacular due to their concentrations of standing (and often aligned) monoliths. In Mongolia, the best-known sites are Ulaan Uushig (Takahama *et al.* 2003, 2006; Kovalev *et al.* 2016), Jargalant (**Fig. 9**) (Turbat *et al.* 2011) and Ulan Tolgoi (Fitzhugh 2003, 2004), which had already attracted the attention of the pioneers of steppe archaeology and led to the first scientific publications (Volkov & Novgorodova 1975; Volkov 1981; Novgorodova 1989; Savinov 1994). The site of Ulaan Uushig is also known for its deer stone with a carved face at the top, a feature of only about ten stelae out of 1500. In the heart of the immense steppe expanses, remote valleys still contain funerary complexes where engraved stelae remain buried in the sand. In 2019, at the source of the Khunnuin Gol valley, the joint Monaco-Mongolia mission used a drone to document a previously unknown necropolis containing more than 30 funerary complexes. On the western confines of the Mongolian plateau, the Altai is also a cross-border region very rich in archaeological remains, and is still being surveyed (Bayarsaikhan 2015; Tishkin 2020).

Fig. 9 – Deer stone stele from the Jargalant site, Arkhangai province, Mongolia. Quartzite, size: 386 x 56 x 35 cm (Photo: J. Magail).

Deer stones are part of a vast group of menhirs left by a mosaic of nomadic tribes from Mongolia to the Ukraine from the 2nd to the 1st millennia BC (Olkhovsky 2005; Tishkin 2013). The stelae in the eastern steppe have been classified into three categories based on the style of their iconography and their geographical distribution (east-west): Mongolian-Transbaikal, Sayan-Altai and Eurasian (**Fig. 10**). The Mongol-Transbaikal type is the most common and warrants the term 'deer stone', as it is distinguished by engravings of hordes of leaping deer (*Cervus elaphus*) (**Figs. 9**, **10a** and **11**). The legs of the deer are folded under their bellies, and their bodies and muzzles are outstretched like a bird in flight. The large antlers of the animals extend along their backs to convey additional movement. The fact that all the deer bear large antlers suggests that they are fully mature males depicted as they appear during the rutting season in early autumn.

When in primary contexts, the Mongolian-Transbaikal type stelae are always embedded in mounds of earth, a few dozen centimetres high, and associated with sites comprising dry-stone structures, with ritual deposits (Magail 2015). The height of these menhirs varies from 1 m to more than 5 m (Ulan Tolgoi site). They stand in the middle of mounds and stone circles that contain, respectively, deposits of horse heads and burnt bone splinters, and they

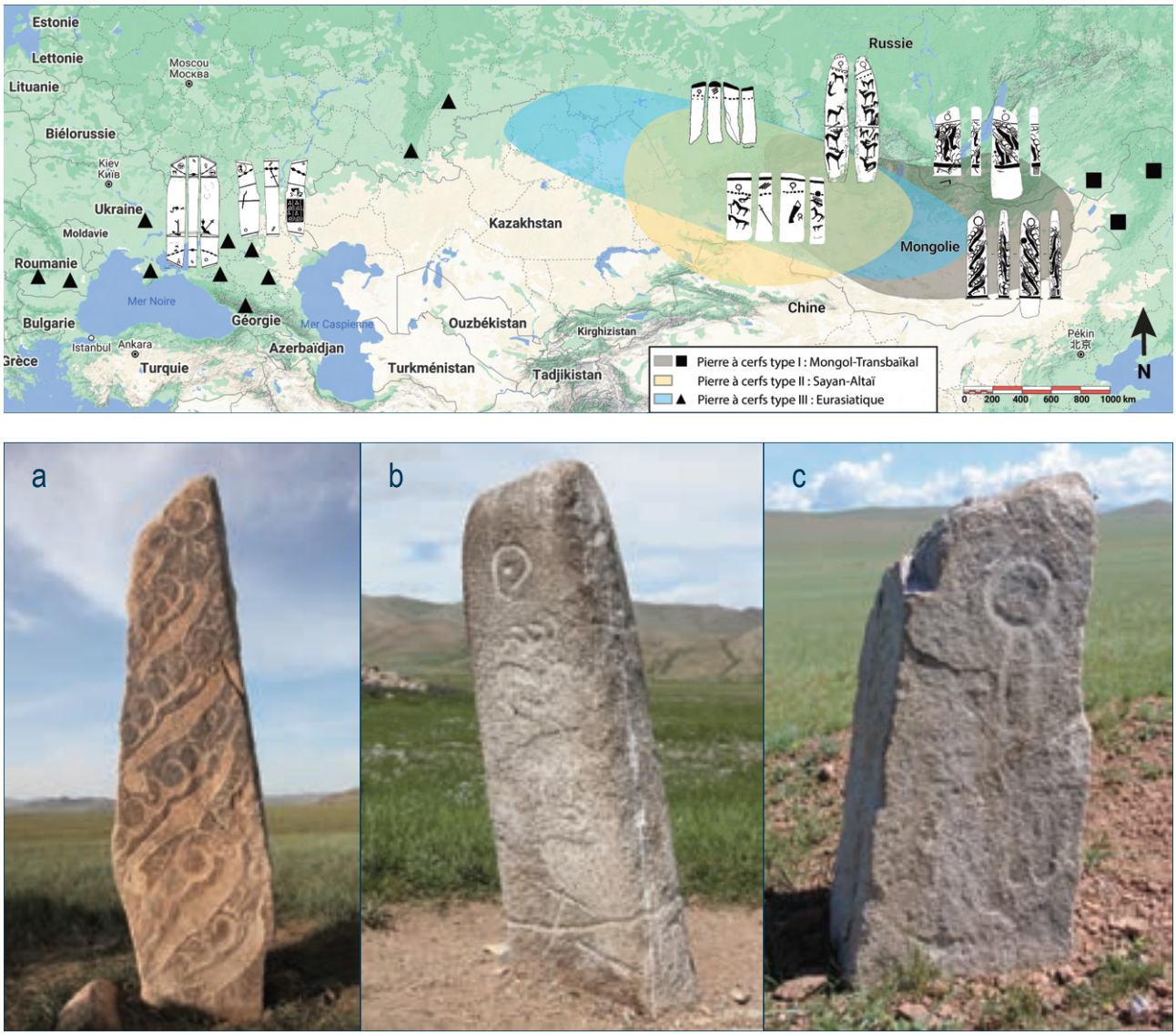

Fig. 10 – Map of distribution types of stelae (After Novgorodova 1989). Examples of the three types of stelae known as 'deer stone': a. Mongolian-Transbaikal type Shivertiin am stele, size: 252 x 28 x 50 cm; b. Sayan-Altai type Doroljiin am stele, size: 121 x 30 x 31 cm; c. Eurasian-type Khavtsalyn am stele, size: 86 x 34 x 35 cm (CAD & photos: J. Magail).

Fig. 11 – Stele from the Khunnu Gol valley: a. Survey of the four faces; b. Reconstruction (Survey and reconstruction by Y. Esin).

often belong to larger funerary complexes called *khirigsuur* (*хиригсуур*) in the Mongolian language (Allard & Erdenebaatar 2005; Broderick *et al.* 2014; Monna *et al.* 2020). The artificial mound, which may cover an area of a few dozen square metres, may be located on the periphery of an individual grave placed under a stone mound, itself surrounded by hundreds of small mounds. The size of the *khirigsuur* vary greatly, from 100 m^2 to several hectares. The two largest examples in Mongolia, measuring 12 and 14 ha respectively, are located in Urt Bulag in the province of Arkhangai (Houle 2010). By identifying the types of structures associated with the stelae, members of the joint Monaco-Mongolia mission uncovered many of the hundred or so stelae in the Upper Tamir Valley (Magail *et al.* 2010; Gantulga *et al.* 2013). Over time, some of the stones have fallen and have been covered by granitic sands.

The Sayan-Altai type stelae in primary context are also found in funerary complexes, but closer to the central burial mound than the Mongol-Transbaikal type stelae installed on their artificial mounds (Tishkin 2020).

About 90% of reused deer stones are found in Early Iron Age (700 BC) slab tombs. They were erected at the four corners of these structures or used in the construction of the sides of the grave along with other slabs set on their sides. Six deer stones were discovered during the excavation of the Tsatsyn Ereg A92 slab tomb (Gantulga *et al.* 2009). Four of these were erected in corners, one had been buried flat above the deceased, and the sixth formed part of the side wall. In 2014, in the same area, the team discovered a further six decorated stelae that had been moved several dozen metres from their primary location in a funerary complex to a set of four slab tombs (Magail 2015). Eight of the 115 menhirs found in Upper Tamir were reused in places of worship built by Turkish populations in the 7th century AD (Magail *et al.* 2010). This reuse has continued until the present day with some 20th century tombstones created from fragments of deer stones. Five such examples have been identified by the joint Monaco-Mongolia mission in modern Upper Tamir cemeteries (Gantulga *et al.* 2015).

In the Republic of Tuva (Russia), the archaeological excavation of the Arjan 2 tumulus uncovered deer stones of the Mongolian-Transbaikal type in Early Iron Age tomb architecture (650 BC) (Chugunov *et al.* 2010). Sayan-Altai type stelae were also sometimes reused; several were found in a Turkish Altai religious enclosure (Tishkin & Shelepova 2014). Engravings of leaping deer are also found on hillside rocks in the same geographical area as stelae and khirigsuur (Novgorodova 1984; Jacobson-Tepfer 2001; Jacobson *et al.* 2001). For example, a rock art site 5 km from Tsatsyn Ereg includes engravings of leaping deer associated with other animal themes, including the ibex (Gantulga *et al.* 2018). Interpretations of the significance of the decorated stelae must take into consideration the use of the image of the deer in all the iconographies of the steppe civilizations. Is this wild animal, which seasonally loses its antlers, a ferryman of souls to the beyond (Magail 2005, 2015)? Understanding the place of the stag in the bestiary and in the founding myths of nomads, hunters, shepherds and warriors will undoubtedly shed light on its megalithic context (Jacobson-Tepfer 2015).

The only anthropological certainty is the strong social coherence that gave rise to the constuction of hundreds of funerary complexes and deer stones using the same technical and religious protocols. Their standardized typology attests to the observance of rigorous rules reproduced over an area of more than a million km^2. The quality of the motifs engraved on materials as hard as granite and quartzite (**Fig. 9**) suggests that engraving techniques were transmitted from one generation to the next, perhaps even taught in workshops. While the decoration and layout of menhirs follow rules, the dry-stone *khirigsuur* structures, some of which extend over several hectares, also exhibit identical layouts despite being hundreds of kilometres apart (Wright 2007, 2014). The distribution of mounds and stone circles around a tumulus suggests a strict ritual, codified by oral tradition, perhaps dedicated to the deceased buried in the centre, who became a supporting spirit of the tribe. Analysis of the archaeological traces of the repetition of rites allows new hypotheses to be formulated regarding the chronology of various cults (Lepetz *et al.* 2019). The systematic deposition of a horse's head under each mound, from Khenti province to 1000 km further west in the Altai, evokes the same sacred gesture (Fitzhugh & Bayarsaikhan 2008, 2009; Makarewicz *et al.* 2018). The practice of uninterrupted nomadism for more than 3000 years explains the astonishing preservation of the remains. This greatly facilitates research on structures and monoliths using the latest methods. A programme of dating the many elements within the Tsatsyn Ereg burial complex, comprising 1023 mounds around the central burial mound, has been started to establish the construction period of the complex (Zazzo *et al.* 2019). Major photo-grammetry campaigns have also been carried out to record the complexes, stelae and iconography (Magail *et al.* 2017; Monna *et al.* 2018, 2020; Rolland *et al.* 2019). Observation of the stele surfaces revealed traces of ochre on deer stones from Arkhangai province (**Fig. 11**) (Esin *et al.* 2018). Research is also in progress to establish chronological relationships between all the successive cultures in the geographical area of deer stones and *khirigsuur* (Taylor *et al.* 2019).

4. The megalithic structures of Tagar aristocratic tombs

During the Iron Age, an aristocracy emerged in southern Siberia (Russia), with some tombs that can be described as megalithic. The valleys of the kings of Arjan and Salbik, located in the republic of Tuva and the republic of Khakassia respectively, are the necropolises with the most impressive kurgans in terms of size. Deer stones were discovered in the Arjan 2 burial mound (Chugunov 2010), but the most gigantic elements can be found in the funerary architecture of the Salbik necropolis. Tomb no. 1, excavated entirely between 1954 and 1956 by a team led by Sergei Kiselev, is one of the largest tombs of the Tagar culture (Marsadolov 2010, 2015). Its megalithic construction is still perfectly visible today thanks to the excavation that removed the whole mound of earth. The peculiarity of the Tagar tombs is their pyramidal shape, originally more than 12 m high, which gradually subsided over 2400 years of natural erosion. The mound is made of sediment but its quadrangular base is bordered by an alignment of slabs lying on their sides, each weighing several tonnes (**Fig. 12**). The base of tomb no. 1 is a 65-m square with an entrance on the east side opening

Fig. 12 – Aerial views of two large aristocratic tombs of the Salbik necropolis: a. Tomb no. 1 whose tumulus was excavated in 1954, size: 65 x 65 m; b. Tomb no. 7, never excavated with its tumulus, size: 55 x 55 m (Photos: F. Monna).

Fig. 13 – Aristocratic tomb at the Safronov site in the south of the Republic of Khakassia (Photo: J. Magail).

onto a path of about 15 m, marked on either side by two large menhirs.

Tagar necropolises with several dozen burials are very numerous in the vast steppe plains of the Khakassia Republic. As the perimeter of each tomb is made up of slabs lying on their sides and stelae, these cemeteries appear as large fields of standing stones (**Fig. 13**). Half of the stelae bear rock engravings that often belong to several protohistoric periods. The distribution of iconography is therefore much less organized than that of the Okuniev stelae and deer stones.

5. Conclusion

The mosaic of High Asian nomadic cultures developed several forms of megalithism from the middle of the 3rd millennium to the end of the 1st millennium BC. It is astonishing that these herding populations, whose way of life was not favourable for construction, nevertheless chose to spend a great deal of energy building monuments. A deer stone quarry, discovered 6 km from Tsatsyn Ereg (Magail 2015), and a slab extraction zone located 12 km from Salbik are evidence of the important logistics linked to the transport of menhirs. The large and ever-increasing number of recorded funerary and ritual structures shows that the organization of nomadic societies has probably been significantly underestimated. The prospects for research are immense.

The similarities between the megalithisms discussed in this article may shed light on the beliefs of these populations. The first is the funerary and ritual context of sites where the aid of the deceased individual was probably invoked through rituals performed on a recurring basis. The hundreds of deposited horse heads, arranged around the Arkhangai mounds and stelae, support this hypothesis. A second common denominator is the predominance of sculptures, engravings and paintings, which contribute to the symbolic success of the monuments. The iconographies of Okuniev menhirs and deer stones are also present in rock art used to mark sacred places which, although different from tombs, were perhaps permeated by or under the protection of the same divinities (spirits, supernatural beings, genies, etc.). Research into traces of paintings is still in its infancy and continued investigation promises future revelations.

Annexe 2.

Lkebir, Noura & Rolland, Tanguy & Monna, Fabrice & Masrour, Moussa & Bouchaou, Lhoussaine & Fara, Emmanuel & Navarro, Nicolas & Wilczek, Josef & el Hassane, Beraaouz & Chateau-Smith, Carmela & Pérez-Lorente, Félix. (2020). Anza palaeoichnological site, Late Cretaceous, Morocco. Part III: Comparison between traditional and photogrammetric records. Journal of African Earth Sciences. 172. 103985. 10.1016/j.jafrearsci.2020.103985.

Journal of African Earth Sciences 172 (2020) 103985

Contents lists available at ScienceDirect

Journal of African Earth Sciences

journal homepage: www.elsevier.com/locate/jafrearsci

Anza palaeoichnological site, Late Cretaceous, Morocco. Part III: Comparison between traditional and photogrammetric records

Noura Lkebir [a], Tanguy Rolland [b], Fabrice Monna [b,*], Moussa Masrour [a], Lhoussaine Bouchaou [a,c], Emmanuel Fara [d], Nicolas Navarro [d,e], Josef Wilczek [b,f], El Hassan Beraaouz [a], Carmela Chateau-Smith [g], Félix Pérez-Lorente [h]

[a] Laboratory of Applied Geology and Geo-Environment, Ibn Zohr University, Agadir, Morocco
[b] ARTEHIS, UMR CNRS 6298, Université de Bourgogne–Franche Comté, 6 Boulevard Gabriel, bât Gabriel, 21000, Dijon, France
[c] International Water Research Institute (IWRI), University of Mohamed VI Polytechnic (UM6P), Benguérir, Morocco
[d] Biogéosciences, UMR CNRS 6282, Université Bourgogne Franche-Comté, 6 boulevard Gabriel, bât Gabriel, 21000, Dijon, France
[e] EPHE, PSL University, 75014, Paris, France
[f] Department of Archaeology, University of Hradec Králové, Rokitanského 62, 50003, Hradec Králové, Czech Republic
[g] CPTC, EA 4178, Université de Bourgogne, 4, boulevard Gabriel, 21000, Dijon, France
[h] Universidad de La Rioja, Edificio CT, Madre de Dios 51-53, 26006, Logroño, Spain

ARTICLE INFO

Keywords:
Dinosaur
Footprint
Documentation
Western high atlas
Ichnology
Recording methods

ABSTRACT

The present study evaluates a methodological workflow that could identify dinosaur tracks and trackways more comprehensively at outcrop scale. The approach described here is based both on 3D modelling by photogrammetry at different resolutions, and on suitably processed digital elevation models (DEMs). The ichnosite of Anza, Morocco, was chosen to demonstrate the efficiency of the proposed pipeline, because 323 dinosaur and pterosaur tracks discovered there have already been published. One subsector containing 89 tracks, identified in the two companion works that followed a traditional approach, was selected and divided into four subzones. By combining different DEM processes (hill-shade, slope, sky-view factor, and positive openness), almost twice as many tracks (175 *vs* 89) are now identified in these subzones. However, the improvement is not homogeneous. In the first subzone, the previous works reported 25 tracks *vs*. 22 with the 3D modelling techniques used here, whereas results for the second and third subzones show considerable improvement with 3D (21 *vs* 38 tracks and 42 *vs* 81 tracks, respectively). The enhancement is even more dramatic for the fourth subzone, where 34 new tracks are now identified, whereas with the traditional approach, only one track was previously reported. It is likely that such improvements depend on several factors, i.e. the surface conditions of the rocks (e.g. irregularities, cracking, etc.), and on the preservation state and depth of the tracks. Morphometric measurements of tracks and trackways obtained from 3D models are very similar to those derived from traditional fieldwork methods. The digital approach can be applied rapidly at different resolutions, but the models acquired with the pole-mounted camera provide a good compromise, with a resolution high enough (~2 mm/pix) to spot tracks, while respecting computational constraints. Once treated, DEMs greatly facilitate the reproduction of track outlines, drawn according to criteria defined by the operator.

1. Introduction

Since the seminal works of Hitchcock (1838, 1848, 1858), interest in dinosaur tracks and trackways has increased, especially in recent decades. This is because tracks provide important information about both palaeobiology, including locomotion, behaviour, size, mass, and identity of trackmakers, and palaeoenvironment, including substrate physical properties, water saturation, and taphonomic features

* Corresponding author.
E-mail addresses: nouralkebir@gmail.com (N. Lkebir), Tanguy.Rolland@u-bourgogne.fr (T. Rolland), Fabrice.Monna@u-bourgogne.fr (F. Monna), moussamasrour5@gmail.com (M. Masrour), l.bouchaou@uiz.ac.ma (L. Bouchaou), emmanuel.fara@u-bourgogne.fr (E. Fara), nicolas.navarro@u-bourgogne.fr (N. Navarro), josef.wilczek@hotmail.com (J. Wilczek), beraaouz@gmail.com (E.H. Beraaouz), chateau.smith21@gmail.com (C. Chateau-Smith), felix.perez@ext.unirioja.es (F. Pérez-Lorente).

https://doi.org/10.1016/j.jafrearsci.2020.103985
Received 28 April 2020; Received in revised form 1 July 2020; Accepted 18 August 2020
Available online 20 August 2020

(Alexander, 1976; Gillette and Lockley, 1989; Lockley et al., 1986; Lockley, 1991; Thulborn, 1990; Lallensack et al., 2016; Falkingham et al., 2016; Pérez-Lorente, 2015). Dinosaurs have always fascinated the general public, and their tracksites are an indisputable asset for regional tourism (Laws and Scott, 2003; Monbaron and Monbaron, 2015; Alcalá et al., 2016; Cobos and Alcalá, 2017). Dinosaur tracksites can be found all over the world, except in Antarctica, where known tracks are extremely rare when compared with the known dinosaur fossil record (Gillette and Lockley, 1989; Olivero et al., 2007; Reguero et al., 2013). Documenting this rich palaeontological heritage worldwide is a challenging and time-consuming task. The most common ichnological method for studying dinosaur tracks (hereafter 'the traditional method') can be seen as a two-step process, involving track detection and measurement. For over a century, this process has generally been performed manually, in situ (Sarjeant, 1989; Thulborn, 1990; Falkingham et al., 2016; Gand et al., 2018). The first step is to mark tracks in the field with chalk (sometimes using a reference grid). The second step usually involves capturing and assembling pictures, vectorizing footprints, and measuring features of interest. In some instances, this step may also involve shading inside the imprints (e.g. highlighting some features, or tracing the track margin), or making an interpretative drawing on transparent paper. When tracks are barely visible, the use of oblique artificial light may be necessary at night, together with several field sessions for data verification or refinement. Typically, this acquisition process is slow, and requires a high level of expertise in the field, with several operators (Falkingham et al., 2016; Gand et al., 2018; Romilio et al., 2017). Over the last three decades, practical alternative or complementary solutions have emerged in ichnology, as considerable progress has been made in the field of 3D modelling and geometrical processing (Moratalla et al., 1988; Ishigaki and Fujisaki, 1989; Matthews and Breithaupt, 2001; Breithaupt et al., 2001, 2004; Matthews et al., 2005, 2006; 2016; Belvedere, 2008; Bates et al., 2008, 2009; Falkingham et al., 2009, 2016; 2018; Wings et al., 2016). Although lasergrammetry and scanners based on structured light were the first to be developed (Falkingham et al., 2016; Adams et al., 2010; Bates et al., 2010), they have not become common practice, due to heavy logistical constraints, and poor performance under direct sunlight (Falkingham et al., 2016; Matthews et al., 2016). In contrast, photogrammetry has become the near-standard approach in ichnology, sometimes associated with lasergrammetry, and more traditional approaches (Breithaupt et al., 2001; Breithaupt and Matthews, 2001; Adams and Breithaupt, 2003; Remondino et al., 2010; Mallison and Wings, 2014; Falkingham et al., 2016; Matthews et al., 2016; Mazin et al., 2016; Romilio et al., 2017; Moreau et al., 2020). Nonetheless, even though photogrammetry is now widely used to illustrate, selected representative tracks, it is only applied sporadically to represent entire sites. Orthomosaics and digital elevation models (DEMs) can be produced either by aerial or ground-based photogrammetry, at different resolutions (Kraus, 2007; Remondino et al., 2010; Falkingham, 2012; Falkingham and Gatesy, 2014; Matthews et al., 2016). Post-processing these DEMs may reveal features of special interest, such as peaks, valleys, ridges, and even anatomical details that would otherwise remain unnoticed in the field (e.g. for archaeological applications, see Magail et al., 2017; Monna et al., 2018). Several algorithms are available, based either on differential geometry (e.g. slope), or on visibility (e.g. sky-view factor, positive openness, and hill-shading). Each method reveals specific features of the relief, and their outputs can easily be integrated into geographical information systems (GIS), facilitating further measurements and spatial analysis (Matthews et al., 2016; Romilio et al., 2017). Although DEM acquisition by photogrammetry together with post-processing are commonly used to describe and document individual tracks and trackways, they have less frequently been combined with aerial imagery, despite the great potential of this approach (Breithaupt and Matthews, 2001; Matthews et al., 2016; Romilio et al., 2017).

The aims of the present study are (*i*) to propose a methodological workflow capable of identifying dinosaur tracks and trackways more comprehensively, at outcrop scale, using 3D modelling at different resolutions, and (*ii*) to provide a quantitative comparison of the resulting outputs with those obtained by a more traditional approach. The workflow relies on images captured by Unmanned Aerial Vehicle (UAV), pole-mounted and hand-held cameras, creation of DEMs by Structure-from-Motion, and post-processing based on differential geometry and visibility. The Moroccan ichnosite of Anza, which is Coniacian-Santonian (Late Cretaceous) in age, is used as a case study. This large, multi-surface tracksite has already yielded 323 dinosaur and pterosaur tracks that have been investigated in companion works, using a traditional ichnological approach (Masrour et al., 2017a,b). It is therefore an ideal candidate for comparisons between the traditional approach and 3D modelling, on the basis of their respective efficiency in spotting tracks, and of the similarity between field-derived and model-derived morphological measurements, both acquired by the same team of ichnologists. For the present study, 3D acquisition focused on a subzone of the Anza ichnosite (namely 1ANZ), where 89 dinosaur tracks have already been reported (Masrour et al., 2017a,b). One of the main questions is to assess the level of 3D modelling resolution and the type of DEM post-processing necessary for specific ichnological analyses (e.g. ichnotaxonomical studies, and/or inventory and documentation of large tracksites).

2. Material and methods

2.1. Study site

The ichnosite of Anza is only briefly described here, as it has been extensively detailed in the two previous companion works (Masrour et al., 2017a,b). It was discovered in 2013, about 5 km north of Agadir, Morocco, after an exceptional swell hit the Atlantic coast. The site consists of several calcareous sandstone beds, dating from the Coniacian-Santonian (Late Cretaceous), and is approximately 100 × 30 m^2 in extent. The area lies in the intertidal zone and is emergent for only a few hours a day. Except in winter, the site is often covered by a sand beach and/or by algae. These conditions considerably complicate the study of the site, but also provide natural protection against erosion. The entire area with mostly well-preserved dinosaur and pterosaur tracks has previously been divided into four geographical zones (i.e. 1ANZ, 2ANZ, 3ANZ, and 4ANZ in Masrour et al., 2017a: Fig. 1). Two groups of vertebrate tracks have been clearly identified: theropod footprints, by far the most abundant (more than 300 tracks), and 11 pterosaur manus tracks found only in zone 2ANZ. At Anza, 56 trackways have previously been identified. Using quantitative morphometric features, Masrour et al. (2017a,b) attributed the theropod tracks to *Grallator*-like or *Eubrontes*-like ichnogenera, and the pterosaur tracks to *Agadirichnus* or *Pteraichnus*. This ichnoassemblage, which also includes three tracks of the rare ichnogenus *Macropodosaurus*, makes Anza an international reference site for ichnology. When the photogrammetric campaign was undertaken, zones 2ANZ, 3ANZ, and 4ANZ were completely or partially covered by beach sand and algae. As it was not necessary to process the entire site to accomplish the aims of this study, only one subzone was targeted, zone 1ANZ, which is densely covered in theropod footprints (89 previously discovered tracks, over a surface area of ca. 80 × 10 m^2). Zone 1ANZ was almost free of sand or algae during photogrammetric acquisition, and exhibited surface rock conditions similar to those encountered during the previous (traditional) study, thus facilitating comparison.

2.2. Traditional approach for track documentation

Tracks at Anza were documented using the traditional method (Fig. 1). The first step was to draw the outline of all visible ichnites (i.e. the top of track walls at their intersection with the sediment surface) manually, with chalk, sometimes highlighting the limit of the extrusion rims and other remarkable features, such as pads and claw marks

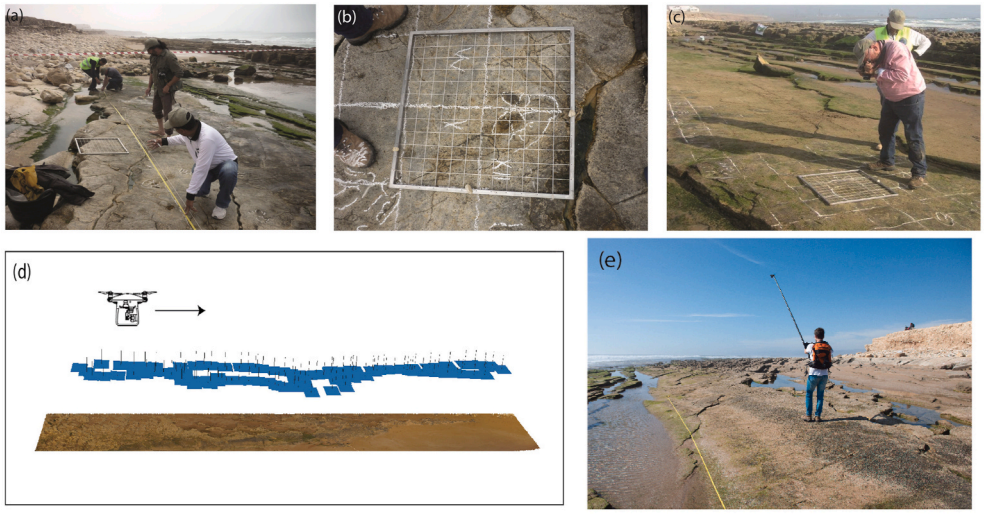

Fig. 1. Illustration of both traditional and 3D modelling methods. Traditional: (a) manual drawing of tracks with chalk, (b) grid drawing and alphanumeric referencing, (c) photographing tracks. 3D modelling: (d) flight of the UAV over the area of interest; blue rectangles correspond to images captured, (e) images captured by pole-mounted camera. (For interpretation of the references to colour in this figure legend, the reader is referred to the Web version of this article.)

(Fig. 1a). A series of 30 × 30 cm^2 squares (Fig. 1b) was also drawn on the track-bearing surface, forming a grid with axes corresponding to the dip and strike lines of the surface (Masrour et al., 2017a,b). Each cell of this grid was referenced using an alphanumeric system, and then photographed as perpendicularly as possible to the bed surface, to obtain views with minimal distortion due to perspective (Fig. 1c). In the laboratory, the photographs were first rectified to eliminate any remaining perspective distortion. They were then assembled with Adobe Photoshop®, a raster graphics editor, to produce a document in a projection plane parallel to the rock surface where the tracks lie. Once scaled and referenced in a metric system, the final photo-assemblage was transferred into Autodesk AutoCAD®, a computer-aided design software, to vectorize the tracks, and to measure a set of morphometric features, including distances, angles, and derived variables (Fig. 2). It is worth mentioning that these measurements were in good agreement with those taken in the field for some selected tracks.

2.3. Photogrammetric workflow

Whatever the size of the objects studied, and the desired DEM resolution, 3D modelling was obtained by Structure-from-Motion. This technique is increasingly used in several scientific fields, e.g. geology and geomorphology (Bemis et al., 2014; Tavani et al., 2016; Westoby et al., 2012), and archaeology and cultural heritage (López et al., 2016; Monna et al., 2018; Reu et al., 2013; Verhoeven et al., 2012). Briefly, a set of pictures covering the area of interest is captured, while (*i*) maintaining an overlap between pictures of at least 70–80%, and (*ii*) changing the point of view between each shot. For nearly flat surfaces, as in our case, the pictures are taken in the nadir direction, as perpendicularly as possible to the surface, to reduce image distortion. A 3D reconstruction is obtained after estimating camera positions and orientations, producing a sparse cloud, densifying this cloud, then meshing, and texturing. The resulting images (i.e. 2.5D grids) are saved in raster format. Note that the resolution of a DEM depends on the size and resolution of the camera sensor, the focal length of the lens, and the distance between the camera and the outcrop. Here, four different resolutions were evaluated. First, the entire site was modelled with the help of the UAV, a DJI Phantom 3 PRO equipped with a GPS and a 12-million-pixel camera (Fig. 1d, Table 1). The flight height of ca. 15 m led to a ground sample distance or GSD (i.e., the distance between the centres of two consecutive pixels) of about 5–6 mm. The result was a georeferenced orthomosaic and DEM covering the whole area. Next, to better define altitudinal surface variation, pictures were also captured at a lower elevation, using a SONY DSC-RX100 MIII (sensor 13.2 × 8.8 mm^2, 20 Mpix), with a 24–70 mm lens, equivalent to a full-frame 35 mm camera set at 24 mm. The camera was mounted on a 4-m-long telescopic Rode pole, and wifi-controlled, using a Samsung Galaxy tablet fixed to the pole (Fig. 1e). A total of 9 slightly overlapping chunks was produced, each about 100 m^2, with a typical GSD of 1–2 mm (Table 1). The other two acquisitions were made with a hand-held NIKON D800 full-frame DSLR (sensor 24 × 36 mm^2, 36 Mpix), equipped with a NIKKOR 50 mm prime lens. Three small areas of about 10–20 m^2, each containing a set of footprints, were selected and photographed at breast height (1.5–1.6 m from the ground), delivering DEMs with a GSD of about

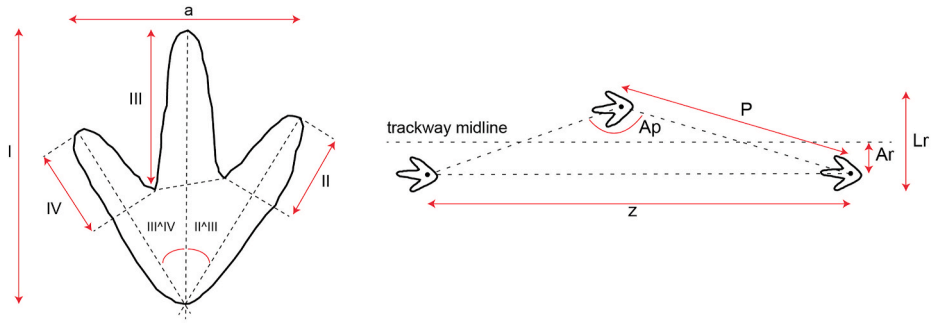

Fig. 2. Ichnological parameters measured in Masrour et al. (2017b) and in the present study. *l*: footprint length; *a*: footprint width; *Ar*: trackway deviation; *Lr*: trackway external width; *P*: pace length; *z*: stride length, *Ap*: pace angle; *II-III-IV*: lengths of digit impressions; *II^III^IV*: interdigital angles.

Table 1
Acquisition settings. Type of view, object targeted, ground distance, camera type, sensor definition, number of pictures processed, focal length of the lens (*: equivalent on full frame, 35 mm camera) and typical resolution of the produced DEMs.

Type of view	Object targeted	Ground distance	Camera type	Definition	Number of pictures processed	Focal length of the lens	Typical resolution of produced DEM
Aerial	Entire site	~15 m	DJI Phantom 3 PRO	12 Mpix	~100 for 1000 m^2	20 mm*	5–6 mm/pix
Pole	Bed	~4 m	SONY RX-100MIII	20 Mpix	~50 per chunk of ca. 50 m^2	24 mm*	1–2 mm/pix
Breast height	Trackways/ footprints	1.5–1.6 m	Nikon D800	36 Mpix	~100–150 per chunk of ca. 20 m^2	50 mm	100–150 μm/pix
Close up	Footprints	0.4–0.6 m	Nikon D800	36 Mpix	10–20 per footprint	50 mm	50–80 μm/pix

100–150 μm. For individual footprints, the best DEM resolution was obtained by capturing images with the operator crouching at 0.5–0.6 m above ground level, generating DEMs with a GSD of ca. 50–80 μm. Only one isolated footprint, 1.3ANZ9, and 15 footprints from trackway 1.3ANZ5 (Masrour et al., 2017b) were acquired at this level of precision. Models produced by terrestrial photogrammetry, generated in an arbitrary reference system, were aligned on the georeferenced UAV orthomosaic, using several ground control points. All georeferenced DEMs and orthomosaics were then integrated into GIS software, for further measurement.

2.4. Algorithms used to treat DEMs

Geomorphologists have developed several algorithms to identify geomorphological features (depressions, slopes, etc.) at the scale of a landscape, which can be used to reveal footprints. Slope describes the maximum rate of change in elevation between each cell of the raster and its neighbours. This is the maximum downhill gradient, calculated as the first derivative of the DEM (e.g. Longley, 2005). The most basic procedure based on visibility is analytical hill-shading, which simulates artificial illumination of the DEM surface (Imhof, 2007). The idea underlying the sky-view factor is that the bottom of a depression receives less light than the summit of a peak. Sky-view factor (SVF) evaluates that part of the hemispheric sky limited by the relief, and visible from a given point within a searched radius, *r* (Fig. 3a). In practice, *n* directions (most often 8) are scanned, and the vertical angles starting from the horizon to the position where the sky becomes visible, γ_i, are assessed; SVF is then computed as follows (Zaksek et al., 2011):

$$SVF = 1 - \frac{\sum_{i=1}^{n} \sin \gamma_i}{n}$$

The same principle governs the calculation of positive openness, reflecting the "degree of dominance or enclosure of a location on an irregular surface" (Yokoyama et al., 2002; Doneus, 2013). The main difference is that the greatest angle before interception with the surface, α, is sought, taking the zenith as reference in place of the horizon, in contrast with sky-view factor (Fig. 3b). Consequently, a constant slope is seen as a flat surface by positive openness, whereas the summit of a peak produces the same result as a horizontal plane with sky-view factor (Fig. 3c). Practically, 8 directions (N, NW, W, SW, S, SE, E, and NE) are evaluated at each point of the DEM, and positive openness, α_{PO}, is obtained by simply averaging:

$$\alpha_{PO} = \frac{(\alpha^0 + \alpha^{45} + \ldots + \alpha^{315})}{8}$$

2.5. Software and hardware

All DEMs were produced using the Agisoft Photoscan Pro software 1.4.5. The hill-shading, slope, and visibility-based rasters were created with either the open-source QGIS (https://www.qgis.org) or SAGA GIS (http://www.saga-gis.org/) software. Traditional morphometric measurements were obtained in QGIS from tracks drawn as vector layers. Unreferenced schemes from the companion studies (Masrour et al.,

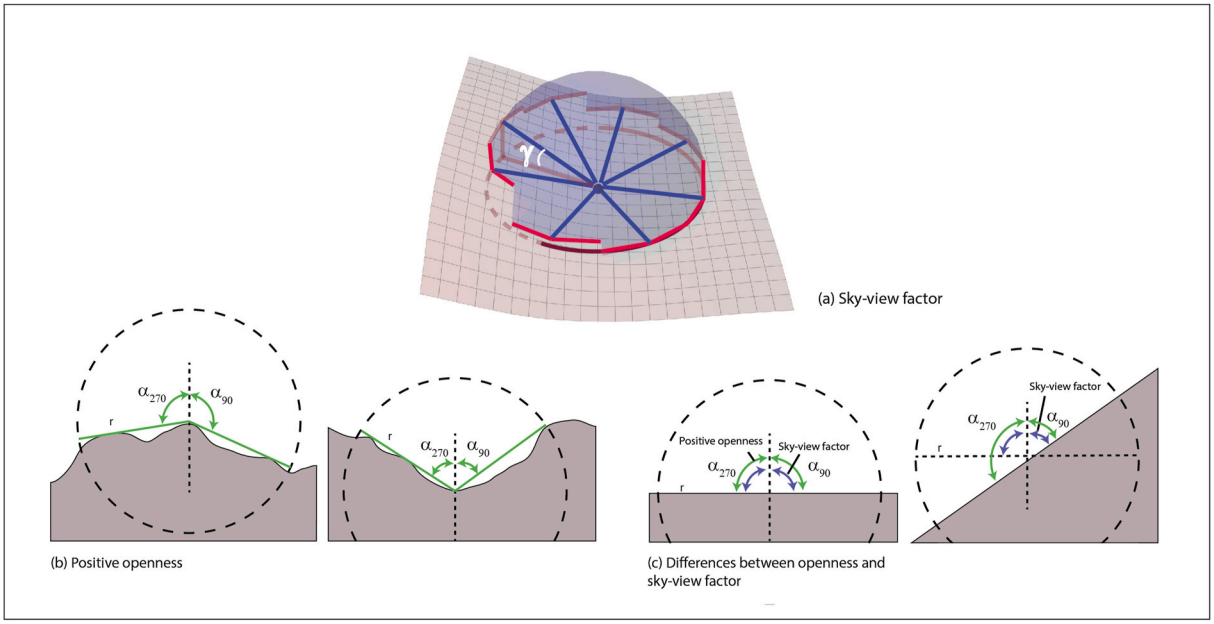

Fig. 3. Principles of (a) sky-view factor, and (b) positive openness; drawing modified from Dozier and Frew (1990) and Monna et al. (2018). The differences between both the two parameters are illustrated in (c).

2017a,b) were registered using a rigid Helmert transformation, selecting several control points on trackways. A consumer-grade computer, i7 5960x, 8 cores, equipped with 64 Go of RAM and two 4 Go-RAM NVIDIA GeForce GTX 980 mounted in SLI, was used for processing.

3. Results and discussion

3.1. Track identification from processed DEMs

Identifying and understanding the factors that have preserved dinosaur footprint morphology is a complex task. The track preservation state results from many factors, such as the nature of the substrate, the depth of the footprint, the effect of erosional processes, and the possible presence of extra-morphological structures. Orthomosaics, DEMs, and derivatives, at all available resolutions, were used to evaluate the intrinsic potential of 3D modelling for track detection and drawing, without reference to field data or previously published schemes. When optimal foot dynamics and substrate properties record the anatomy of the foot, depressions caused by a moving dinosaur should be characterized by low sky visibility (i.e. low values of sky-view factor and positive openness), surrounded by subvertical footprint walls (i.e. steeply sloped contours). Even when tracks have been identified, drawing individual tracks sufficiently well is always a challenge, as there is often room for debate on where the track contours should be drawn (Graversen et al., 2007; Milàn and Loope, 2007; Falkingham, 2016; Lallensack et al., 2016). Following many authors (e.g. Ishigaki and Fujisaki, 1989; Lallensack et al., 2016), and similarly to the previous companion works, the outline of the track wall is preferred here (i.e. at the top of the track wall) to allow quantitative comparison. Fig. 4 depicts orthomosaic, DEM, hill-shaded DEM, slope, sky-view factor, and positive openness raster maps of footprint 1.3ANZ9, together with the values for each parameter, along an A-B profile crossing the footprint. This example, based on a well-preserved footprint, presents acquisition at the highest resolution ('close-up' in Table 1). The guidelines mentioned below are valid whatever the resolution. Here, the outline is barely visible on the orthomosaic, blurred by texture variation due to erosion and algae (Fig. 4a). From the DEM, incisions made by digits become unambiguous; the talwegs (Fig. 4b, n°1 and n°3) can be positioned precisely, as well as the ridge (Fig. 4b, n°2), but it is still difficult to delineate the footprint with precision without DEM post-processing. Hill-shaded raster is effective for quickly perceiving the relief, which is rendered realistically (Fig. 4c). However, there are major differences in the depiction of slopes in terms of brightness, depending on their orientation relative to artificial light (from the northwest in this case). The steepness of slopes is poorly rendered. Ridges and talwegs are displayed in mid-grey. The rear wall of the footprint, parallel to the light beam (Fig. 4c, n°4), is not clearly distinguished because of its orientation. Slope raster can be used to alleviate the above-mentioned drawbacks. The footprint is easily visible, marked by steep slopes (darker colour in Fig. 4d). Its outline is characterized by a sharp decrease in slope, which can also be observed for talwegs. To compute sky-view factor and positive openness, the maximum search radius needs to be tuned, which is not the case for hill-shading and slope (Fig. 4e and f). Search radius, an important parameter, must be set by taking into account the size of the features to be highlighted: higher values enhance the main structures, while details are better depicted when the radius decreases. As a rule of thumb, if the entire depression must be darkened, the search radius must be at least half the diameter of the object (Mara et al., 2010; Zaksek et al., 2011). The 1.3ANZ9 footprint measures approximately 20 × 20 cm^2, and a search radius greater than 10 cm would be a good first guess. However, with such a value, most of the details inside the footprint would disappear, which is why a smaller radius (5 cm) was used here. With both sky-view factor and positive openness (Fig. 4e and f), contrasts with steep slopes within the track are well marked in dark tones, and may ultimately help to delineate the outline, while the "heel" is identified by a small (darker) hollow within the larger depression formed by the entire footprint. Imprints of digits II and III are extremely dark because the corresponding impressions are very deep and narrow. At first glance, the drawings based on each individual treatment appear quite similar (see blue contours in Fig. 4c–f, and Fig. 4g, where all contours are superimposed). However, some notable differences can be observed. Using hill-shading, a gap without any clear information had to be filled in at the bottom left outer limit of the footprint (dashed line in Fig. 4d). The identification of this limit is easier with the slope raster, as well as with the sky-view factor and positive openness. However, both the slope and the hill-shaded rasters suggest some sinuosity in the imprint of digit III (Fig. 4c–d, n° 5), which cannot be perceived with the other two processes. Sky-view factor and positive openness produce similar outputs, except that positive openness slightly outperforms sky-view factor in detecting hypices (Fig. 4e–f, n°6). It is well known that defining the contours of dinosaur tracks is somewhat subjective (Thulborn, 1990; Bates et al., 2008; Romilio and Salisbury, 2014; Falkingham, 2016; Falkingham et al., 2018), and can challenge the operator during the drawing phase. The best solution here is probably the detailed examination of every raster map, including the orthomosaic. The definitive outline is then produced by following an interpretative process, which takes advantage of the features of interest provided by each treatment (Fig. 4h). A return to the field may, however, be worthwhile to refine the final drawing of the tracks.

3.2. Mapping and track census

Except for the deepest tracks (depth>2 cm, as for 1.3ANZ9), the resolution obtained here from aerial photography by UAV (~5–6 mm for x and y, 1 cm for z) is not good enough to perceive dinosaur footprints (see the slope raster map for track 1.3ANZ5.13, Fig. 5). Its usefulness is mainly limited to georeferencing the other layers, and also obtaining an overall image of the study area. In contrast, the outputs obtained from images taken at breast height or crouching are extremely well defined (Fig. 5). Although the resolution for images captured when crouching is about twice that of those taken at breast height, no significant discrepancy is observed. Unfortunately, high-resolution acquisition was limited here to a few specific areas, because covering the entire Anza ichnosite would require too much computation power for the hardware available for this study. This is one of the drawbacks of the 3D approach, in comparison with traditional methods. Identification and drawings were therefore essentially based on the models acquired with the pole-mounted camera (resolution ~2 mm/pix, Fig. 5), which provide a good compromise, with resolution high enough to spot tracks, while respecting computational constraints. In cases where some doubt persists, it is still possible to inspect other available raster maps obtained at higher resolutions, because GIS allows a seamless switch across layers. As the study area is elongated, it was divided into four zones (red rectangles in Fig. 6), with the same designation as in Masrour et al. (2017b) for the first three zones (1.1ANZ, 1.2ANZ, and 1.3ANZ), and a fourth zone (1.4ANZ), created specifically for the present study. In total, 175 easily distinguishable footprints were recorded, without any input from the previous companion works (Masrour et al., 2017a,b), which identified 89 tracks using the traditional approach (Fig. 7). However, this increase in the number of tracks is not homogeneous across the four zones in Anza 1. The traditional approach revealed 25 tracks *vs.* 22 with 3D modelling techniques in zone 1.1ANZ (Fig. 7). The 3D approach outclasses the previous study by a factor of almost two, for zones 1.2ANZ (21 *vs* 38 tracks) and 1.3ANZ (42 *vs* 81 tracks). This discrepancy is even more pronounced for zone 1.4ANZ, where 34 new footprints are now identified, while only one track was reported with the traditional approach (Fig. 7). In zone 1.1ANZ, the lower rate of identification using raster maps is probably due to strong surface irregularities and erosion/cracking. Such irregular surfaces impede the unambiguous recognition of footprints from post-processed DEMs. In this case, careful inspection in the field clearly outperforms 3D modelling and associated processing methods. For well-marked footprints, visible even to a

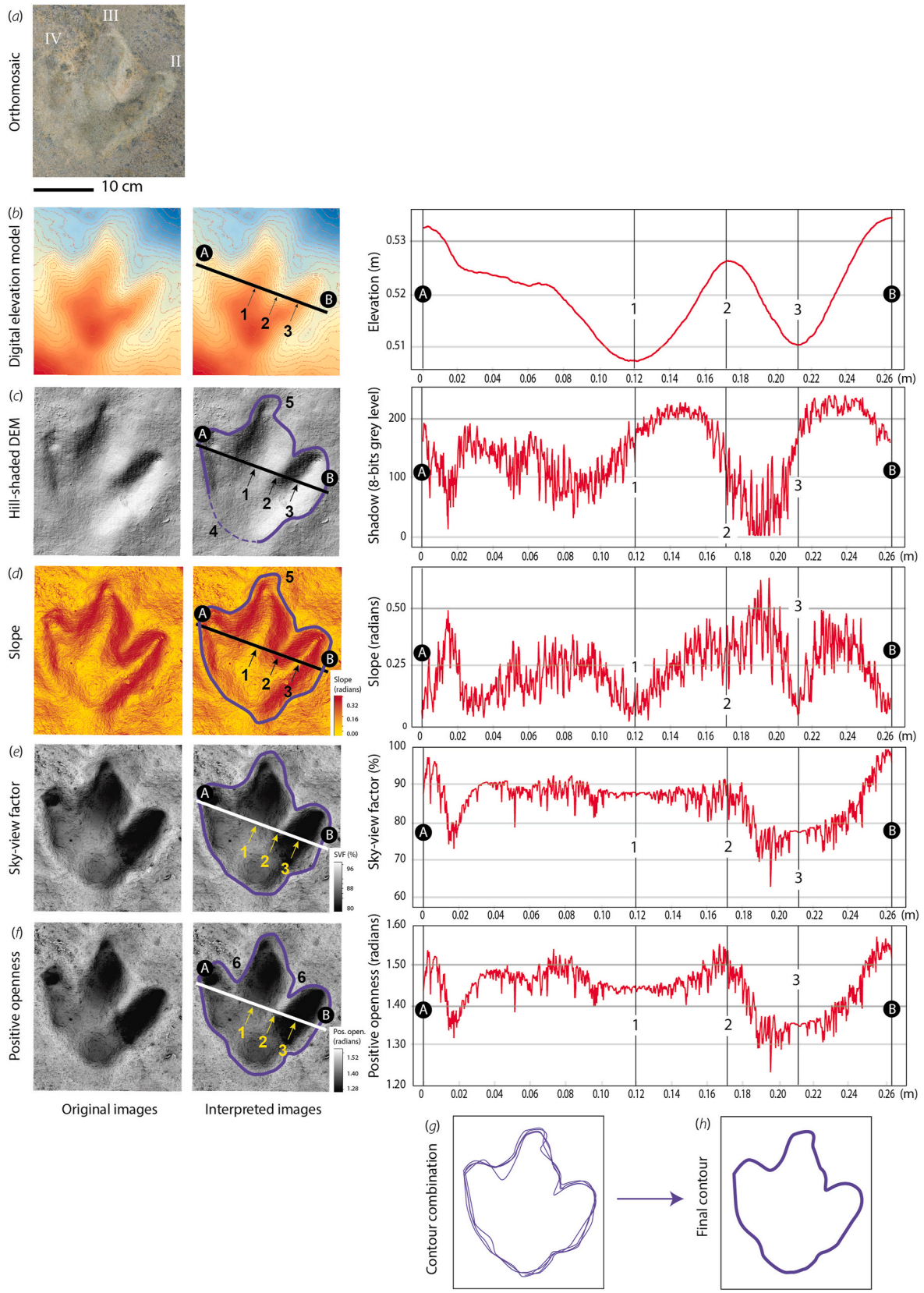

Fig. 4. Algorithm tests on footprint 1.3ANZ9 track, approximately 20 × 20 cm^2 wide. (a) orthomosaic; (b) coloured DEM and contour lines (2 mm interval); (c) hill-shaded DEM; (d) slope; (e) sky-view factor; (f) positive openness; (g) combination of contours obtained from each DEM treatment; (h) final interpretative contour. Sky-view factor and positive openness were computed with a radius of 5 cm. On the left-hand side, the original raster maps, and their interpretation; on the right-hand side, values along an A-B profile across the footprint. Numbers refer to special points of interest (see text for details).

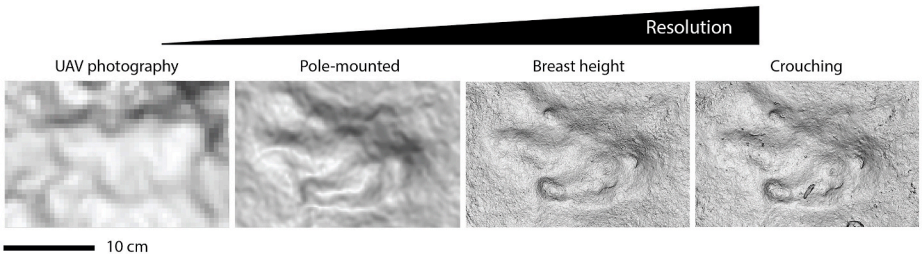

Fig. 5. Typical rendering of a footprint (1.3ANZ5.13) at the four resolutions evaluated. Resolution increases from left to right.

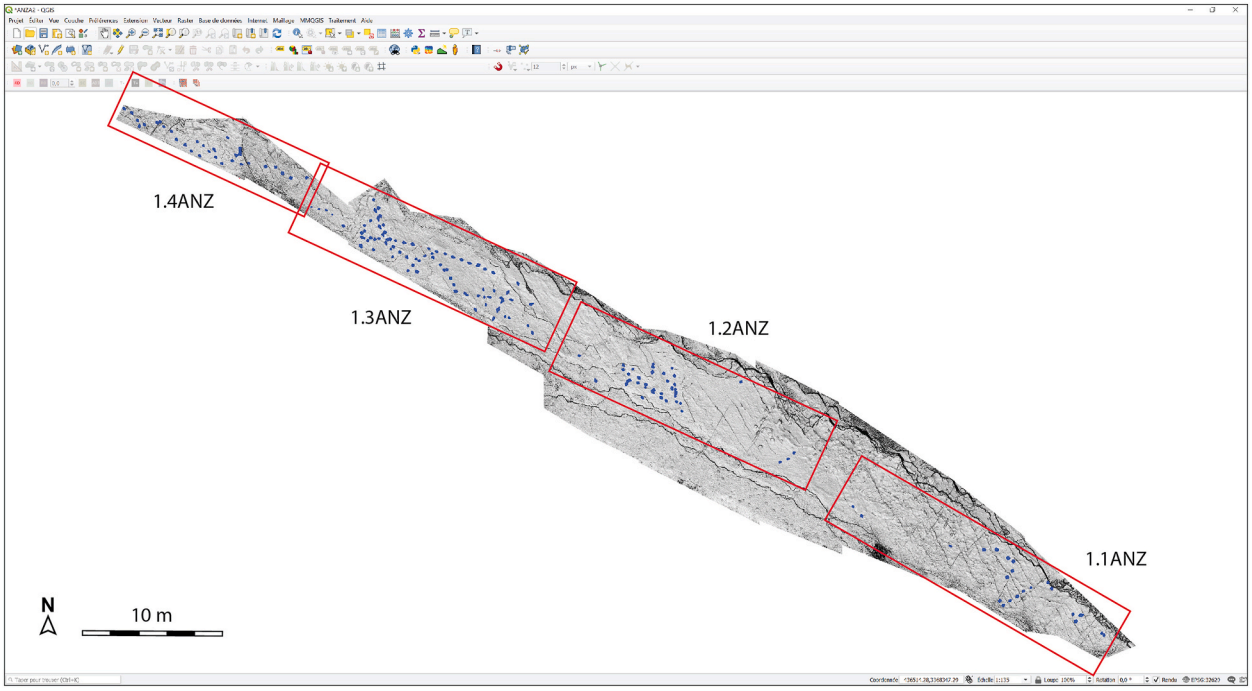

Fig. 6. Processed raster maps of the Anza ichnosite in a geographical information system (QGIS). Zone 1ANZ processed with hill-shading. The study area is divided into four subzones, following the denominations in Masrour et al. (2017b) for zones 1.1ANZ, 1.2ANZ, 1.3ANZ, together with the newly created zone 1.4ANZ. Drawings of dinosaur tracks identified in this study appear as an overlying shapefile in blue. (For interpretation of the references to colour in this figure legend, the reader is referred to the Web version of this article.)

non-specialist, the two approaches provide the same results. By contrast, post-processed DEMs reveal very small variations in elevation that would have not be visible in the field without special equipment, e.g. artificial light by night. This level of definition, and the possibility of visualizing a trackway in its entirety, together explain why raster maps efficiently complement the traditional method, essentially based on field work. Finally, positioning tracks by 3D modelling is likely to be more accurate, because the necessary movements of the palaeontologist in the field, even when proceeding cautiously, will almost always produce outputs somewhat undermined by the cumulative effect of small positioning errors.

The time factor is also worth mentioning. Only half a day was necessary for one operator to acquire photographs at the four resolutions used here, with a further ten days for DEM production and post-processing. Interestingly, this pipeline requires very little supervision by the operator. This time frame should be evaluated in comparison with several weeks of work at best, requiring the presence of two (or more) palaeontologists, where progress may well be impeded by external factors, such as the recurrence of the tide, as in the case of the Anza ichnosite. The only potential drawback is that producing a photogrammetry-based ichnological record is still computer-intensive at the time of writing.

3.3. Morphometric measurements

Another aim of this work was to evaluate the efficiency of raster maps in producing accurate morphometric measurements. As no true reference values exist, the results obtained from 3D models can only be compared to the data published in Masrour et al. (2017b). Derived variables obtained from two (or more) measurements are discarded; only primary variables are kept: footprint length, footprint width, trackway deviation (distance between footprint midpoint and trackway midline), trackway external width, pace length, stride length, pace angle, footprint orientation (angle between footprint axis and midline of trackway), length of digit impressions, interdigital angle, and trackway direction. Results for the two approaches are summarized in Table 2. They are reported as averages of distances and angles of footprints and trackway for the traditional approach. For the 3D method, they are given as a range of values when $n < 4$, and as a mean with its 95% confidence interval in all other cases. At the Anza ichnosite, there is overall agreement between measurements for the two approaches, and cases of mismatch are rare (in bold in Table 2), with divergence at only 10–15%. Such convergence may also be the result of the greater number of footprints discovered through 3D modelling. The pertinence of the results obtained by the two approaches nevertheless remains dependent

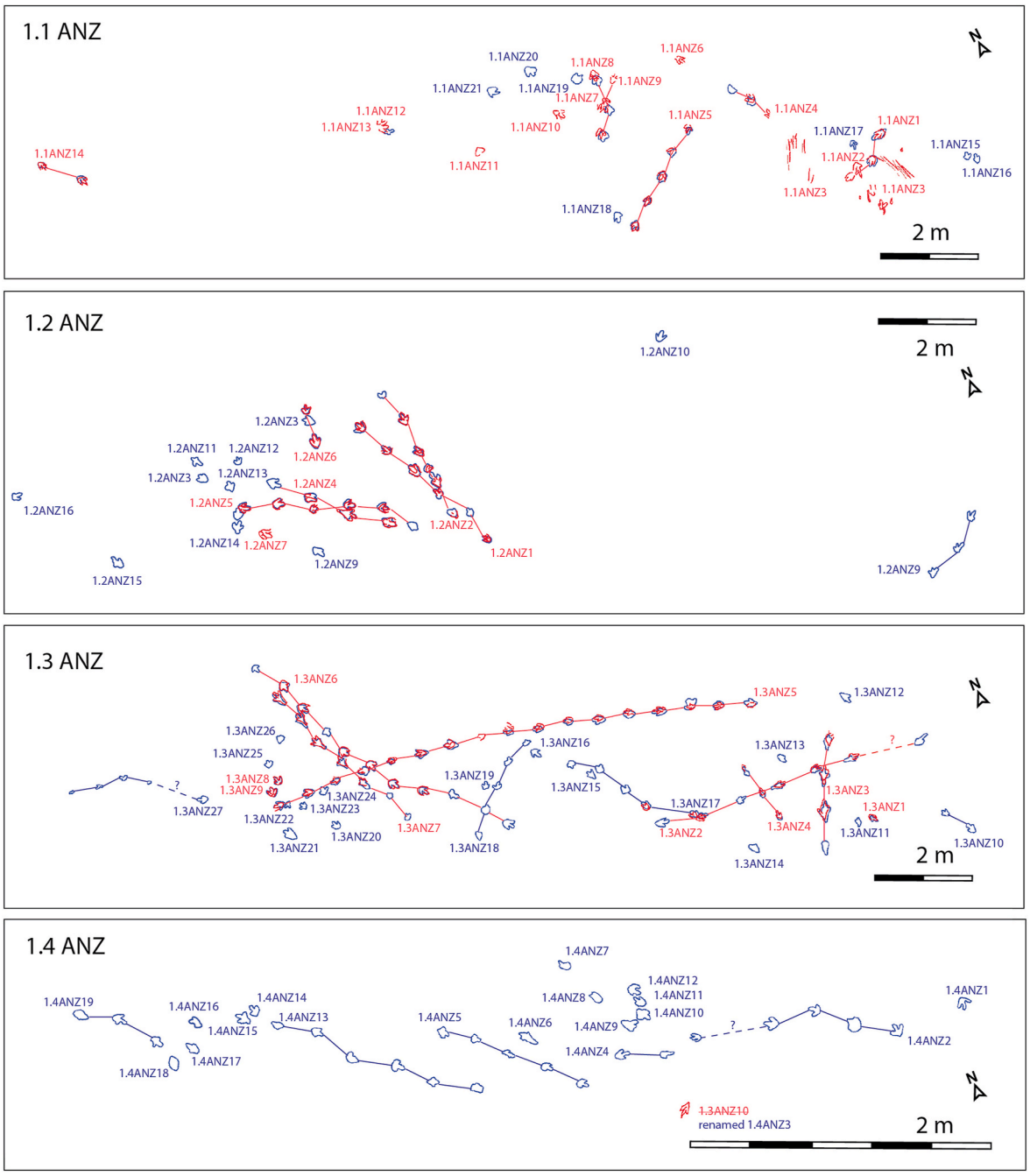

Fig. 7. All dinosaur tracks, showing those from Masrour et al. (2017b) in red, and those identified in the present study using medium resolution (pole-mounted camera) in blue. Names of tracks/trackways follow the denominations in Masrour et al. (2017b). Note that footprint 1.3ANZ10, which originally belonged to the 1.3ANZ subzone, was renamed 1.4ANZ3 to fit the creation of a new subzone (1.4ANZ). (For interpretation of the references to colour in this figure legend, the reader is referred to the Web version of this article.)

on the choices made by palaeontologists with regard to what should be measured.

4. Concluding remarks

The results obtained from the Anza ichnosite show that the proposed protocol may outperform the traditional method in some instances, in terms of the number of footprints discovered (here the number of footprints identified is increased by a factor of two), and probably also in terms of the information necessary for contour drawings. Such great improvement in terms of track identification is obviously not expected for all sites, especially for those with well-preserved tracks, where both methods should produce very similar results. It is important to note that many of the new discoveries in this study concerned poorly preserved, vanishing, shallow tracks, with barely defined walls, identified without ambiguity by the 3D approach. An additional pterosaur track was also detected in zone 2ANZ (not shown here) by means of this methodological workflow. The greatest benefit of this method is undoubtedly the small amount of time spent in the field. Field study is probably the most limiting factor for massive acquisition, especially for sites at some distance from the laboratory, which are often time-constrained, and where repeated access on demand may be difficult, due to cost, schedules, seasonal constraints, etc.

The optimal methodological pipeline may consist first in screening

Table 2
Measurements in centimetres from Masrour et al. (2017b), referred to as the traditional method (Trad. meth.) and measurements derived from the 3D models of the present study. Abbreviations: *n*: number of footprints taken into account in the calculation; *l*: footprint length; *a*: footprint width; *Ar*: trackway deviation; *Lr*: trackway external width; *P*: pace length; *z*: stride length, *Ap*: pace angle; *O*: footprint orientation; *II-III-IV*: lengths; *II^III^IV*: interdigital angles; *N-E*: trackway direction (e.g. N243). For the traditional method, the values correspond to measurement averages. For the 3D-derived measurements, the values are provided as range, when n < 4, and as mean with its 95% confidence interval, otherwise. Cases where the 3D approach does not match the traditional method are noted in bold. NA for Not Available.

Trackways		*n*	l	A	Ar	Lr	P	z	Ap	O	II-III-IV	II^III^IV	N … E
1.1ANZ1	Trad. meth.	3		18	8	36	58	113	160			13–31	243
	3D	2		17–18	7	NA	62	NA	NA			17–30	242
1.1ANZ5	Trad. meth.	5	23	17	1	23	59	119	172	0		25–30	237
	3D	5	22 ± 4	16 ± 3	1	26	57–62	116–121	168–173	0		27–34	243
1.1ANZ8	Trad. meth.	3	**23**	**21**	7	34	63	123	153		12–15 - 19	23–42	203
	3D	2	**24–25**	**24–26**	8	NA	71	NA	NA		11 - 15 - 16	29–44	207
1.1ANZ14	Trad. meth.	2	**22**	18			93						140
	3D	2	**24–26**	13–19			94						147
1.2ANZ1	Trad. meth.	5	18		2	23	60	**120**	171	−4	14	19–26	337
	3D	6	21 ± 4		2	26	62 ± 6	**122–123**	163–174	−5	13–00 - 00	20–26	330
1.2ANZ2	Trad. meth.	4	23	18	2	19	62	123	**172**	7	09 - 13 - 16	36–36	356
	3D	5	24 ± 4	18 ± 3	3	25	58–70	122–127	**163–171**	8	10–14 - 15	34–36	362
1.2ANZ4	Trad. meth.	3	25	20	4		**77**	**154**	170				131
	3D	4	24–28	19–25	4		**62–72**	**132–142**	170–174				129
1.2ANZ5	Trad. meth.	5	20	18	3	25	62	123	170	−1	10–13 - 16	30–35	114
	3D	5	27 ± 11	21 ± 3	2	26	66 ± 22	116–133	162–174	0	9 - 12 - 17	32–35	120
1.2ANZ6	Trad. meth.	2	23	19			51					21–31	353
	3D	2	22–27	18–21			63					22–31	360
1.3ANZ2	Trad. meth.	3		14	1	18	80	160	175				98
	3D	6		15 ± 2	0	20	84 ± 9	167 ± 15	168–177				100
1.3ANZ4	Trad. meth.	3	15	10	0	11	57	115	180	0			354
	3D	3	20–23	14–16	1	12	54–60	115	175	0			350
1.3ANZ5	Trad. meth.	17	**20**	13	1	16	62	124	175	0	09 - 13 - 15	25–23	267
	3D	16	**25 ± 1**	15 ± 2	1	15	6 ± 2	125 ± 2	175 ± 1	1	10–14 - 15	25–24	261
1.3ANZ6	Trad. meth.	6	24	20	5	23	60	119	165	−5		12–30	156
	3D	8	28 ± 2	18 ± 2	5	25	62 ± 3	123 ± 4	162 ± 12	−4		14–33	155
1.3ANZ7	Trad. meth.	5		21	4	31	61	122	170	−2		30–40	344
	3D	7		21 ± 1	4	33	60 ± 5	117 ± 5	165 ± 11	−1		32–39	340

the area of interest using the UAV, to obtain a georeferenced orthomosaic, to which will be attached the other models (even simple photographs), at higher resolution. An even better solution would be to use an available UAV equipped with a high-quality camera sensor, at lower altitude, thus replacing the acquisition steps using a pole. Whether derived from UAV or pole images, 3D models with resolution from about 1 to 2 mm lead to good recognition of tracks (at least here), in particular because entire trackways can be depicted on raster map outputs. At the current level of technical and computational constraints, it may be difficult to produce models over large areas, at resolution better than 100 μm per pixel. This resolution is nevertheless adequate when assessing rock surface condition (e.g. the effect of bioturbation and erosion), and for determining and interpreting ichnotaxa. While awaiting further technical improvements and better calculation power, such high-resolution models should probably be limited to smaller areas, studied for specific purposes, or for verification, after preliminary screening at a lower resolution. In any case, a return to the field is strongly recommended to confirm and refine the results obtained computationally. Even if the documentation thus produced is probably more reliable and less operator-dependent than the traditional method, the identification and the interpretative drawings made by the operator still require a high level of expertise, as several choices must be made. Interestingly, the production of several maps derived from the DEM (hill-shaded DEM, slope, sky-view factor, and positive openness) should help palaeontologists to draw track outlines, in accordance with the criteria used for defining track contours. The workflow described here, using an appropriate UAV, may be applied safely to hard-to-reach ichnological sites, such as those found on strongly tilted (or even vertical) surfaces. Finally, for rapidly eroding sites such as Anza, these methods allow the operators to record quickly and efficiently a large number of potentially vulnerable tracks, which is complicated logistically with traditional casting methods. The 3D documentation may also serve to assess the impact of erosion dynamics on the morphology of fossil tracks. This method complements manual drawing, making tridimensional geometry available for future scientific research, 3D printing, virtual reality, presentation in museums, and other techniques of digital scientific outreach via the web.

Declaration of competing interest

The authors declare that they have no known competing financial interests or personal relationships that could have appeared to influence the work reported in this paper.

Acknowledgements

We are grateful to Martin G. Lockley, an anonymous reviewer, and the associate editor for their constructive comments, which have greatly improved the manuscript.

Appendix A. Supplementary data

Supplementary data to this article can be found online at https://doi.org/10.1016/j.jafrearsci.2020.103985.

References

Adams, T.L., Strganac, C., Polcyn, M.J., Jacobs, L.L., 2010. High resolution three-dimensional laser scanning of the type specimen of *Eubrontes*(?) *glenrosensis* Shuler, 1935, from the Comanchean (Lower Cretaceous) of Texas: implications for digital archiving and preservation. Palaeontol. Electron. 13 (3), 11p.

Adams, T.C., Breithaupt, B.H., 2003. Mid jurassic dinosaurs of northern Wyoming: evidence from yellow brick road dinosaur tracksite, bighorn basin, Wyoming. Wyoming Geo Notes 78, 39–46.

Alexander, R.M.N., 1976. Estimates of speeds of dinosaurs. Nature 261, 129–130.

Alcalá, L., Lockley, M.G., Cobos, A., Mampel, L., Royo-Torres, R., 2016. Evaluating the dinosaur track record: an integrative approach to understanding the regional and global distribution, scientific importance, preservation, and management of tracksites. In: Falkingham, P.L., Marty, D., Richter, A. (Eds.), Dinosaur Tracks: the Next Steps. Indiana University Press, Bloomington; Indianapolis, pp. 101–117, 2016.

Bates, K.T., Manning, P.L., Vila, B., Hodgetts, D., 2008. Three-dimensional modelling and analysis of dinosaur trackways. Palaeontology 51, 999–1010.
Bates, K.T., Falkingham, P.L., Hodgetts, D., Farlow, J.O., Breithaupt, B.H., O'Brien, M., Matthews, N., Sellers, W.I., Manning, P.L., 2009. Digital imaging and public engagement in palaeontology. Geol. Today 25, 134–139.
Bates, K.T., Falkingham, P.L., Rarity, F., Hodgetts, D., Purslow, A., Manning, P.L., 2010. Application of high-resolution laser scanning and photogrammetric techniques to data acquisition, analysis and interpretation in palaeontology. Int. Arch. Photogram. Rem. Sens. Spatial Inf. Sci. 38, 68–73.
Belvedere, M., 2008. Ichnological Researches on the Upper Jurassic Dinosaur Tracks in the Iouaridène Area (Demnat, Central High-Atlas, Morocco). Ph.D thesis, Degli Studi Di Padova University, p. 128.
Bemis, S.P., Micklethwaite, S., Turner, D., James, M.R., Akciz, S., Thiele, S.T., Bangash, H.A., 2014. Ground-based and UAV-Based photogrammetry: a multi-scale, high-resolution mapping tool for structural geology and paleoseismology. J. Struct. Geol. 69, 163–178.
Breithaupt, B.H., Matthews, N.A., 2001. Preserving paleontological resources using photogrammetry and geographic information systems. In: Harmon, D. (Ed.), Crossing Boundaries in Park Management: Proceedings of the 11th Conference on Research and Resource Management in Parks and Public Lands. The George Wright Society, Hancock, Michigan, pp. 62–70.
Breithaupt, B.H., Southwell, E.H., Adams, T., Matthews, N.A., 2001. Innovative documentation methodologies in the study of the most extensive dinosaur tracksite in Wyoming. In: Santucci, V.L., McClelland, L. (Eds.), Proceedings of the 6th Fossil Research Conference. National Park Service D-2228. National Park Service. Geological Resources Division, Lakewood, Colorado, pp. 113–122.
Breithaupt, B.H., Matthews, N.A., Noble, T.A., 2004. An integrated approach to three-dimensional data collection at dinosaur tracksites in the Rocky Mountain West. Ichnos 11 (1–2), 11–26.
Cobos, A., Alcalá, L., 2017. Palaeontological heritage as a resource for promoting geotourism in the rural setting: el Castellar (Teruel, Spain). Geoheritage 10, 405–414.
Doneus, M., 2013. Openness as visualization technique for interpretative mapping of airborne Lidar derived digital terrain models. Rem. Sens. 5, 6427–6442.
Dozier, J., Frew, J., 1990. Rapid calculation of terrain parameters for radiation modeling from digital elevation data. IEEE Trans. Geosci. Rem. Sens. 28, 963–969.
Falkingham, P.L., Margetts, L., Smith, I.M., Manning, P.L., 2009. Reinterpretation of palmate and semi-palmate (webbed) fossil tracks ; insights from finite element modelling. Palaeogeogr. Palaeoclimatol. Palaeoecol. 271, 69–76.
Falkingham, P.L., 2012. Acquisition of high resolution three-dimensional models using free, open-source, photogrammetric software. Palaeontol. Electron. 15 (1), 15.
Falkingham, P.L., 2016. Applying objective methods to subjective track outlines. In: Falkingham, P.L., Marty, D., Richter, A. (Eds.), Dinosaur Tracks: the Next Steps. Indiana University Press, Bloomington; Indianapolis, pp. 72–80, 2016.
Falkingham, P.L., Gatesy, S.M., 2014. The birth of a dinosaur footprint: subsurface 3D motion reconstruction and discrete element simulation reveal track ontogeny. Proc. Natl. Acad. Sci. Unit. States Am. 111 (51), 18279–18284.
Falkingham, P.L., Marty, D., Richter, A., 2016. Dinosaur Tracks : the Next Step. Indiana University Press, Bloomington; Indianapolis, p. 611.
Falkingham, P.L., Bates, K.T., Avanzini, M., Bennett, M., Bordy, E.M., Breithaupt, B.H., Castanera, D., Citton, P., Diaz-Martinez, I., Farlow, J.O., Fiorillo, A.R., Gatesy, S.M., Getty, P., Hatala, K.G., Hornung, J.J., Hyatt, J.A., Klein, H., Lallensack, J.N., Martin, A.J., Marty, D., Matthews, N.A., Meyer, C.A., Milàn, J., Minter, N.J., Razzolini, N.L., Romilio, A., Salisbury, S.W., Sciscio, L., Tanaka, I., Wiseman, A.L.A., Xing, L.D., Belvedere, M., 2018. A standard protocol for documenting modern and fossil ichnological data. Palaeontology 61 (4), 469–480.
Gand, G., Fara, E., Durlet, C., Moreau, J.D., Caravaca, G., André, D., Lefillatre, R., Passet, A., Wiénin, M., Gély, J.P., 2018. Les pistes d'archosauriens : *Kayentapus ubacensis* nov. isp. (Théropodes) et crocodylomorphes du Bathonien des Grands-Causses (France). Conséquence paléo-biologiques, environnementales et géographiques. Ann. Paleontol. 104 (3), 183–216.
Gillette, D.D., Lockley, M.G., 1989. Dinosaur Tracks and Traces. Cambridge Univ. Press, Cambridge, p. 454.
Graversen, O., Milàn, J., Loope, D.B., 2007. Dinosaur tectonics: a structural analysis of theropod undertracks with a reconstruction of theropod walking dynamics. J. Geol. 115, 641–654.
Hitchcock, E., 1838. Report on a Re-examination of the Economical Geology of Massachusetts. Dutton and Wentworth. State printers, p. 152.
Hitchcock, E., 1848. An attempt to discriminate and describe the animals that made the fossil footmarks of the United States, and especially of New England. Mem. Am. Acad. Arts Sci. 3, 129–256.
Hitchcock, E., 1858. Ichnology of New England: A Report on the Sandstone of the Connecticut Valley Especially its Fossil Footmarks, Made to the Government of the Commonwealth of Massachusetts. William White printer, p. 374.
Imhof, E., 2007. Cartographic Relief Presentation. Environmental Systems Research Institute Inc., U. S, third ed. ESRI Press, Redlands, p. 434.
Ishigaki, S., Fujisaki, T., 1989. Three-dimensional representation of *Eubrontes* by the method of moiré topography. In: Gillette, D.D., Lockley, M. (Eds.), Dinosaur Tracks and Traces. Cambridge University Press, Cambridge, UK, pp. 421–425.
Kraus, K., de Gryter, Walter, 2007. Photogrammetry Geometry from Images and Laserscans. In: second ed., p. 459.
Lallensack, J.N., Van Heteren, A.H., Wings, O., 2016. Geometric morphometric analysis of intratrackway variability: a case study on theropod and ornithopod dinosaur trackways from Münchehagen (Lower Cretaceous, Germany). Peer J 4, e2059.
Laws, E., Scott, N., 2003. Developing new tourism services: dinosaurs, a new drive tourism resource for remote regions? J. Vacat. Mark. 9, 368–380.
Lockley, M.G., Houck, K.J., Prince, N.K., 1986. North America's largest dinosaur trackway site: implications for Morrison Formation paleoecology. Geol. Soc. Am. Bull. 97 (10), 1163–1176.
Lockley, M.G., 1991. Tracking Dinosaurs: a New Look at an Ancient World. Cambridge University Press., Cambridge, p. 238.
Longley, P., 2005. Geographic Information Systems and Science. John Wiley and Sons, p. 560.
López, J.A.B., Jiménez, G.A., Romero, M.S., García, E.A., Martín, S.F., Medina, A.L., Guerrero, J.A.E., 2016. 3D modelling in archaeology: the application of Structure from Motion methods to the study of the megalithic necropolis of Panoria (Granada, Spain). J. Archaeol. Sci. Rep. 10, 495–506.
Magail, J., Monna, F., Esin, Y., Wilczek, J., Yeruul-Erdene, C., Gantulga, J.-O., 2017. Applications de la photogrammétrie à la documentation de l'art rupestre, des chantiers de fouilles du bâti – mission du Musée d'Anthropologie préhistorique de Monaco. Bull. Musee Anthropol. Prehist. Monaco 56, 69–92.
Mallison, H., Wings, O., 2014. Photogrammetry in paleontology – a practical guide. Journal of Paleontological Techniques 12, 1–31.
Mara, H., Krömker, S., Jakob, S., Breuckmann, B., 2010. GigaMesh and gilgamesh - 3D multiscale integral invariant cuneiform character extraction. Proc. VAST Int. Symposium on Virtual Reality, Archaeology and Cultural Heritage 131–138.
Masrour, M., Pascual-Arribas, C., de Ducla, M., Hernández-Medrano, N., Pérez-Lorente, F., 2017a. Anza palaeoichnological site. Late Cretaceous. Morocco. Part I. The first African pterosaur trackway (manus only). J. Afr. Earth Sci. 134, 766–775.
Masrour, M., Lkebir, N., Pérez-Lorente, F., 2017b. Anza palaeoichnological site. Late Cretaceous. Morocco. Part II. Problems of large dinosaur trackways and the first African Macropodosaurus trackway. J. Afr. Earth Sci. 134, 776–793.
Matthews, N.A., Breithaupt, B.H., 2001. Close-range photogrammetric experiments at dinosaur ridge. Mt. Geol. 38 (3), 147–153.
Matthews, N.A., Breithaupt, B.H., Noble, T.A., Titus, A., Smith, J., 2005. A geospatial look at the morphological variation of tracks at the Twentymile Wash dinosaur tracksite, Grand Staircase-Escalante National Monument, Utah. J. Vertebr. Paleontol. 25, 90A.
Matthews, N.A., Noble, T.A., Breithaupt, B.H., 2006. The application of photogrammetry, remote sensing and geographic information systems (GIS) to fossil resource management. Bull. N. M.Mus. Nat. Hist. Sci. 34, 119–131.
Matthews, N.A., Noble, T.A., Breithaupt, B.H., 2016. Close-range photogrammetry for 3-D ichnology: the basics of photogrammetric ichnology. In: Falkingham, P.L., Marty, D., Richter, A. (Eds.), Dinosaur Tracks: the Next Steps. Indiana University Press, Bloomington; Indianapolis, pp. 29–55, 2016.
Mazin, J.M., Hantzpergue, P., Pouech, J., 2016. The dinosaur tracksite of loulle (early kimmeridgian; jura, France). Geobios 49 (3), 211–228.
Milàn, J., Loope, D.B., 2007. Preservation and erosion of theropod tracks in eolian deposits: examples from the Middle Jurassic Entrada Sandstone, Utah. U.S.A. J Geol. 115, 375–386.
Monna, F., Esin, Y., Magail, J., Granjon, L., Navarro, N., Wilczek, J., Saligny, L., Couette, S., Dumontet, A., Chateau, C., 2018. Documenting carved stones by 3D modelling – example of Mongolian deer stones. J. Cult. Herit. 34, 116–128.
Monbaron, M., Monbaron, J., 2015. La route des dinosaures : Itinéraires à travers le Geoparc M'Goun, Haut Atlas, Maroc. Région Tadla-Azilal, p. 142.
Moratalla, J.J., Sanz, J.L., Jimenez, S., 1988. Multivariate analysis on Lower Cretaceous dinosaur footprints: discrimination between ornithopods and theropods. Geobios 21, 395–408.
Moreau, J.-D., Trincal, V., Fara, E., Baret, L., Jacquet, A., Barbini, C., Flament, R., Wienin, M., Bourel, B., Jean, A., 2020. Middle Jurassic tracks of sauropod dinosaurs in a deep karst cave from France. J. Vertebr. Paleontol. https://doi.org/10.1080/02724634.2019.1728286.
Olivero, E.B., Ponce, J.J., Marsicano, C.A., Martinioni, D.R., 2007. Depositional settings of the basal lópez de Bertodano formation, maastrichtian, Antarctica. Rev. Asoc. Geol. Argent. 62, 521–529.
Pérez-Lorente, F., 2015. Dinosaur Footprints and Trackways of La Rioja Life of the Past. Indiana University Press, p. 374.
Reguero, M., Goin, F., Acosta Hospitaleche, C., Dutra, T., Marenssi, S., 2013. Late Cretaceous/Paleogene West Antarctica terrestrial biota and its intercontinental affinities. Springer Briefs in Earth System Sciences, South America and the Southern Hemisphere, pp. 55–110.
Remondino, F., Rizzi, A., Girardi, S., Massimo, P.F., Avanzini, M., 2010. 3D Ichnology—recovering digital 3D models of dinosaur footprints. Photogramm. Rec. 25 (131), 266–282.
Reu, J.D., Plets, G., Verhoeven, G., Smedt, P.D., Bats, M., Cherretté, B., Maeyer, W.D., Deconynck, J., Herremans, D., Laloo, P., Meirvenne, M.V., Clercq, W.D., 2013. Towards a three-dimensional cost-effective registration of the archaeological heritage. J. Archaeol. Sci. 40, 1108–1121.
Romilio, A., Salisbury, S.W., 2014. Large dinosaurian tracks from the Upper Cretaceous (Cenomanian–Turonian) portion of the Winton formation, Lark Quarry, central-western Queensland, Australia: 3D Photogrammetric analysis renders the 'stampe de trigger' scenario unlikely. Cretac. Res. 51, 186–207.
Romilio, A., Hacker, J.M., Zlot, R., Poropat, G., Bosse, M., Steven, W.S., 2017. A multidisciplinary approach to digital mapping of dinosaurian tracksites in the lower cretaceous (Valanginian-Barremian) broome sandstone of the dampier peninsula, western Australia. Peer J. https://doi.org/10.7717/Peerj.3013.
Sarjeant, W.A.S., 1989. Ten paleoichnological commandments: a standardized procedure for the description of fossil vertebrate footprints. In: Gilette, D.D., Lockley, M.G. (Eds.), Dinosaur Tracks and Traces. Cambridge Univ. Press, Cambridge, p. 454.
Tavani, S., Corradetti, A., Billi, A., 2016. High precision analysis of an embryonic extensional fault-related fold using 3D orthorectified virtual outcrops: the viewpoint importance in structural geology. J. Struct. Geol. 86, 200–210.

Thulborn, T., 1990. Dinosaur Tracks. Chapman and Hall, p. 424.
Verhoeven, G., Doneus, M., Briese, C., Vermeulen, F., 2012. Mapping by matching: a computer vision-based approach to fast and accurate georeferencing of archaeological aerial photographs. J. Archaeol. Sci. 39, 2060–2070.
Westoby, M.J., Brasington, J., Glasser, N.F., Hambrey, M.J., Reynolds, J.M., 2012. 'Structure-from-Motion' photogrammetry: a low-cost, effective tool for geoscience applications. Geomorphology 179, 300–314.
Wings, O., Lallensack, J.N., Mallison, H., 2016. The Early Cretaceous dinosaur trackways in Münchehagen (Lower Saxony, Germany): 3-D photogrammetry as basis for geometric morphometric analysis of shape variation and evaluation of material loss during excavation. In: Falkingham, P.L., Marty, D., Richter, A. (Eds.), Dinosaur Tracks: the Next Steps. Indiana University Press, Bloomington; Indianapolis, pp. 57–71, 2016.
Yokoyama, R., Shlrasawa, M., Pike, R.J., 2002. Visualizing topography by openness: a new application of image processing to digital elevation models. Photogramm. Eng. Rem. Sens. 68, 257–265.
Zaksek, K., Ostir, K., Kokalj, Z., 2011. Sky-view factor as a relief visualization technique. Rem. Sens. 3, 398–415.

Annexe 3.

	Shape	LaneIn	ArmIn	StrctIn	FenceIn	FrontMound	BackMound	Mound2	Mound3
Diameter	6.817417e-32	6.546045e-08	4.468985e-08	6.353591e-22	4.639691e-05	5.291517e-38	1.348068e-13	1.623530e-27	8.034996e-74
Area	6.985017e-40	5.332233e-11	3.013062e-08	2.565651e-24	6.111118e-05	4.342515e-38	1.126026e-14	1.274267e-27	1.655311e-60
	Mound4	Ring2	Ring2	Ring3	Ring3	Ring4	SuppStrct	CornerSt	Platform
Diameter	3.205575e-26	5.662049e-71	5.533493e-59	1.011304e-46	3.048966e-55	3.924736e-26	1.222029e-14	3.786446e-49	5.804322e-16
Area	3.230991e-27	9.417378e-54	1.499313e-48	5.384095e-40	1.463716e-45	4.898335e-28	8.854805e-15	5.067350e-62	6.459063e-21

Table 1 Results of U Mann-Whitney or Kruskal-Wallis tests for possible dependence of size on other qualitative descriptors

Annexe 4.

Characteristics details for the seven types of khirigsuurs

Type I

Shape	Area	Diameter	LaneIn	ArmIn	StrctIn	FenceIn	FrontMound	BackMound	Mound2
trapezium :10	Min. : 2340	Min. :18.60	faux:8	faux:9	faux:3	faux:9	faux: 0	absent :3	Min. :0.00
autres : 0	1st Qu.: 6708	1st Qu.:21.77	vrai:2	vrai:1	vrai:7	vrai:1	vrai:10	center :0	1st Qu.:1.25
circle : 0	Median :10091	Median :26.05						complet :1	Median :2.00
DSstrc : 0	Mean :16949	Mean :26.02						corners :3	Mean :1.90
incomplets: 0	3rd Qu.:24779	3rd Qu.:30.07						corners+center :1	3rd Qu.:2.00
mixe : 0	Max. :44675	Max. :35.00						corners+center+between:2	Max. :4.00
(Other) : 0									

Mound3	Mound4	Ring1	Ring2	Ring3	Ring4	SuppStrct	DSStrct	CornerStr	Platform	Name
Min. : 2.00	Min. : 0.0	Min. : 3.00	Min. : 2	Min. :2.00	Min. :0	faux:1	faux:3	: 0	0:4	GMo071 :1
1st Qu.: 5.25	1st Qu.: 5.0	1st Qu.: 4.50	1st Qu.: 4	1st Qu.:2.25	1st Qu.:3	vrai:9	vrai:7	absent : 0	2:6	Khu041 :1
Median : 7.00	Median : 5.5	Median : 9.00	Median : 5	Median :3.00	Median :3			pierres levees: 0	4:0	Khu067 :1
Mean : 8.40	Mean : 9.2	Mean : 9.70	Mean : 5	Mean :3.20	Mean :3			tertres :10		Khu069 :1
3rd Qu.:11.00	3rd Qu.:11.5	3rd Qu.:12.75	3rd Qu.: 6	3rd Qu.:3.75	3rd Qu.:4					KTa239 :1
Max. :20.00	Max. :30.0	Max. :20.00	Max. :10	Max. :6.00	Max. :4					KTa286 :1
										(Other):4

X	Y	Azimuth
Min. :653152	Min. :5268118	Min. : 87.69
1st Qu.:659971	1st Qu.:5300624	1st Qu.: 98.49
Median :685967	Median :5332437	Median :101.97
Mean :686644	Mean :5324668	Mean :103.23
3rd Qu.:699368	3rd Qu.:5343570	3rd Qu.:111.35
Max. :749871	Max. :5360025	Max. :122.51

Type II

Shape	Area	Diameter	LaneIn	ArmIn	StrctIn	FenceIn	FrontMound	BackMound	Mound2
trapezium:40	Min. : 832.5	Min. : 9.40	faux:42	faux:41	faux:22	faux:46	faux: 8	absent :28	Min. :0.0000
rectangle: 3	1st Qu.: 1472.4	1st Qu.:13.00	vrai: 6	vrai: 7	vrai:26	vrai: 2	vrai:40	center : 6	1st Qu.:0.0000
square : 3	Median : 2503.6	Median :14.00						complet : 1	Median :1.0000
circle : 2	Mean : 3250.7	Mean :15.03						corners :10	Mean :0.8125
autres : 0	3rd Qu.: 3433.3	3rd Qu.:16.15						corners+center : 3	3rd Qu.:1.0000
DSstrc : 0	Max. :16192.1	Max. :24.00						corners+center+between: 0	Max. :3.0000
(Other) : 0		NA's :1							

Mound3	Mound4	Ring1	Ring2	Ring3	Ring4	SuppStrct	DSStrct	CornerStr	Platform
Min. :0.000	Min. :0.000	Min. :0.000	Min. :0.000	Min. :0.000	Min. :0.000	faux:17	faux:36	: 0	0:25
1st Qu.:2.000	1st Qu.:0.000	1st Qu.:1.750	1st Qu.:1.000	1st Qu.:1.000	1st Qu.:1.000	vrai:31	vrai:12	absent : 0	2:22
Median :2.000	Median :1.000	Median :2.000	Median :2.000	Median :1.000	Median :1.000			pierres levees: 0	4: 1
Mean :2.542	Mean :1.479	Mean :2.479	Mean :1.771	Mean :1.438	Mean :1.542			tertres :48	
3rd Qu.:3.000	3rd Qu.:2.000	3rd Qu.:3.000	3rd Qu.:2.000	3rd Qu.:2.000	3rd Qu.:2.000				
Max. :6.000	Max. :6.000	Max. :8.000	Max. :5.000	Max. :5.000	Max. :5.000				

Name	X	Y	Azimuth
Jar001 : 1	Min. :561763	Min. :5268274	Min. : 81.27
Jar002 : 1	1st Qu.:665221	1st Qu.:5291933	1st Qu.: 95.30
Khu032 : 1	Median :669843	Median :5296643	Median :106.83
Khu042 : 1	Mean :662378	Mean :5320332	Mean :105.20
Khu045 : 1	3rd Qu.:682172	3rd Qu.:5328457	3rd Qu.:112.93
Khu068 : 1	Max. :704303	Max. :5500962	Max. :133.86
(Other):42			

Type III

Shape	Area	Diameter	LaneIn	ArmIn	StrctIn	FenceIn	FrontMound	BackMound	Mound2
trapezium:21	Min. : 141.1	Min. : 5.900	faux:32	faux:35	faux:31	faux:39	faux:27	absent :38	Min. :0.0000
rectangle: 8	1st Qu.: 588.8	1st Qu.: 9.975	vrai: 9	vrai: 6	vrai:10	vrai: 2	vrai:14	center : 0	1st Qu.:0.0000
circle : 6	Median : 991.3	Median :11.750						complet : 2	Median :0.0000
mixe : 4	Mean :1417.9	Mean :11.832						corners : 0	Mean :0.2195
square : 2	3rd Qu.:1887.6	3rd Qu.:13.025						corners+center : 1	3rd Qu.:0.0000
autres : 0	Max. :6412.4	Max. :26.500						corners+center+between: 0	Max. :2.0000
(Other) : 0		NA's :1							

Mound3	Mound4	Ring1	Ring2	Ring3	Ring4	SuppStrct	DSStrct	CornerStr	Platform
Min. :0.000	Min. :0.0000	Min. :0.00	Min. :0.0000	Min. :0.0000	Min. :0.000	faux:22	faux:34	: 0	0:34
1st Qu.:1.000	1st Qu.:0.0000	1st Qu.:1.00	1st Qu.:0.0000	1st Qu.:0.0000	1st Qu.:0.000	vrai:19	vrai: 7	absent :11	2: 7
Median :1.000	Median :0.0000	Median :1.00	Median :1.0000	Median :1.0000	Median :1.000			pierres levees: 1	4: 0
Mean :1.268	Mean :0.3902	Mean :1.39	Mean :0.9756	Mean :0.8293	Mean :1.049			tertres :29	
3rd Qu.:2.000	3rd Qu.:0.0000	3rd Qu.:2.00	3rd Qu.:2.0000	3rd Qu.:1.0000	3rd Qu.:1.000				
Max. :4.000	Max. :3.0000	Max. :5.00	Max. :3.0000	Max. :7.0000	Max. :4.000				

Name	X	Y	Azimuth
GMo011 : 1	Min. :519609	Min. :5271556	Min. : 44.41
GMo076 : 1	1st Qu.:670769	1st Qu.:5287998	1st Qu.: 92.23
GMo077 : 1	Median :676191	Median :5295514	Median :101.59
GMo078 : 1	Mean :673821	Mean :5326760	Mean :103.69
GMo079 : 1	3rd Qu.:688227	3rd Qu.:5359523	3rd Qu.:114.97
GMo080 : 1	Max. :714827	Max. :5644623	Max. :163.05
(Other):35		NA's :4	

Type IV

```
      Shape         Area             Diameter       LaneIn    ArmIn    StrctIn   FenceIn   FrontMound                  BackMound      Mound2
 trapezium:48   Min.   :  51.87   Min.   : 3.300   faux:65   faux:72   faux:68   faux:70   faux:62    absent               :72   Min.   :0.0000
 rectangle: 9   1st Qu.: 379.97   1st Qu.: 8.525   vrai: 8   vrai: 1   vrai: 5   vrai: 3   vrai:11    center               : 1   1st Qu.:0.0000
 square   : 8   Median : 687.66   Median : 9.500                                                     complet              : 0   Median :0.0000
 mixe     : 6   Mean   : 877.46   Mean   : 9.631                                                     corners              : 0   Mean   :0.1507
 circle   : 2   3rd Qu.: 947.00   3rd Qu.:11.250                                                     corners+center       : 0   3rd Qu.:0.0000
 autres   : 0   Max.   :4392.51   Max.   :14.800                                                     corners+center+between: 0   Max.   :2.0000
 (Other)  : 0                     NA's   :3
     Mound3          Mound4          Ring1           Ring2           Ring3           Ring4        SuppStrct DSStrct            CornerStr
 Min.   : 0.0000   Min.   :0.0000   Min.   :0.0000   Min.   :0.0000   Min.   :0.0000   Min.   :0.0000   faux:38   faux:70                : 0
 1st Qu.: 0.0000   1st Qu.:0.0000   1st Qu.:0.0000   1st Qu.:0.0000   1st Qu.:0.0000   1st Qu.:0.0000   vrai:35   vrai: 3   absent       : 0
 Median : 1.0000   Median :0.0000   Median :1.0000   Median :0.0000   Median :0.0000   Median :0.0000                       pierres levees: 4
 Mean   : 0.8904   Mean   :0.1233   Mean   :0.7808   Mean   :0.5616   Mean   :0.3699   Mean   :0.4658                       tertres       :69
 3rd Qu.: 1.0000   3rd Qu.:0.0000   3rd Qu.:1.0000   3rd Qu.:1.0000   3rd Qu.:1.0000   3rd Qu.:1.0000
 Max.   :14.0000   Max.   :1.0000   Max.   :3.0000   Max.   :3.0000   Max.   :3.0000   Max.   :2.0000

 Platform      Name          X               Y              Azimuth
 0:66     GMo032 : 1   Min.   :561847   Min.   :5267635   Min.   : 47.77
 2: 7     GMo065 : 1   1st Qu.:672094   1st Qu.:5290288   1st Qu.: 85.58
 4: 0     GMo069 : 1   Median :678715   Median :5323361   Median :105.08
          GMo070 : 1   Mean   :679935   Mean   :5332387   Mean   :105.87
          GMo073 : 1   3rd Qu.:704049   3rd Qu.:5362707   3rd Qu.:117.72
          GMo074 : 1   Max.   :835054   Max.   :5501139   Max.   :261.87
          (Other):67                                      NA's   :16
```

Type V

```
      Shape         Area           Diameter       LaneIn     ArmIn     StrctIn    FenceIn    FrontMound                  BackMound      Mound2
 trapezium:53   Min.   :  44.6   Min.   : 2.900   faux:164   faux:164   faux:164   faux:164   faux:164   absent               :164   Min.   :0.00000
 square   :41   1st Qu.: 156.2   1st Qu.: 5.800   vrai:  0   vrai:  0   vrai:  0   vrai:  0   vrai:  0   center               :  0   1st Qu.:0.00000
 mixe     :32   Median : 244.6   Median : 7.300                                                          complet              :  0   Median :0.00000
 rectangle:23   Mean   : 375.2   Mean   : 7.497                                                          corners              :  0   Mean   :0.02439
 circle   :14   3rd Qu.: 479.5   3rd Qu.: 8.850                                                          corners+center       :  0   3rd Qu.:0.00000
 oval     : 1   Max.   :4736.0   Max.   :13.800                                                          corners+center+between:  0   Max.   :1.00000
 (Other)  : 0                    NA's   :5
     Mound3          Mound4          Ring1           Ring2           Ring3           Ring4        SuppStrct  DSStrct             CornerStr
 Min.   :0.0000   Min.   :0.00000   Min.   :0.0000   Min.   :0.0000   Min.   :0.00000   Min.   :0.0000   faux:164   faux:164                :  0
 1st Qu.:0.0000   1st Qu.:0.00000   1st Qu.:0.0000   1st Qu.:0.0000   1st Qu.:0.00000   1st Qu.:0.0000   vrai:  0   vrai:  0   absent       :  0
 Median :0.0000   Median :0.00000   Median :0.0000   Median :0.0000   Median :0.00000   Median :0.0000                         pierres levees:  0
 Mean   :0.2256   Mean   :0.01829   Mean   :0.2622   Mean   :0.1463   Mean   :0.06707   Mean   :0.1402                         tertres       :164
 3rd Qu.:0.0000   3rd Qu.:0.00000   3rd Qu.:0.0000   3rd Qu.:0.0000   3rd Qu.:0.00000   3rd Qu.:0.0000
 Max.   :2.0000   Max.   :1.00000   Max.   :3.0000   Max.   :2.0000   Max.   :1.00000   Max.   :2.0000

 Platform      Name          X               Y              Azimuth
 0:164    GMo001 :  1   Min.   :564689   Min.   :5267615   Min.   : 50.18
 2:  0    GMo002 :  1   1st Qu.:675433   1st Qu.:5287762   1st Qu.: 87.39
 4:  0    GMo004 :  1   Median :678810   Median :5295037   Median : 99.12
          GMo005 :  1   Mean   :686140   Mean   :5317563   Mean   :107.19
          GMo006 :  1   3rd Qu.:712466   3rd Qu.:5359556   3rd Qu.:113.93
          GMo007 :  1   Max.   :834760   Max.   :5460348   Max.   :288.60
          (Other):158                                     NA's   :118
```

Type VI

```
      Shape          Area            Diameter       LaneIn     ArmIn     StrctIn    FenceIn    FrontMound                  BackMound
 circle   :195   Min.   :  10.18   Min.   : 1.800   faux:318   faux:318   faux:316   faux:318   faux:319   absent               :318
 square   : 52   1st Qu.:  50.41   1st Qu.: 3.600   vrai:  1   vrai:  1   vrai:  3   vrai:  1   vrai:  0   center               :  0
 trapezium: 36   Median : 102.72   Median : 5.400                                                          complet              :  0
 rectangle: 23   Mean   : 212.52   Mean   : 6.004                                                          corners              :  1
 mixe     : 11   3rd Qu.: 216.60   3rd Qu.: 7.700                                                          corners+center       :  0
 oval     :  2   Max.   :3966.02   Max.   :26.100                                                          corners+center+between:  0
 (Other)  :  0                    NA's   :23
     Mound2          Mound3          Mound4          Ring1           Ring2           Ring3           Ring4        SuppStrct  DSStrct
 Min.   :0.00000   Min.   :0.0000   Min.   :0.000000   Min.   :0.0000   Min.   :0.00000   Min.   :0.0000   Min.   :0.0000   faux:301   faux:317
 1st Qu.:0.00000   1st Qu.:0.0000   1st Qu.:0.000000   1st Qu.:0.0000   1st Qu.:0.00000   1st Qu.:0.0000   1st Qu.:0.0000   vrai: 18   vrai:  2
 Median :0.00000   Median :0.0000   Median :0.000000   Median :0.0000   Median :0.00000   Median :0.0000   Median :0.0000
 Mean   :0.00627   Mean   :0.1285   Mean   :0.003135   Mean   :0.1881   Mean   :0.08777   Mean   :0.0627   Mean   :0.0815
 3rd Qu.:0.00000   3rd Qu.:0.0000   3rd Qu.:0.000000   3rd Qu.:0.0000   3rd Qu.:0.00000   3rd Qu.:0.0000   3rd Qu.:0.0000
 Max.   :1.00000   Max.   :2.0000   Max.   :1.000000   Max.   :3.0000   Max.   :2.00000   Max.   :3.0000   Max.   :2.0000

          CornerStr   Platform      Name           X               Y              Azimuth
               :  1   0:315    Dur001 :  1   Min.   :525536   Min.   :5267575   Min.   : 46.82
 absent        :318   2:  4    GMo003 :  1   1st Qu.:675302   1st Qu.:5288810   1st Qu.: 88.11
 pierres levees:  0   4:  0    GMo009 :  1   Median :680037   Median :5333660   Median : 96.57
 tertres       :  0            GMo010 :  1   Mean   :682071   Mean   :5332850   Mean   :100.89
                               GMo013 :  1   3rd Qu.:712746   3rd Qu.:5362901   3rd Qu.:116.60
                               GMo014 :  1   Max.   :715055   Max.   :5531055   Max.   :179.43
                               (Other):313                                     NA's   :273
```

Type VII

```
      Shape          Area            Diameter       LaneIn     ArmIn     StrctIn    FenceIn    FrontMound                  BackMound      Mound2
 square   :60   Min.   : 16.28   Min.   : 1.800   faux:135   faux:135   faux:135   faux:135   faux:135   absent               :135   Min.   :0
 rectangle:25   1st Qu.: 54.79   1st Qu.: 3.800   vrai:  0   vrai:  0   vrai:  0   vrai:  0   vrai:  0   center               :  0   1st Qu.:0
 trapezium:25   Median : 88.98   Median : 4.300                                                          complet              :  0   Median :0
 mixe     :17   Mean   :119.40   Mean   : 4.863                                                          corners              :  0   Mean   :0
 circle   : 8   3rd Qu.:162.87   3rd Qu.: 5.900                                                          corners+center       :  0   3rd Qu.:0
 autres   : 0   Max.   :508.84   Max.   :10.600                                                          corners+center+between:  0   Max.   :0
 (Other)  : 0                   NA's   :14
     Mound3      Mound4      Ring1           Ring2           Ring3           Ring4        SuppStrct  DSStrct             CornerStr   Platform
 Min.   :0   Min.   :0   Min.   :0.00000   Min.   :0.000000   Min.   :0.000000   Min.   :0.00000   faux:135   faux:135                :  0   0:135
 1st Qu.:0   1st Qu.:0   1st Qu.:0.00000   1st Qu.:0.000000   1st Qu.:0.000000   1st Qu.:0.00000   vrai:  0   vrai:  0   absent       :  0   2:  0
 Median :0   Median :0   Median :0.00000   Median :0.000000   Median :0.000000   Median :0.00000                         pierres levees:135   4:  0
 Mean   :0   Mean   :0   Mean   :0.02222   Mean   :0.007407   Mean   :0.007407   Mean   :0.01481                         tertres       :  0
 3rd Qu.:0   3rd Qu.:0   3rd Qu.:0.00000   3rd Qu.:0.000000   3rd Qu.:0.000000   3rd Qu.:0.00000
 Max.   :0   Max.   :0   Max.   :1.00000   Max.   :1.000000   Max.   :1.000000   Max.   :1.00000

     Name          X               Y              Azimuth
 GMo016 :  1   Min.   :564736   Min.   :5267511   Min.   : NA
 GMo017 :  1   1st Qu.:675815   1st Qu.:5288989   1st Qu.: NA
 GMo022 :  1   Median :679906   Median :5296222   Median : NA
 GMo023 :  1   Mean   :687818   Mean   :5321117   Mean   :NaN
 GMo024 :  1   3rd Qu.:712943   3rd Qu.:5359513   3rd Qu.: NA
 GMo030 :  1   Max.   :714724   Max.   :5460414   Max.   : NA
 (Other):129                                     NA's   :135
```

Annexe 5.

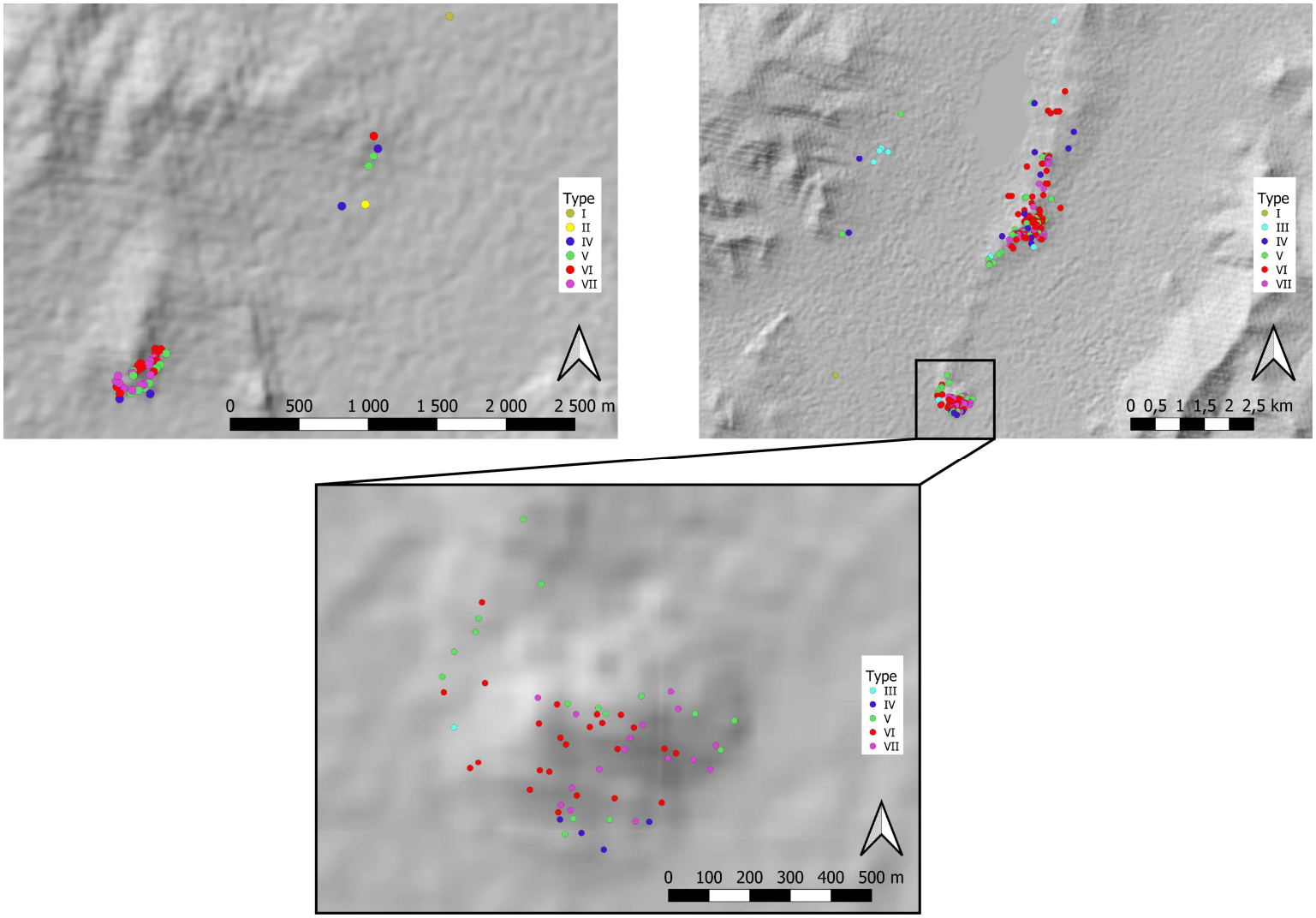

Distribution of the khirigsuur types over part of the Khunui river. The bottom map shows details of at necropolis in the valley.

Annexe 6.

Thésaurus pour l'encodage des symboles sur les stèles

Motifs géométriques

Spirale : spiral	**SP**			
Disque : disc	**DQ** **DC**			
Grand cercle = large circle	**GC** **LC**	**Rayon**		
		Absence	**0**	
		Un	**1**	
		Deux	**2**	
		Trois	**3**	
		Quatre et plus	**4**	
		Ornement		
		Absence	**0**	
		Présence	**1**	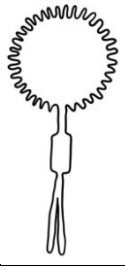
		Remplissage		
		Aucun	**0**	
		Points	**1**	

		Animaux	**2**	
		Autres	**3**	
Petit cercle = small circle	**PC** **SC**	**Rayon**		
		Absence	**0**	
		Un	**1**	
		Deux	**2**	
		Trois	**3**	
		Quatre et plus	**4**	
		Ornement		
		Absence	**0**	
		Présence	**1**	
Obliques : diagonal	**OB** **DI**	**Nombre**		
		Effectif	**1-9**	**1, 2, 3…**
		Orientation (point bas)		
		Droite	**0**	
		Gauche	**1**	
Bandeau : blindfold	**BD** **BF**	**Epaisseur**		
		Large	**0**	
		Fin	**1**	

Collier = necklace	**CONE**	**Motif**		
		Trait	**0**	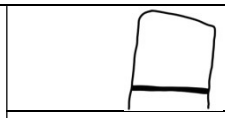
		Cupules	**1**	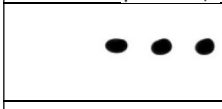
		Trait+cupules	**2**	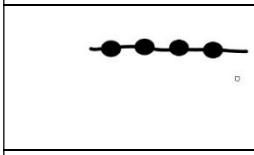
		Trait verticaux	**3**	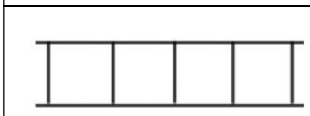
		Pendentif		
		Absence	**0**	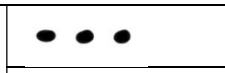
		Présence	**1**	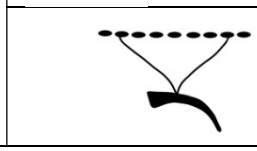
		Fermoir		
		Absence	**0**	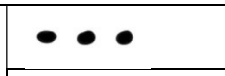
		Présence	**1**	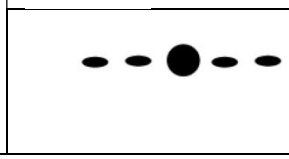

Objets

Masse : mallet	**MS** **MS**			
Matraque : baton	**MT** **BT**			
Char : wagon	**CH** **WA**			
Tresse : braid	**CB** **BR**			
Ceinture = belt	**CE** **BE**	**Forme**		
		Corde	**0**	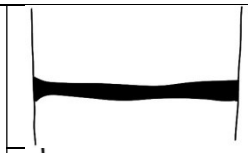
		Ruban	**1**	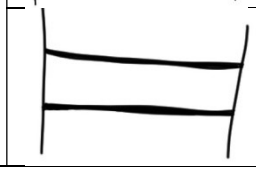
		Remplissage		
		Vide	**A**	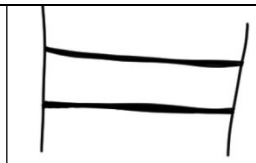
		Plein	**B**	
		Angle	**C**	
		Angle 90°	**D**	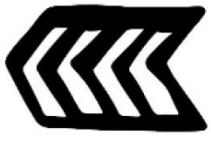

		Maille	**E**	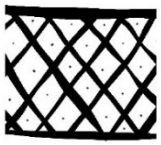
		Losange	**F**	
		Lignes horizontales	**G**	
		Lignes verticales	**H**	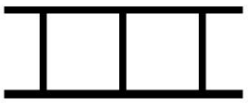
		Onde	**I**	
		Points	**J**	
		Rectangle	**K**	
		Embellissement		
		Rien	**0**	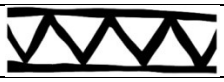
		Points	**1**	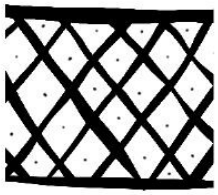 
		Triangle	**2**	 
		Angle	**3**	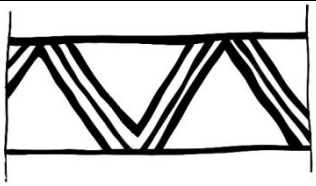
		Traits	**4**	

		Losange	**5**	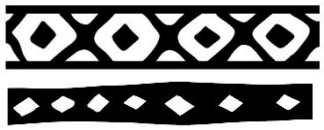
		Point de symétrie	**6**	
Couteau : knife	**CT** **KN**	**Fourreau**		
		Absence	**0**	
		Présence	**1**	
		Forme de la lame		
		En ‘C’	**0**	
		En ‘S’	**1**	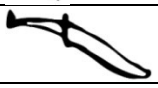
		Pommeau		
		Absence	**0**	
		Trou	**1**	
		Tête zoomorphe	**2**	
		Attache		
		Absence	**0**	
		Présence	**1**	
Poignard : dagger	**PO** **DA**	**Fourreau**		
		Absence	**0**	
		Plein	**1**	

		Vide	**2**	
		Décoré	**3**	
		Poignée		
		Vide	**0**	
		Pleine	**1**	
		Avec garde	**2**	
		Pommeau		
		Simple	**0**	
		Cercle	**1**	
		Double cercle	**2**	
		Losange	**3**	
		Tête zoomorphe	**4**	

		Attache		
		Absence	**0**	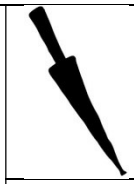
		Présence	**1**	
Carquois : quiver	**CA** **QV**	**Attache**		
		Absence	**0**	
		Un	**1**	
		Deux	**2**	
		Trois	**3**	
		Associé arc		
		Oui	**0**	
		Non	**1**	
		Attaché Ceinture		
		Oui	**0**	

		Non	**1**	
Hache : axe	**HA** **AX**	**Manche**		
		Plein	**0**	
		Creux	**1**	
		Gradué	**2**	
		Attache		
		Absence	**0**	
		Présence	**1**	
		Attaché Ceinture		
		Sans contact	**0**	
		Attaché	**1**	
		Recouvrant	**2**	
Pic : pick	**PI**	**Manche**		
		Plein	**0**	

		Creux	**1**	
		Gradué	**2**	
		Attache		
		Absence	**0**	
		Présence	**1**	
		Attaché Ceinture		
		Sans contact	**0**	
		Attaché	**1**	
		Recouvrant	**2**	
Pierre à aiguiser : sharpen stone	**PA SS**	**Forme attache**		
		Trou	**0**	
		Trait	**1**	

		Attache ceinture		
		Oui	**0**	
		Non	**1**	
Crochet : hook	**CR** **HK**	**Forme**		
		En ‘C’	**0**	
		En ‘W‘	**1**	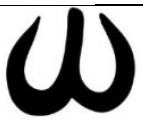
		En ‘Pl’	**2**	
		Pointe		
		Rentrante	**0**	
		Sortante	**1**	
Bouclier : shield	**BO** **SH**	**Forme**		
		Rectangulaire	**0**	
		Pentagonal	**1**	
		Remplissage		
		Angle	**0**	
		Arête	**1**	

		Losange	**2**	
		Losange tressé	**3**	
		Embellissement		
		Rien	**0**	
		Cercle	**1**	
		Cercles concent.	**2**	
		Cercles mult.	**3**	
		Cercles mult. liés	**4**	
		Losanges	**5**	
		Disque tronqué	**6**	
		Vertical	**7**	
Arc : bow	**AR BW**	**Flèche**		
		Sans	**0**	
		Symétrique	**1**	

		Dissymétrique	**2**	
		Côté	**3**	
Lance	**LA**			

Animaux

Bouquetin : ibex	**BQ** **IB**			
Poisson : fish	**PS** **FI**			
Yack : yak	**YK**	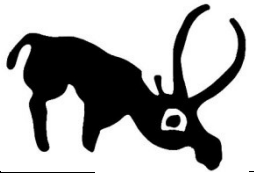		
Oiseau = bird	**OI** **BI**			
Sanglier : boar	**SG** **BO**	**Crinière**		
		Absence	**0**	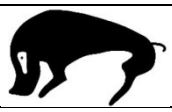
		Présence	**1**	
Cheval : horse	**CV** **HS**	**Corps**		
		Plein	**0**	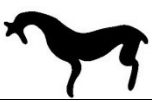
		Canal	**1**	

Félin : feline	**FL**	**Position**		
		Debout	**0**	
		Enroulé	**1**	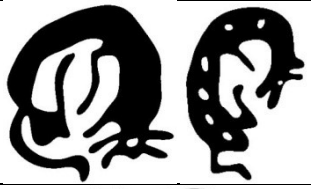
		Couché	**2**	
		Corps		
		Vide	**0**	
		Traits	**1**	
		Points	**2**	
		Taches	**3**	
		Chevrons	**4**	
Cerf =deer	**CF DE**	**Orientation**		
		N	**0**	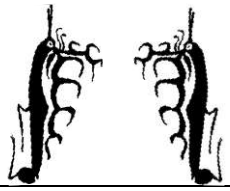
		NE	**1**	

		E	**2**	
		SE	**3**	
		S	**4**	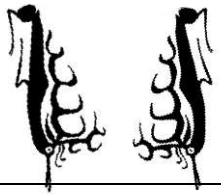
		SW	**5**	
		W	**6**	
		NW	**7**	
		Tête		
		Droite	**0**	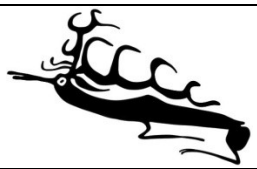
		Retourné	**1**	
		Tronqué		

		Non	**0**	
		Oui (avec pattes)	**1**	
		Oui (sans patte)	**2**	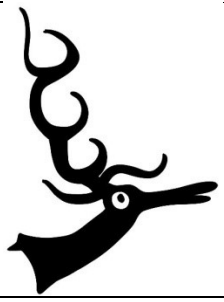
		Nombre de bois		
		Aucun	**0**	
		Un	**1**	
		Deux	**2**	
		Pattes complètes		
		Aucune	**0**	
		Une	**1**	
		Deux	**2**	

		Corps		
		Vide	**0**	
		Trait épaule	**1**	
		Zébré	**2**	
		Andouiller		
		Vide	**0**	
		Point	**1**	
		Cerf	**2**	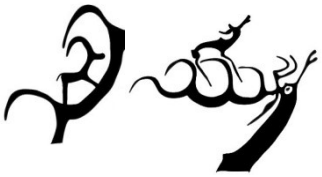
		Cheval	**3**	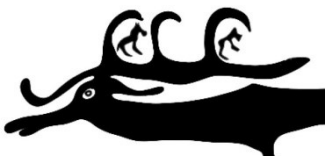 

Visage = Face	**VH** **MF**